Synthesis and Characterisation of Some Layered and Perovskite Materials

by

Nicola Narmada Muthumanike Gurusinghe

A thesis submitted to

The University of Birmingham

for the degree of

Doctor of Philosophy

School of Chemistry

The University of Birmingham

Birmingham

B15 2TT, UK

November 2012

Abstract

The perovskites $LaSr_2Fe_2SbO_9$ and $La_2Sr_2Fe_3SbO_{12}$ crystallise in $P2_1/n$ space group with Fe^{3+} occupying the two crystallographically distinct six-coordinate sites in a ratio of approximately 1:2. Neutron diffraction data suggest a G-type long-range antiferromagnetism in both materials at 2 K and 300 K.

The *A* site cation ordering in $Ln_2SrFe_2O_7$ (Ln = La, Nd, Eu) and $La_2BaFe_2O_7$ increases as the mismatch in *A* site cation size increases. These phases exhibit long-range antiferromagnetic ordering at 300 K and 2 K; the magnetic moments in $La_2BaFe_2O_7$ and $Nd_2SrFe_2O_7$ gradually rotate in the temperature ranges 210 K to 190 K and 17 K to 9 K, respectively. The fluorine incorporation into these phases happens *via* anion insertion and anion substitution. The partial cation ordering or large overall size of the *A* site cations allows accommodation of more F^- ions causing no change to the Fe oxidation state.

Both $CaMnO_{3-\delta}$ and $SrFeO_{3-\delta}$ are amenable to phosphate and sulphate anion incorporation. The unit cell sizes increase with the increase of dopant level. The oxy-anion insertion stabilises the cubic structure in all doped phases of $SrFeO_{3-\delta}$, but only the higher phosphate levels of $CaMnO_{3-\delta}$ phases. The anion incorporation induced some mixed ion valencies but failed to introduce extra oxygen vacancies.

Acknowledgments

I would like to gratefully and sincerely thank Prof Colin Greaves for his guidance, understanding and most importantly, his patience during my studies. His mentorship was paramount in providing a well rounded experience, and encouraged me to not only grow as an experimentalist but also as an independent thinker.

I am deeply grateful to Prof F J Berry for his assistance, guidance and encouragement. Also I'm so thankful for him for recording and interpreting Mössbauer spectra. I would also like to thank the instrument scientist Dr Vladimir Pomjakushin for his support in recording neutron diffraction data. Special thanks to Dr Louise Male and Dr Jackie Deans for technical supports. Thanks to The University of Birmingham, College of Physical Sciences and Engineering for awarding me an 'Elite Postgraduate Scholarship' to support my studies. Many thanks go into all past and present members of Materials Chemistry group for their encouragement, support and friendship.

To my ever loving grandma, my strength and the role model of my life, to whom I owe much for loving me so much simply because I'm her eldest grandchild!!

Words fail me to express my appreciation to my one and only brother Nicoloy for his clever advices, suggestions and thoughtful support, as, without those, all my work, would not have been possible. He is my wings to my endeavours.

Where would I be without my parents? They gave me life, gave my name and strength to my weak soul. Their love, guidance, hard work, dedication, courage and confidence made me a victorious person as my name, Nicola implies. They deserve all credits of my achievements. I'm so proud of them and their pride for me is the main goal in my life.

Table of Contents

CHAPTER ONE: *Introduction*

CHAPTER TWO: *Experimental Techniques*

CHAPTER 3: *Synthesis and Characterisation of Double Perovskites* $LaSr_2Fe_2SbO_9$ *and* $La_2Sr_2Fe_3SbO_{12}$

Abbreviations

AFM	Antiferromagnetism
EXAFS	Extended X-ray absorption fine structure
FC	Field-cooled
FM	Ferromagnetism
NPD	Neutron powder diffraction
RP	Ruddlesden-Popper
SEM	Scanning electron microscopy
SOFC	Solid oxide fuel cell
T_C	Curie temperature
TGA	Thermogravimetric analysis
T_N	Néel temperature
XRPD	X-ray powder diffraction
ZFC	Zero-field-cooled

CHAPTER ONE

Introduction

1.1 Background

Perovskites and perovskite-related materials exhibit a variety of valuable physical properties that can be used in a wide range of applications. These materials are flexible in composition and this can be exploited to modify their structure and physical properties. This thesis describes the synthesis and characterisation of some novel perovskite-related materials and studies of anion manipulation to control the structure and properties of such materials. This chapter provides a background to the work presented in this thesis. The chapter begins with an introduction to the crystal structures that appear in later chapters of this thesis. The magnetic properties, the different forms of bulk magnetism, electronic and ionic conductivity in solids are also discussed. The aims of this project are discussed at the end of this chapter; detailed description of the materials studied and previous work related to this research are provided in the following chapters.

1.2 Perovskites and Related Structures

1.2.1 Perovskite Structure

Perovskite is a ternary oxide which was named after the identification of $CaTiO_3$ by L A Perovski.[1] The typical chemical formula of perovskite is ABO_3, where *A* and *B* denote two different cations. The ideal structure of perovskite, illustrated in *Figure 1.1*, is a cubic lattice where the larger *A* cation is in the centre of the unit cell, surrounded by twelve *X*

anions halfway along each edge of the unit cell. The smaller *B* cations are in the corners of the unit cell and are coordinated by six *X* anions. The *A* cations are normally alkaline earth or lanthanide cations while *B* cations are transition metals and *X* anions can be oxide or halide anions. In *Figure 1.1b*, the perovskite structure has been described as a three dimensional net of corner sharing BX_6 octahedra with *A* cations in the twelve fold cavities in between the polyhedra.

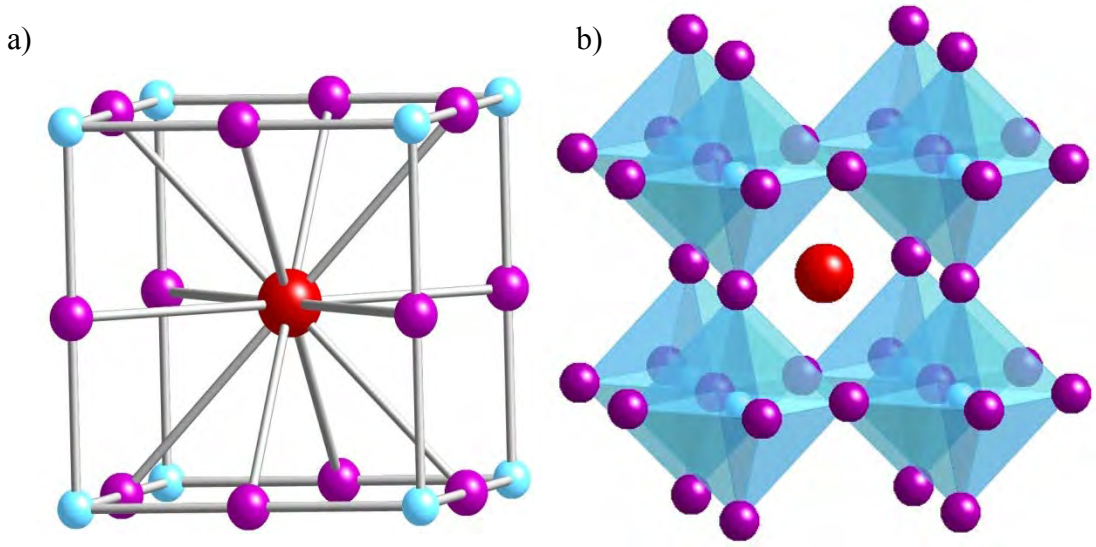

Figure 1.1 Ideal cubic perovskite structure a) unit cell with *A* and *B* cations shown in red and blue, respectively and *X* anions shown in purple, b) shows corner linked BX_6 octahedra in blue with *X* anions and the *A* site cations shown in purple and red, respectively.

Although few compounds have this ideal cubic structure, many perovskite materials have slightly distorted variants with lower symmetry. This distortion occurs mainly because of size effects, the Jahn-Teller effect and deviations from the ideal composition.[2] Although a distortion of a certain perovskite compound can be assigned to a single effect, most of the time it is due to several factors acting on the compound. In the case of the ideal structure,

there is contact between *A*, *B* and *X* and the relationship between the radii of *A*, *B* and *X* as described in Equation 1.1 holds true:

$$r_A + r_X = \sqrt{2}\,(r_B + r_X) \tag{1.1}$$

where r_A, r_B and r_X are the ionic radii of the *A* and *B* cations and *X* anions, repectively.

The deviation from the ideal structure in perovskite can be expressed using the Goldschmidt tolerance factor *t* as described in Equation 1.2.

$$t = \frac{r_A + r_X}{\sqrt{2}\,(r_B + r_X)} \tag{1.2}$$

where r_A, r_B and r_X are the ionic radii of the *A* and *B* cations and *X* anions, respectively.

The ideal cubic perovskite has a tolerance factor of one. If the *B* cation is larger in size compared to the *A* site cation then the *t* value becomes smaller than one, compressing the *B* – *X* bonds and putting *A* – *X* bonds under tension. As a result, the BX_6 octahedra tilt in order to fill space. The cubic structure exists in the range $0.9 \leq t \leq 1$. Lower values of *t* lower the symmetry of the crystal structure. If *t* is larger than one due to a large *A* cation or a proportionally too small *B* cation, then *B* cations displace from the centre of the BX_6 octahedra in order to improve the *B* – *X* bonding.[3] Displacement of the *B* cation towards an apex of the octahedra is known as a tetragonal displacement, whilst displacement towards an equatorial edge of the octahedra is known as an orthorhombic displacement and in a rhombohedral displacement, the *B* cation displaces towards a face of the octahedra.[4]

1.2.2 Ordered Perovskites

Ordered perovskites are derivatives of the simple ternary perovskite ABX_3 structure when either or both *A* and *B* site cations are replaced by combinations of other cations. When cations are ordered only at one site double perovskites may form whereas if ordering occurs at both sites complex or quadruple perovskites are formed. The common *B* site ordered perovskites have the general formula $A_2B'B''X_6$ or $A_3B'B''_2X_9$ where *B*' and *B*" are different cations. The ordering at the *B* site in these compounds give 1 : 1 and 1 : 2 ordering, respectively. The 1 : 1 type ordering is also known in the *A* site, $A'A''B_2X_6$ where *A*' and *A*" are different cations. The 1 : 3 type ordering of *A* site cations, $A'A''_3B_4X_{12}$ is quite common, *e.g*. $CaCu_3Mn_4O_{12}$,[5] whereas 1 : 3 ordering of *B* site, $A_4B'B''_3X_{12}$ is relatively rare, *e.g*. $Ba_4LiSb_3O_{12}$.[6]

Ideal 1 : 1 *B* site ordered perovskites are derivatives of the ideal cubic ABX_3 perovskites in which the *B* cations are ordered along the (1 1 1) planes, as shown in *Figure 1.2*. These compounds crystallise in the space group $Fm\bar{3}m$ and have a cubic 2*a* unit cell. There are two crystallographic sites for *B* cations and they exhibit long-range order with no mixing of the *B* site cations over the two sites. In the ordered structure there are two *B* cation sublattices (*Figure 1.3*) and no tilting of the BO_6 or $B'O_6$ polyhedra. Similarly, ideal 1 : 2 double perovskites are formed when the *B* cations are ordered along (1 1 1) planes (*Figure 1.4*) and the BO_6 or $B'O_6$ polyhedra are not tilted. The magnitude of the charge difference between the *B* site cations of these compounds plays a significant role in determining the degree of ordering, and compounds with the greatest difference have the greatest propensity to form completely ordered structures.[7]

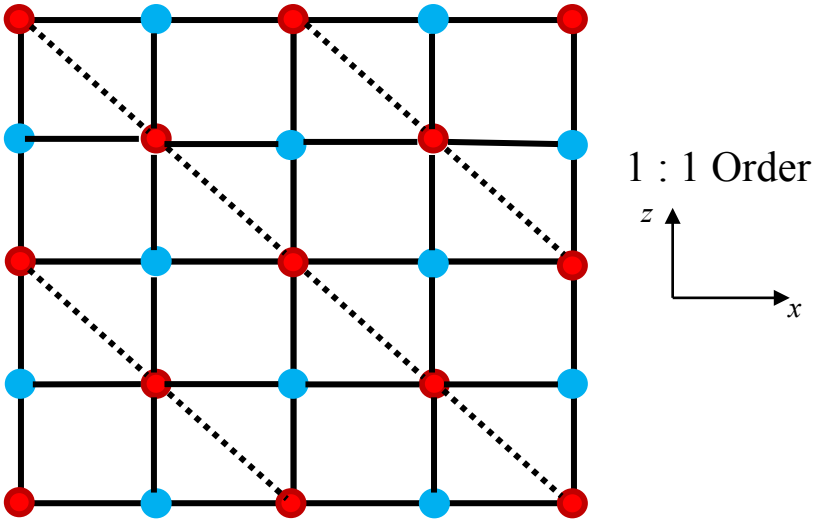

Figure 1.2 Ideal *B* site 1 : 1 ordering along the *xz* plane in $Fm\bar{3}m$ $A_2BB'X_6$ double perovskite.

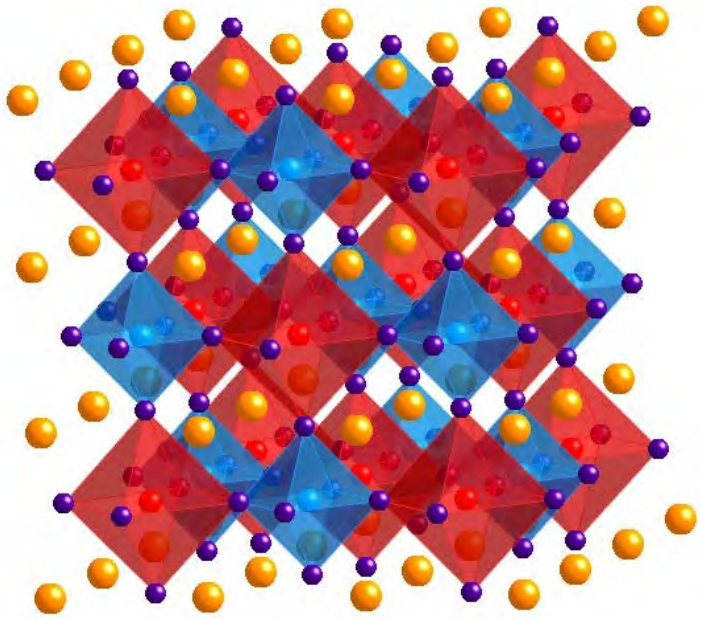

Figure 1.3 Ideal *B* site ordering in $Fm\bar{3}m$ $A_2BB'X_6$ double perovskite, showing the ordering of BX_6 (red) and $B'X_6$ (blue) polyhedral on sublattices.

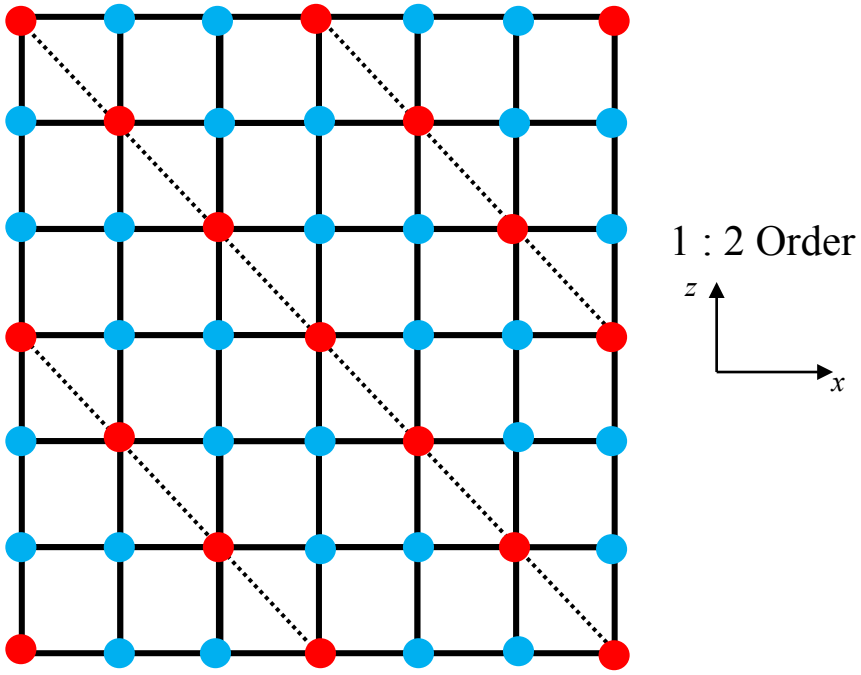

Figure 1.4 Ideal *B* site 1 : 2 ordering along the *xz* plane in $Fm\bar{3}m$ $A_2BB'X_6$ double perovskite.

1.2.3 Ruddlesden-Popper Phases

Ruddlesden-Popper Phases are layered perovskites with the general formula $AX(ABX_3)_n$ where *AX* represents a rock-salt structure that separates the blocks of perovskite layers characterised by n = 1, 2, 3.....∞. The ideal structures of n = 1 and n = 2 Ruddlesden-Popper phases are shown in *Figure 1.5*. The corner sharing BX_6 octahedra form layers along the *c* axis, with *A* cations occupying the nine and twelve coordinate interstitial sites. The first characterised Ruddlesden-Popper phases were the Sr_2TiO_4 series, fully characterised by Ruddlesden and Popper.[8] It is well known that synthesis of these materials is difficult, especially phases with higher n values, so less attention has been devoted to these materials.

a) b)

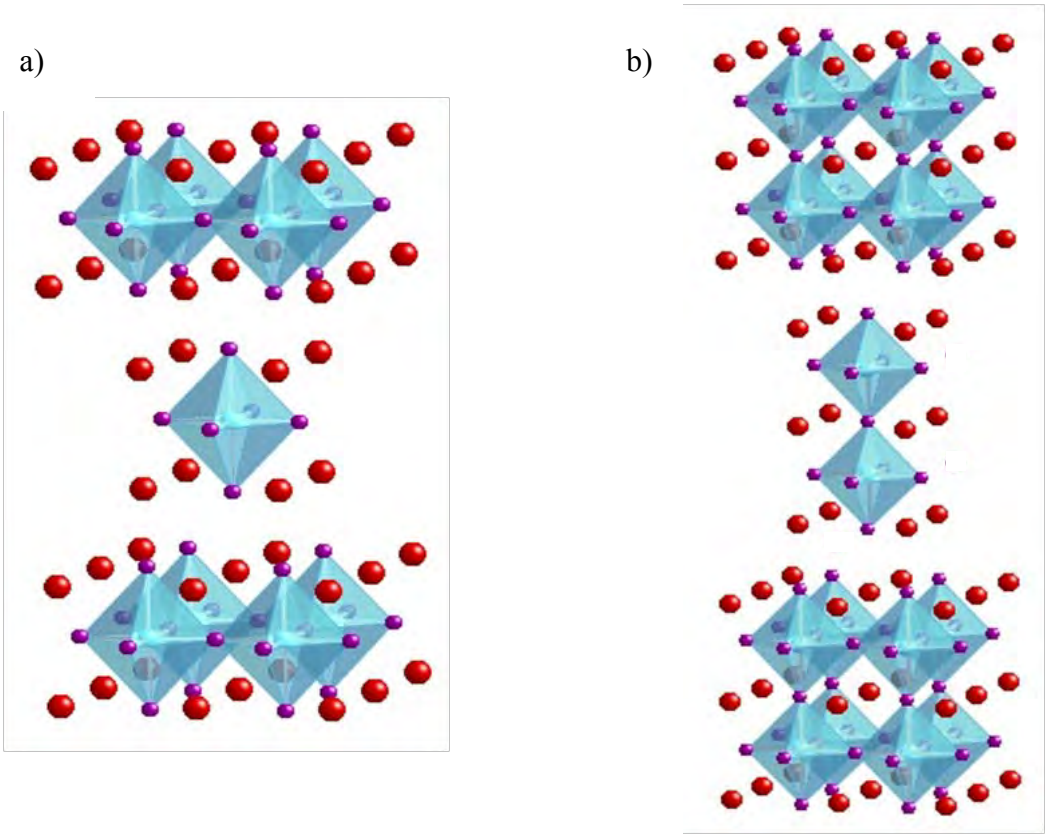

Figure 1.5 Ideal structures of a) n = 1 Ruddlesden-Popper phase, b) n = 2 Ruddlesden-Popper phase, showing corner linked BX_6 octahedra in blue, A cations shown in red and X anions shown in purple.

1.3 Magnetism and Magnetic Properties

1.3.1 Magnetic Induction and Magnetisation

A magnetic field is produced whenever electrical charges are in motion. This can be due to an electrical current flowing in a conductor. Electrons in an atom can also produce a magnetic field due to the orbital motions and spins of electrons. The magnetic field is often represented by lines indicating the direction of the force. When a magnetic field has been generated in a volume of space, the response of the volume is known as its magnetic

induction. The magnetic induction, B also known as flux density, measured in tesla (T) can be related to the strength of the magnetic field H as follows

$$B = \mu H \tag{1.3}$$

where μ = permeability of the volume, or permeability of free space, μ_0, if in a vaccum.

The magnetic induction is associated with the motion of electrons in the sample such that an interaction between the material and the applied field exists. So to allow for the interaction of the sample with the field, the magnetisation term, M, is introduced into the expression for magnetic induction;

$$B = \mu H + \mu M \tag{1.4}$$

Magnetisation is negative for diamagnetic materials while paramagnets possess positive values of magnetisation.

Magnetisation is usually described in terms of magnetic susceptibility, χ, and is related to magnetisation by Equation 1.5 where χ = magnetic susceptibility and H = applied magnetic field strength.

$$\chi = \frac{M}{H} \tag{1.5}$$

Magnetic susceptibility provides the measure of the response of a sample to an applied magnetic field and it is usually used as the main parameter in characterising magnetic properties.[9, 10, 11, 12]

1.3.2 Paramagnetism and diamagnetism

Diamagnetism is present in all substances and is usually very weak. This is generated by the motion of electrons in their orbitals. Non-interacting atoms with closed shells lead to the expulsion of all magnetic fields reducing the flux density. As a result, diamagnets display negative values of magnetic susceptibility.

Paramagnetism is caused by randomly oriented unpaired electrons. Electrons in each atom of a solid possess their own magnetic moment. In paramagnetism, the moments of these atoms are isolated from each other and they do not interact strongly with each other. But upon the application of an external magnetic field the moments attempt to line up with the field. However, thermal energy favours the random arrangement of moments and hinders the alignment of these moments.

The Curie law (Equation 1.6) describes the effect of thermal randomisation on the magnetic susceptibility of paramagnetic materials.

$$\chi = \frac{C}{T} \tag{1.6}$$

where C is the Curie constant, defined by the magnetic moment corrected for diamagnetism and T = temperature (K).

The Curie law was modified to the Curie-Weiss law (Equation 1.7) in order to describe the high temperature paramagnetic behaviour of materials containing interacting magnetic ions.

$$\chi = \frac{C}{T - \theta} \tag{1.7}$$

where θ is the Weiss constant which depends on the type of interaction.[9, 10, 11, 12]

1.3.3 Magnetic Interactions

The most important magnetic properties of materials come from cooperative interactions between magnetic ions. Ferromagnetism results when magnetic moments interact so as to align their spin in the same direction. This occurs below the Curie temperature, T_C, with $\theta > 0$ in zero applied field. The ferromagnetic ordering of spins acquires a random arrangement above the Curie temperature and displays paramagnetic behaviour.

Antiferromagnetic behaviour is observed if the magnetic moments align their spins in anti-parallel fashion. This type of ordering occurs below the Néel temperature T_N. At temperatures below the Néel temperature T_N, magnetic susceptibility decreases and as the temperature increases above T_N, the thermal disorder removes the antiferromagnetic alignments of spins. Thus, the material displays paramagnetic behaviour above the Néel temperature.

The temperature dependence of the magnetic susceptibility of diamagnetic, paramagnetic, ferromagnetic and antiferromagnetic materials is illustrated in *Figure 1.6*, while *Figure 1.7* shows the temperature dependence of inverse magnetic susceptibility.

Ferrimagnetism occurs when different sized moments interact. The antiferromagnetic interactions of dissimilar moments give rise to ferrimagnetism which has a net ferromagnetic moment despite aligning in antiferromagnetic manner. Canted antiferromagnetism occurs when moments are aligned antiferromagnetically, but are not arranged in collinear fashion. Spin glass behaviour is observed in some materials below the Curie temperature due to magnetic frustration which is characterised by the non-exponential decay of the remnant magnetisation after cooling in a magnetic field.[9, 10, 11, 12]

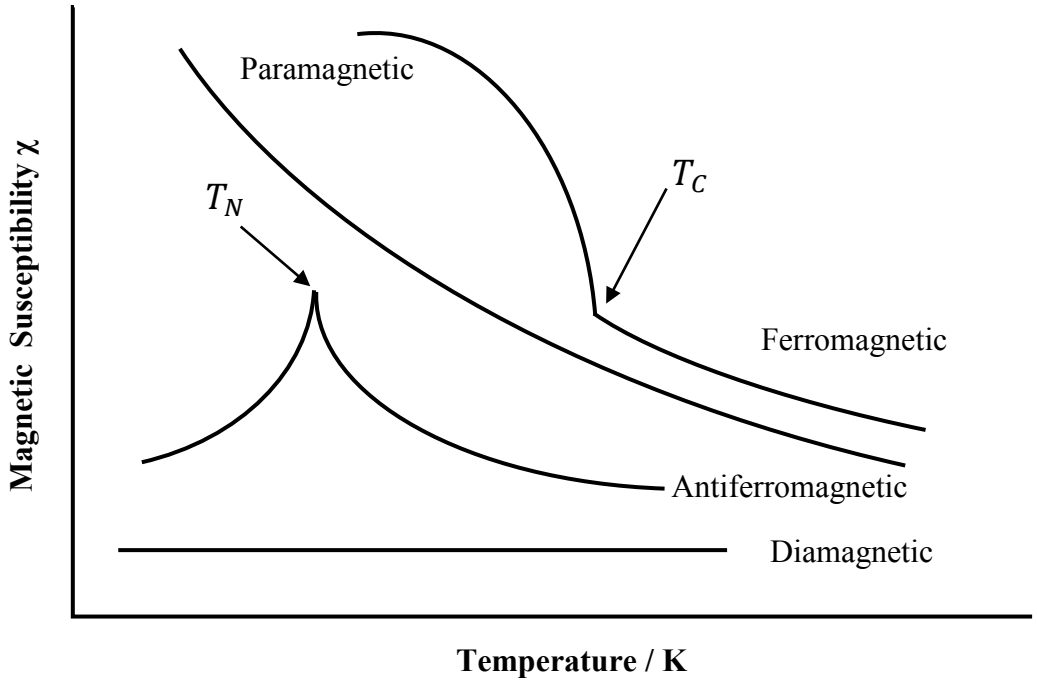

Figure 1.6 The temperature dependence of the magnetic susceptibility of diamagnetic, paramagnetic, ferromagnetic and antiferromagnetic materials.

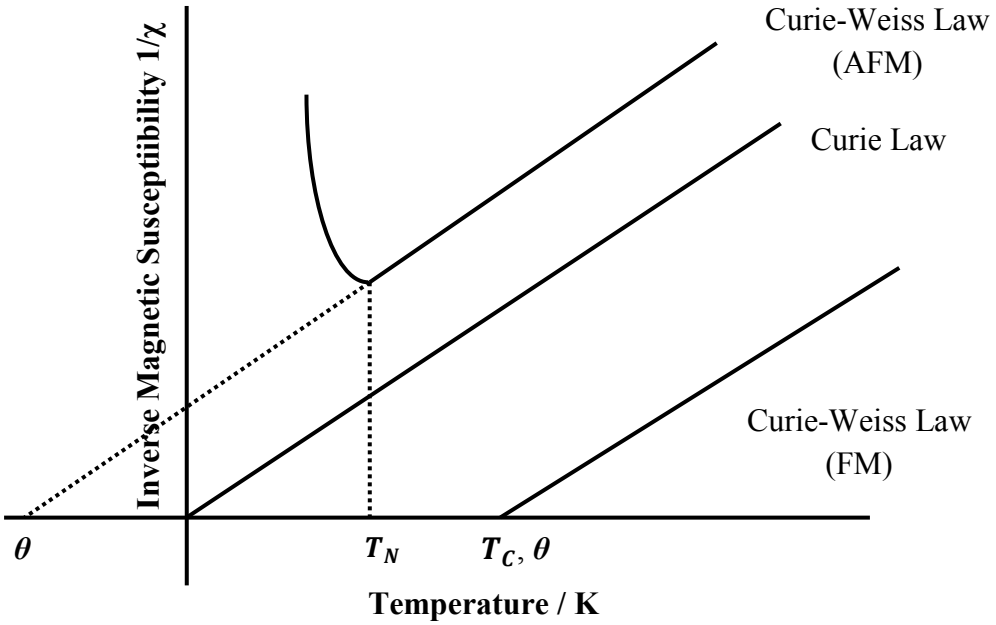

Figure 1.7 The temperature inverse magnetic susceptibility showing the Curie law, the Curie-Weiss law for ferromagnetic behaviour and the Curie-Weiss law for antiferromagnetic behaviour.

1.3.3.1 Superexchange Interactions

The superexchange interactions describe mechanisms of magnetic coupling between magnetic cations through intervening non-magnetic anions. This was first proposed by Kramers[13] and Anderson.[14, 15] The *d* orbitals of the magnetic cations overlap with the outer *p* orbitals of the intermediate anions, such as O^{2-}. The overlap may occur either along (σ) or orthogonal (π) to the $B - O - B$ bond, where *B* is the magnetic cation. When the *d* orbitals of the cation overlap sufficiently with the *p* orbitals of the anion, a degree of covalency is introduced and mixing or hybridization of these orbitals lowers the energy of the system. The electrons in the magnetic cation and the overlapping anion lobe should possess opposite spins in order for this process to be favoured. The antiferromagnetic ordering in

MnO, NiO, $CaMnO_3$ and $LaMnO_3$ can be explained using superexchange. The superexchange interaction that gives rise to antiferromagnetic ordering in MnO is illustrated in *Figure 1.8*. The strength of interactions depends on the nature of $B - O - B$ bonding. The σ type interactions are generally stronger compared to those of π type interactions. The long-range magnetic ordering resulting from superexchange depends on both the electronic configurations of the magnetic cations and the angle of interactions. The Goodenough-Kanamori rules can be used to predict whether the superexchange interactions result in long-range ferromagnetic or antiferromagnetic ordering.[16, 17, 18]

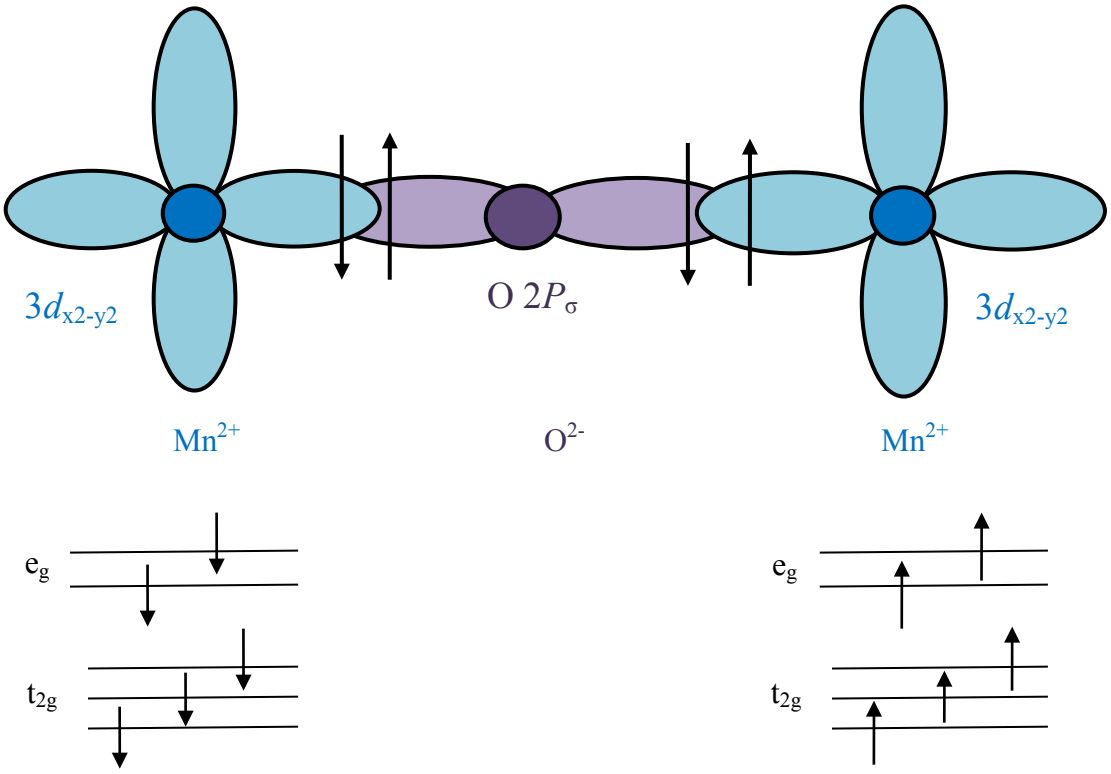

Figure 1.8 Schematic representation of superexchange interaction that gives rise to antiferromagnetic ordering in MnO, the Mn^{2+} $3d_{x2-y2}$ orbitals are shown in blue and the individual electron spins of Mn^{2+} are shown by black arrows.

1.3.3.2 Double Exchange Interactions

The doule exchange mechanism was first proposed by Zener[19] and predicts the relative ease of exchanging an electron between two species. Double exchange can occur between mixed valent magnetic ions *via* an intervening anion.

The double exchange mechanism can be used to explain magnetic properties of the manganese perovskites $La_{1-x}A_xMnO_{3-\delta}$ (A = Ca, Sr, Ba).[20, 21] The end members $LaMnO_3$ and $AMnO_3$ were found to be antiferromagnetic insulators due to superexchange interactions. However, when the A site is occupied by both divalent and trivalent cations or non-stoichiometry with respect to oxygen is such that mixed Mn^{3+} and Mn^{4+} ions are present in the material, the material could be cooled to become a ferromagnetic conductor. In $LaAMnO_3$, the Mn^{3+} has a d^4 configuration, where three electrons are in the t_{2g} level and a single electron in the e_g level. The Mn^{4+} ion has a d^3 configuration and its e_g level is unoccupied. Thus, the electron in the e_g level of Mn^{3+}ion is able to hop to the vacancy in the e_g level of Mn^{4+} ion *via* an intervening O^{2-} anion, as illustrated in *Figure 1.9*. The hopping of Mn^{3+} electrons to a vacancy in the e_g level of Mn^{4+} is feasible only if it can retain its spin. In this example, hopping can only occur if the t_{2g} electrons on the Mn^{4+} cation are aligned parallel or ferromagnetically to the Mn^{3+} cation.

As a result of double-exchange interactions, conduction electrons are able to move through the material in a metallic manner, coupling with incomplete d shells of the same spin, resulting in a ferromagnetic state.[21]

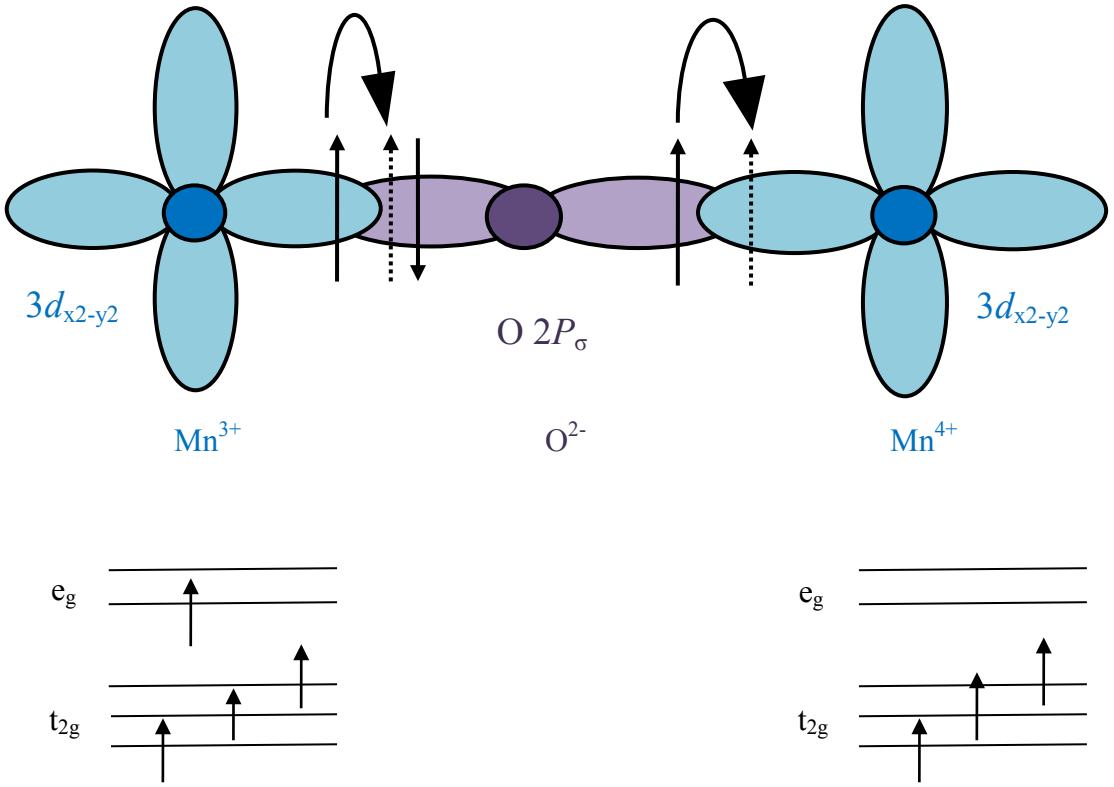

Figure 1.9 Schematic representation of double exchange interaction that gives rise to ferromagnetic ordering in $LaMnO_{3-\delta}$, the electron spins of the cations are shown as black arrows and electron hopping shown in black.

1.3.3.3 Colossal Magnetoresistance

Magnetoresistance is defined as the change in electrical resistance upon the application of a magnetic field and is described by the Euquation 1.8[22]

$$\mathrm{MR} = \frac{\Delta\rho}{\rho(0)} = \frac{[\rho(H) - \rho(0)]}{p(0)} \tag{1.8}$$

where MR = magnetoresistance, $\Delta\rho$ = change in resistivity, $\rho(0)$ = resistivity at a given temperature in the absence of any applied magnetic field and $\rho(H)$ = resistivity at a given temperature with applied magnetic field, H.

Most materials exhibit at least a small magnetoresistance, but certain materials display significantly larger magnetoresistance and so these are classified based on the magnitude of this effect. Materials containing magnetic multilayers, consisting of ferromagnetic layers of iron separated by non-magnetic layers, give rise to much larger magnetoresistance and are called as 'giant magnetoresistance'. In the absence of an applied magnetic field, alternating iron layers are aligned antiferromagnetically to one another. Hence the electrical resistivity is at a maximum. But upon the application of a sufficient magnetic field, the iron layers have spins aligned parallel, facilitating the propagation of conduction electrons and reducing the resistivity.[23]

Materials with magnetoresistance values which are several orders of magnitude larger than normal magnetoresistance are defined as colossal magnetoresistance (CMR).[24, 25] Several perovskite and perovskite related materials have been reported for exhibiting colossal magnetoresistance and have extensive applications including the read heads of hard disk drives, random access memory, magnetic sensors and in the field of spintronics.[26, 27]

1.3.4 Related Magnetic Structures

The magnetic properties of perovskite-related materials result from interactions between spin- and orbital- ordering of electron spins. The spin ordering present within these materials gives rise to the overall magnetic structure. Neutron diffraction and magnetic susceptibility measurements are usually used to deduce the magnetic structure of materials. Wollan and Koehler[28] used neutron diffraction in order to determine the magnetic structures of the $La_{1-x}Ca_xMnO_{3-\delta}$ series including the end members $LaMnO_3$ and $CaMnO_3$. The phases $LaMnO_3$, $CaMnO_3$ and $La_{0.2}Ca_{0.8}MnO_3$ were found to display antiferromagnetic behaviour arising from different magnetic structures. The phase composition range around $La_{0.65}Ca_{0.35}MnO_3$ was ferromagnetic and the F-type ferromagnetic structure is shown in *Figure 1.10*. The different types of antiferromagnetic structures in perovskites are illustrated in *Figures 1.11–1.13*.

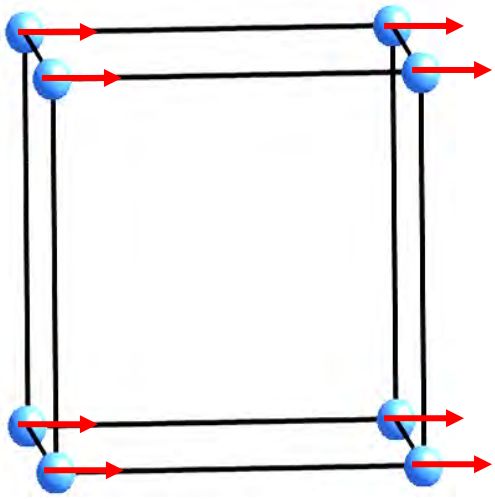

Figure 1.10 F-type ferromagnetic structure, as exhibited by $La_{0.65}Ca_{0.35}MnO_3$.

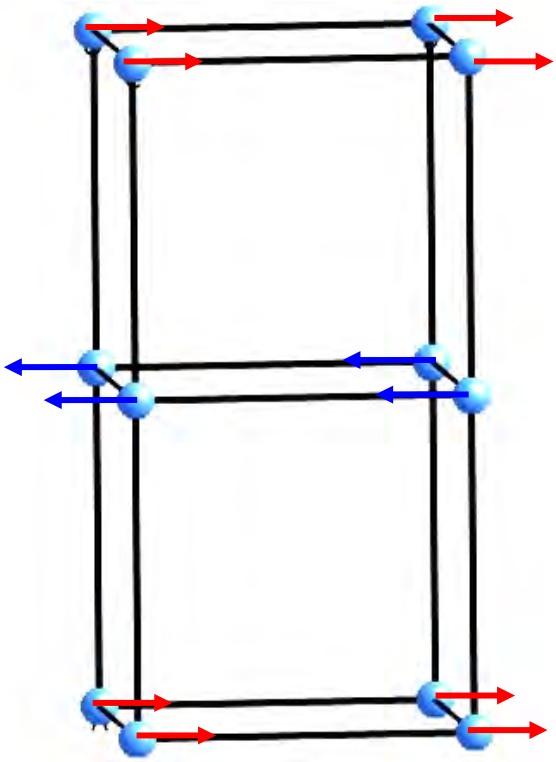

Figure 1.11 A-type antiferromagnetic structure, as exhibited by $LaMnO_3$.

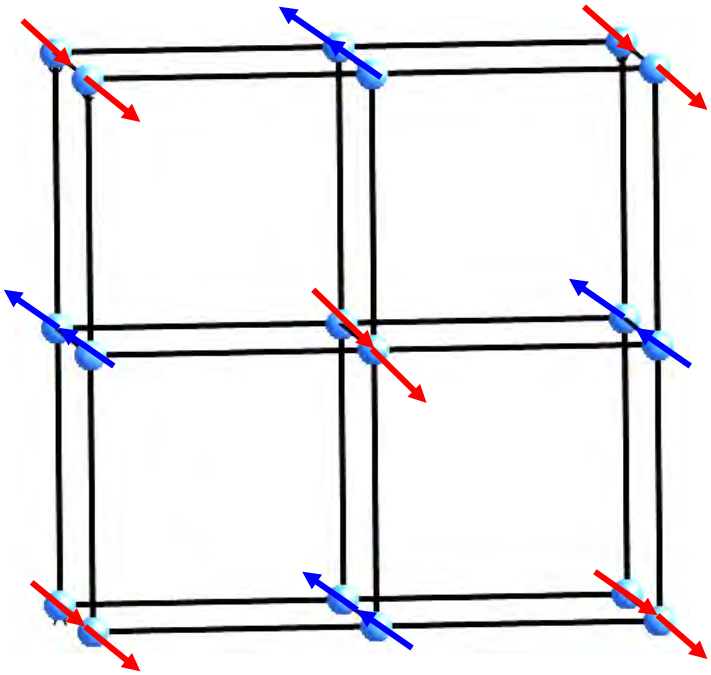

Figure 1.12 C-type antiferromagnetic structure, as exhibited by $La_{0.2}Ca_{0.8}MnO_3$.

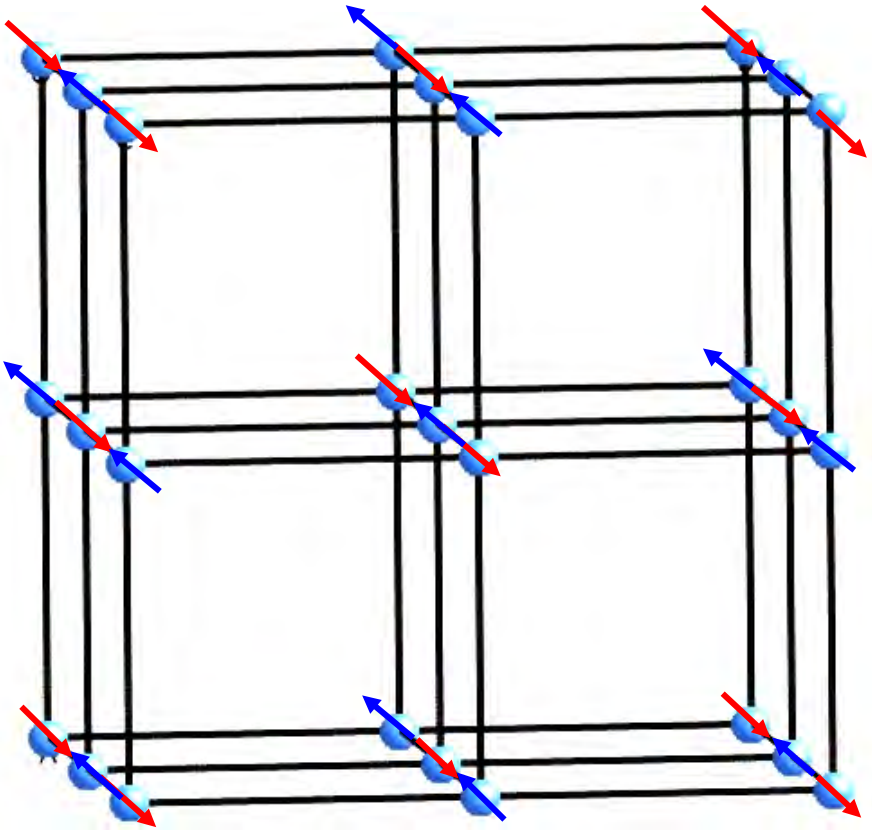

Figure 1.13 G-type antiferromagnetic structure, as exhibited by $CaMnO_3$.

1.4 Conductivity

Electrical conduction of metal oxides ideally occurs through the long-range migration of either electrons or ions. The cations, anions and foreign ions such as impurity ions, dopant ions and protons are the ionic charge carriers while the electrons and electron holes are the electron charge carriers. The amount of electron and ionic charge carriers present in a metal oxide is related to the defect structure of the material.

1.4.1 Defects

It is not possible to make crystals that are perfect in every respect. The presence of defects increases the entropy of the crystal and above absolute zero some intrinsic defects are always present. In general there are three types of defects present in solids: intrinsic defects, extrinsic defects and extended defects.[29]

1.4.1.1 Intrinsic Defects

These defects may occur in isolation due to the increase in entropy of the crystal. Schottky and Frenkel are two common types of intrinsic defect. As the temperature increases, the thermal vibration of ions in their lattice sites increases and if the vibration of a particular ion is large enough, it may jump out of its lattice site creating a point defect. At higher temperatures there is greater chance for the lattice site to be unoccupied. So these are called thermodynamic defects as the number of defects depends upon the temperature.

A Schottky defect consists of a cation vacant site and an anion vacant site for a 1 : 1 solid *MX* as shown in *Figure 1.14a*. For an MX_2 type structure, a Schottky defect will consist of one M^{2+} cation vacant site and two anion vacant sites. A Frenkel defect occurs when an atom or ion moves into an interstitial position and this is illustrated in *Figure 1.14b*. This may occur on either the anion or cation sublattice. Cation Frenkel defects are more common than anion defects as cations are smaller than anions and hence easier to accommodate in interstitial positions. A consequence of Frenkel defects is that a crystalline solid that has these defects may conduct electricity to a small extent.[30, 31]

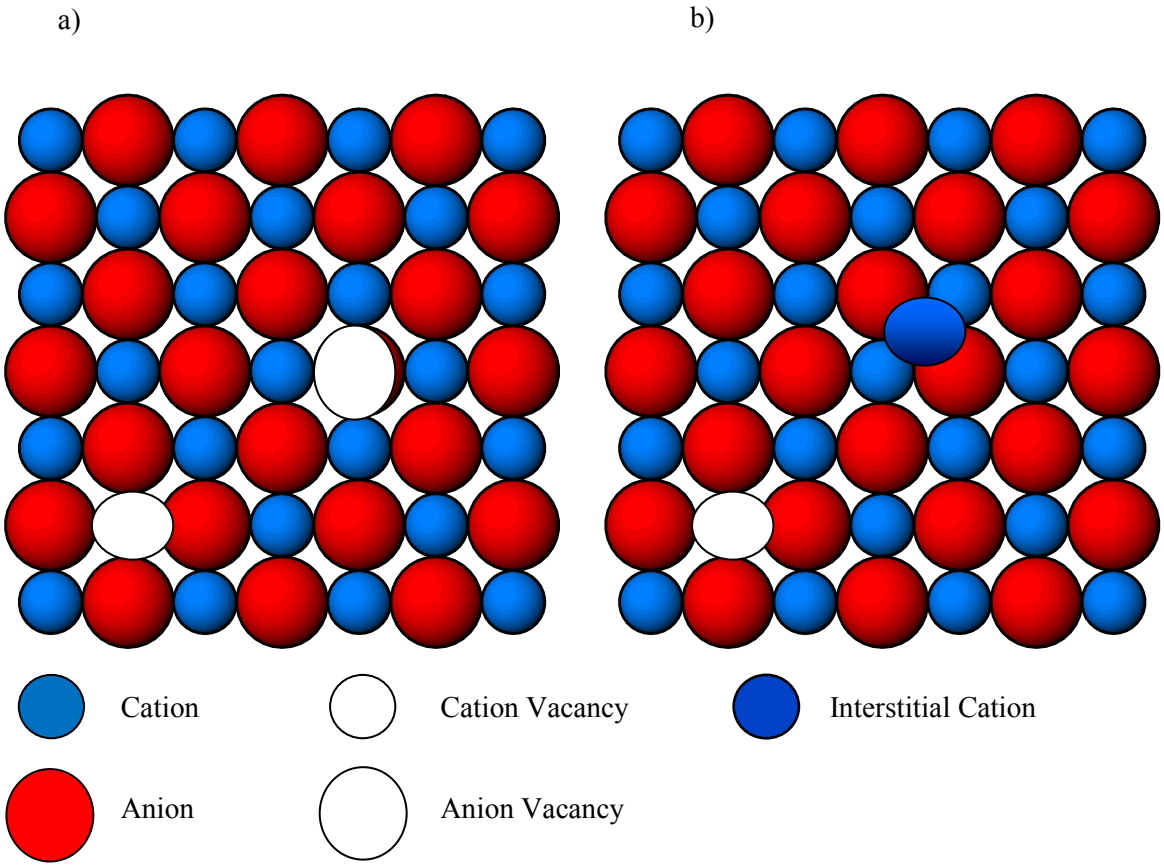

Figure 1.14 Illustration of intrinsic defects in a crystal of composition *MX*: a) Schottky defect b) Frenkel defect.

1.4.1.2 Extrinsic Defects

If cationic impurities are introduced into a solid and the dopant does not have the same valence as the cation it is replacing extrinsic defects will be introduced. Real crystals contain both intrinsic and extrinsic defects and the dominant defect type depends upon temperature and the doping / non-stoichiometry level.

In many compounds it is possible to replace a metal atom or ion with another element that has similar size and bonding requirements. Substitution of these foreign atoms or ions is termed aliovalent substitution. If an ion is replaced by one with different oxidation state

there has to be a charge compensation mechanism in order to maintain the electroneutrality. This results in creating cation vacancies, anion vacancies, interstitial anions and cations.[29, 30, 31, 32]

1.4.2 Total and Partial Conductivity

The sum of the partial conductivities σ_i of the different charge carriers equals to the total electrical conductivity σ of a substance,

$$\sigma = \sum_i \sigma_i \tag{1.9}$$

The transport number is the ratio of the partial conductivity of the i^{th} species, σ_i to the total conductivity, σ,

$$t_i = \frac{\sigma_i}{\sigma} \tag{1.10}$$

The electrons and ions are the charge carriers in a binary oxide. Each of these may have contributions from different transport mechanisms. The most important is the contributions to electronic conductivity from defect (conduction band) electrons called *n*-type conductivity and from electron holes, called *p*-type conductivity. The total conductivity is then given by

$$\sigma = \sigma_{ion} + \sigma_{ele} = \sigma_c + \sigma_a + \sigma_n + \sigma_p$$

(1.11)

where σ_c, σ_a, σ_n and σ_p are the conductivities of cations, anions, electrons and electron holes, respectively. The ionic conductivity is σ_{ion} and the electronic conductivity is σ_{ele}.

The individual conductivities in Equation 1.11 can be expressed in terms of their transport numbers,

$$\sigma = \sigma(t_{ion} + t_{ele}) = \sigma\left(t_c + t_a + t_n + t_p\right)$$

(1.12)

The total of the transport numbers of all the ionic and electron charge carriers is equal to one.[33, 34]

$$t_{ion} + t_{ele} = t_c + t_a + t_n + t_p = 1$$

(1.13)

1.4.3 Electronic Conductivity

For most oxides the electronic conductivity is greater than the ionic conductivity even when the electron charge carrier concentration is smaller than that of ionic charge carriers as the mobility of electron charge carriers are much higher than the ionic mobility. Usually one type of charge carrier predominates in an oxide at a particular temperature and oxygen pressure.

The band theory can be used to describe the electronic structures of metals, semiconductors and many other solids. The band structure of a metal is illustrated in *Figure 1.15*, in which

the highest occupied band, the valence band, is only partly full. Since the electrons in singly occupied states close to the Fermi level are able to move metals exhibit higher conductivity.

In an insulator, the valence band is completely filled and is separated by a large energy gap from the next empty band. Very few electrons have sufficient thermal energy necessary to overcome the energy gap and so the conductivity is negligibly small. The band structure of an insulator, diamond, is illustrated in *Figure 1.16* and typical band gaps for insulators, semiconductors and metals are listed in *Table 1.1*.[10, 31, 32, 35]

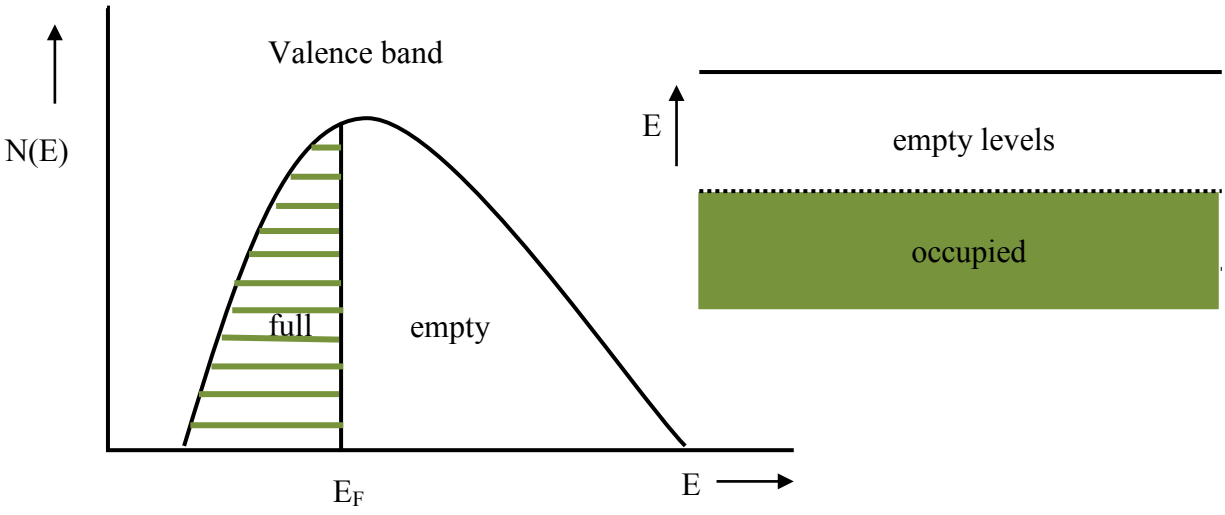

Figure 1.15 Band structure of a metal.

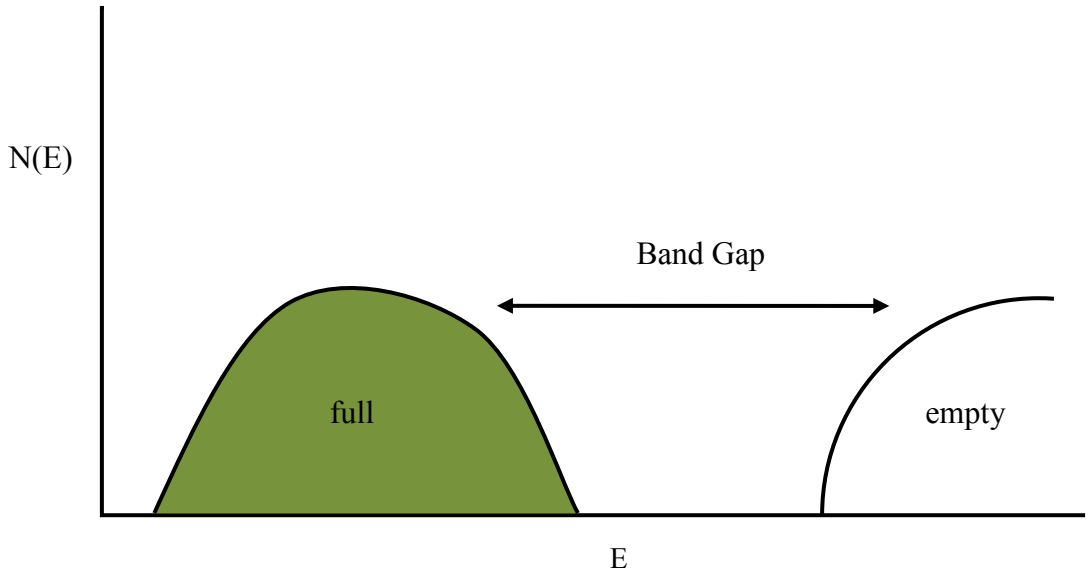

Figure 1.16 Band structure of an insulator, carbon (diamond).

Table 1.1 Band gaps of some selected elements.[10]

Element	**Band gap (eV)**	**Type of material**
Diamond, C	6.0	Insulator
Si	1.1	Semiconductor
Ge	0.7	Semiconductor
Pb	0	Metal

The band structure of semiconductors is similar to that of insulators but has a band gap; which is in the range 0.5 to 3.0 eV. Electrons may be thermally promoted from the valence band into an upper, empty band, called the conduction band. Under an applied potential, the negative charge carriers in this band would move towards a positive electrode. The vacant electron holes that left behind in the valence band can be regarded as positive holes.

These holes move upon entering an electron into them, leaving its own position vacant and a fresh positive hole is formed. Positive holes therefore move in the opposite direction to electrons.

There are two groups of semiconductors; intrinsic and extrinsic semiconductors. Intrinsic semiconductors are pure materials and their band structure can be illustrated as in *Figure 1.17*. In these materials, the number of electrons in the conduction band is determined by the magnitude of the band gap and the temperature.

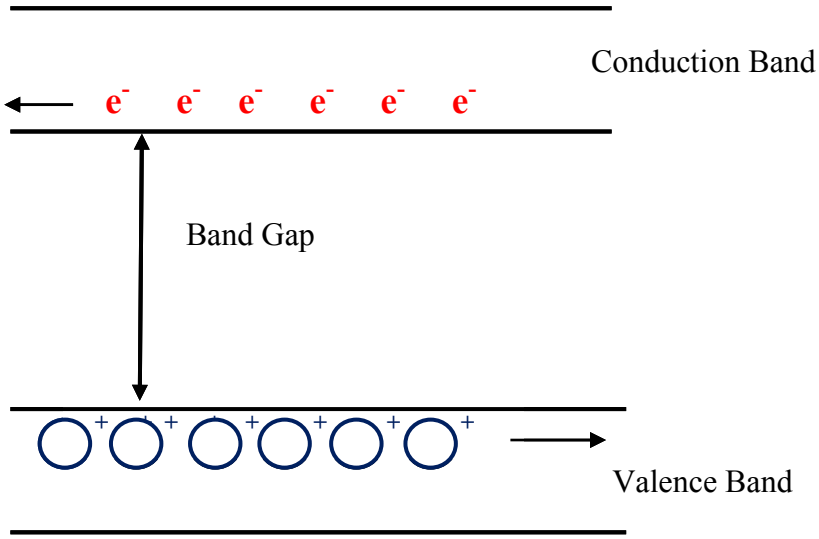

Figure 1.17 Positive and negative charge carriers.

In extrinsic semiconductors, the conductivity is controlled by the addition of dopants. Pure silicon which is originally an intrinsic semiconductor can be converted into an extrinsic semiconductor by doping with an element from either Group III or Group V of the periodic table. When silicon is doped with a small amount of gallium (1 ppm) it forms a discrete

level just above the valence band as gallium has only three valence electrons while silicon has four electrons. This level is capable of accepting electrons and is called the acceptor level. Since the energy gap between the acceptor level and valence band is small, electrons in the valence band have sufficient thermal energy to move into the acceptor levels. It is not possible for electrons in the acceptor level to contribute to conduction as the acceptor levels are discrete because the concentration of gallium atoms (1 ppm) is small. The positive holes that are left behind in the valence band are responsible for the conduction in these materials and so act as positive hole or *p*-type semiconductor, shown in *Figure 1.18*.

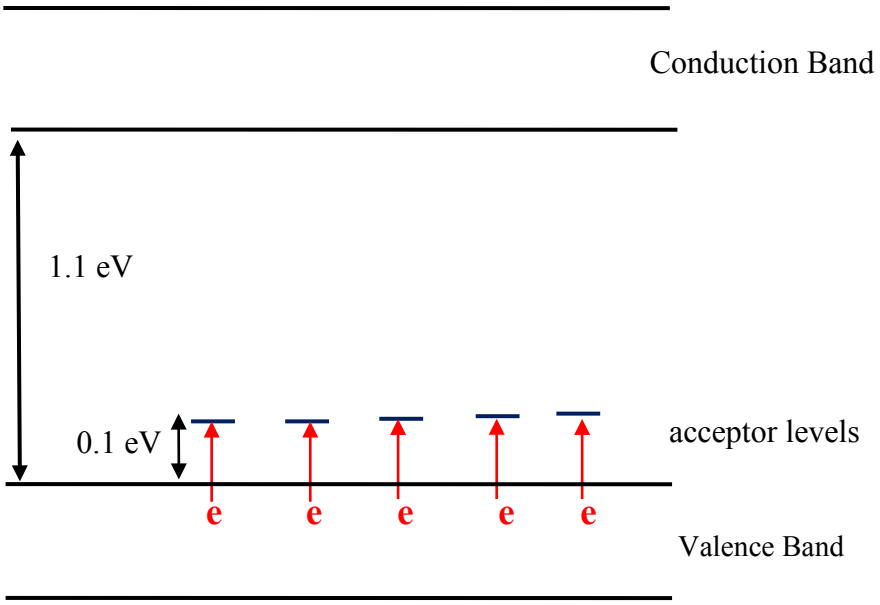

Figure 1.18 *p*-type semiconductivity in gallium-doped silicon.

When silicon is doped with a small amount of arsenic (1 ppm) the extra electron in arsenic occupies a discrete level about 0.1 eV below the bottom of the conduction band as shown in *Figure 1.19*. These levels cannot contribute to the conduction directly as there is only a small amount of electrons in these levels. But electrons in these levels have sufficient

energy to move into the conduction band and thus act as donor levels. Such materials are known as *n*-type semiconductors.

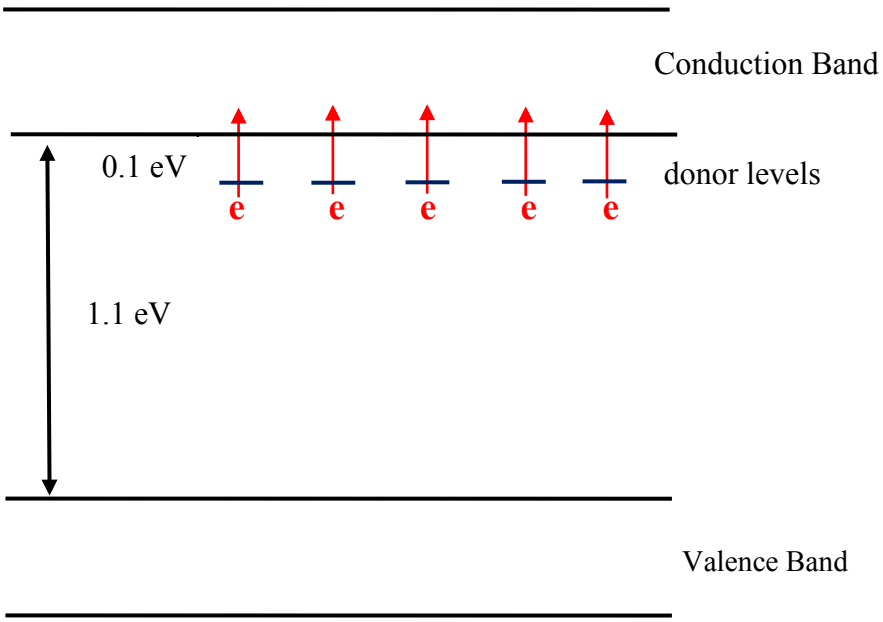

Figure 1.19 *n* -type semiconductivity in arsenic-doped silicon.

At normal temperatures, the extrinsic carrier concentration is much higher than the intrinsic concentration and hence the conductivity is controlled by the extrinsic carrier concentration. But at sufficiently high temperatures, a conversion to intrinsic behaviour would be observed as the intrinsic carrier concentration is greater than the extrinsic value. The temperature dependence of carrier concentration and conductivity for a semiconducting material which is extrinsic at low temperature and intrinsic at higher temperatures is shown in *Figure 1.20*.[32, 35]

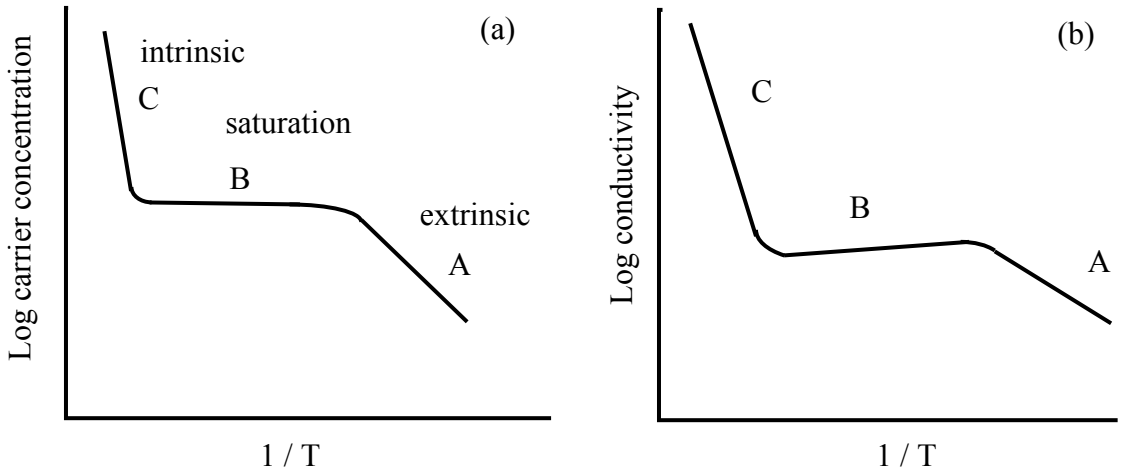

Figure 1.20 Temperature dependence of (a) carrier concentration and (b) conductivity for a semiconducting material.

1.4.4 Ionic Conductivity

Defects in ionic solids allow the ions to migrate in an applied electric field. Migrations of vacancies and interstitial ions result in ionic conduction. The magnitude of ionic conductivity depends on the number of defects present in the crystal. For conduction *via* vacancies, the vacancies can be created by one of two methods. The number of vacancies present in the crystal increases upon heating and these are known as intrinsic vacancies. The other method is introducing aliovalent impurities. These vacancies are called extrinsic vacancies as these are not present in the pure crystal. The number of intrinsic vacancies present at low temperature is very small and is much less than the concentration of extrinsic vacancies. The intrinsic behaviour dominates at some higher temperature. The temperature dependence of ionic conductivity is given by the Arrhenius equation[10]

$$\sigma = A \exp\left(\frac{-E}{RT}\right) \tag{1.14}$$

where σ is the ionic conductivity, E the activation energy, R the gas constant, T the absolute temperature and A is the pre-exponential factor.

1.5 Aims of the Project

The main focus of this project was to synthesise and characterise some layered and perovskite materials.

The synthesis and characterisation of double perovskites $LaSr_2Fe_2SbO_9$ and $La_2Sr_2Fe_3SbO_{12}$ is presented in Chapter 3. The crystal structure and magnetic properties of these materials depend on the size and electronic structure of the two transition metal cations present in the *B* site of the structure. Both crystal and magnetic structures of these materials are thoroughly investigated. The effect of cationic distribution on magnetic behaviour of these compounds is discussed.

The $n = 2$ Ruddlesden-Popper phases containing different lanthanides (La, Nd, Eu) and alkaline metals (Sr, Ba) in the *A* site have been investigated. There are two distinct crystallographic sites for the *A* cations in the crystal structure and the cation ordering at the *A* site with different cations has been studied. Further, the characterisation of both crystal and magnetic structures of these materials has been investigated and is presented in Chapter 4.

The structural and physical properties of layered metal oxides can be modified through fluorine insertion reactions. Fluorine insertion reactions into the layered $n = 2$ Ruddlesden-Popper phases characterised in Chapter 4 are the main subject of Chapter 5. The influence

of the inserted fluoride anions on the structure of these materials has been investigated and is presented.

The most common method for changing the structure and electronic properties of materials is cation substitution. However, anion substitution mechanisms can also be employed to change the structure and the electronic properties of materials. Oxy-anions have been inserted into perovskite materials and the detailed structural characterisation of these phases is discussed in Chapter 6.

1.6 References

1. Goodenough, J. B.; Longo, J. M., *Crystallographic and Magnetic Properties of Perovskites and Perovskite Related Compounds*. Lando lt-Bormstein, Springer Verlag: 1970.
2. Kobayashi, K. I.; Kimura, T.; Sawada, H.; Terakura, K.; Tokura, Y. *Nature* **1998**, 395, 677.
3. Goodenough, J. B. *Rep*. *Prog*. *Phys*. **2004**, 67, 1915.
4. Yake, H. L. *Acta Cryst.* **1955**, 8, 394.
5. Chenavas, J.; Joubert, J. C.; Marezio, M.; Bochu, B. *J. Solid State Chem*. **1975**, 14, 25.
6. Jacobson, A. J.; Collins, B. M.; Fender, B. E. F. *Acta Cryst*. **1974**, B30, 1705.
7. Mitchell, R. H., *Perovskites: Modern and Ancient*. Almaz Press: Canada, 2002.
8. Ruddlesden, S. N.; Popper, P. *Acta Cryst*. **1958**, 11, 54.
9. Smart, L. E.; Moore, E. A., *Solid State Chemistry: An Introduction*. Bacon Raton, Taylor & Francis: 1992.
10. West, A. R., Solid *State Chemistry and its Applications*. John Wiley & Sons Ltd.:1984.
11. Weller, M. T., *Inorganic Materials Chemistry*. Oxford University Press: New York, 1996.
12. Orchard, A. F., *Magnetochemistry*. Oxford University Press: New York, 2003.
13. Kramers, P. W. *Physica*. **1934**, 1, 182.
14. Anderson, P. W. *Phys. Rev*. **1950**, 79, 350.
15. Anderson, P. W. *Phys. Rev*. **1950**, 79, 705.
16. Goodenough, J. B. *J. Phys. Chem. Solids.* **1958**, 6, 287.
17. Kanamori, J. *J. Phys. Chem. Solids.* **1959**, 10, 87.
18. Goodenough, J. B., *Magnetism and the chemical Bond*. John Wiley & Sons: 1963.
19. Zener, C. *Phys. Rev*. **1951**, 82, (3), 403.
20. Jonker, G. H.; Santen, J. H. v. *Physica*. **1950**, 16, (3), 337.
21. Santen, J. H. v.; Jonker, G. H. *Physica*. **1950**, 16, 7-8, 599.
22. Tipler, P. A., *Physics for Scientists and Engineers*. W. H. Freeman and Company: New York, 2001.
23. Goldman, A. M. *Science* **1996**, 274, 1630.

24. Hemlot, R. v.; Wecker, B.; Hollzapfel, B.; Schultz, L.; Samwer, K. *Phys. Rev. Lett*. **1993**, 71, (14), 2331.
25. Raveau, R*., Colossal Magnetoresistance*, *Charge Ordering and Related Properties of Manganese Oxides*. World Scientific Publishing Co: 1998.
26. Daughton, J. M. *J. Magn. Magn*. *Matter* **1999**, 192, 334.
27. Foncuberta, J.; Balcells, L.; Bibes, M.; Navarro, J.; Frontera, C.; Santiso, J.; Fraxedas, J.; Martinez, B.; Nadolski, S.; Wojcik, M.; Jedryka, E.; Casanove, M. J. *J. Magn. Magn. Matter* **2002**, 242-245, 98.
28. Wollan, E. C.; Koehler, W. C. *Phys. Rev*. **1955**, 100, (2), 545.
29. Rao, C. N. R.; Gopalakrishnan, J., *New Directions in Solid State Chemistry*. Cambridge University Press: 1997.
30. Frenkel, J. *Z. Phys*. **1926**, 35, 652.
31. Cox, P. A., *The Electronic Structure and Chemistry of Solids*. Oxford University Press: Oxford, 1987.
32. Bach, H. I.; Luth H., *Solid State Physics*. Springer Verlag: Berlin, 1991.
33. Friauf, R. T. *Phys. Rev*. **1962**, 105, 843.
34. Manning, J. R. *J. Appl. Phys*. **1962**, 33, 2145.
35. Wolfe, C. M.; Holonyak, N.; Stillman, G. E., *Physical Properties of Semiconductors*. Englewood Cliffs, N. J., Prentice Hall: 1989.

CHAPTER TWO

Experimental Techniques

2.1 Synthesis of Materials

2.1.1 Solid State Reactions

The materials presented in this work were synthesised using the standard ceramic method. The method involved grinding of stoichiometric amounts of suitable reagents using an agate pestle and a mortar to obtain a homogeneous mixture of reaction particles. High purity binary oxides or carbonates of appropriate cations were used for the work presented in this thesis. The reaction mixtures were then heated in alumina crucibles at appropriate temperatures in suitable reaction environments. Reaction environments can be oxidising (in air or flowing $O_2(g)$) or reducing (flowing $N_2(g)$ or $H_2(g)$ / $N_2(g)$ mixes) atmospheres.

Solid state reactions occur at the interface between reactant grains where product particles begin to form. Therefore, these reactions depend on diffusion rate of ions towards the grain boundaries. The ions also need sufficient energy to migrate towards these boundaries. These reactions as a result require higher temperatures and longer reaction times. The product grains increase in size as the reaction proceeds, hence the rate of the reaction decreases as diffusion path lengths for reacting ions increases. Frequent regrinding between successive heat treatments increases the rate of reaction by creating new interfaces between reactant particles and thus shorter diffusion path lengths.[1]

2.1.2 Fluorination

Fluorination was carried out by reacting the starting oxide material with a mixture of 10% F_2(g) / 90% N_2(g). The apparatus used is illustrated in *Figure 2.1*. Components constructed from nickel, copper and polytetrafluoroethylene (PTFE) were used in this apparatus to avoid attack by F_2(g) and HF. Firstly, the apparatus was flushed with N_2(g) to remove any traces of moisture. All the gases were dried by passing over a desiccant and NaF pellets which removes any traces of HF. The oxide placed in a nickel foil boat inside the nickel furnace tube was heated to the reaction temperature (typically 290 ℃ - 400 ℃) while flowing N_2(g) through the furnace. The 10% F_2(g) / 90% N_2(g) mixture was then allowed to pass through the furnace tube for a period of time. The reaction times were 15 to 30 minutes. The system was again purged with N_2(g) after the reaction whilst cooling to room temperature before removing the sample.[2]

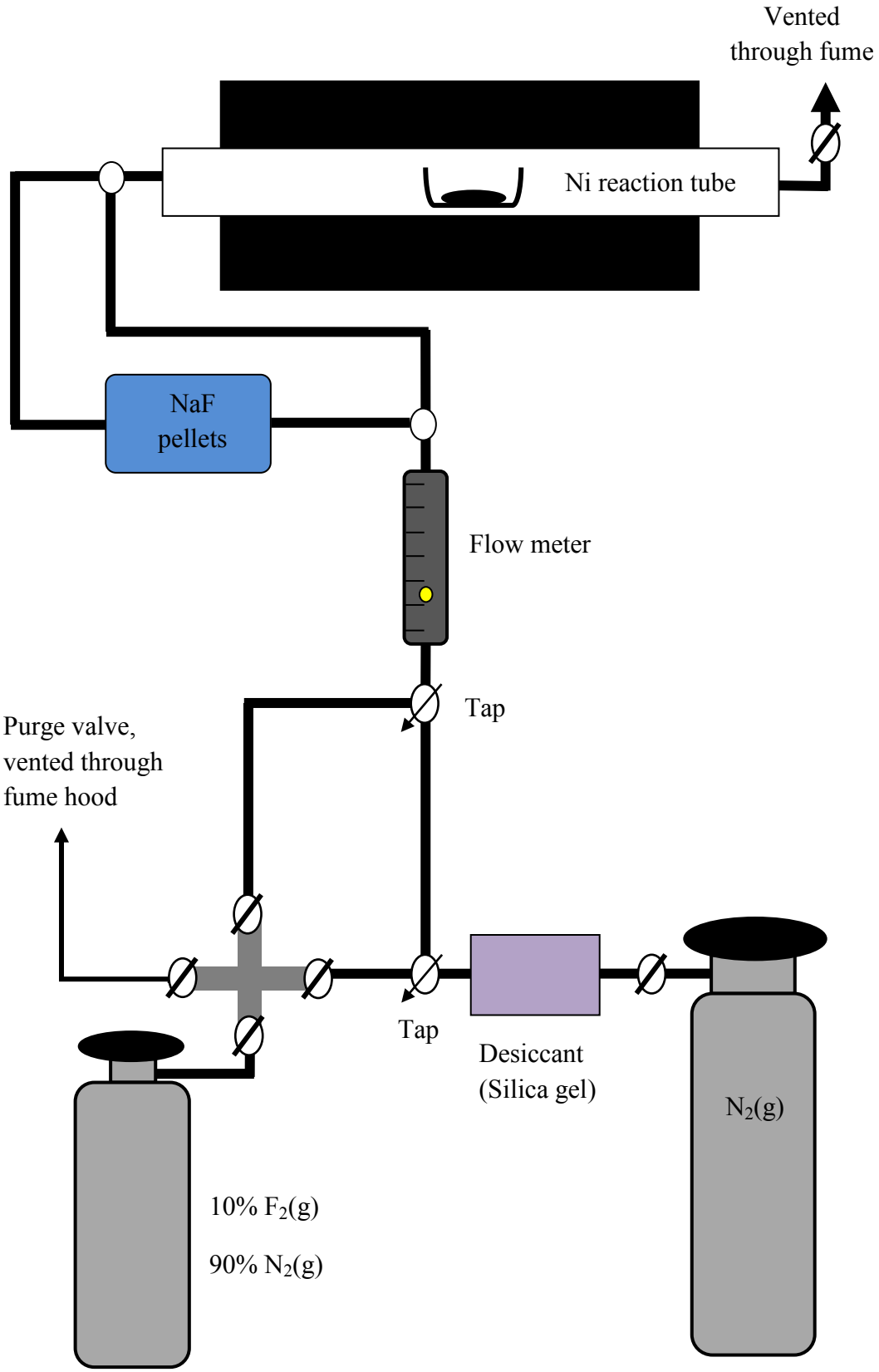

Figure 2.1 Illustration of apparatus used for fluorination reactions.

2.2 Diffraction Techniques

2.2.1 Powder Diffraction

X-ray and neutron powder diffraction are widely used techniques for the determination of precise atomic positions, interatomic distances and bond angles of inorganic solids.[1] These two techniques were used for structural characterisation of materials presented in this work.

2.2.1.1 Bragg Equation

X-rays are electromagnetic radiation with wavelength about as long as the distance between neighbouring atoms which are regularly placed in crystals. Thus, atoms in a crystal act as scattering centres and thereby diffract X-rays. Diffraction can be constructive or destructive depending on how the waves overlap one another. Constructive interference occurs when the waves are moving in phase with each other. This results in diffraction patterns. Destructive interference occurs when the waves are out of phase. Powder diffraction can be understood by considering the Bragg equation.

A section of a crystal with atoms arrange on a set of parallel planes (*hkl*) and space a distance *d* apart is shown in *Figure 2.2*. When a beam of monochromatic radiation with wave length λ strikes the planes of the crystal at an angle θ, the rays reflected by the lower plane travel a longer distance than those reflected from the upper plane. This extra distance is equal to the sum of the distance $AX + BX$

$$AX + BX = 2d \sin\theta$$

(2.1)

In order for constructive interference to occur, this extra distance should be equal to an integral number of wavelengths,

$$n\lambda = AX + BX$$

(2.2)

Therefore,

$$n\lambda = 2d\ \sin\theta$$

(2.3)

This was first formulated by Bragg known as the Bragg equation.[1] This equation states the essential conditions which must be met if diffraction to occur. The *n* in the Bragg equation is known as the order of reflection.

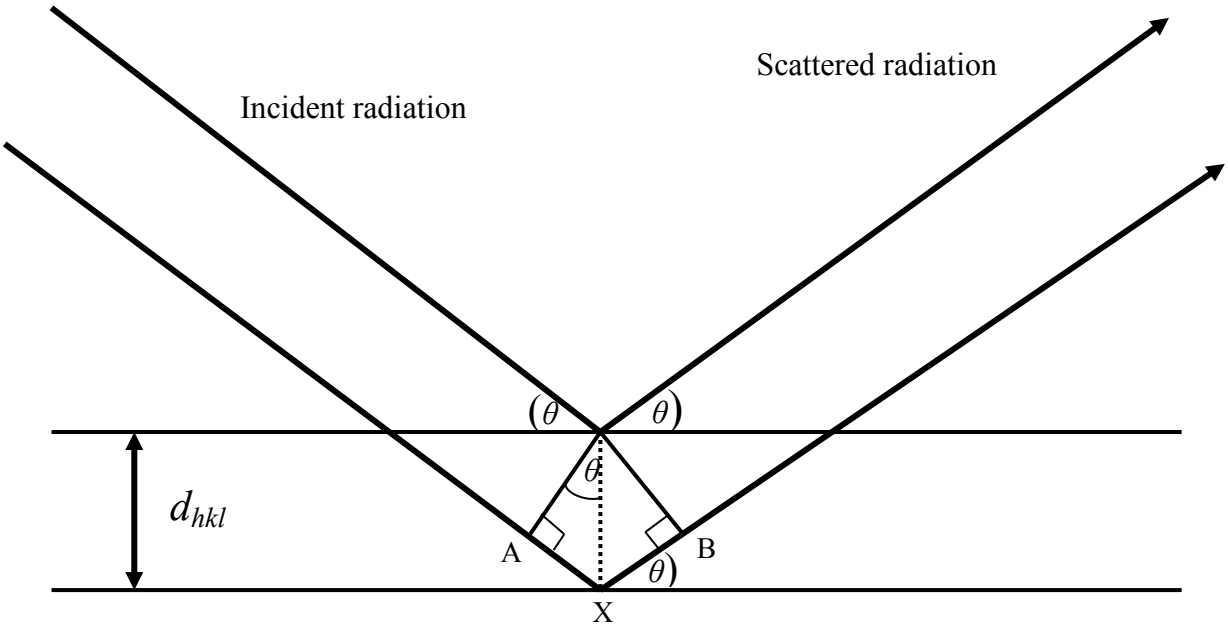

Figure 2.2 Bragg's law from reflections of incident radiation from successive planes.

The peak positions in the diffraction pattern can be indexed to determine the unit cell size and symmetry. The computer programs INDEX[3] and CELL[4] were used initially to obtain lattice parameters.

2.2.2 X-ray Powder Diffraction

2.2.2.1 Production of X-rays

X-ray powder diffraction is a laboratory based technique widely used for both preliminary characterisations such as phase identification, structure determination and to check sample purity.

X-rays are produced by the continuous bombardment of a metal anode with high energy electrons produced by thermionic emission of a tungsten filament. The electrons are decelerated by the metal's electrons as they reach the target. This produces a continuous spectrum of radiation, known as Bremstrahlung radiation. The energy of these bombarding electrons is sufficient to excite an electron in the *K* shell to a higher, unoccupied state, creating an unoccupied state. Thus, electrons in *L* or *M* shells are able to make transitions into the *K* shell, emitting X-rays. Transitions from the *L* shell to the *K* shell give rise to the *Kα* line and these transitions are actually doublets, $K\alpha_1$ and $K\alpha_2$ radiations caused by the two *L* to *K* transitions. These are close in energy but differ due to the spin multiplicity of the 2*p* electrons. The transitions from the *M* shell to the *K* shell cause *Kβ* line.[5]

The X-ray powder data of all compounds presented in this work were collected using a Bruker D8 diffractometer operating in transmission mode. This instrument generates a X-ray beam containing Cu $K\alpha_1$ and $K\alpha_2$ and *Kβ* radiation. The curved primary beam

germanium monochromator fitted to the diffractometer selects only the $K\alpha_1$ line (λ = 1.5406 Å). So the X-rays used were of a single wavelength.

2.2.2.2 Intensities of X-ray Reflections

Intensities of X-ray reflections are important in determining unknown crystal structures and characterising materials. The intensity I_{hkl} for each reflection is given by

$$I_{hkl} = K \times p_{hkl} \times L_\theta \times P_\theta \times A_\theta \times T_{hkl} \times E_{hkl} \times F_{hkl}^2 \quad (2.4)$$

where K is the scale factor, p_{hkl} is the multiplicity factor which accounts for the number of equivalent reflections that contribute to an observed Bragg peak, L_θ the Lorentz factor is a geometric factor that depends on the type of instrument and varies with θ, P_θ the polarisation factor accounts for the angular dependence of intensity scattered by electrons, A_θ is the absorption factor, T_{hkl} is the preferred orientation factor, E_{hkl} is the extinction multiplier and F_{hkl} is the structure factor.[6] The absorption factor accounts for the reduction in the intensity of the diffracted X-ray beam due to absorption by the sample. An absorption correction was carried out using the computer program "ABSORB"[7] for all the data collected in transmission mode.

The structure factor for a peak (hkl), F_{hkl}, the resultant of the waves scattered by all atoms n in the unit cell is given by the equation

$$F_{hkl} = \sum_{j=1}^{n} g_j t_j(s)\, f_j(s) exp\left[2\pi i\left(hx_j + ky_j + lz_j\right)\right]$$

(2.5)

where g_j is the population factor of the j^{th} atom, t_j the atomic displacement parameter of the j^{th} atom, f_i is the scattering factor, x_j, y_j and z_j are the fractional coordinates of the j^{th} atom.[8]

Thermal vibrations of atoms decrease intensities of diffracted beams and increase background scatter.[6] The atomic displacement parameter t_j of the j^{th} atom also known as the temperature factor describes the influence of the motions of atoms and is given by

$$t_j = exp\left[-B_j \frac{\sin^2\theta}{\lambda^2}\right]$$

(2.6)

where B_j is the isotropic displacement parameter for the j^{th} atom and this can be related to the vibration of the j^{th} atom by

$$B_j = 8\pi^2 U_j$$

(2.7)

where U_j is the mean square amplitude of vibration of the atom in Å^2.[9]

X-rays are scattered by crystalline material due to their interaction with the electrons in the material. This is described by the scattering factor f_n which depends on the atomic number Z or rather on the number of electrons present in the atom. Due to this dependence scattering from heavy atoms can dominate X-ray diffraction patterns and it can be difficult

to obtain reliable information on light atoms from X-ray diffraction data. X-rays scattered from different parts of the atom can interfere destructively due to the relatively diffuse nature of the electron cloud. This gives rise to a significant decrease in scattered intensity with increasing angle as the scattering factor f_n decreases from a value of Z at $2\theta = 0$. This can result in a loss of information from the high angle region of XRPD patterns.

2.2.3 Neutron Powder Diffraction

Neutron powder diffraction is a valuable but an expensive technique which provides information, especially on magnetic materials, that is not attainable with other techniques. The experiments are usually carried out at central laboratories which provide a user service. This technique requires significantly larger samples as the interaction of the neutron with the sample is much weaker compared to that of X-rays.

2.2.3.1 Neutron Powder Diffraction Instrumentation

Neutron powder diffraction requires a sufficiently intense neutron flux which can be generated by both reactor and spallation neutron sources. The reactor neutron source produces a continuous spectrum of neutrons by nuclear fission of uranium. A moderator is used to control the energy of neutron and a monochromator to select a particular wave length. The method needs longer data collection times as the intensity of monochromatic radiation is low.

In this work, neutron powder diffraction data were recorded on the high resolution powder diffractometer for thermal neutrons (HRPT) at SINQ, PSI, using wavelengths of 1.8852 Å

and 1.4942 Å. In SINQ neutron source, neutrons are produced by proton spallation. A beam of fast protons generated by a proton accelerator strikes a block of lead (the target). The collision of fast protons on the lead target results in emission of ~10 to 20 neutrons for every proton. The neutrons generated are much too fast for experiments and in order to decelerate the neutrons, the whole target is placed in a tank filled with heavy water. The neutrons are decelerated by collisions with the nuclei of the heavy hydrogen in this water. This produces thermal neutrons which can be used in structure determination of crystals. The large position sensitive (PSD) ^{3}He detector in the multi detector HRPT diffractometer allows obtaining simultaneous measurements within a scattering angle range of 160° with angular step 0.1°.[10]

2.2.3.2 Intensity of Diffracted Neutron Beam

Neutrons are scattered both by nuclei of atoms and by magnetic moments on the nuclei. The overall neutron structure factor is given by

$$|F_{hkl}|^2 = |F_N|^2 + |F_M|^2 \tag{2.8}$$

where F_N and F_M are the nuclear and magnetic scattering factors, respectively.

The intensity of the diffracted neutron beam I_{hkl} is proportional to the square of the structure factor F_{hkl}

$$I_{hkl} = mF_{hkl}^2 \frac{CA}{L}$$

(2.9)

where m is the multiplicity factor, A the absorption factor, L the Lorentz factor and C is an instrument constant.[11, 12]

The scattering power of nuclear neutrons does not decrease significantly compare to that of X-ray scattering with increasing angle, 2θ as nuclei behave as point scatterers because the dimensions of the nuclei are much smaller than the wavelength of the neutron. So neutron powder diffraction provides more information at high angles and can be used to determine reliable temperature factors and site occupancies.

As the scattering factors for X-ray radiation increase with the increase of atomic number, those of light elements are relatively low. The neutron scattering length, b does not show systematic variation with atomic number, but varies between isotopes. As a result, neutron powder diffraction can be used to locate light elements and distinguish atoms of similar atomic numbers.

Neutrons possess a nuclear spin of 1/2 and have a magnetic moment which can be scattered by the magnetic moment of atoms with unpaired electrons. The sample will have randomly oriented magnetic spins at temperatures above the magnetic ordering temperature and the magnetic scattering will entirely contribute to the background of the neutron powder diffraction pattern. But when the material exhibits a magnetically ordered state, extra peaks or increased intensity on certain nuclear peaks can be observed due to additional Bragg scattering. The magnetic scattering of neutrons provides information both on the magnitude and orientation of the ordered magnetic moments.

The magnetic scattering occurs due to the interaction of neutrons with the electron cloud which contributes to the atom's magnetic moment. The magnetic scattering therefore

decreases with the increase of angle, 2θ due to the increased size of the electron cloud. The magnetic form factor describes the magnetic scattering and the magnetic scattering length is given by

$$p = \frac{e^2\gamma}{mc^2} Sf \tag{2.10}$$

where e and m are the charge and mass of an electron, c is the velocity of light, γ is the neutron's magnetic moment, S is the effective spin quantum number and f is the form factor.[13]

2.2.4 The Rietveld Method

The Rietveld method allows structural refinement of both powder X-ray and neutron diffraction data using a whole pattern least square method.[14] In powder diffraction, intensities of scattered radiation y_i are recorded as increments of Bragg angle 2θ, neutron time of flight or X-ray energy. At certain reflection positions diffraction peaks may overlap or be in very close proximity to each other making individual peaks difficult to resolve and considering powder diffraction as a whole is essential to solve the crystal structure.

The Rietveld method is a refinement technique where least squares refinement refines a number of parameters to obtain the best agreement between the calculated pattern and the observed data. Among these parameters are lattice parameters, atomic coordinates, site occupancies and temperature factors which describe the crystal structure. Instrumental parameters such as wavelength and profile parameters that describe peak shapes are also

refined. Both instrumental factors such as radiation source and sample effects such as crystallite size, stress and strain contribute to the peak shape. Thus, peak shape should be well fitted. The peak shapes in powder X-ray diffraction data are described as a combination of Lorentzian and Gaussian functions, modelled by a pseudo-Voigt function while constant wave length neutron powder diffraction commonly produces Gaussian peaks.[15] In this study, Rietveld profile refinements were performed on the XRPD and NPD data using the GSAS suite of programs.[16]

A good starting model for crystal structure including the space group, approximate lattice parameters and atom positions is required for the Rietveld method in order to obtain the global minimum and not a local minimum. The quantity minimised in the refinement is the residual S_y

$$S_y = \sum_i w_i (y_i - y_{ci})^2 \tag{2.11}$$

where w_i is a weighing function, y_i is the observed intensity of data point i and y_{ci} is the calculated intensity of data point i.

Several reliability or R factors are used to evaluate the quality of fit between the observed data and calculated pattern: the profile residual (R_p), the weighted profile residual (R_{wp}), the expected profile residual (R_{exp}) and the Bragg residual (R_B).

$$R_p = \frac{\sum |y_i - y_{ci}|}{\sum y_i} \tag{2.12}$$

$$R_{wp} = \left\{ \frac{\sum w_i (y_i - y_{ci})^2}{\sum w_i y_i^2} \right\}^{1/2}$$

(2.13)

$$R_{exp} = \left\{ \frac{(n - p + c)}{\sum w_i y_i^2} \right\}^{1/2}$$

(2.14)

where *n* is the number of observations, *p* the number of parameters and *c* the number of constraints.

$$R_B = \frac{\sum |I_j - I_{cj}|}{\sum I_j}$$

(2.15)

The goodness of fit of the refinement is analysed by the parameter χ^2, taking into account the quality of the data and the number of parameters refined.[17]

$$\chi^2 = \left[\frac{R_{wp}}{R_{exp}} \right]^2$$

(2.16)

2.3 Mössbauer Spectroscopy

Mössbauer Spectroscopy is an important technique in many areas of science especially in mineralogy which can provide specific information for the study of bonding, structural, magnetic, time dependent and dynamical properties of various systems.[18]

In Mössbauer spectroscopy, transitions that take place between nuclear energy levels of an atomic nucleus are involved. A highly monochromatic beam of γ-rays produced by decay

of radioactive elements such as $^{57}Fe_{26}$ or $^{119}Sn_{50}$ is used as the incident radiation. The γ-emission is associated with the change in population of energy levels in the nuclei responsible. This radiation may then be absorbed by a sample containing similar atoms to those responsible for the emission. The energy of the γ-rays can be varied by the use of Doppler effect moving the γ-ray source at a constant velocity either towards or away from the sample which is placed in a fixed position. The absorption of γ-rays by the sample is monitored as a function of energy. A schematic illustration of the technique is given in *Figure 2.3*.

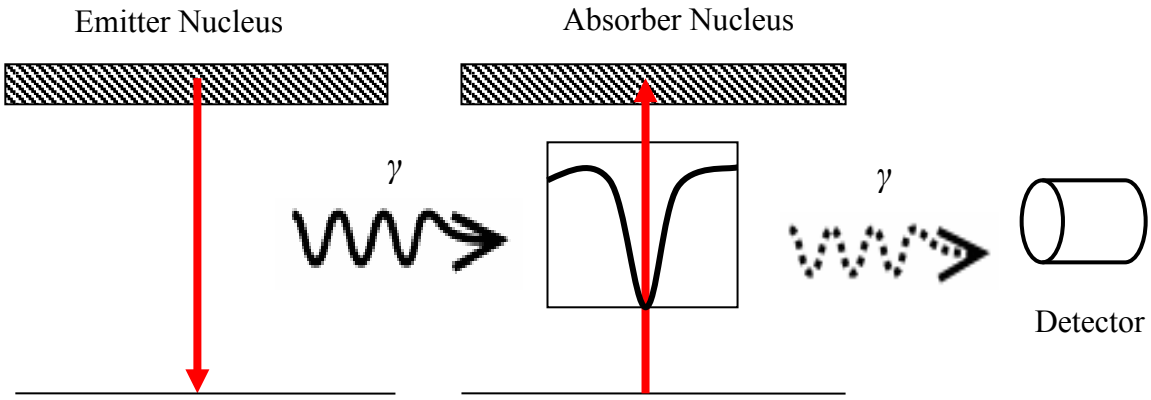

Figure 2.3 Simple Mössbauer spectrum from identical source and absorber.

2.3.1 The Isomer Shift

The nuclear energy levels of the source and the absorber are affected by the Coulomb interaction between the *s* electrons density at the nucleus with the nuclear charge. A change in the *s* electron densities between the source and absorber shifts the whole spectrum positively or negatively by changing the resonance energy of the transition. The

parameter corresponding to this displacement is called the isomer shift (δ). The observed chemical isomer shift is given by

$$\delta = \Delta E_S - \Delta E_A \tag{2.17}$$

where ΔE_S and ΔE_A are the change in nuclear energy levels of the source and absorber, respectively.

The isomer shift can be related to the measured shift in Doppler velocity as the shift cannot be measured directly. The isomer shift provides information about the electron density at the nucleus which can be used to determine the valency states and ligand bonding states.[18]

2.3.2 Quadrupole Splitting

A non-spherical charge distribution is present in nuclei with an angular momentum quantum number $I > 1/2$. This creates a nuclear quardrupole moment. If the nucleus having a quardrupole moment is in an electric field gradient nuclear energy levels split and hence split peaks in the Mössbauer spectrum.

The excited states of both Fe and Sn split into two substates $m_I = \pm 1/2$ and $m_I = \pm 3/2$ as nuclear spin quantum number of both isotopes in the excited state is $I = 3/2$. This gives a doublet as shown in *Figure 2.4*.[18]

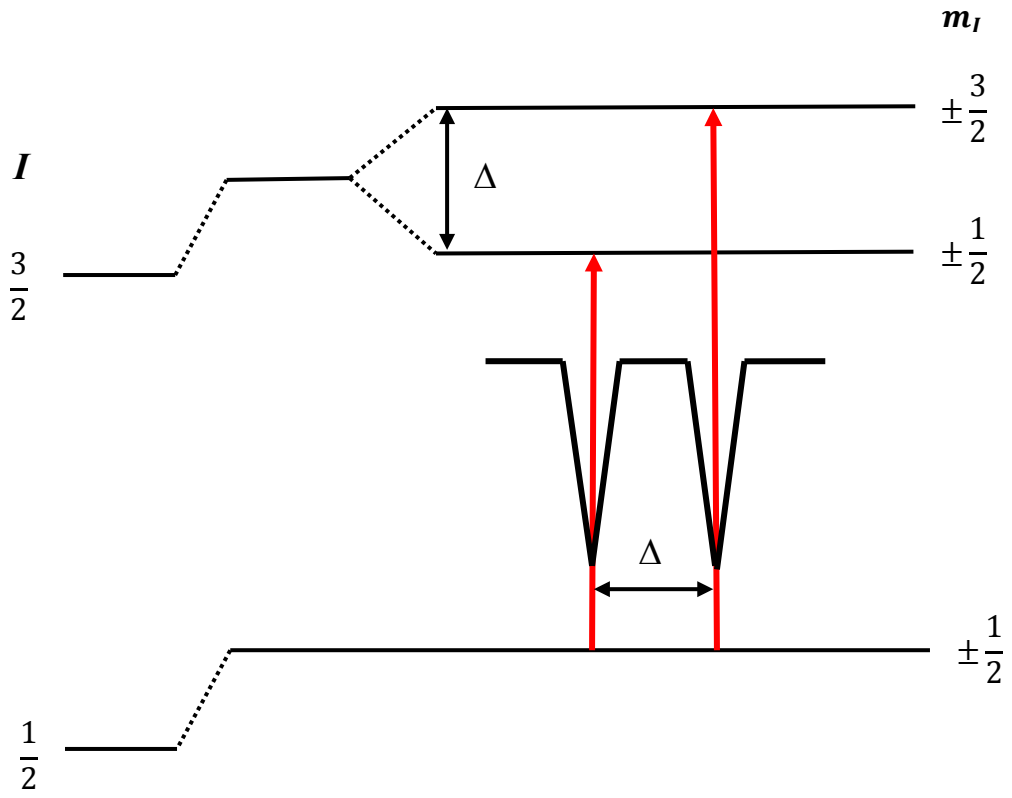

Figure 2.4 Quadrupole splitting for a 3/2 to 1/2 transition. Delta (Δ) is the magnitude of quadrupole splitting.

2.3.3 Magnetic Splittng

When a magnetic field is present each energy level of a nucleus with a spin *I* splits into 2*I* + 1 substates. This is shown in *Figure 2.5* for ^{57}Fe. For the transitions to happen between the excited state and ground state m_I should change by 0 or 1. Thus, there are six possible transitions for 3/2 to 1/2 transition as shown in *Figure 2.5*.[18]

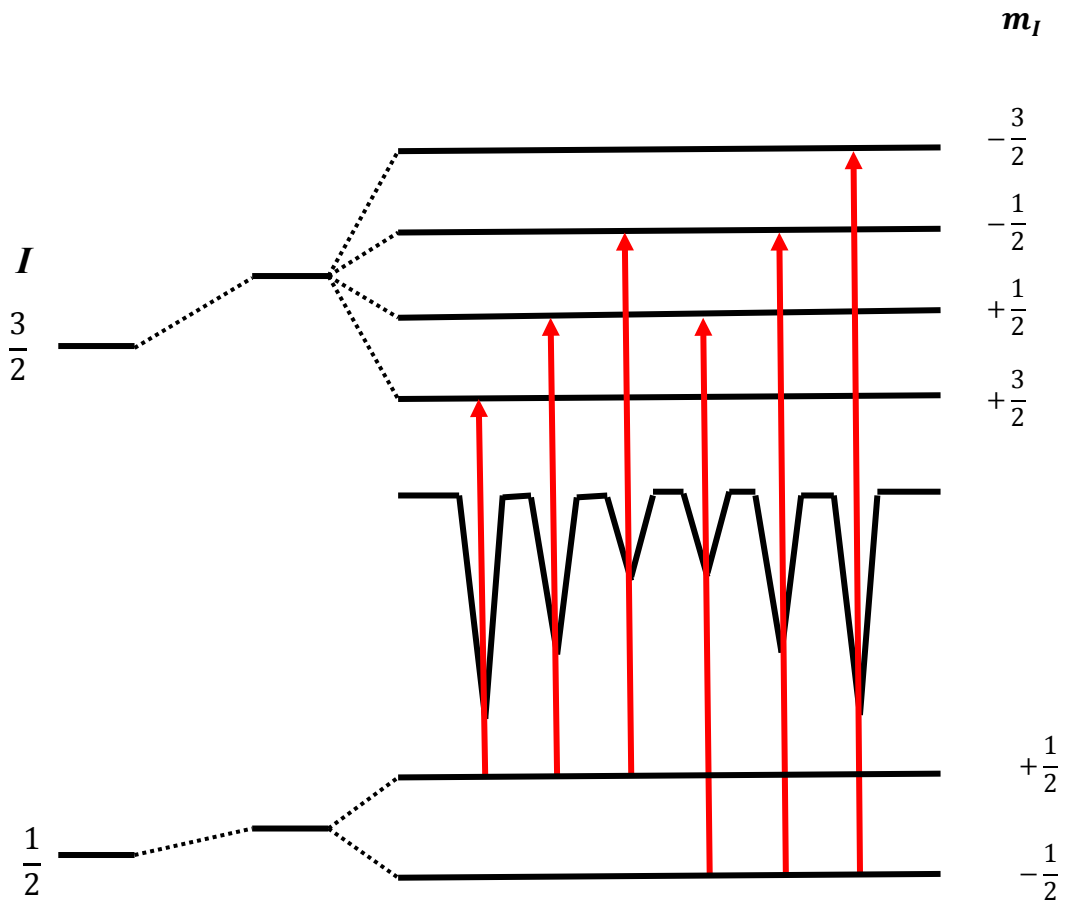

Figure 2.5 Magnetic splitting of the nuclear energy levels.

2.3.4 Mössbauer Spectroscopy Instrumentation

The ^{57}Fe Mössbauer spectra were recorded in the temperature range 298 K to 16 K using a constant acceleration transmission mode Mössbauer spectrometer with a 25 mCi ^{57}Co / Rh source. Low temperature data were collected with a helium closed-cycle cryorefrigerator. The spectrometer velocity is calibrated with the source and metallic iron foil. All the spectra were computer-fitted and the chemical isomer shift data were quoted relative to metallic iron at room temperature. All the Mössbauer data presented in this work were recorded and interpreted by Professor Frank J Berry.

2.4 Thermogravimetric Analysis

In thermogravimetric analysis the change in weight of a sample is measured as a function of temperature. In this work, analysis was carried out by heating few milligrams of sample at a rate of 10 ℃ per minute in a reducing atmosphere (10% H_2(g) / 90% N_2(g)) to the appropriate temperature (ranged from 600 ℃ to 1100 ℃). The mass loss could be used to determine the stoichiometry of the initial sample. A Netzsch STA 449 was used in this work.

2.5 Magnetic Measurements

The magnetic susceptibility of the compounds presented in this work was measured as a function of temperature using a Quantum Design Magnetic Property Measurement System (MPMS) Superconducting Quantum Interference Device (SQUID) magnetometer. Both zero-field-cooled (ZFC) and field-cooled (FC) measurements were carried out using the DC extraction method. Data were collected upon warming after cooling the sample in the absence of a magnetic field (ZFC) and after cooling in the presence of a magnetic field (FC).

2.6 Scanning Electron Microscopy

Electron microscopy, especially scanning electron microscopy (SEM) provides information on particle sizes and shapes over a wide range of magnification. Electron microscopes are of either transmission or reflection design. For examination in

transmission electron microscopy (TEM), samples thinner than ~2000 Å are used as electrons interact strongly with matter and are completely absorbed by thicker particles. In this case, the sample preparation is quite difficult. The main reflection instrument is the scanning electron microscopy which covers a wide range, from $\sim 10^{-2}$ to $\sim 10^{2}$ μm.

Some SEM and TEM instruments have the additional feature of providing an elemental analysis of sample composition. This technique is known as various names including electron probe microanalysis (EPMA), electron microscopy with microanalysis (EMMA) and analytical electron microscopy (AEM). But in general this technique is known as the energy dispersive X-ray detection (EDX). When a sample is bombarded with high energy electrons X-rays are generated. This technique identifies elements by scanning either the wavelength or the energy of emitted X-rays.[19, 20, 21]

In this work, scanning electron microscopy studies were performed on a JEOL 6060 instrument.

2.7 References

1. Cheetham, A. K.; Day, P., *Solid State Chemistry Techniques*. Oxford University Press: 1990.
2. McCabe, E. E.; Greaves, C. *J. Fluorine Chem*. **2006**, 128, 448.
3. Boultif, A.; Louer, D. *J. Appl. Cryst*. **2004**, 37, 724.
4. Pye, M. F. *Inorganic Chemistry Laboratory*, *Oxford*.
5. Cullity, B. D.; Stock, S. R., *Elements of X-ray Diffraction*. Prentice Hall.: 2001.
6. Pecharsky, V. K.; Zavalij, P. Y., *Fundamentals of Powder Diffraction and Structural Characterisation*. Springer: New York, 2003.
7. Greaves, C. *School of Chemistry*, *University Birmingham*.
8. Wormald, J., *Diffraction Methods*. Clarendon Press: Oxford, 1973.
9. Ladd, M. F. C.; Plamer, R. A., *Structure determination by X-ray crystallography*. Plenum Press: New York, 1985.
10. Fischer, P.; Frey, G.; Koch, M.; Könnecke, M.; Pomjakushin, V.; Schefer, J.; Thut, R.; Schlumpf, N.; Bürge, R.; Greuter, U.; Bondt, S.; Berruyer, E. *Physica* **2000**, B 276, 146.
11. Bacon, G. E., *Neutron Diffraction*. ed.; The Clarendon Press: Oxford, 1955.
12. Smith, R. I., Neutron Diffraction. In *The Neutron Training Course*, *ISIS*, Rutherford Appleton Laboratory, CLRC.
13. Izyumov, Y. A.; Naish, V. E.; Ozerov, R. P., *Neutron Diffraction of Magnetic Materials*. Consultants Bureau: A Division of Plenum Publishing Corporation: New York, 1991.
14. Rietveld, H. *J. Appl. Cryst*. **1969**, 2, 65.
15. McCusker, L. B.; Dreele, R. B. V.; Cox, D. E.; Louer, D.; Scardi, P. *J. Appl. Cryst*. **1999**, 32, 36.
16. Larson, A. C.; von Dreele, R. B. *General Structural Analysis System, Los Alamos National Laboratory, Los Alamos, NM* **1994**.
17. Young, R. A., *The Rietveld Method*. ed.; Oxford University Press: Oxford, 1996.
18. Dickson, D. P. E.; Berry, F. J., *Mössbauer Spectroscopy*. Cambridge University Press: 1986.
19. Eyring, L. *J. Chem. Ed*. **1980**, 57, 565.

20. Hawkes, P. W., *Elecron Optics and Electron Microscopy*. Taylor and Francis, London: 1972.
21. Honig, J. M.; Rao, C. N. R., *Elecron Preparation and Characterisation of Materials*. Academic Press: 1981.

CHAPTER THREE

Synthesis and Characterisation of Double Perovskites

$LaSr_2Fe_2SbO_9$ and $La_2Sr_2Fe_3SbO_{12}$

3.1 Background

The ordered perovskites as described in Chapter 1 with the formula $ABB'O_6$ or $AA'BB'O_6$, especially those that exhibit *B* site ordering have attracted much attention owing to their interesting physical properties.[1, 2] The crystal structure and magnetic properties of these compounds depend on the size and electronic structure of the two transition metal cations *B* and *B*'.[1] Compounds with greater difference in their charge are more likely to form completely ordered structures. If the two cations are similar in size and charge they distribute over the six-coordinate sites in a disordered manner. The presence of cation ordering results in lowering the symmetry of the ordered unit cell, compared to that of the disordered unit cell, as the octahedral cation sites are no longer equivalent.[1, 2]

Previous work on these compounds has shown them to exhibit unusual magnetic properties such as spin glass magnetic order when they contain more than one magnetic cation or when the crystal structure shows a degree of atomic disorder.[3, 4, 5, 6]

In Sr_2FeNbO_6 paramagnetic Fe^{3+} and diamagnetic Nb^{5+} cations are distributed in a disordered manner over the two six-coordinate sites of the perovskite structure. The magnetic susceptibility and hysteresis data suggest that Sr_2FeNbO_6 behaves as a spin glass below 32.5 K and shows no long-range magnetic order.[7] Rodriguez *et al.*[7] suggests this behaviour is due to the existence of short-range structural ordering between Fe^{3+} and Nb^{5+},

but EXAFS and Mössbauer studies have subsequently failed to find any evidence for such an effect.[8]

Both neutron powder diffraction and Mössbauer spectroscopy show that Fe^{3+} and Sn^{4+} cations are randomly distributed over the six-coordinate sites of $SrLaFeSnO_6$ and magnetically ordered as a G-type antiferromagnet at 1.7 K, with a relatively very small average atomic moment.[1, 9, 10] The magnetic susceptibility of this compound shows hysteresis between field-cooled and zero-field-cooled data at all temperatures below 250 K and a maximum at 38 K. $SrLaFeSnO_6$ has been described as being intermediate between a true antiferromagnet and a spin glass.[1, 9]

Similar magnetic properties have been observed in $SrEuFeSnO_6$ and $BaLaFeSnO_6$.[11] This complex magnetic behaviour has been explained by assuming that competition between nearest-neighbour and next-nearest-neighbour superexchange interactions leads to magnetic frustration which reduces the magnetic ordering temperature of ALnFeSnO$_6$ (A = Sr, Ba and Ln = La, Eu) and prevents long-range magnetic ordering in Sr_2FeNbO_6.[1, 9]

Sr_2FeTaO_6, which has a disordered distribution of Fe and Ta cations over the six-coordinate cation sites behaves as a spin glass below 23 K as proved by both susceptibility and Mössbauer data. No evidence for long-range magnetic ordering below 23 K has seen in neutron powder diffraction data recorded at lower temperature.[12]

In contrast, neutron powder diffraction studies on Sr_2FeSbO_6 at 1.5 K have revealed the presence of long-range A-type magnetic ordering with an average ordered moment of 3.06(9) μ_B per Fe atom on the Fe-dominated octahedral site. Both temperature dependent NPD data and magnetic susceptibility data have shown that the long-range magnetic ordering is lost at 37 K. Thus, an ordered backbone of spins and a spin glass fraction

coexist in Sr_2FeSbO_6 as a result of the partial cation ordering.[9, 12] The crystal structure of Sr_2FeSbO_6 has been described in the monoclinic space group[12] $P2_1/n$ which allows ordering of the Fe and Sb cation over the cation sites. The two cation sites in Sr_2FeSbO_6 are occupied in a partially ordered manner by Fe^{3+} ions in a ratio of 0.795(6) : 0.205(6).[12]

This study reports the synthesis and characterisation of two new compounds $LaSr_2Fe_2SbO_9$ ($La_{0.33}Sr_{0.67}Fe_{0.67}Sb_{0.33}O_3$) and $La_2Sr_2Fe_3SbO_{12}$ ($La_{0.50}Sr_{0.50}Fe_{0.75}Sb_{0.25}O_3$) which are analogues of Sr_2FeSbO_6. More iron has been introduced into the *B* site of these compounds and in order to maintain the charge neutrality La^{3+} is added to the *A* site. The idea is to achieve more cation order at the *B* site and more magnetically ordered iron which would give rise to a ferrimagnet.

3.2 Experimental Procedure

Polycrystalline samples of $LaSr_2Fe_2SbO_9$ and $La_2Sr_2Fe_3SbO_{12}$ were synthesised by weighing out stoichiometric amounts of high purity La_2O_3, $SrCO_3$, Fe_2O_3 and Sb_2O_3 (Aldrich, >99%). The reactants were initially ground together using a mortar and a pestle and heated at 1200 ℃ in air for 48 hours with several intermediate grindings. Initial structural characterisation of both samples was carried out using X-ray powder diffraction data. Neutron powder diffraction data were collected on both compounds at 2 K and 300 K. In order to further understand the magnetic behaviour of these compounds Mössbauer data of $LaSr_2Fe_2SbO_9$ and $La_2Sr_2Fe_3SbO_{12}$ were recorded at 16 K and 300 K.

3.3 Results and Discussion

3.3.1 Results and Discussion for $LaSr_2Fe_2SbO_9$

3.3.1.1 X-ray Powder Diffraction

Since $LaSr_2Fe_2SbO_9$ correlates to the structure of Sr_2FeSbO_6 Rietveld analysis of the X-ray powder diffraction data was carried out in the monoclinic space group $P2_1/n$ which has been used to describe the crystal structure of Sr_2FeSbO_6. During the course of the refinement, the cationic distribution of Fe^{3+} and Sb^{5+} over the two sites was constrained in such a way that the sites remained fully occupied and the overall Fe^{3+} : Sb^{5+} ratio remained 2 : 1. The thermal parameters of these two sites were constrained to be equal. Also the isotropic temperature factors of La^{3+} and Sr^{2+} were constrained to be equal. The values of refined parameters are listed in *Table 3.1* and the refinement profiles are shown in *Figure 3.1*. According to X-ray refinement data one of the two crystallographically distinct

octahedral sites (*B*) in the monoclinic structure contains 55(8)% of Fe^{3+} and 45(8)% of Sb^{5+} while 79(8)% of Fe^{3+} and 21(8)% of Sb^{5+} are present in the second site (*B*'). Although some degree of order between the octahedral sites is indicated, the occupation parameters have high standard deviations.

Table 3.1 Structural parameters of $LaSr_2Fe_2SbO_9$ in space group $P2_1/n$ using XRPD data.

Atom	**Site symmetry**	***x***	***y***	***z***	$\mathbf{U_{iso} \times 100 / Å^2}$
La/Sr	4e	0.996(5)	0.002 (4)	0.247(2)	0.8(1)
B	2d	0.5	0	0	1.7(1)
B'	2c	0	0.5	0	1.7(1)
O(1)	4e	0.28(2)	0.28(1)	0.025(6)	4(2)
O(2)	4e	0.17 (1)	0.146(7)	0.479(8)	0.4(2)
O(3)	4e	0.93(2)	0.53(2)	0.282(4)	6(2)

Fractional occupancies on *B*: 0.55(8) Fe^{3+} 0.45(8) Sb^{5+}; on *B*': 0.79(8) Fe^{3+}, 0.21(8) Sb^{5+}

a = 5.564 (2) Å, b = 5.577(2) Å, c = 7.8898(8) Å, β = 89.81°(1)

χ^2 = 1.75, R_{wp} = 3.74%

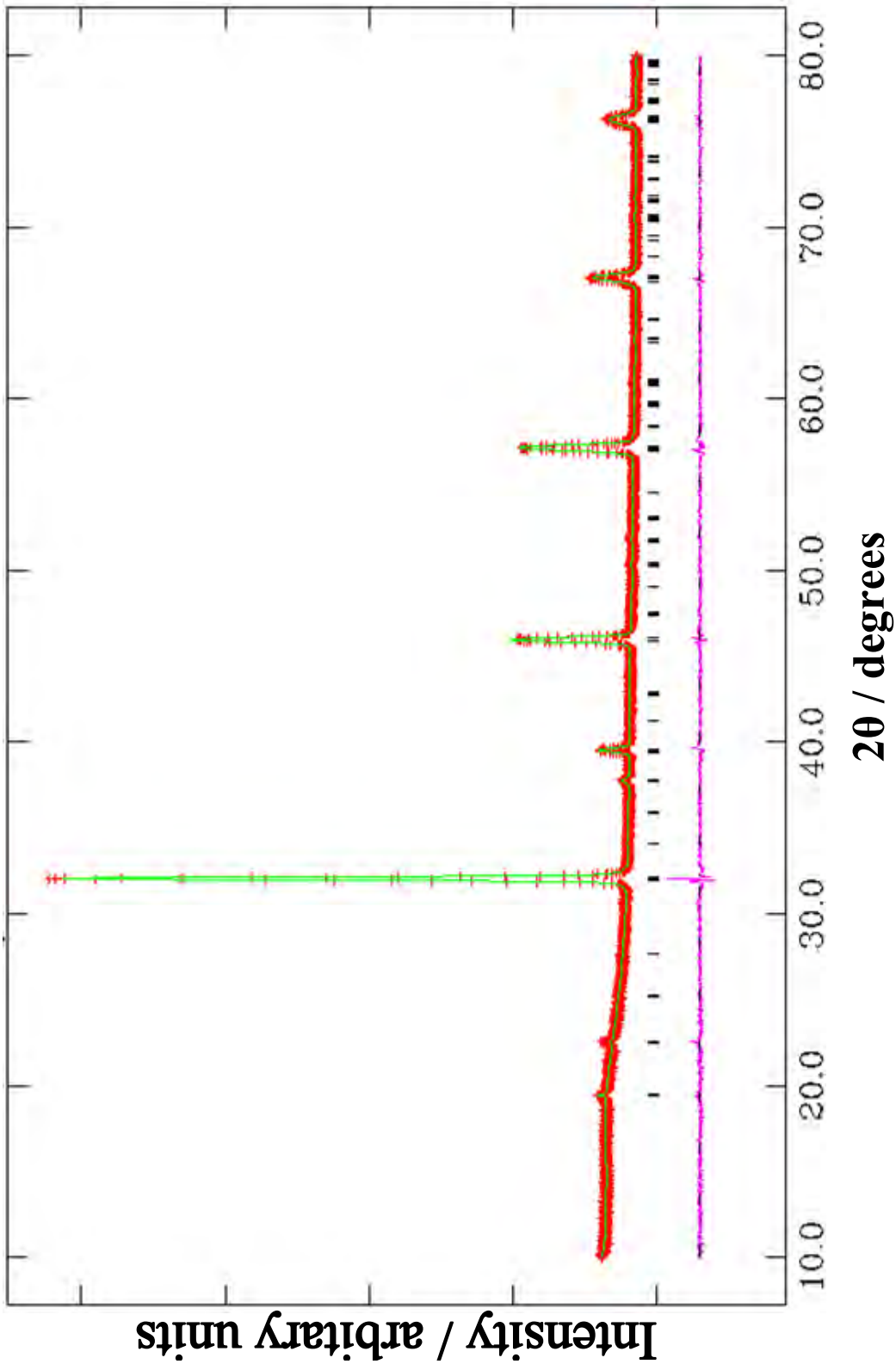

Figure 3.1 Observed (red +), calculated (green) and difference (pink) profiles of $LaSr_2Fe_2SbO_9$, as generated by the Rietveld refinement of XRPD data, the reflections of $LaSr_2Fe_2SbO_9$ are shown by black vertical lines.

3.3.1.2 Neutron Powder Diffraction

The Rietveld refinement was performed on the neutron powder diffraction data collected at 2 K and 300 K in the same space group $P2_1/n$ used in XRPD data refinement. The diffraction data collected at both temperatures contained additional Bragg reflections indicative of the presence of long-range magnetic ordering. At both temperatures the compound ordered as a G-type antiferromagnet and the magnetic structure used is illustrated in *Figure 3.2*.

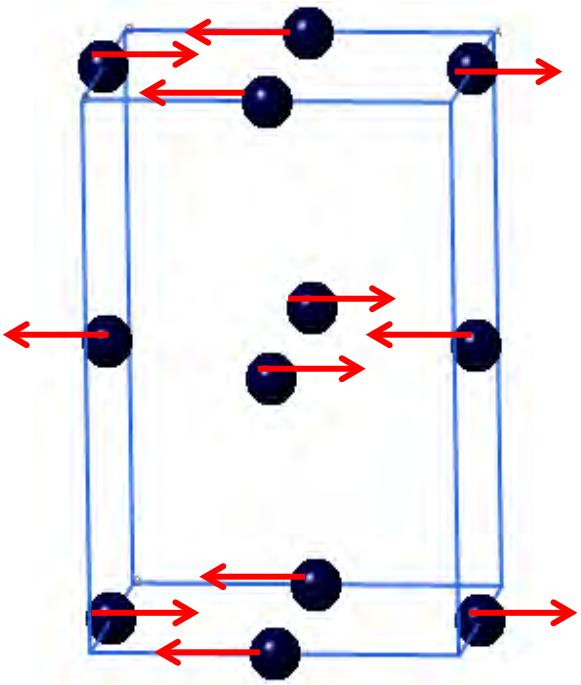

Figure 3.2 The G-type antiferromagnetic unit cell for $LaSr_2Fe_2SbO_9$.

A simultaneous Rietveld refinement of the crystal and the magnetic structures was performed using the free-ion form factor[13] of Fe^{3+} to describe the angular dependence of the magnetic scattering amplitude. The size of the magnetic unit cell is the same as that of

the crystallographic unit cell. At both temperatures the magnetic moment was constrained to lie along the crystallographic *x* axis and the cationic distribution of Fe^{3+} and Sb^{5+} over the two sites was constrained in such a way that the sites remained fully occupied and the overall Fe^{3+} : Sb^{5+} ratio remained 2 : 1. The final structural parameters of $LaSr_2Fe_2SbO_9$ at 300 K and 2 K are listed in *Tables 3.2* and *3.3*. The refinement profiles of $LaSr_2Fe_2SbO_9$ at 300 K and 2 K are shown in *Figures 3.3* and *3.4*.

Table 3.2 Structural parameters of $LaSr_2Fe_2SbO_9$ in space group $P2_1/n$ using NPD data recorded at 300 K.

A					
La/Sr	4e	0.9961(9)	0.008(1)	0.247(3)	1.25(3)
B	2d	0.5	0	0	0.52(2)
B'	2c	0	0.5	0	0.52(2)
O(1)	4e	0.253(2)	0.263(2)	0.0258(6)	1.0(1)
O(2)	4e	0.262(2)	0.274(2)	0.4611(6)	1.5(2)
O(3)	4e	0.9624(9)	0.499(1)	0.254(3)	1.37(9)

Among the two crystallographically distinct *B* sites, the first site (*B*) contains 57(13)% of Fe^{3+} and the second site (*B*') contains 77(13)% of Fe^{3+} ions at 300 K. The magnetic moment directed along the crystallographic *x* axis was found to be 3.076(6) μ_B per Fe^{3+} cation at 2 K and at 300 K it was 2.385(8) μ_B per Fe^{3+} cation.

Fractional occupancies on *B*: 0.57(13) Fe^{3+}, 0.43(13) Sb^{5+}; on *B*': 0.77(13) Fe^{3+}, 0.23(13) Sb^{5+}
a = 5.5989(3) Å, b = 5.5773(3) Å, c = 7.8788(5) Å, β = 89.96°(1)
χ^2 = 7.751, R_{wp} = 5.26%

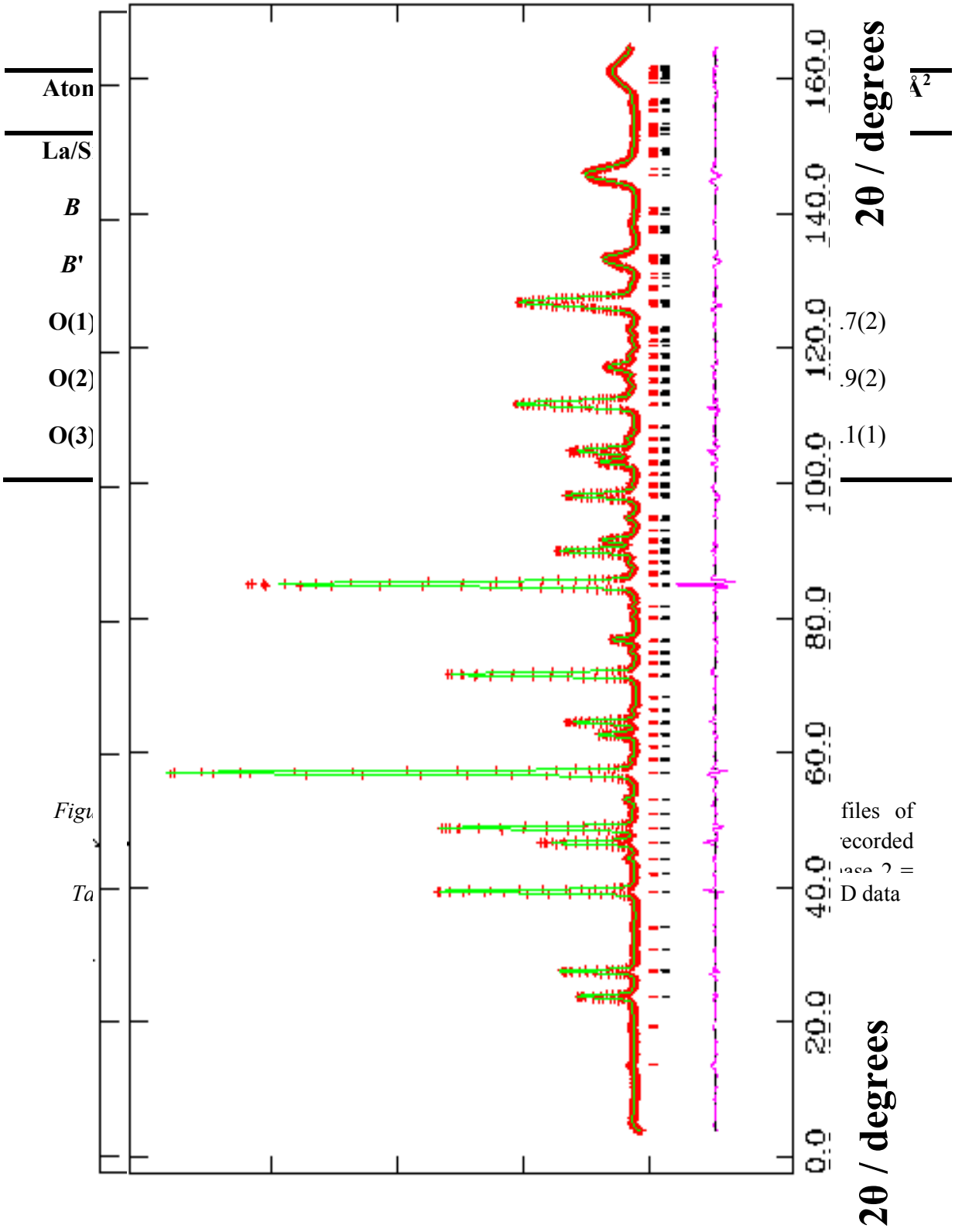

Figu files of ecorded ase 2 = D data

Ta

Fractional occupancies on *B*: 0.59(12) Fe^{3+}, 0.41(12) Sb^{5+}; on *B*': 0.75(12) Fe^{3+}, 0.25(12) Sb^{5+}

a = 5.5885(3) Å, *b* = 5.5697(3) Å, *c* = 7.8685(5) Å, *β* = 89.93°(1)

χ^2 = 6.357, R_{wp} = 5.19%

3.3.1.3 Mössbauer Spectroscopy

The ^{57}Fe Mössbauer spectroscopy recorded at 298 K, illustrated in *Figure 3.5* is complex showing the presence of two magnetic sextets together with a paramagnetic quadrupole split absorption and a singlet. The spectrum recorded at 16 K (the ^{57}Fe Mössbauer parameters are given in *Table 3.4*) is less complex being amenable to fitting to two magnetically split sextet patterns. Both components have chemical isomer shifts characteristic of Fe^{3+}. The results imply that occupation of the two sites is in the approximate ratio 1 : 2 within the experimental error.

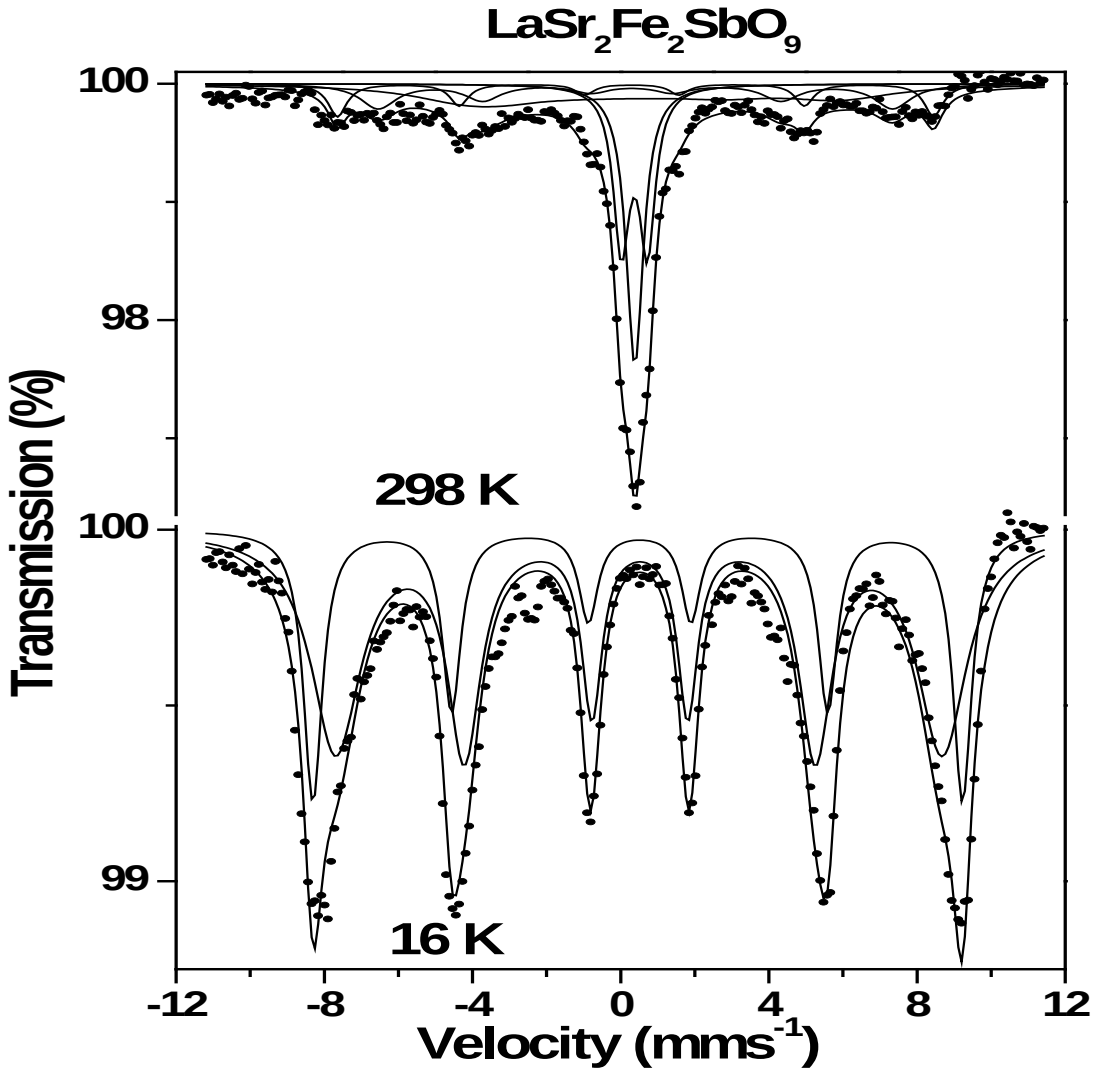

Figure 3.5 Mössbauer spectra recorded from $LaSr_2Fe_2SbO_9$ at 16 K and 298 K.

Table 3.4 ^{57}Fe Mössbauer parameters recorded from $LaSr_2Fe_2SbO_9$ at 16 K.

	$\delta \pm 0.02$ / mms^{-1}	**$e^2qQ/2 \pm 0.04$ / mms^{-1}**	**H $\pm$ 0.5 / T**	**Area $\pm$ 5 %**
$LaSr_2Fe_2SbO_9$	0.49	-0.03	54	32
	0.51	-0.01	51	68

3.3.1.4 Discussion

The cation ratio of 1 : 2 suggested by Mössbauer data for the occupation of Fe^{3+} between the two sites is in reasonable agreement with that deduced from NPD and XRPD data given the high standard deviations for the site occupancies. The Mössbauer data are highly reliable as the technique directly probes the environment of Fe^{3+} nuclei as described in Chapter 2. Even though NPD and XRPD refinements produced similar results for the cation distribution the occupancies obtained from NPD refinement consist of larger standard deviations, whereas the occupancies obtained from XRPD are in better agreement with Mössbauer data within the experimental error. The presence of magnetic Bragg peaks in the neutron powder diffraction patterns is consistent with $LaSr_2Fe_2SbO_9$ exhibiting long-range magnetic order both at 2 K and 300 K which is also confirmed by the two sextets present in Mössbauer spectra recorded at 16 K and 298 K. Also it is clear that the T_N is higher than 300 K. The refined magnetic moment per Fe^{3+} cation (3.076(6) μ_B) at 2 K is lower than that expected for Fe^{3+} (5.0 μ_B) due to the participation of *d* electrons in covalent bonding. The refined magnetic moment decreases with the increase of temperature and at 300 K it is 2.385(8) μ_B . The parent compound Sr_2FeSbO_6 exhibits long-range antiferromagnetic order in the temperature range 1.5 K to 37 K, with an average magnetic moment of 3.06(9) μ_B per Fe atom on the Fe-dominated octahedral site at 1.5 K[12] which is close to that obtained for $LaSr_2Fe_2SbO_9$ at 2 K. The considerably lower magnetic moment, as explained by Cussen *et al.*[12] for the Sr_2FeSbO_6 phase, could be due to the incomplete antiferromagetic order because of incomplete *B* site cation order.

3.3.2 Results and Discussion for $La_2Sr_2Fe_3SbO_{12}$

3.3.2.1 X-ray Powder Diffraction

The initial structural characterisation was carried out using X-ray powder diffraction data in monoclinic space group $P2_1/n$. The Fe^{3+} / Sb^{5+} distribution over the two crystallographically distinct *B* sites was allowed to vary with the constraint that the 3 : 1 ratio was maintained. The isotropic temperature parameters of these two sites were constrained to be equal. The refined parameters are given in *Table 3.5* and the refined profiles are shown in *Figure 3.6*. The refined data indicate that one of the two crystallographically distinct octahedral sites (*B*) in the monoclinic structure contains 70(3)% of Fe^{3+} while 80(3)% of Fe^{3+} is in the second site (*B*'). Because of the high standard deviations, it is not clear that any *B* site order exists.

Table 3.5 Structural parameters of $La_2Sr_2Fe_3SbO_{12}$ in space group $P2_1/n$ using XRPD data.

Atom	**Site symmetry**	***x***	***y***	***z***	$\mathbf{U_{iso} \times 100 / Å^2}$
La/Sr	4e	0.987(1)	0.008(1)	0.251(2)	1.0 (1)
B	2d	0.5	0	0	2.5 (1)
B'	2c	0	0.5	0	2.5 (1)
O(1)	4e	0.235(8)	0.253(9)	0.026(3)	4.3(8)
O(2)	4e	0.18(1)	0.19(1)	0.441(5)	9(2)
O(3)	4e	0.933(4)	0.511(7)	0.259 (9)	3(1)

Fractional occupancies on *B*: 0.70(3) Fe^{3+}, 0.30(3) Sb^{5+}; on *B*': 0.80(3) Fe^{3+}, 0.20(3) Sb^{5+}
a = 5.5893(3) Å, b = 5.5666(3) Å, c = 7.8715(4) Å, β = 90.104°(8),
χ^2 = 1.747, R_{wp} = 3.74%

Figure 3.6 Observed (red +) calculated (green) and difference (pink) profiles of ta, the .

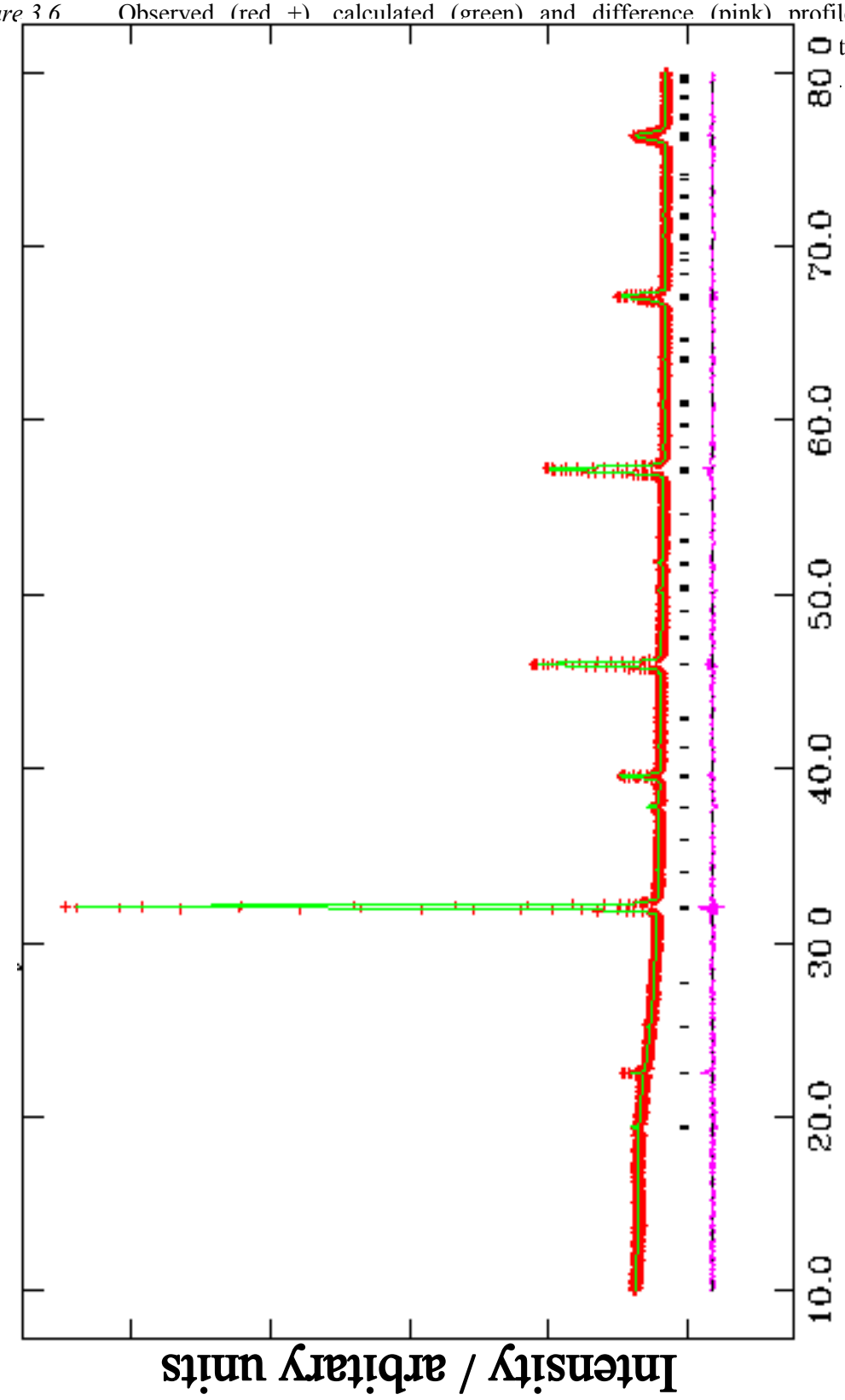

3.3.2.2 Neutron Powder Diffraction

Neutron powder diffraction data recorded from $La_2Sr_2Fe_3SbO_{12}$ at 300 K and 2 K consisted of additional Bragg reflections which suggest the presence of long-range magnetic ordering. The crystal symmetry remained unchanged at both temperatures and the Rietveld refinement was performed in the space group $P2_1/n$. The compound ordered as a G-type antiferromagnet at both temperatures with the magnetic moments on the cations arranged in a similar fashion to that observed previously for $LaSr_2Fe_2SbO_9$, shown in *Figure 3.2*.

In order to obtain the details of the magnetic structure a magnetic phase was included in the Rietveld refinement in addition to the main phase. The free-ion form factor[13] of Fe^{3+} was used to describe the angular dependence of the magnetic scattering amplitude. The ordered moment was constrained to lie along the crystallographic *x* axis and the cationic distribution of Fe^{3+} and Sb^{5+} over the two sites was varied with the constraint that the overall Fe^{3+} : Sb^{5+} ratio remained at 3 : 1. The refined structural parameters of $La_2Sr_2Fe_3SbO_{12}$ at 300 K and 2 K are listed in *Tables 3.6* and *3.7*. The refined profiles of $La_2Sr_2Fe_3SbO_{12}$ at 300 K and 2 K are illustrated in *Figures 3.7* and *3.8*, respectively.

Figure 3.7 Observed (red +), calculated (green) and difference (pink) profiles of $La_2Sr_2Fe_3SbO_{12}$, as generated by the Rietveld refinement of NPD data recorded at 300 K, where phase 1 = $La_2Sr_2Fe_3SbO_{12}$ (black vertical lines) and phase 2 = $La_2Sr_2Fe_3SbO_{12}$ magnetic reflections (red vertical lines).

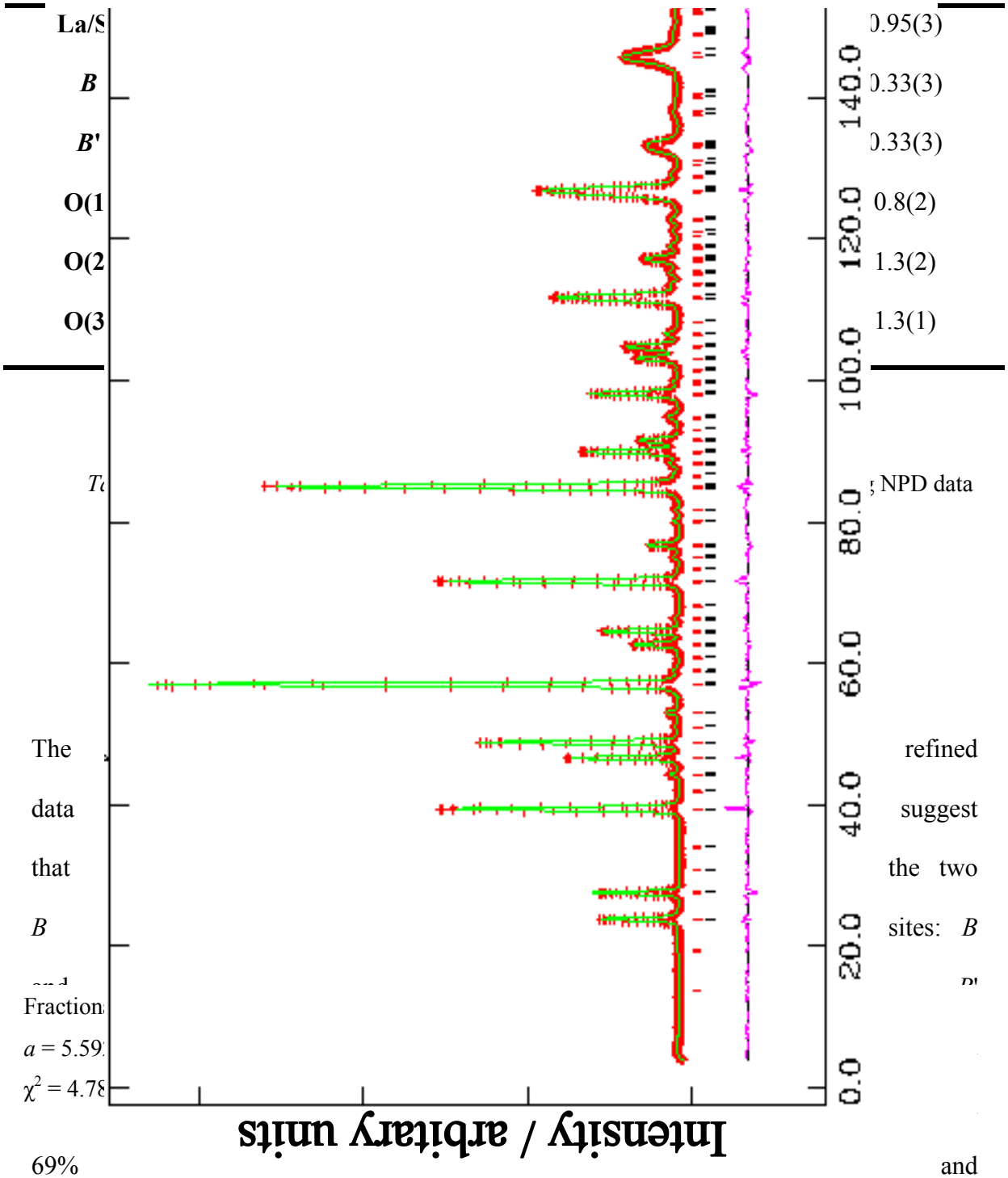

/ Å^2

La/S 0.95(3)

B 0.33(3)

B' 0.33(3)

O(1 0.8(2)

O(2 1.3(2)

O(3 1.3(1)

T ; NPD data

The refined

data suggest

that the two

B sites: *B*

and *B'*

Fraction

a = 5.59

χ^2 = 4.78

69% and

81% of Fe^{3+}

at both temperatures, respectively. It is not clear whether any order exists. The magnetic moments refined to values of 3.55(2) μ_B per Fe^{3+} cation at 2 K and 2.92(2) μ_B per Fe^{3+} cation at 300 K. At both temperatures the moments aligned along the crystallographic *x* axis.

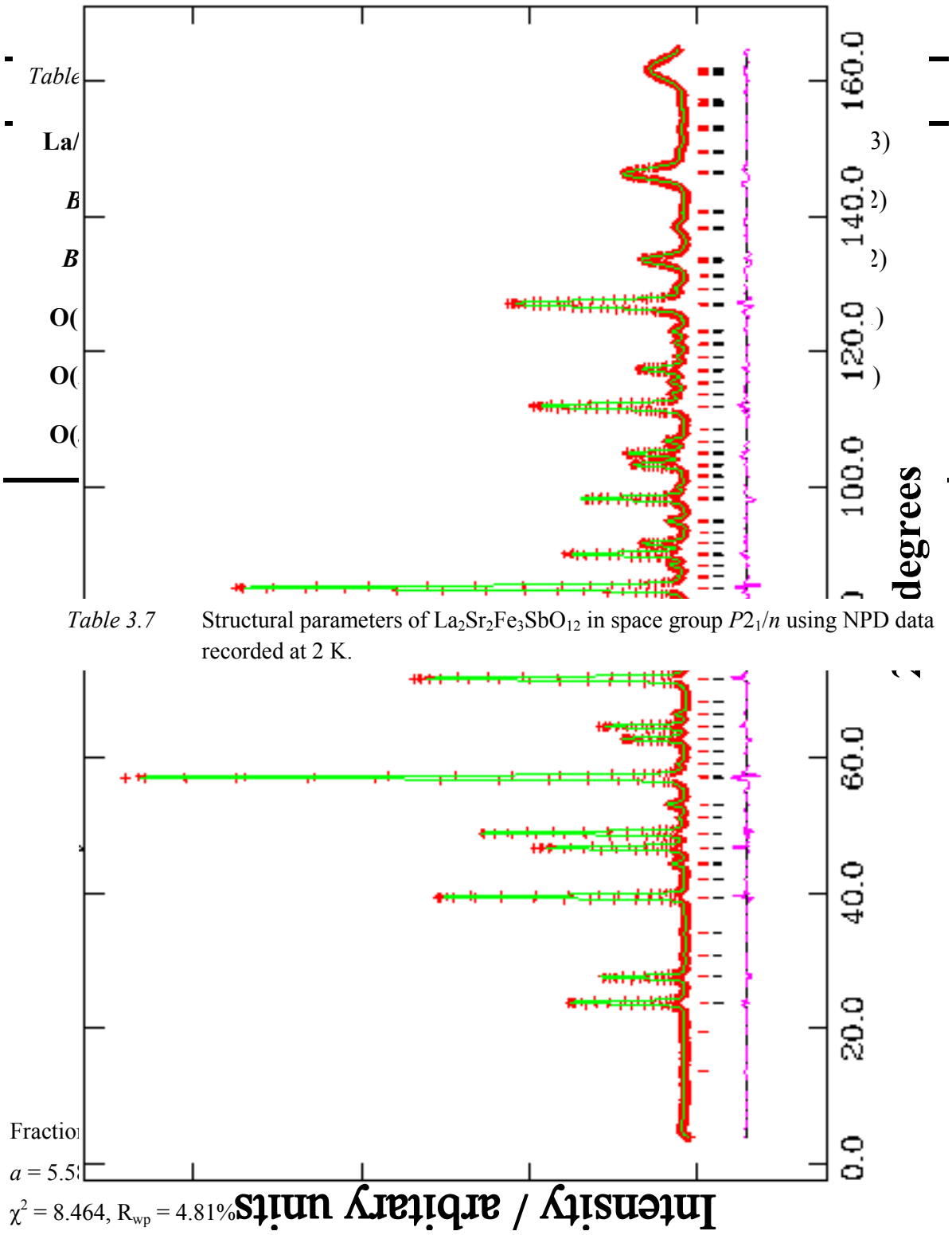

Table 3.7 Structural parameters of $La_2Sr_2Fe_3SbO_{12}$ in space group $P2_1/n$ using NPD data recorded at 2 K.

Figure 3.8 Observed (red +), calculated (green) and difference (pink) profiles of $La_2Sr_2Fe_3SbO_{12}$, as generated by the Rietveld refinement of NPD data recorded at 2 K, where phase 1 = $La_2Sr_2Fe_3SbO_{12}$ (black vertical lines) and phase 2 = $La_2Sr_2Fe_3SbO_{12}$ magnetic reflections (red vertical lines).

3.3.2.3 Mössbauer Spectroscopy

The spectrum recorded at 298 K is complex but shows more iron in a magnetically ordered state at 298 K as compared to the situation in $LaSr_2Fe_2SbO_9$, illustrated in *Figure 3.9*. The spectrum recorded at 16 K (*Table 3.8*) shows two magnetically split sextet patterns with chemical isomer shift characteristic of Fe^{3+} and also with an occupation of the two sites in a ratio of approximately 1 : 2. Although the insensitivity of XRPD and NPD is insufficient to provide clear evidence for the ordering, Mössbauer data provide stronger evidence that the two octahedral sites have different Fe : Sb ratios.

Table 3.8 ^{57}Fe Mössbauer parameters recorded for $La_2Sr_2Fe_3SbO_{12}$ at 16 K.

	$\delta \pm 0.02$ / mms^{-1}	**$e^2qQ/2 \pm 0.04$ / mms^{-1}**	**H $\pm$ 0.5 / T**	**Area $\pm$ 5 %**
$La_2Sr_2Fe_3SbO_{12}$	0.47	-0.03	54	35
	0.49	-0.03	52	65

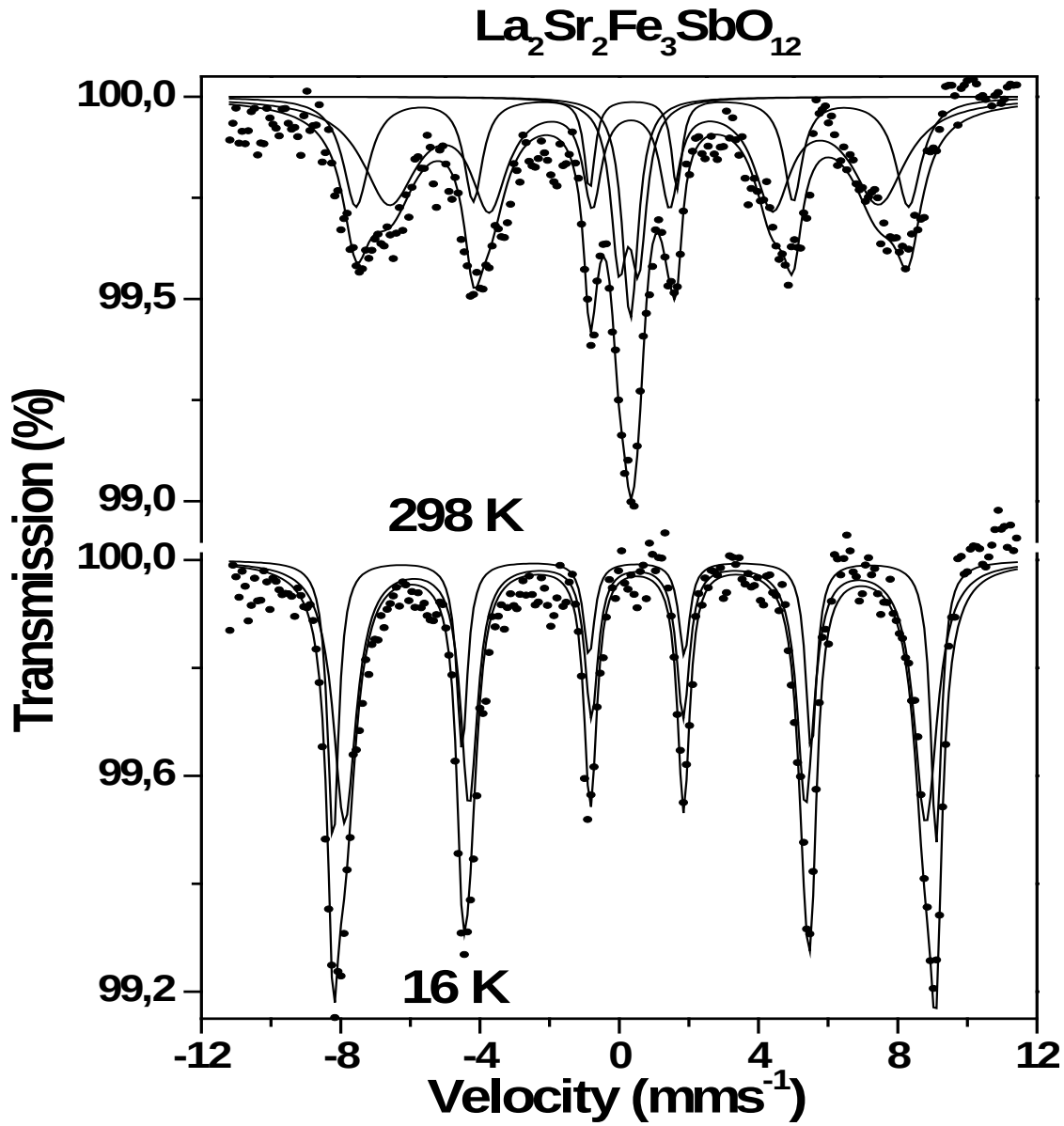

Figure 3.9 Mössbauer spectra recorded from $La_2Sr_2Fe_3SbO_{12}$ at 298 K and 16 K.

3.3.2.4 Discussion

The distribution of Fe^{3+} between the two sites is similar as indicated by NPD and XRPD data, but Mössbauer data suggest a cation ratio of 1 : 2 for the Fe^{3+} distribution. As previously discussed, Mössbauer data have a greater degree of reliability since the technique directly analyses the Fe^{3+} environment. The thermal parameters determined by

XRPD especially for the weakly scattering oxygen are rather large and are not reliable. Neutron powder diffraction data indicate that the compound also exhibits long-range magnetic order both at 2 K and 300 K. These results are consistent with the Mössbauer data recorded at 16 K and 298 K which also indicate the presence of more magnetically ordered iron at 298 K. The refined magnetic moments at 2 K (3.55(2) μ_B per Fe^{3+} cation) and 300 K (2.92(2) μ_B per Fe^{3+} cation) are larger than those observed for $LaSr_2Fe_2SbO_9$ at 2 K and 300 K. The presence of magnetic Bragg scattering at 300 K also suggests that the T_N of this compound is higher than 300 K.

3.4 Conclusion

The crystal and magnetic structures of $LaSr_2Fe_2SbO_9$ and $La_2Sr_2Fe_3SbO_{12}$ have been determined using neutron powder diffraction and Mössbauer spectroscopy. The compounds exhibit long-range antiferromagnetic order and the Néel temperatures for both compounds are higher than 300 K. It is confirmed that for both compounds the distribution of Fe^{3+} between the two *B* sites is of 1 : 2 ratio. The results also indicate the possibility of modifying the magnetic properties of these types of materials by increasing the magnetic ion content at the *B* site.

3.5 References

1. Attfield, M. P.; Battle, P. D.; Bollen, S. K.; Gibb, T. C.; Whitehead, R. J. *J. Solid State Chem*. **1992**, 100, 37.
2. Mitchell, R. H., *Perovskites: Modern and Ancient*. Almaz Press: Canada, 2002.
3. Battle, P. D.; Gibb, T. C.; Jones, C. W.; Studer, F. *J. Solid State Chem*. **1989**, 78, 281.
4. Battle, P. D.; Macklin, W. J. *J. Solid State Chem*. **1984**, 52, 138.

5. Gibb, T. C.; Battle, P. D.; Bollen, S. K.; Whitehead, R. J. *J. Mater. Chem*. **1992**, 2, 111.
6. Kim, S. H.; Battle, P. D. *J. Solid State Chem*. **1995**, 114, 174.
7. Rodriguez, R.; Fernandez, A.; Isalgue, A.; Rodriguez, J.; Labarta, A.; Tejada, J.; Obradors, X. *J. Phys. C: Solid State Phys*. **1985**, 18, L401.
8. Gibb, T. C. *J. Mater. Chem*. **1993**, 3, 441.
9. Battle, P. D.; Gibb, T. C.; Herod, A. J.; Hodges, J. P. *J. Mater. Chem*. **1995**, 5, 75.
10. Gibb, T. C. *J. Mater. Chem*. **1992**, 2, 415.
11. Gibb, T. C.; Whitehead, R. J. *J. Mater. Chem*. **1993**, 3, 591.
12. Cussen, E. J.; Vente, J. F.; Battle, P. D.; Gibb, T. C. *J. Mater. Chem*. **1997**, 7, 459.
13. Dianoux, A. J.; Lander, G., *Neutron Data Booklet*. Institute of Laue-Langevin: France, 2003.

CHAPTER FOUR

Synthesis and Characterisation of n = 2 Ruddlesden-Popper Phases $Ln_2SrFe_2O_7$ (Ln = La, Nd, Eu) and $La_2BaFe_2O_7$

4.1 Background

The structural and the magnetic properties of n = 2 Ruddlesden-Popper phases with the general formula $Ln_2SrFe_2O_7$ (Ln = La, Nd, Sm, Eu, Gd) and $Ln_2BaFe_2O_7$ (Ln = La, Nd, Sm, Eu, Gd, Tb) were first reported by Samaras *et al*.[1-6] The structures of these phases have been resolved by X-ray and neutron powder diffraction. Most of these compounds are antiferromagnetic with Néel temperatures of about 550 K[4, 7] and crystallise with tetragonal unit cells in the space group *I*4/*mmm*, except for the phases those contain Tb, Eu in their *A* site which crystallise in the space group $P4_2/mnm$.[1-4]

The nature and the size of Ln / Sr ions present in the *A* site of Ruddlesden-Popper phases play a major role in determining the structure and physical properties of these phases.[8, 9] In the Ruddlesden-Popper structure there are two sites within which the *A* cations can be distributed, the larger twelve-coordinate site in the perovskite blocks and the smaller nine-coordinate site in the rock-salt layers, illustrated in *Figure 4.1*. Seshadri *et al*.[10] reported that in the layered manganites $Ln_{1.2}Sr_{1.8}Mn_2O_7$ (Ln = La, Pr, Nd) the smaller lanthanide cations have a greater preference to occupy the nine-coordinate sites in the structure. The larger lanthanide / alkaline earth metal cations present in the rock-salt layers significantly affect the cell parameters by elongating the interlayer distance, thus increasing the *c* parameter.[11]

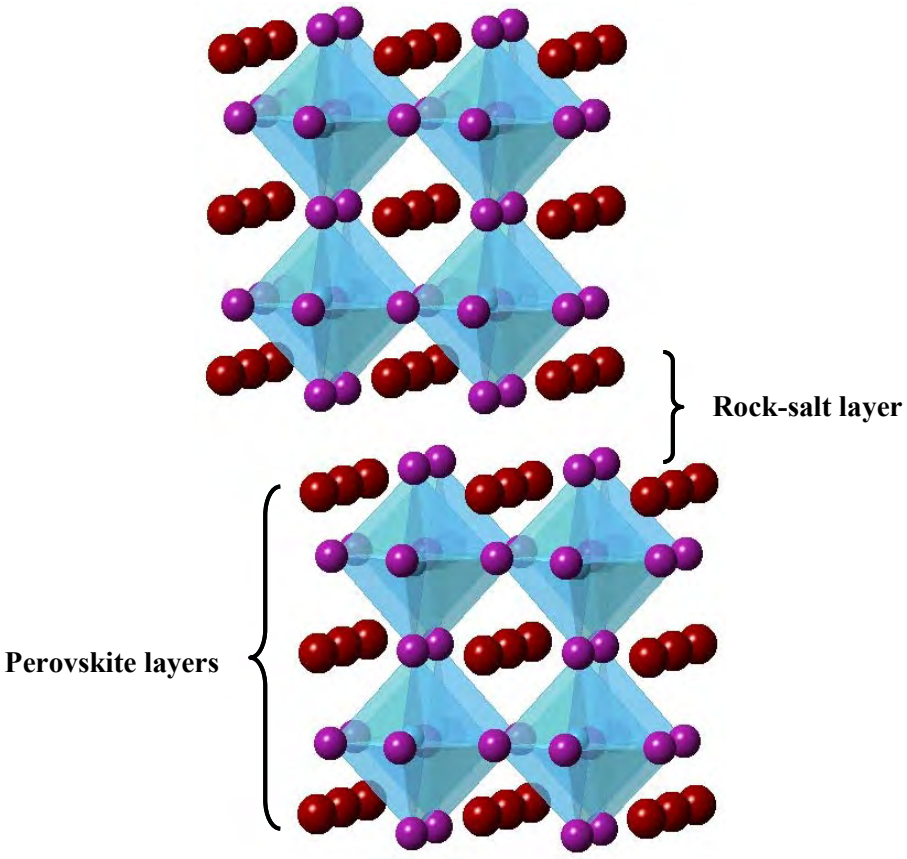

Figure 4.1 Structure of the $n = 2$ Ruddlesden-Popper phase $A_3B_2O_7$, illustrating the rock-salt and perovskite layers, with A cations shown in red, oxygen anions in purple and BO_6 octahedra shown in blue.

The studies carried out by Sharma *et al.*[12] on magnetic susceptibility suggest that $La_2SrFe_2O_7$ and $Nd_2SrFe_2O_7$ are antiferromagnetic while $Gd_2SrFe_2O_7$ and $Dy_2SrFe_2O_7$ are ferromagnetic (solely based on the sign of the Weiss constant). Further, the electrical resistivity in these phases decreases with the decrease in the ionic size of the lanthanide cation.[12]

The magnetic structures of $Ln_2Sr(Ba)Fe_2O_7$ (Ln = La, Nd, Gd, Tb) have been studied using neutron powder diffraction and Mössbauer spectroscopy. At room temperature the magnetic moments of these phases are aligned along the [110] direction.[3, 5, 13] But upon lowering the temperature to 4.2 K, different reorientations of the magnetic moment have

been observed. In $Tb_2SrFe_2O_7$ and $Nd_2SrFe_2O_7$ the magnetic moments move from the basal plane to along the *c* axis, whereas in $La_2BaFe_2O_7$ and $Gd_2SrFe_2O_7$ the magnetic moments rotate in the basal plane itself, the rotation angle being $\pi/4$ and $\pi/2$, respectively.[3, 5, 13]

It is interesting to investigate whether the magnetic moments of these materials change in direction gradually on lowering the temperature or at a particular temperature between room temperature and 4.2 K, thus this phenomenon in $La_2BaFe_2O_7$ and $Nd_2SrFe_2O_7$ has been thoroughly studied in this chapter using neutron powder diffraction data in the temperature range 2 K to 300 K.

As mentioned before, the smaller lanthanide cations in the *A* site prefer to occupy the nine-coordinate sites in the rock-salt layers. The distribution of *A* site cations in the Ruddlesden-Popper phases $Ln_2SrFe_2O_7$ has not yet been studied. In this chapter compounds containing different lanthanide (La, Nd, Eu) and alkaline earth metal (Sr, Ba) cations have been investigated in order to understand the affect of cation size on the cation distribution. The cation radii of these ions in nine-coordination are given in *Table 4.1*. Both X-ray powder diffraction and neutron powder diffraction were used for the structural characterisation as the X-ray scattering factors of La and Ba and the neutron scattering factors of Nd and Sr are similar,[14] see *Table 4.2*.

Table 4.1 Cation radii of different *A* site cations present in $Ln_2Sr(Ba)Fe_2O_7$ phases in 9-fold coordination.[16]

Cation	**La^{3+}**	**Nd^{3+}**	**Eu^{3+}**	**Sr^{2+}**	**Ba^{2+}**
Radii (Å)	1.22	1.16	1.12	1.31	1.47

Table 4.2 Neutron scattering factors of the *A* site cations present in $Ln_2Sr(Ba)Fe_2O_7$ phases.[14]

Atom	La	Nd	Sr	Ba
Scattering factor (f_m)	8.24(4)	7.69(5)	7.02(2)	5.07(3)

4.2 Experimental Procedure

Polycrystalline samples of $La_2SrFe_2O_7$, $La_2BaFe_2O_7$, $Nd_2SrFe_2O_7$ and $Eu_2SrFe_2O_7$ were synthesised by reacting the stoichiometric quantities of high purity La_2O_3, Nd_2O_3, Eu_2O_3, $SrCO_3$, $BaCO_3$ and Fe_2O_3 (Aldrich, >99%). The reagents were initially ground together and heated at 1375 ℃ for 48 hrs in air with intermittent grinding. All these phases were initially characterised using X-ray powder diffraction. Cationic distributions and the magnetic structures of these phases were thoroughly investigated using neutron powder diffraction and Mössbauer spectroscopy.

4.3 Results and Discussion

4.3.1 Structural Characterisation of $La_2SrFe_2O_7$

4.3.1.1 X-ray Powder Diffraction

Rietveld analysis of X-ray powder diffraction data was carried out in space group *I*4/*mmm*. The La / Sr distribution over the crystallographically distinct *A* sites was allowed to vary with the constraint that the 2 : 1 ratio was maintained. The thermal parameters of these two sites were also constrained to be equal. The lattice parameters for the prepared $La_2SrFe_2O_7$ were a = 3.89082(6) Å and c = 20.3602(4) Å. The refinement profiles are shown in *Figure 4.2* and refinement details are given in *Table 4.3*.

Table 4.3 Details from the refinement of $La_2SrFe_2O_7$ in space group *I*4/*mmm* using XRPD data.

Atom	**Site symmetry**	***x***	***y***	***z***	**Fractional occupancies**	**$U_{iso} \times 100$ / Å^2**
La/Sr(1)	2b	0	0	0.5	0.48(1)/0.52 (1)	1.9(1)
La/Sr(2)	4e	0	0	0.3187(9)	0.762(5)/0.238(5)	1.9(1)
Fe	4e	0	0	0.0967(2)	1	2.3(2)
O(1)	2a	0	0	0	1	4.6 (3)
O(2)	4e	0	0	0.2010(7)	1	0.8(3)
O(3)	8g	0	0.5	0.0990(7)	1	4.3 (3)

a = 3.89082(6) Å and c = 20.3602(4) Å
χ^2 = 3.218, R_{wp} = 4.93%

The *A* site

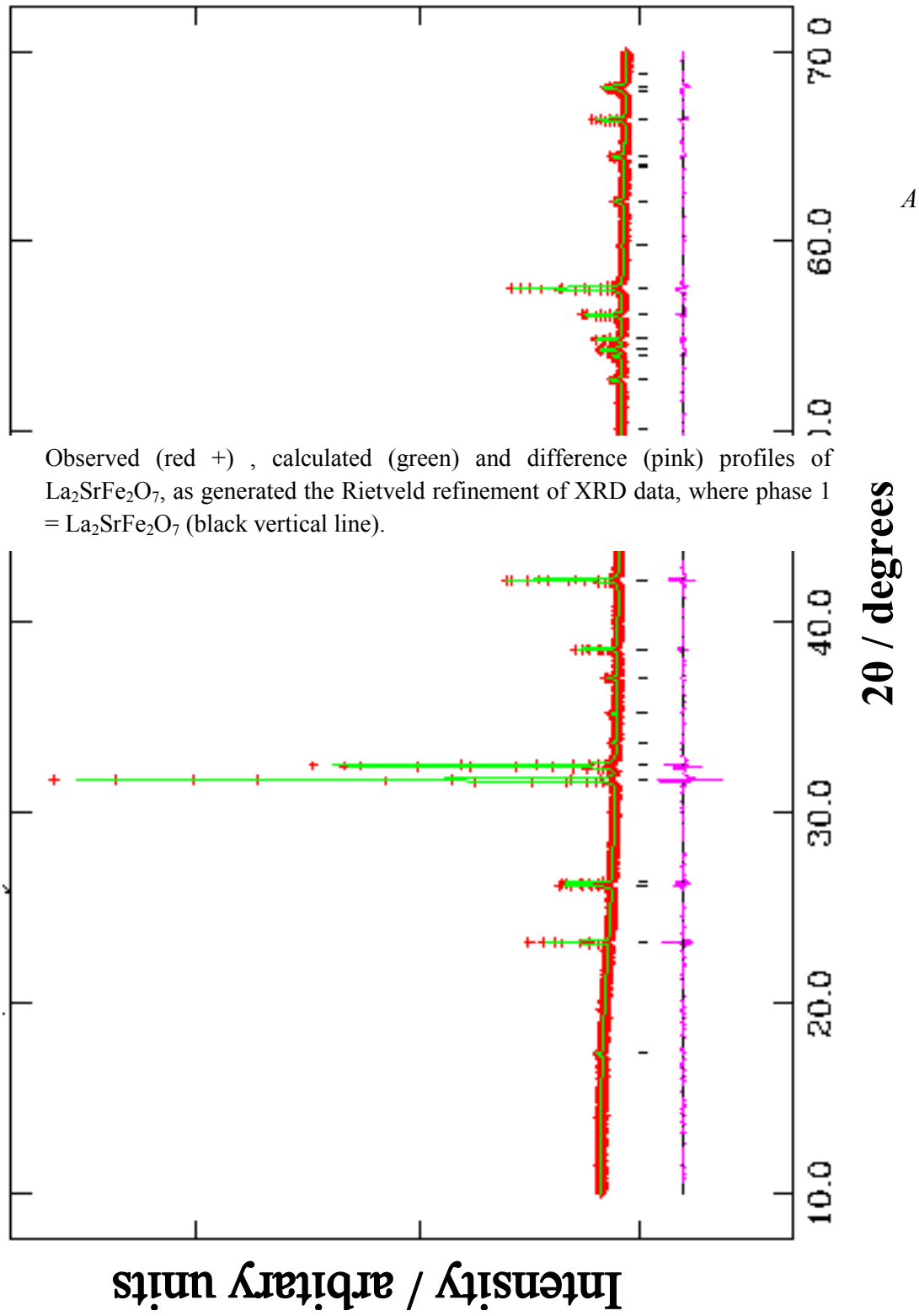

Figure 4.1 Observed (red +) , calculated (green) and difference (pink) profiles of $La_2SrFe_2O_7$, as generated the Rietveld refinement of XRD data, where phase 1 = $La_2SrFe_2O_7$ (black vertical line).

Figure 4.2 Observed (red +), calculated (green) and difference (pink) profiles of $La_2SrFe_2O_7$, as generated by the Rietveld refinement of XRPD data, the reflections of $La_2SrFe_2O_7$ are shown by black vertical lines.

cations, La^{3+} and Sr^{2+} distribute over the twelve-coordinate site within the perovskite blocks (at (0,0,1/2)) and the nine-coordinate site in the rock-salt layers (at (0,0,*z*)) of $La_2SrFe_2O_7$. According to refined data, 48(1)% La^{3+} and 52(1)% Sr^{2+} have occupied the twelve-coordinate site while 76.2(5)% La^{3+} and 23.8(5)% Sr^{2+} have occupied the nine-coordinate site. This reveals that larger strontium has a slight preference to occupy the twelve-coordinate site and lanthanum the smaller nine-coordinate site.

4.3.1.2 Neutron Powder Diffraction

The Rietveld refinements using neutron powder diffraction data recorded at 2 K and 300 K were analysed in the space group *I*4/*mmm*. At both temperatures additional Bragg scattering was observed. This indicates the presence of long-range magnetic ordering. A G-type antiferromagnetic structure, shown in *Figure 4.3a* was used in the refinement. The magnetic unit cell is larger than the crystallographic unit cell as illustrated in *Figure 4.3b.* A simultaneous Rietveld refinement of the crystal and magnetic structures was performed using the free-ion form factor[14] of Fe^{3+} in order to describe the angular dependence of the magnetic scattering amplitude. At both temperatures the magnetic moment was constrained along the *x* axis of the magnetic unit cell. An improved description of the crystal structure at 300 K was achieved by performing a refinement on NPD and XRPD data simultaneously. The final refinement data for $La_2SrFe_2O_7$ at 300 K and 2 K are listed in *Tables 4.4* and *4.5* and the refinement profiles are shown in *Figures 4.4* and *4.5*, respectively.

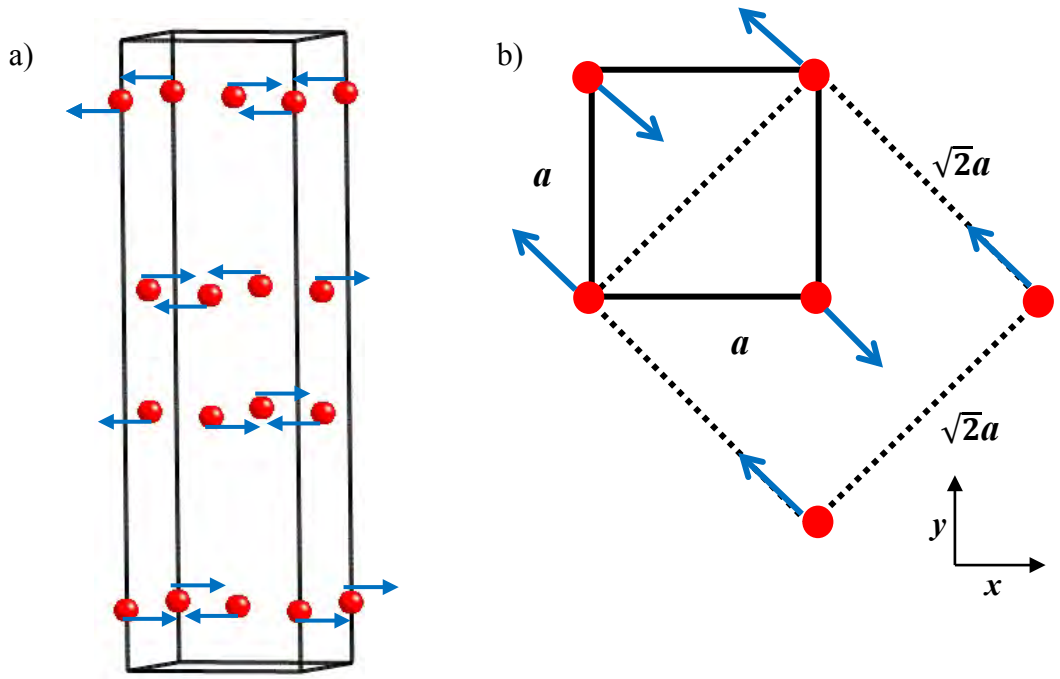

Figure 4.3 The G-type antiferromagnetic structure of $La_2SrFe_2O_7$ a) the magnetic unit cell b) the *xy* plane of the $La_2SrFe_2O_7$ crystal structure illustrating the crystallographic unit cell (—), magnetic unit cell (····) and the direction of the magnetic moment in blue arrows.

Table 4.4 Structural parameters of $La_2SrFe_2O_7$ in space group *I*4/*mmm* using NPD data recorded at 300 K.

Atom	**Site symmetry**	***x***	***y***	***z***	**$U_{iso} \times 100$ / Å^2**	**Fractional occupancy**
La(1)/Sr(1)	2b	0.0	0.0	0.5	0.53(5)	0.47(2)/0.53(2)
La(2)/Sr(2)	4e	0.0	0.0	0.31877(9)	0.53(5)	0.76(1)/0.24(1)
Fe	4e	0.0	0.0	0.0963(1)	0.55(5)	1
O(1)	2a	0.0	0.0	0.0	4.9(2)	1
O(2)	4e	0.0	0.0	0.2041(2)	2.68(7)	1
O(3)	8g	0.0	0.5	0.0982(1)	1.96(5)	1

a = 3.8911(2) Å and c = 20.3697(8) Å
χ^2 = 21.22, R_{wp} = 10.3%

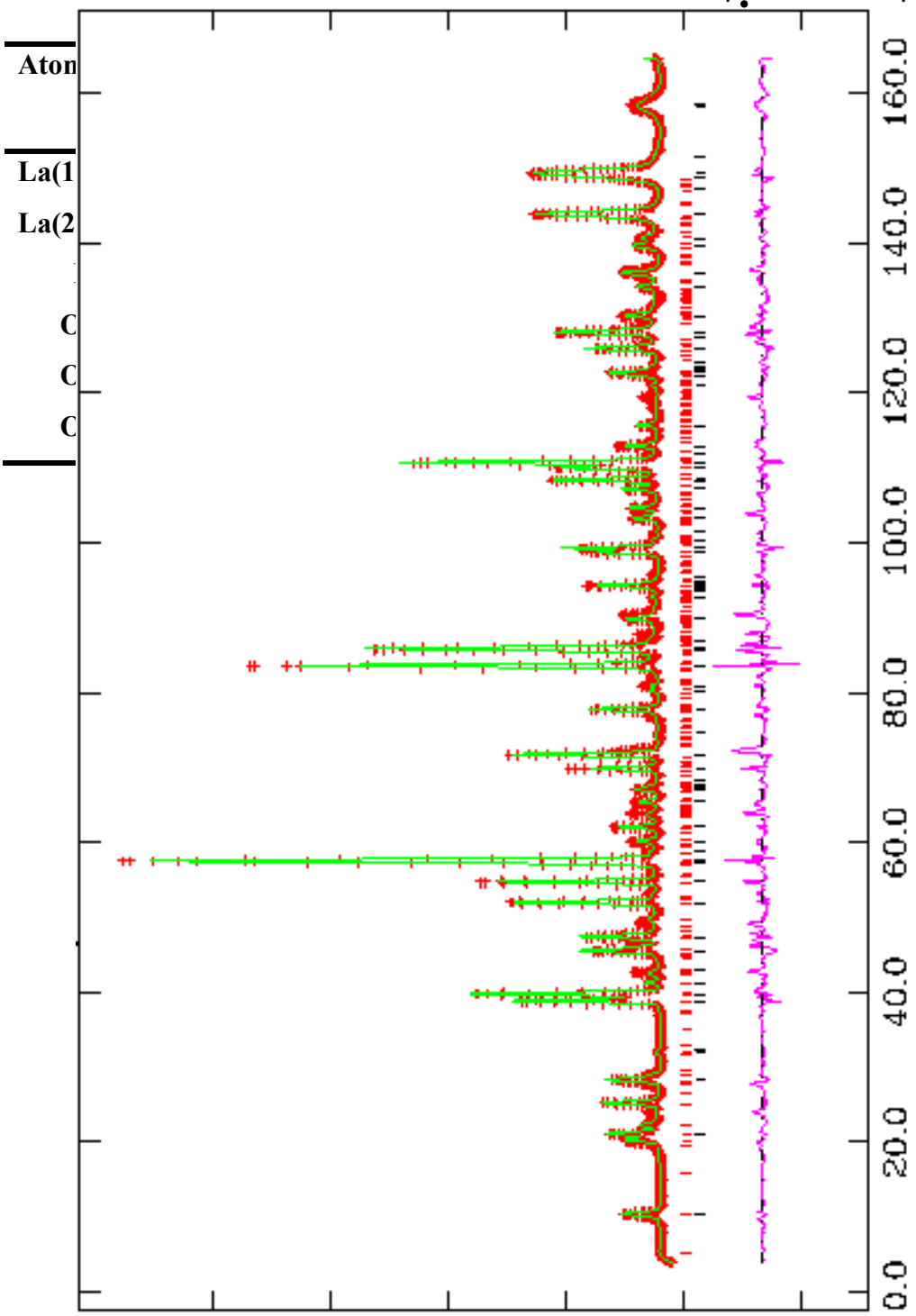

Aton	Fractional occupancy
La(1	8(7)/0.52(7)
La(2	5 (3)/0.24(3)
	1
C	0.25
C	1
C	1

Figure 4.4 Observ
La_2SrF
where
magnet

Table 4.5 Structural para
at 2 K.

The thermal parameter for the

a = 3.9054(1) Å and c = 20.3
χ^2 = 14.23, R_{wp} = 10.4%
at 2 K was extremely high. A

subsequent refinement carried out using the anisotropic thermal parameter made no change to the value. The O(1) site was subsequently displaced along the [100] direction which significantly improved the refinement. The displacement of the atom was more isotropic and so the thermal parameter was modelled isotropically (*Table 4.5*). The magnetic moment at both temperatures was directed along the *x* axis of the magnetic cell as shown in *Figure 4.3*. The magnetic moment obtained at 2 K (3.44(4) μ_B per Fe^{3+} cation) is indicative of the presence of antiferromagnetic interactions, but the value is much smaller than that expected for Fe^{3+} cations (5 μ_B) due to the participation of *d* electrons in covalent bonding. The moment decreases at higher tempteratures and at 300 K it is 2.83(3) μ_B per Fe^{3+} cation.

Figure 4.5 Observed (red +), calculated (green) and difference (pink) profiles of $La_2SrFe_2O_7$, as generated by the Rietveld refinement of NPD data at 2 K, where phase 1 = $La_2SrFe_2O_7$ (black vertical lines), phase 2 = $La_2SrFe_2O_7$ magnetic reflections (red vertical lines).

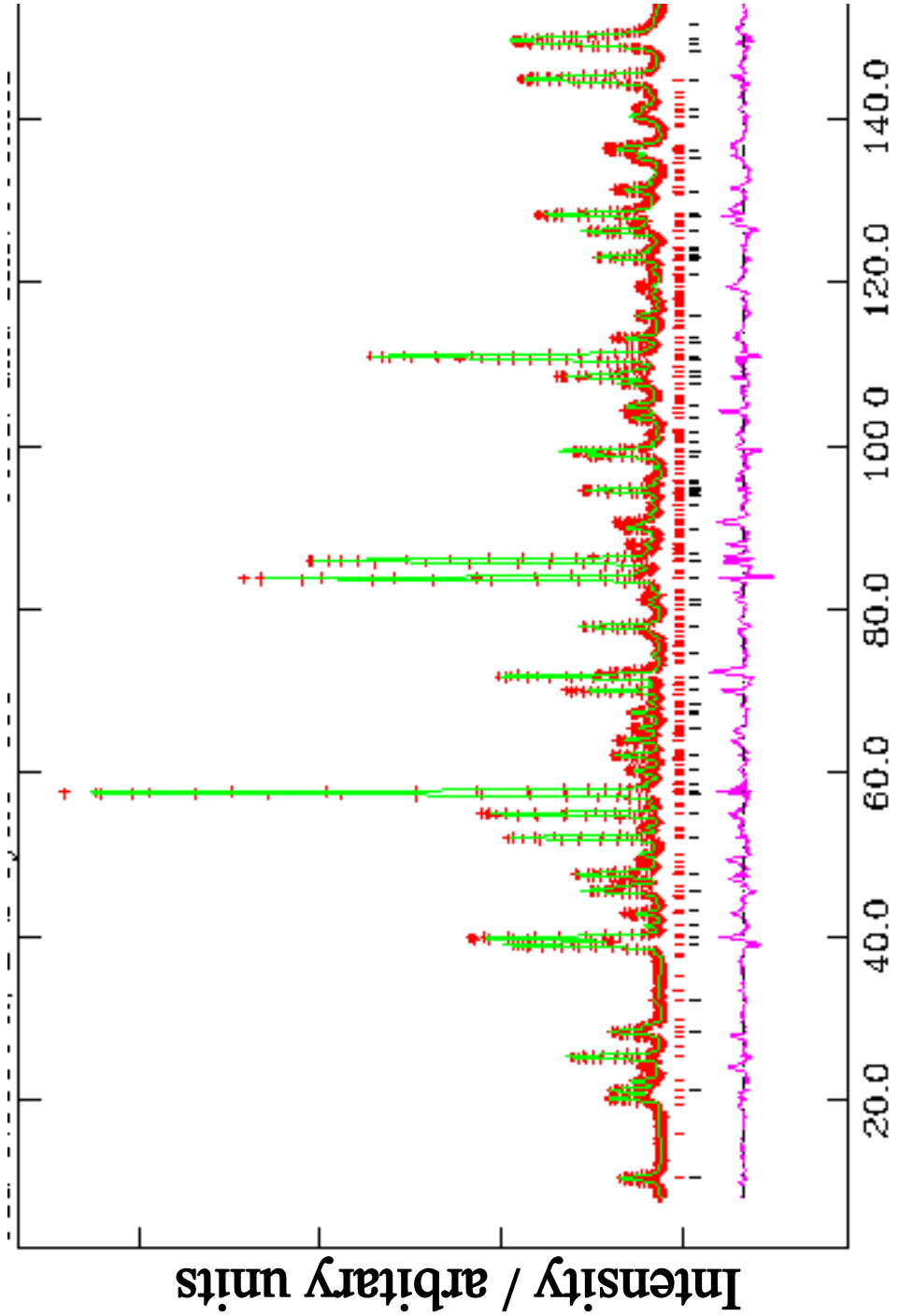

4.3.1.3 Mössbauer Spectroscopy

A series of ^{57}Fe Mössbauer spectra were recorded as the material was heated *in vacuo* from 290 K to 600 K and on subsequent cooling to 290 K and are shown in *Figure 4.6*. The ^{57}Fe Mössbauer parameters are contained in *Table 4.6*. For this purpose a different sample of $La_2SrFe_2O_7$ which contained $LaFeO_3$ (11.4(2)% by weight) was used. However, the structural parameters obtained from this sample from XRPD were consistent with those reported earlier in this chapter. The spectrum recorded at 290 K was best fitted to two sextets, with chemical isomer shifts characteristic of Fe^{3+} and associated with the $La_2SrFe_2O_7$ phase, together with a small singlet with chemical isomer shift typical of Fe^{4+}. The spectrum recorded at 500 K shows that heating induces broadening of the spectral lines, with the smaller Fe^{4+} component being incorporated within the major Fe^{3+} pattern, and a concomitant decrease in magnetic hyperfine splitting and the development of a doublet indicative of the onset of paramagnetism. At 600 K the material is paramagnetic.

Subsequent cooling to 550, 520 and 500 K shows the development of magnetic order but, interestingly, the spectrum at 500 K recorded on cooling from 600 K is considerably different from that recorded at 500 K after heating from 290 K. Furthermore, the spectrum recorded from the sample cooled at 290 K is also different from the spectrum originally recorded at 290 K before heating in that (i) the pattern characterising $La_2SrFe_2O_7$ has narrower line widths and can be satisfactorily fitted to a single sextet, (ii) the intensity of the Fe^{4+} singlet is reduced and (iii) a new sextet, H *ca*. 52.4 T, appears. Interestingly, $LaFeO_3$ has a magnetic hyperfine field of 52.1 T at 296 K.[15]

The inclusion of strontium within a small particle $LaFeO_3$ impurity phase (the presence of which was confirmed by X-ray powder diffraction) could account for the paramagnetic

Fe^{4+} component in the spectrum of the as prepared $La_2SrFe_2O_7$. It is suggested that heating at 600 K *in vacuo* induces a loss of oxygen from the strontium-doped lanthanum ferrite impurity causing reduction of Fe^{4+} to Fe^{3+} which is reflected in the new sextet (H *ca*. 52.4 T) at 290 K.

Table 4.6 ^{57}Fe Mössbauer parameters recorded from $La_2SrFe_2O_7$ following heating and cooling.

Temperature of measurement / K	**Assignment**	**δ ± 0.02 / mms^{-1}**	**Δ or $e^2Qq/2$ ± 0.05 / mms^{-1}**	**H ± 5 / T**	**Area / %**
290	Fe^{3+}	0.34	-0.32	44.3	48
	Fe^{3+}	0.34	-0.47	43.9	48
	Fe^{4+}	0.18			4
500	Fe^{3+}	0.12	-0.26	16.3	58
	Fe^{3+}	0.23	0.66		42
600	Fe^{3+}	0.14	0.69		100
550	Fe^{3+}	0.17	-0.70		100
520	Fe^{3+}	0.20	-0.32	20.5	91
	Fe^{3+}	0.27	-0.17	41.2	9
500	Fe^{3+}	0.20	-0.35	25.8	89
	Fe^{3+}	0.27	-0.04	42.9	11
290	Fe^{3+}	0.34	-0.37	45.5	87
	Fe^{3+}	0.34	-0.04	52.4	10
	Fe^{4+}	0.13			3

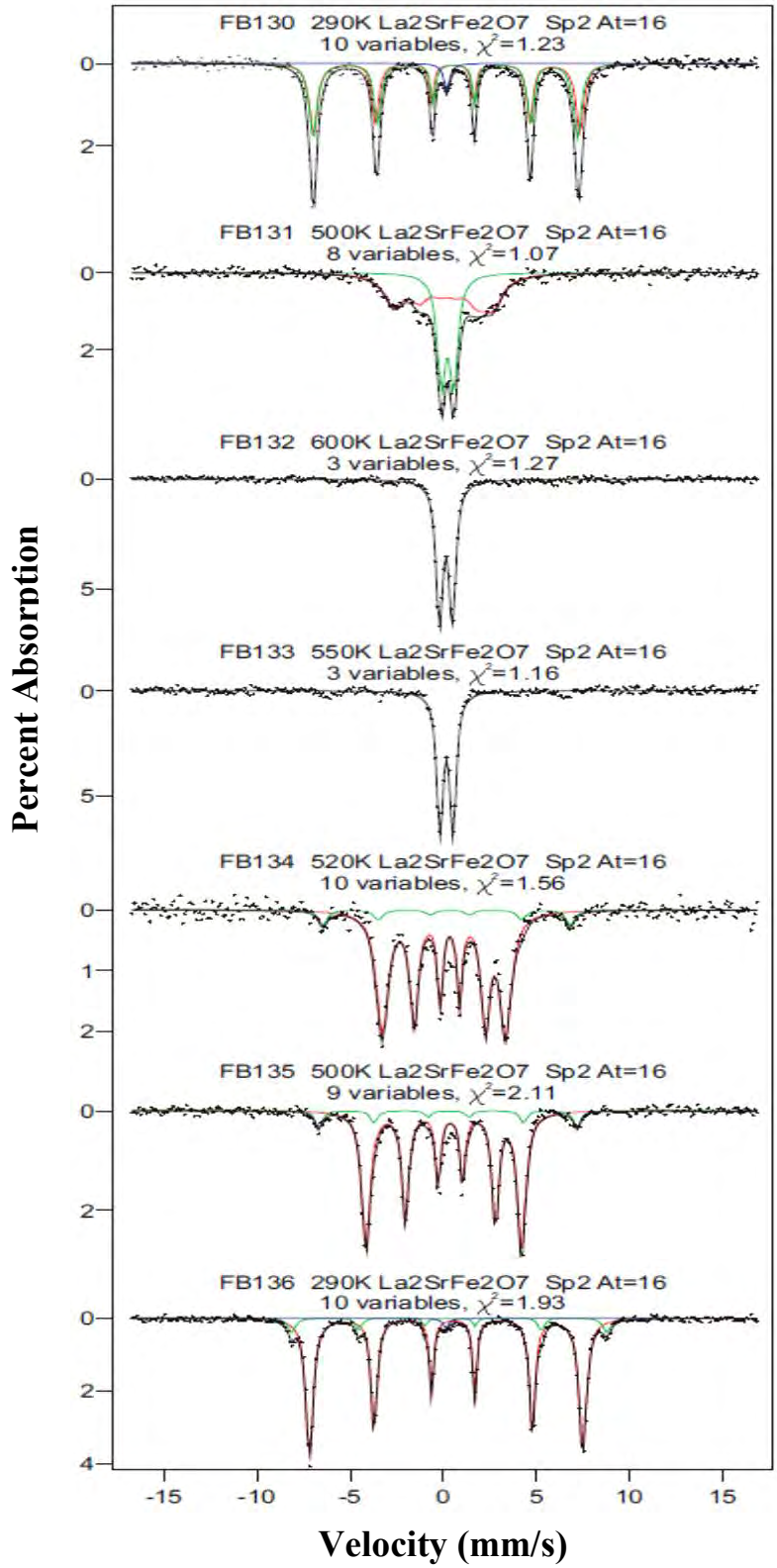

Figure 4.6 Mössbauer spectra recorded from $La_2SrFe_2O_7$ upon heating from 290 K to 600 K and upon cooling from 600 K to 290 K.

Further spectra recorded from a different sample of $La_2SrFe_2O_7$ for which the neutron powder diffraction data were recorded are shown in *Figure 4.7* and the ^{57}Fe Mössbauer parameters are collected in *Table 4.7*. The material was also subjected to heating and cooling regimes in *vacuo* and the results broadly replicate those shown in *Figure 4.6* in that spectra recorded at a given temperature in heating mode differ from those at the same temperature in cooling mode (see for example spectra recorded at 500 K). The results also indicate a magnetic ordering temperature of *ca* 520 K (see spectra recorded at 515 K and 525 K). The final spectrum recorded at 295 K at the conclusion of the heating and cooling cycle shows only a marginal decrease in the intensity of the paramagnetic component seen in the initial material at 300 K but with no evidence of the appearance of a new sextet with larger magnetic hyperfine field characteristic of the magnetically ordered reduced strontium doped lanthanum ferrite impurity phase. The isomer shift of the paramagnetic component is nearer to that of Fe^{3+} and it is possible that this feature reflects the presence of a small particle Fe^{3+} containing phase.

Table 4.7 ^{57}Fe Mössbauer parameters recorded from $La_2SrFe_2O_7$ (on which NPD data was recorded) following heating and cooling.

Temperature of measurement / K	**Assignment**	**$\delta \pm 0.02$ / mms^{-1}**	**Δ or $e^2Qq/2 \pm 0.05$ / mms^{-1}**	**H ± 5 / T**	**Area / %**
300	Fe^{3+}	0.34	-0.39	44.5	96
	Fe^{3+}	0.25			4
500	Fe^{3+}	0.14	-0.32	15.4	59
	Fe^{3+}	0.22	0.56		41
550	Fe^{3+}	0.17	0.65		100
515	Fe^{3+}	0.14	-0.25	16.4	37
	Fe^{3+}	0.20	0.65		63
525	Fe^{3+}	0.19	0.67		100
520	Fe^{3+}	0.13	-0.17	17.5	21
	Fe^{3+}	0.20	0.63		79
600	Fe^{3+}	0.15	0.66		100
500	Fe^{3+}	0.20	-0.34	25.6	87
	Fe^{3+}	0.25	0.48		13
525	Fe^{3+}	0.18	-0.33	18.5	80
	Fe^{3+}	0.27	0.56		20
535	Fe^{3+}	0.12	-0.35	11.7	29
	Fe^{3+}	0.19	0.66		71
530	Fe^{3+}	0.16	-0.34	15.2	74
	Fe^{3+}	0.26	0.55		26
295	Fe^{3+}	0.34	-0.36	45.6	98
	Fe^{3+}	0.21			2

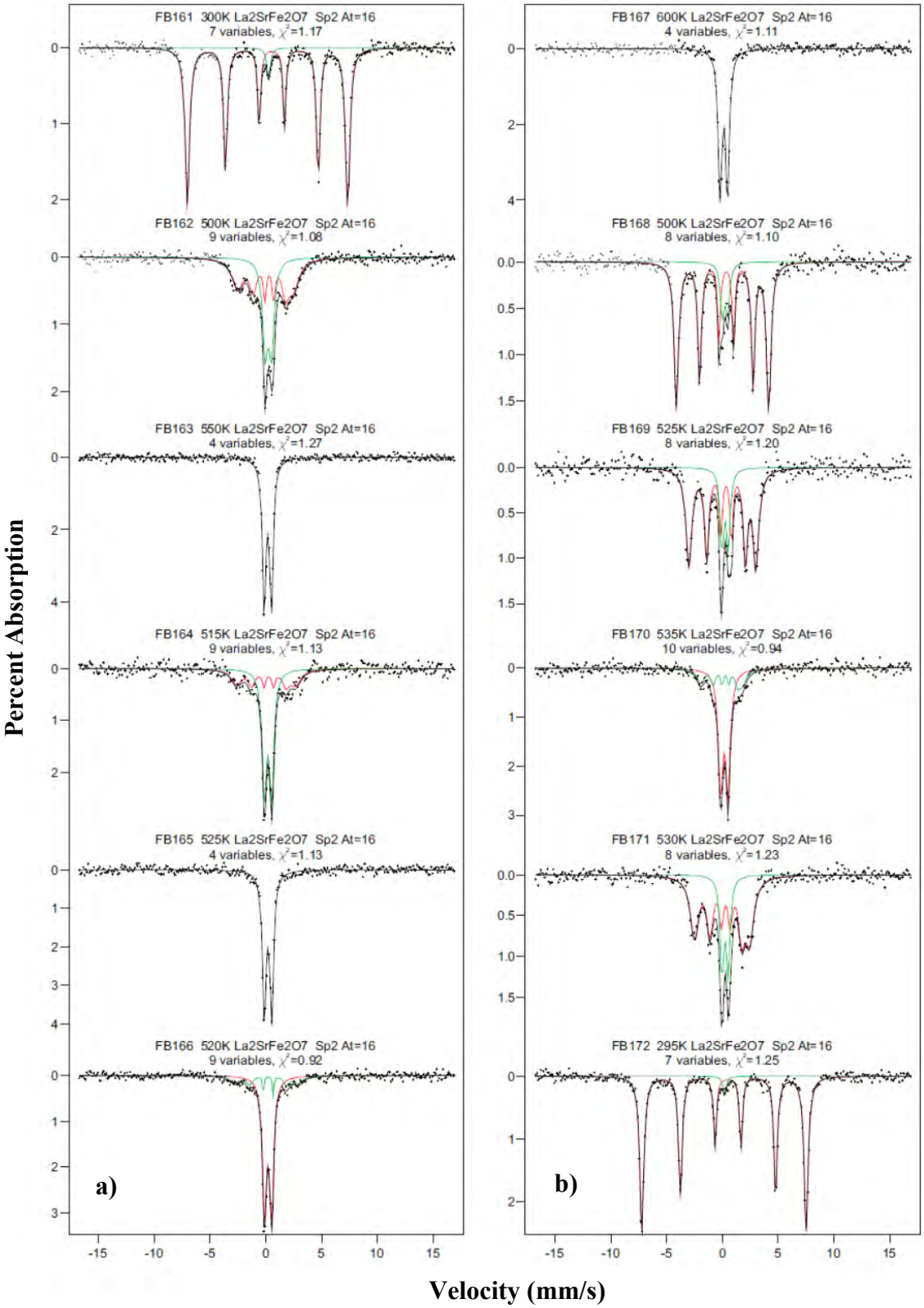

Figure 4.7 Mössbauer spectra recorded from $La_2SrFe_2O_7$ (neutron sample) a) upon heating from 290 K to 600 K and b) upon cooling from 600 K to 290 K.

4.3.2 Structural Characterisation of $La_2BaFe_2O_7$

4.3.2.1 X-ray Powder Diffraction

The structural characterisation was initially carried out using XRPD and the structure was found to be consistent with the literature reports.[6, 12] The lattice parameters a = 3.92308(4) Å and c = 20.8122(3) Å were obtained by Rietveld refinement carried out in space group *I4/mmm*. The isotropic temperature factors of the two *A* sites were constrained to be equal. The refinement profiles are shown in *Figure 4.8* and refinement details are given in *Table 4.8*.

Table 4.8 Details from the refinement of $La_2BaFe_2O_7$ in space group *I*4/*mmm* using XRPD data.

Atom	**Site symmetry**	***x***	***y***	***z***	**Occupancy**	$\mathbf{U_{iso} \times 100 / Å^2}$
La/Ba(1)	2b	0	0	0.5	0/1	1.03(7)
La/Ba/(2)	4e	0	0	0.31810(7)	1/0	1.03(7)
Fe	4e	0	0	0.0951(2)	1	1.5(1)
O(1)	2a	0	0	0	1	1.4(2)
O(2)	8g	0	0.5	0.1032(5)	1	1.4(2)
O(3)	4e	0	0	0.2032(7)	1	1.4(2)

a = 3.92308(4) Å and c = 20.8122(3) Å
χ^2 = 2.478, R_{wp} = 4.42%

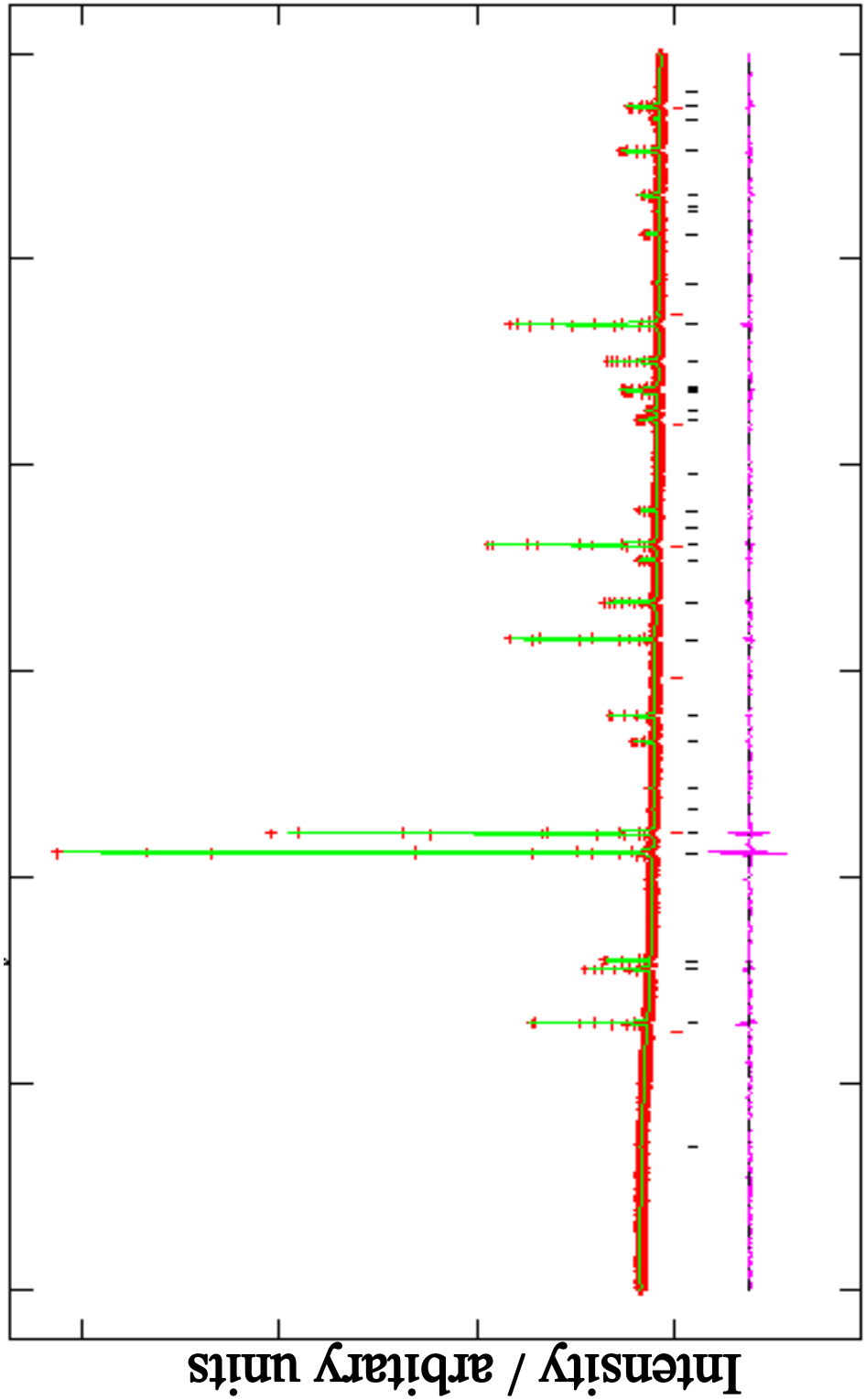

Figure 4.8 Observ
La_2Ba
phase
weight

scatteri
ng
lengths
of La^{3+}
and
Ba^{2+}
are
identica
l, so it
is
impossi
ble to
determi
ne the
cationic
distribu
tion
betwee
n the
two

sites using XRPD data. As discussed in the previous section, the larger cation present in the *A* site has a preference to occupy the twelve-coordinate site. Hence, more barium was expected to occupy the twelve-coordinate site compared to that of strontium in $La_2SrFe_2O_7$ and, for simplicity in the XRPD refinement, the twelve-coordinate site (0,0,1/2) was modelled as occupied by barium and the nine-coordinate site (0,0,0.3180(7)) by lanthanum.

4.3.2.2 Nuclear and Magnetic Refinement based on NPD Data

Neutron powder diffraction data collected from $La_2BaFe_2O_7$ at 2 K and 300 K showed additional Bragg peaks; however the relative intensities of these peaks was different at these temperatures. These observations indicate the presence of long-range magnetic ordering but different magnetic orientations at these temperatures. In order to fully understand the magnetic behaviour of this compound, NPD data were recorded in the temperature range 2 K to 300 K. The compound was found to order as a G-type antiferromagnet at all temperatures and the same magnetic structure used for $La_2SrFe_2O_7$ was employed in the refinement, illustrated in *Figure 4.3*.

A simultaneous Rietveld refinement of the crystal and magnetic structures was carried out using the free-ion form factor[14] of Fe^{3+} to describe the angular dependence of the magnetic scattering intensity. The sample contained a perovskite impurity, $LaFeO_3$, and in the refinement this phase was included as a second phase.

The neutron scattering lengths of La^{3+} and Ba^{2+} are different (*Table 4.2*) and can be used to distinguish between the two cations. The La / Ba distribution over the two crystallographically distinct *A* sites was varied with the constraint that the 2 : 1 ratio was maintained. The isotropic temperature factors of the two *A* sites were constrained to be equal. There was no evidence of any major change in the crystal structure between 2 K and 300 K. The refined parameters of $La_2BaFe_2O_7$ at 300 K and 2 K are given in *Tables 4.9* and *4.10* and the refinement profiles are illustrated in *Figures 4.9* and *4.10*.

Table 4.9 The refined parameters of $La_2BaFe_2O_7$ at 300 K in space group *I*4/*mmm* using NPD data.

Atom	**Site symmetry**	***x***	***y***	***z***	**$U_{iso} \times 100$ / Å^2**	**Fractional Occupancies**
La(1) / Ba(1)	2b	0	0	0.5	0.62(3)	0.270(8)/0.7308(8)
La(2) / Ba(2)	4e	0	0	0.31807(5)	0.62(3)	0.865(4)/0.135(4)
Fe(1)	4e	0	0	0.09510(5)	0.42(3)	1
O(1)	2a	0	0	0	1.85(6)	1
O(2)	8g	0	0.5	0.10222(5)	0.94(3)	1
O(3)	4e	0	0	0.2036(1)	2.25(4)	1

a = 3.92783(5) Å and c = 20.8457(3) Å
χ^2 = 6.788, R_{wp} = 4.7%

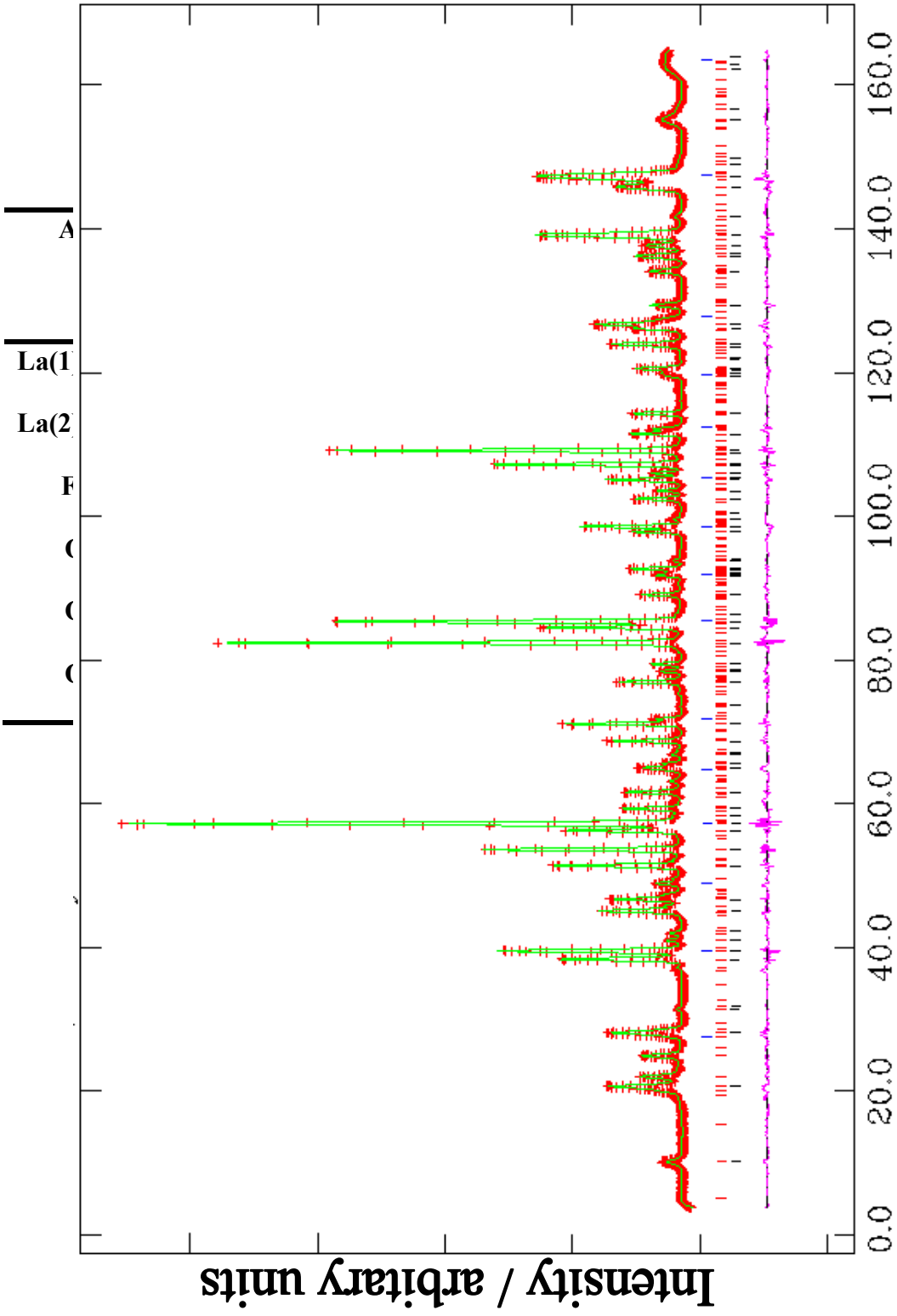

Figure 4.9 Observ
La_2Ba
where
magne
blue v
data.

A	tional
	pancies
La(1	/0.72 (2)
La(2	)/0.137(8)
F	1
(	1
(	1
(	1

a = 3.9232 (1) Å and c =
χ^2 = 5.910, R_{wp} = 5.45%

The distribution of La^{3+} over the twelve-coordinated and nine-

coordinated sites is around 27% and 86%, respectively. It can be noted that more La^{3+} is present in the smaller nine-coordinated site and more Ba^{2+} is in the larger twelve-coordinated site compared to that observed in $La_2SrFe_2O_7$. This is due to the greater difference in the two cationic radii, see *Table 4.1*.

Figure 4.10 Observed (red +), calculated (green) and difference (pink) profiles of $La_2BaFe_2O_7$, as generated by the Rietveld refinement of NPD data at 2 K, where phase 1 = $La_2BaFe_2O_7$ (black vertical lines), phase 2 = $La_2BaFe_2O_7$ magnetic reflections (red vertical lines), phase 3 = $LaFeO_3$ (7.1(2)% by weight, blue vertical lines).

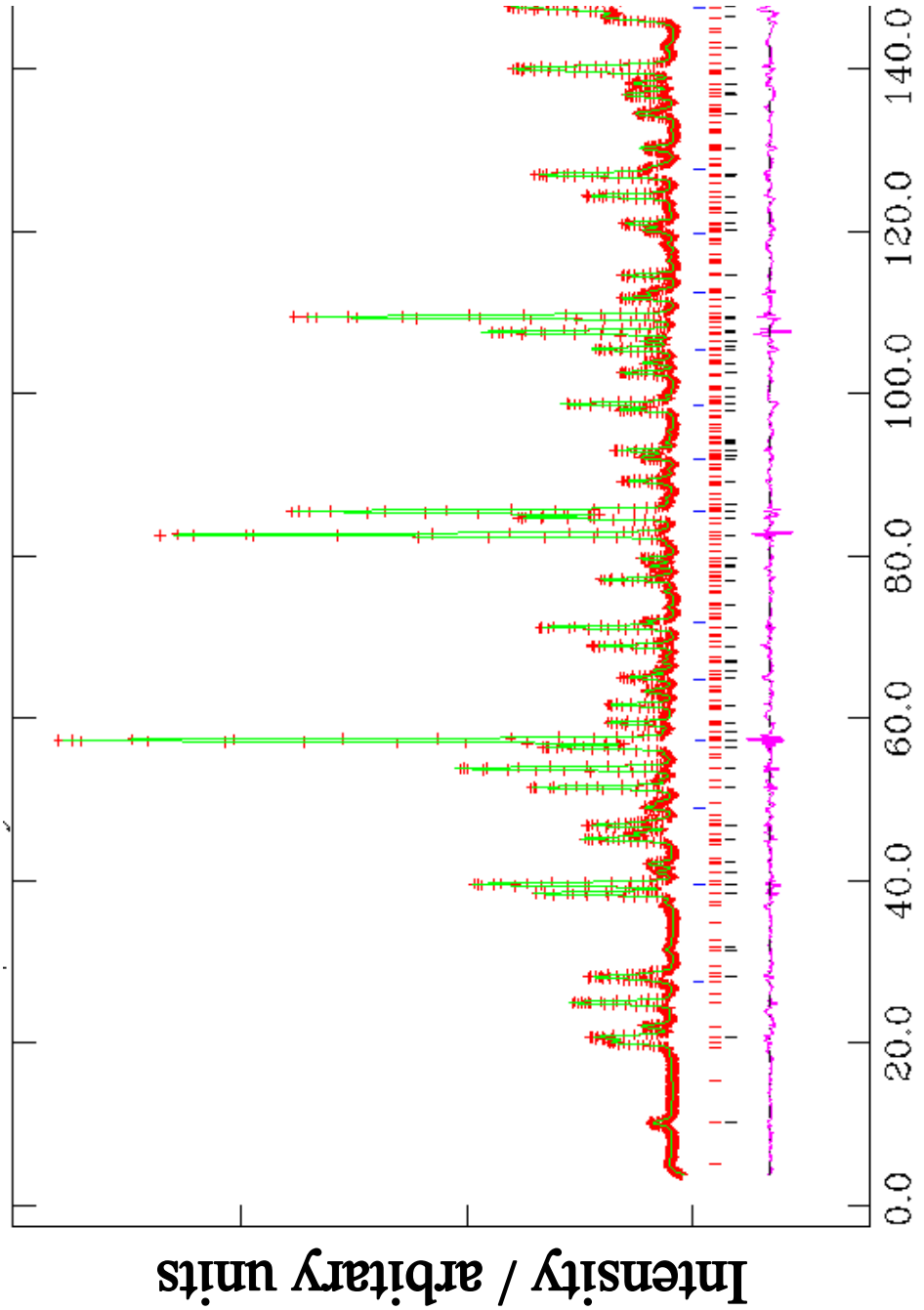

performed on the NPD data collected in the temperature range 2 K to 300 K indicates that the compound adopts a G-type magnetic structure at all temperatures, but changes orientation of the magnetic moment on lowering the temperature. At 300 K the magnetic moment is directed along the crystallographic *x* axis with a magnitude of 2.82(4) μ_B per Fe^{3+} cation and this situation is retained until 210 K. At 190 K rotation is occurred to align along [110] as shown in *Figure 4.11*. The rotation angle is $\pi/4$. At 2 K the moment along the [110] direction is 3.85(4) μ_B per Fe^{3+} cation. The lattice parameters *a* and *c* of the compound do not show any obvious change in the temperature range 210 K to 190 K, see *Figure 4.12*.

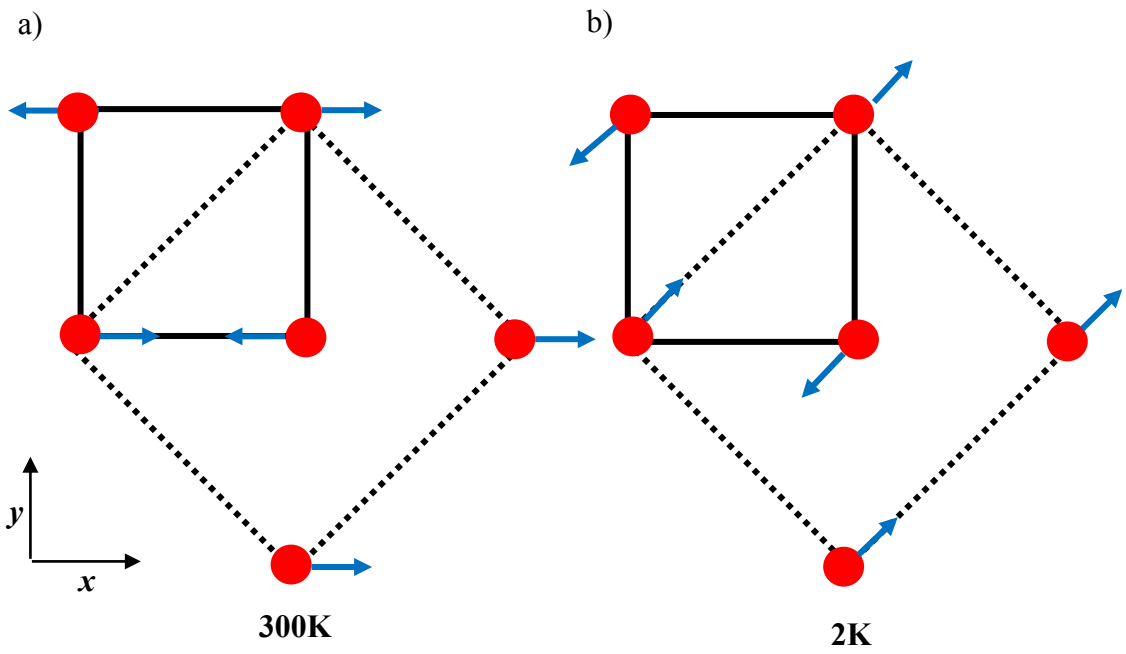

Figure 4.11 The *xy* plane of $La_2BaFe_2O_7$ illustrating the orientation of the magnetic moment at a) 300 K and b) 2 K. The crystallographic unit cell (—), magnetic unit cell (····) and the direction of the magnetic moments (blue arrows) are also shown.

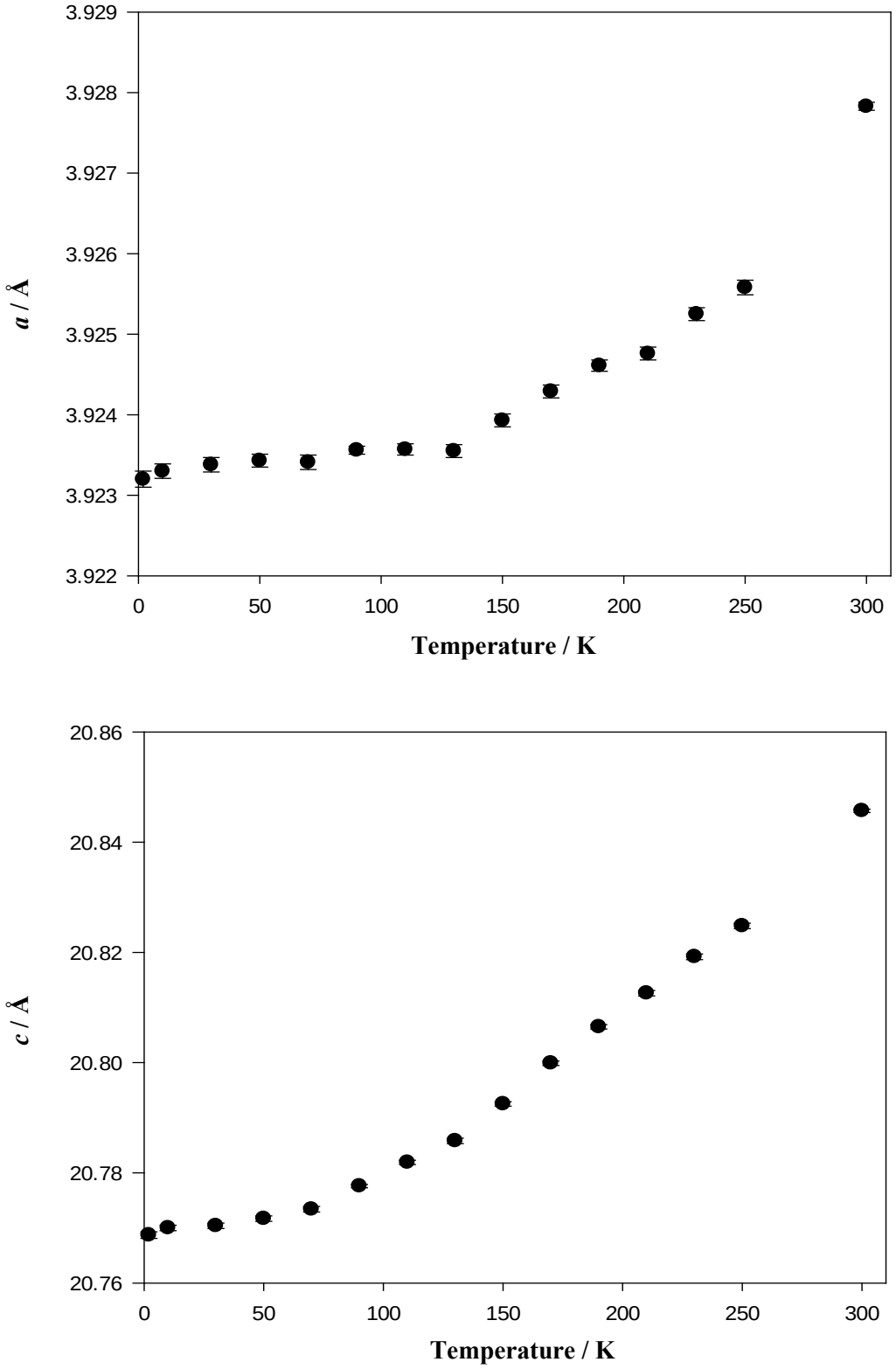

Figure 4.12 The variation of *a* (top) and *c* (bottom) parameters of $La_2BaFe_2O_7$ in the temperature range 2 K to 300 K.

The temperature dependence of the resulting magnetic moment of Fe^{3+} is plotted in *Figure 4.13* and there appears to be an enhanced reduction of the moment with increasing temperature above the reorientation temperature, 190 K.

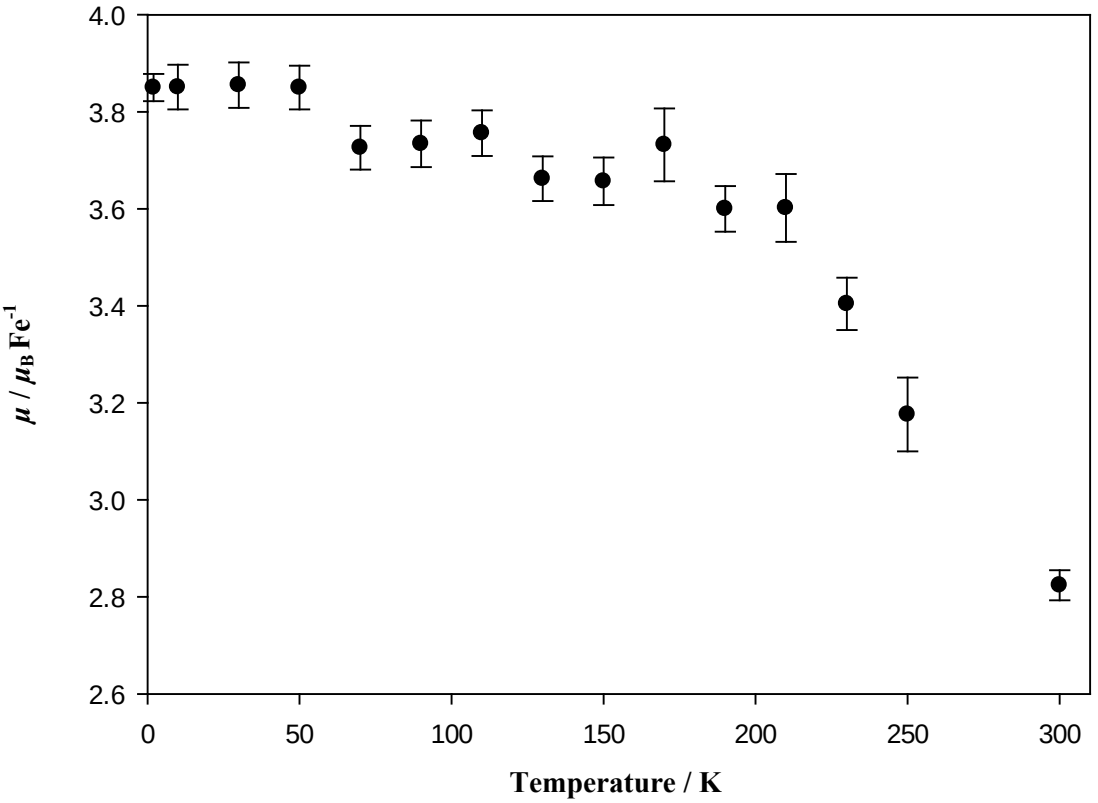

Figure 4.13 The temperature dependence of the resulting magnetic moment of Fe^{3+} in $La_2BaFe_2O_7$.

4.3.2.3 Mössbauer Spectroscopy

The ^{57}Fe Mössbauer spectrum recorded from $La_2BaFe_2O_7$ at 300 K is shown in *Figure 4.14* and the ^{57}Fe Mössbauer parameters are contained in *Table 4.11*. The spectrum was best fitted to two sextets with chemical isomer shifts δ = 0.36 mms^{-1} characteristic of Fe^{3+} and accounting for *ca*. 97% of the spectral area together with a singlet with chemical isomer

shift δ = 0.10 mms^{-1} characteristic of Fe^{4+} and accounting for *ca*. 3% of the spectral area. As described in the previous section, this can be due to the inclusion of barium within a small particle $LaFeO_3$ impurity phase.

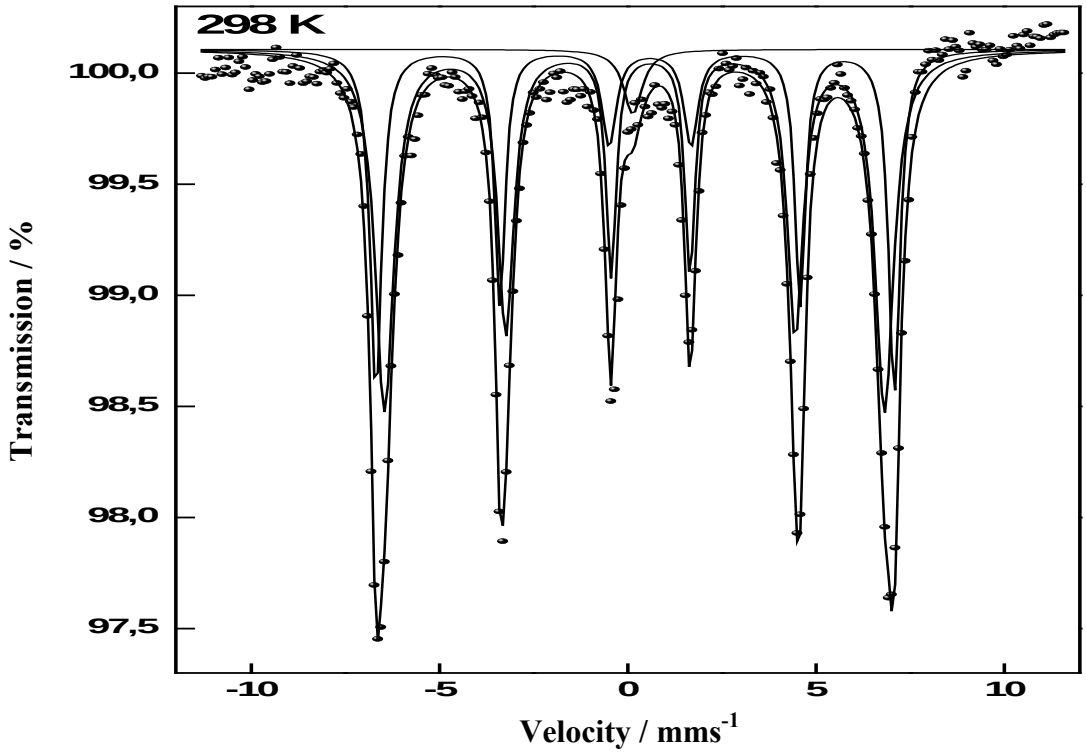

Figure 4.14 Mössbauer spectrum of $La_2BaFe_2O_7$ recorded at 300 K.

Table 4.11 ^{57}Fe Mössbauer parameters recorded from $La_2BaFe_2O_7$ at 300 K.

Temperature / K	Component	$\delta \pm 0.02$ / mms^{-1}	$e^2Qq/2 \pm 0.05$ / mms^{-1}	H $\pm$ 5 / T	Area / %
300	Sextet 1	0.36	-0.20	43	36
	Sextet 2	0.36	-0.21	41	61
	Singlet	0.10			3

4.3.3 Structural Characterisation of $Nd_2SrFe_2O_7$

4.3.3.1 X-ray Powder Diffraction

XRPD data recorded from the polycrystalline sample of $Nd_2SrFe_2O_7$ was used for refinement in the tetragonal space group *I*4/*mmm* with unit cell parameters a = 3.89086(5) Å and c = 20.1228(3) Å. The Nd / Sr distribution over the two crystallographically distinct *A* sites was varied with the constraint that the 2 : 1 composition ratio was maintained. The isotropic temperature factors of these two sites were also constrained to be equal. The refined structural data are collected in *Table 4.12* and the fitted profile is illustrated in *Figure 4.15*. More cationic order is observed in $Nd_2SrFe_2O_7$ compare to that observed in $La_2SrFe_2O_7$ with 78(1)% of Sr^{2+} in twelve-coordinate site within the perovskite blocks and 88.9(5)% of Nd^{3+} in the nine-coordinated site in the rock-salt layers.

Table 4.12 The refined parameters of $Nd_2SrFe_2O_7$ in space group *I*4/*mmm* from XRPD data.

Atom	**Site symmetry**	***x***	***y***	***z***	**$U_{iso} \times 100$ / Å^2**	**Fractional occupancy**
Nd(1)/ Sr(1)	2b	0	0	0.5	1.0(1)	0.22(1)/0.78(1)
Nd(2)/ Sr(2)	4e	0	0	0.3181(1)	1.0(1)	0.889(5)/0.111(5)
Fe	4e	0	0	0.0959(3)	0.6(2)	1
O(1)	2a	0	0	0	6(1)	1
O(2)	4e	0	0	0.207(1)	1.5(6)	1
O(3)	8g	0	0.5	0.1015(8)	4.3(5)	1

a = 3.89086(5) Å and c = 20.1228(3) Å
χ^2 = 2.976, R_{wp} = 4.06%

Figure 4.15 Observed (red +), calculated (green) and difference (pink) profiles of $Nd_2SrFe_2O_7$, as generated by the Rietveld refinement of XRPD data, where phase 1 = $Nd_2SrFe_2O_7$ (black vertical lines), phase 2 = $NdFeO_3$ (0.05(9)% by weight, red vertical lines).

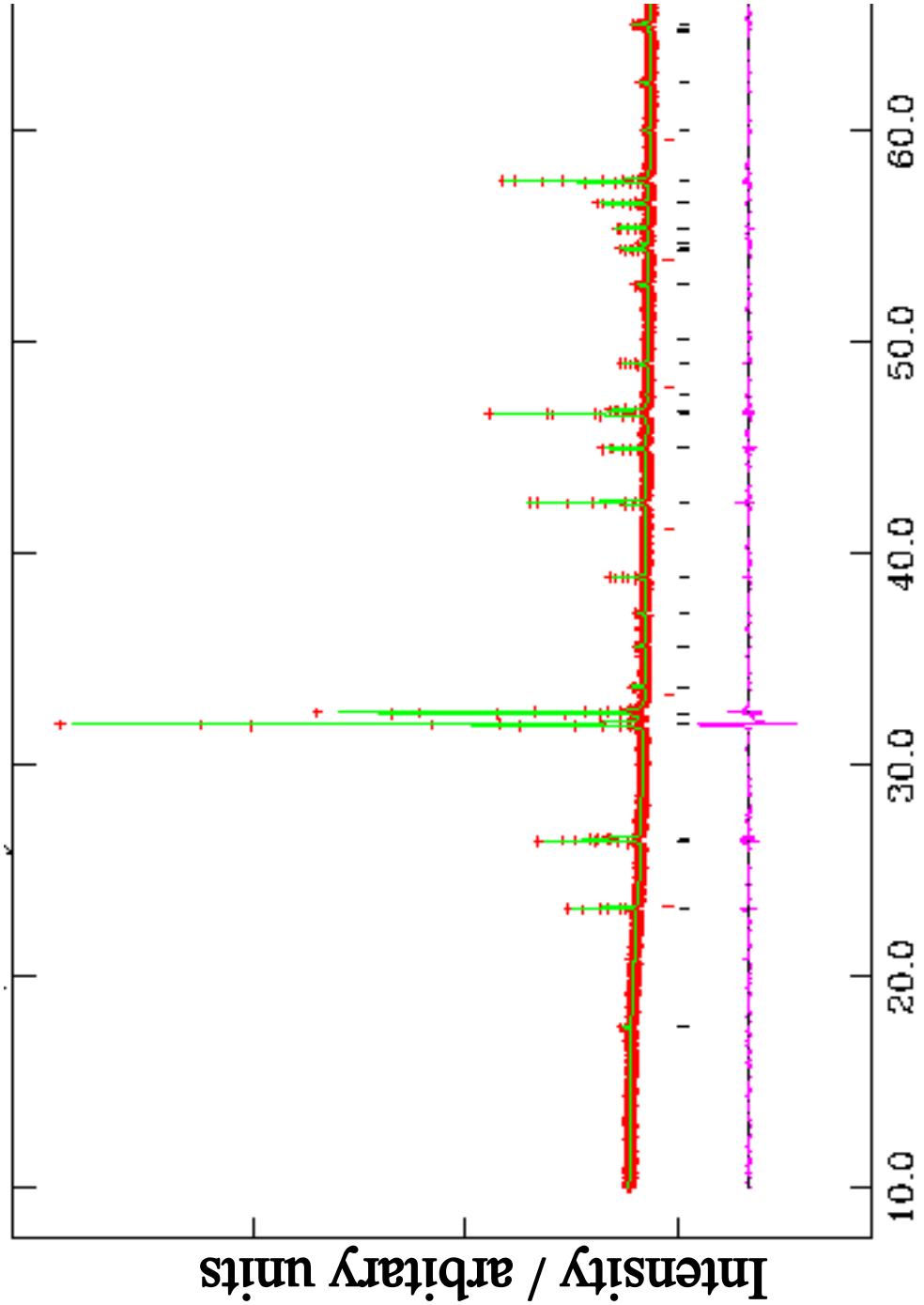

4.3.3.2 Nuclear and Magnetic Refinement based on NPD Data

The refinements based on the NPD data recorded at 300 K and 2 K were carried out in tetragonal space group $P4_2/mnm$ as the attempts to refine the crystal structure in space group $I4/mmm$ were unsuccessful. The tilting of the BO_6 octahedra due to the small cationic size of Nd^{3+} could result in lowering the symmetry. It should also be noted that the refinement based on the XRPD data in space group $P4_2/mnm$ was unstable. The Nd / Sr distribution over the two crystallographic *B* sites was varied in such a way that the 2 : 1 composition ratio was maintained. Since the neutron scattering lengths of Nd^{3+} and Sr^{2+} are similar (*Table 4.2*), slightly negative values were obtained for the cation occupancies, so it was considered that Nd^{3+} and Sr^{2+} are fully ordered. The additional Bragg scattering observed at both temperatures is indicative of the presence of long-range magnetic ordering. The different relative intensities of these peaks at both temperatures suggest the presence of different magnetic behaviour at different temperatures as observed in $La_2BaFe_2O_7$. Further analysis of the magnetic structure was carried out in the temperature range 2 K to 300 K. At all temperatures the compound ordered as a G-type antiferromagnet. Simultaneous Rietveld refinement of the crystal and magnetic structure was performed at each temperature using the free-ion form factors[14] of Fe^{3+} and Nd^{3+} in order to describe the angular dependence of the magnetic scattering amplitude. At low temperatures both Fe^{3+} and Nd^{3+} contribute to the magnetic moment and free-ion form factors of both Fe^{3+} and Nd^{3+} were used in the refinement. At higher temperatures only Fe^{3+} is ordered and so only the form factor of Fe^{3+} was used. The size of the magnetic unit cell is the same as that of the crystallographic unit cell due to the large crystallographic unit cell in space group $P4_2/mnm$. The magnetic structures used for Fe^{3+} and Nd^{3+} are shown in *Figure 4.16*. A second phase was included in the refinement to account for the

impurity phase, $NdFeO_3$. A magnetic phase was included for the impurity phase in order to improve the refinement at 2 K and is shown in *Figure 4.17*. The refined structural parameters at 300 K and 2 K are listed in *Tables 4.13* and *4.14* and the refined profiles are shown in *Figures 4.18* and *4.19*, respectively.

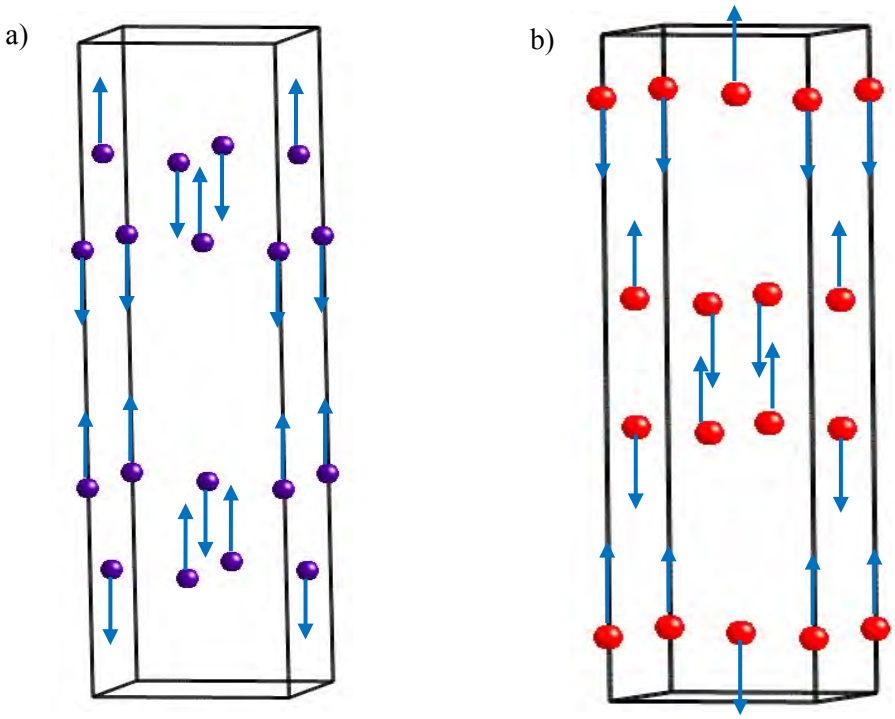

Figure 4.16 The G-type aniferromagnetic unit cells used for a) Nd^{3+} and b) Fe^{3+} ions in $Nd_2SrFe_2O_7$ at 2 K.

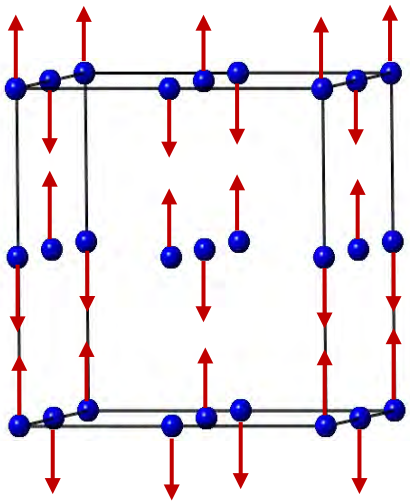

Figure 4.17 The magnetic structure used for Fe^{3+} ions in $NdFeO_3$ at 2 K.

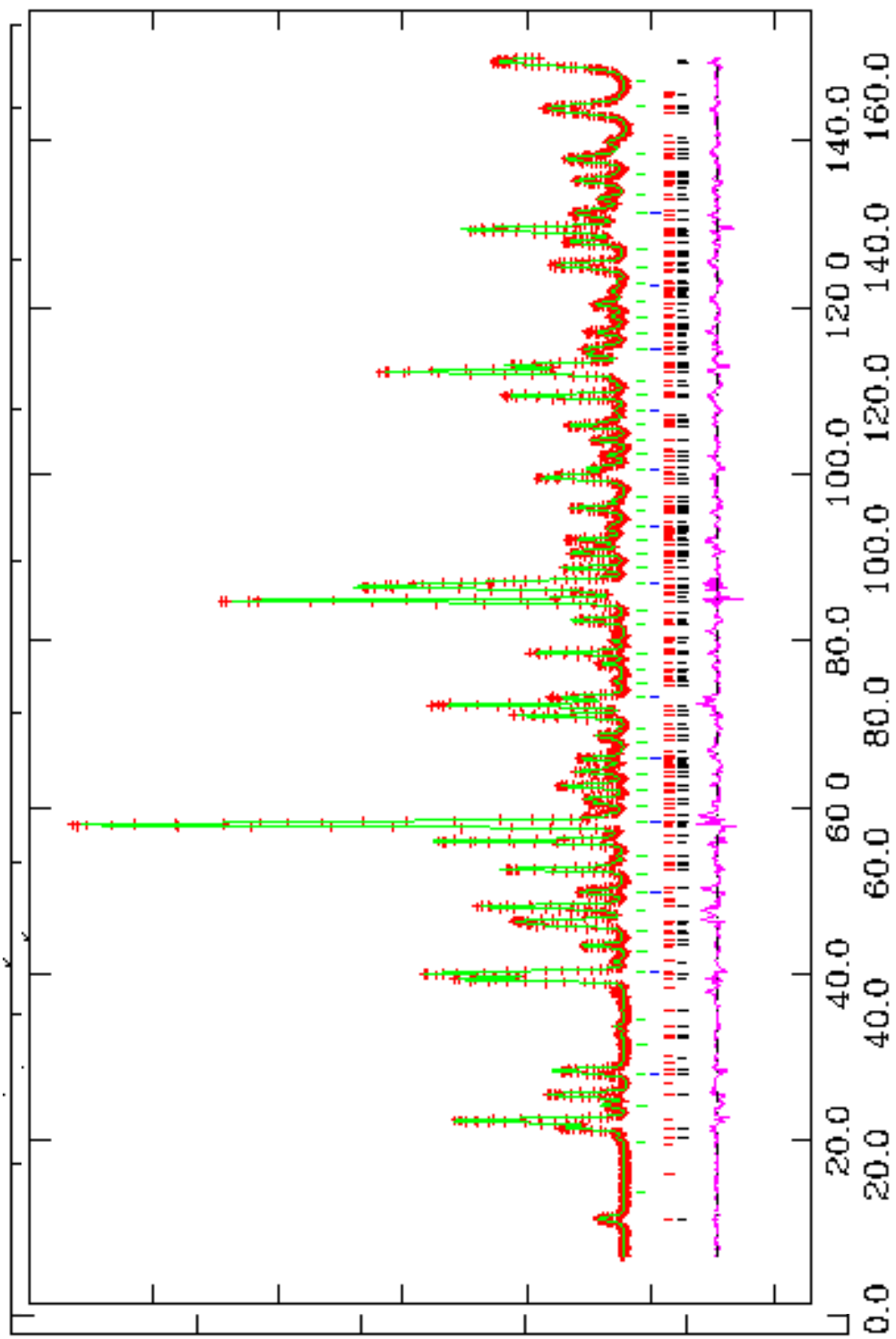

Figure 4.18 Observ
Nd_2Sr
where
magne
weight

Table 4.13 The NI

Figure 4.19 Observed
Nd_2SrFe
where pl

Atom	Site symmetry	*x*	*y*	*z*	$U_{iso} \times 100$ / Å^2
Nd	8j	0.2377(4)	0.2377(4)	0.18236(9)	0.80(7)
Sr	4f	0.2455(8)	0.2455(8)	0	0.62(9)
Fe	8j	0.2443(5)	0.2443(5)	0.40416(9)	0.46(6)
O(1)	8h	0	0.5	0.3961(3)	1.2(1)
O(2)	8j	0.2930(5)	0.2930(3)	0.2951(2)	1.18(9)
O(3)	4e	0	0	0.0864(3)	1.1(2)
O(4)	4e	0	0	0.3860(3)	0.1(1)
O(5)	4g	0.2842(9)	0.7158(9)	0	2.1(2)

a = 5.5062(1) Å and *c* = 20.14404(4) Å
χ^2 = 9.872, R_{wp} = 5.43%

Initially, the ordered moment at each temperature was constrained along different directions in order to identify the correct alignment that gives the best fit to NPD data. Between room temperature and 17 K the magnetic moment was found to align along the crystallographic *x* axis. Below 17 K it acquired a different orientation along the crystallographic *xz* direction and remained in that direction until 10 K. At temperatures below 10 K the magnetic moment continued the rotation to be fully aligned with the *z* axis. Thus, the magnetic moment of $Nd_2SrFe_2O_7$ rotates from the *x* [100] to *z* [001] direction between 17 K to 9 K and the rotation angle is $\pi/2$ as illustrated in *Figure 4.20*. At 300 K the magnetic moment is 3.05(5) μ_B per Fe^{3+} cation and at 2 K it is 3.97(1) μ_B per Fe^{3+} cation. The temperature dependence of the resulting magnetic moment of Fe^{3+} is plotted in *Figure 4.21*. The magnetic moment of Nd^{3+} at 2 K is 2.70(8) μ_B per Nd^{3+} cation which is close to that expected for Nd^{3+} (3.27 μ_B). An upturn in the *a* parameter is observed in the

temperature range 17 K to 9 K, which could correspond to the reorientation of the magnetic moment (*Figure 4.22*).

Table 4.14 The NPD refined parameters of $Nd_2SrFe_2O_7$ in space group $P4_2/mnm$ at 2 K.

Atom	**Site symmetry**	***x***	***y***	***z***	$\mathbf{U_{iso} \times 100 / Å^2}$
Nd	8j	0.2378(4)	0.2378(4)	0.1823(1)	0.05(8)
Sr	4f	0.2453(9)	0.2453(9)	0	0.01(9)
Fe	8j	0.2434(5)	0.2434(5)	0.4040(1)	0.21(7)
O(1)	8h	0	0.5	0.3964(2)	0.1(1)
O(2)	8j	0.2953(5)	0.2953(5)	0.2960(2)	0.3(1)
O(3)	4e	0	0	0.0841(3)	0.3(2)
O(4)	4e	0	0	0.3840(3)	0.5(1)
O(5)	4g	0.285(1)	0.715(1)	0	1.7(2)

a = 5.5024(1) Å and c = 20.0647(6) Å
χ^2 = 8.703, R_{wp} = 6.14%

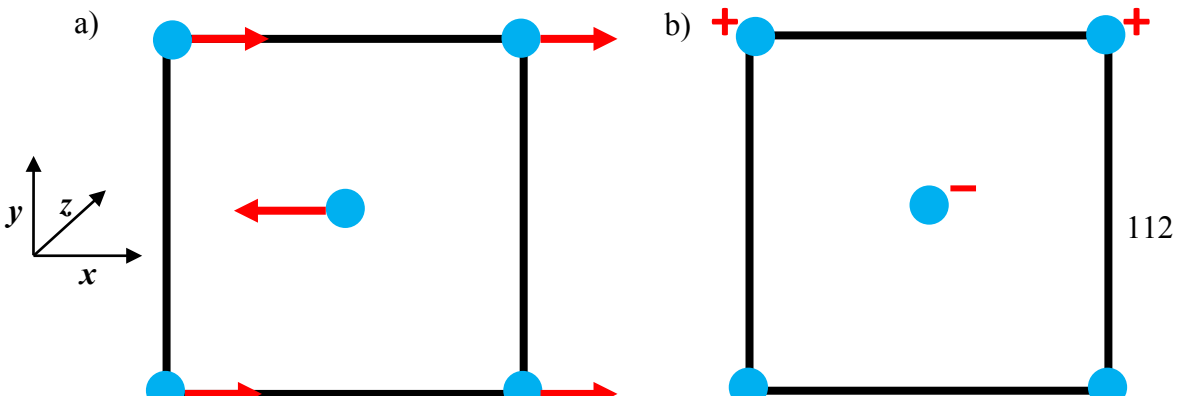

Figure 4.20 The *xy* plane of $Nd_2SrFe_2O_7$ crystal structure illustrating the orientation of magnetic moment at a) 300 K and b) 2 K, also shown the unit cell (—) and the direction of the magnetic moment in red arrows.

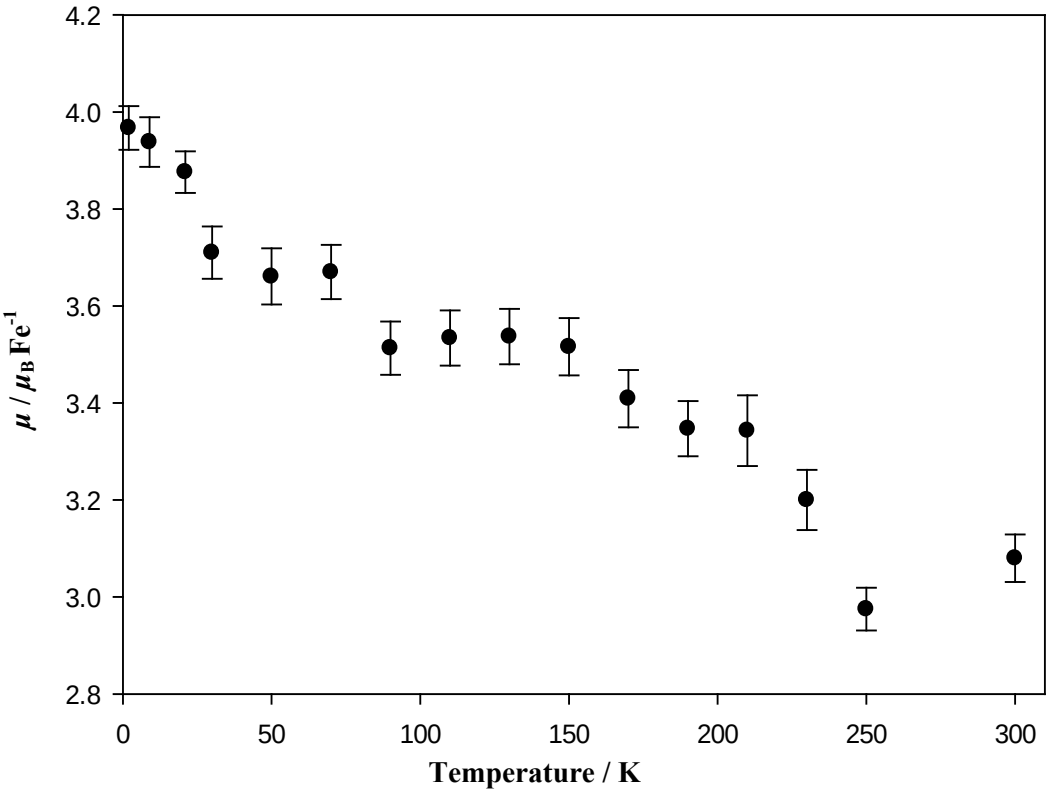

Figure 4.21 Average magnetic moment of Fe^{3+} in $Nd_2SrFe_2O_7$ as a function of temperature.

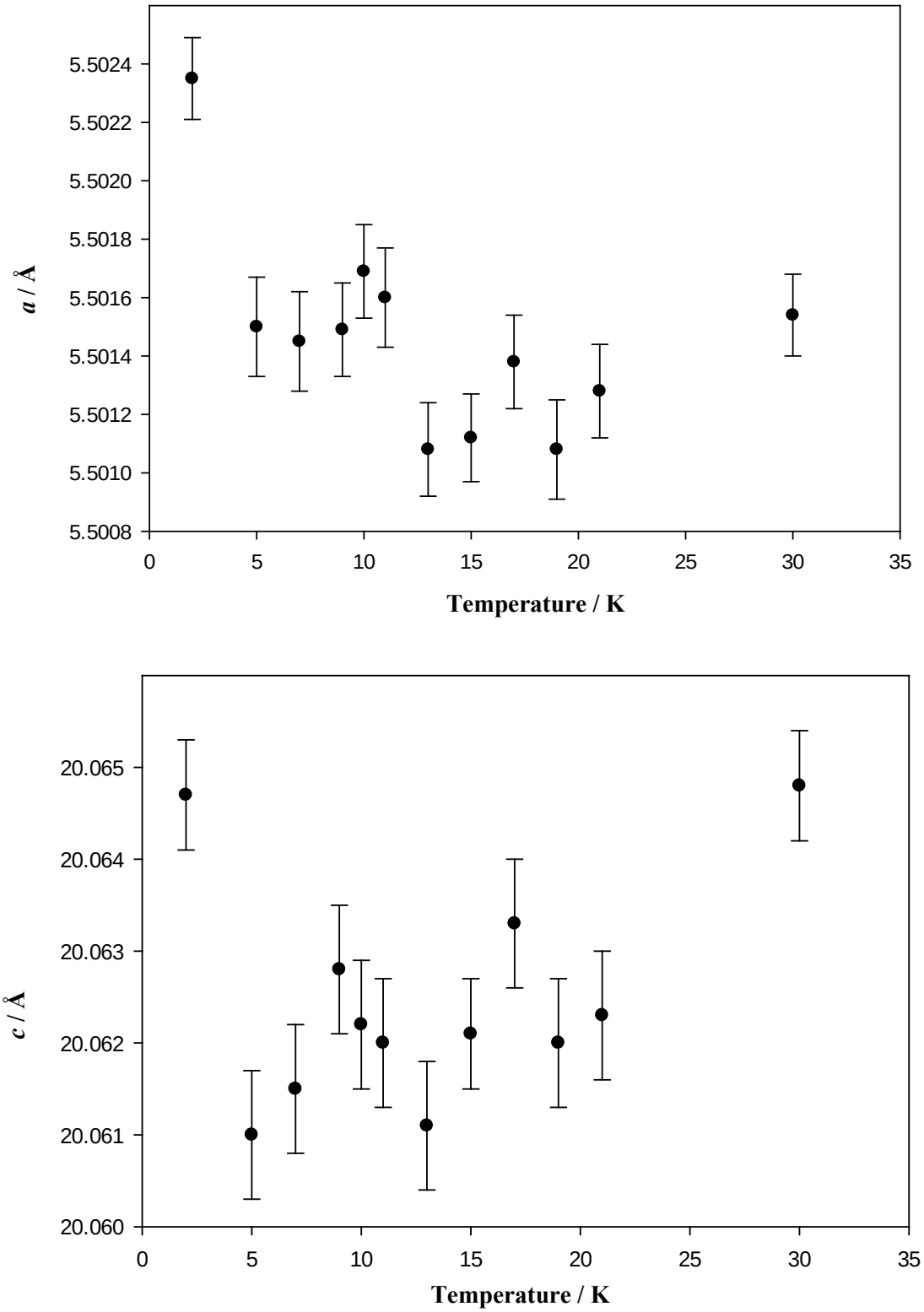

Figure 4.22 The variation of *a* (top) and *c* (bottom) parameters of $Nd_2SrFe_2O_7$ in the temperature range 2 K to 30 K (The level of error bars = two sigma).

4.3.3.3 Mössbauer Spectroscopy

The ^{57}Fe Mössbauer spectra recorded from $Nd_2SrFe_2O_7$ at 300 K and 77 K were fitted to two Fe^{3+} sextets and a paramagnetic Fe^{4+} component and are similar to those recorded from $La_2SrFe_2O_7$. The spectra are shown in *Figure 4.23* and the ^{57}Fe Mössbauer parameters are given in *Table 4.15*. The small Fe^{4+} component observed at 298 K and accounting for *ca.* 4% of the spectral area appears to be incorporated within the two dominant Fe^{3+} sextets at 16 K.

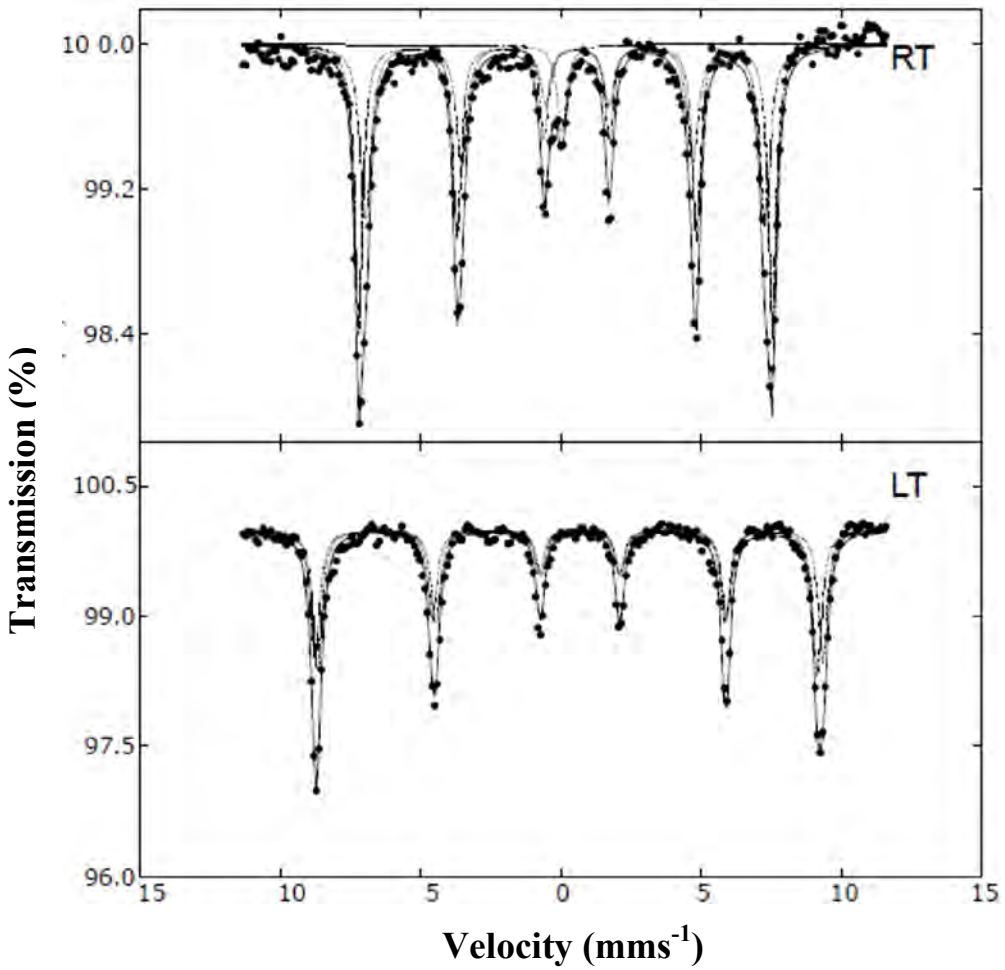

Figure 4.23 Mössbauer spectra of $Nd_2SrFe_2O_7$ recorded at 300 K (RT) and 77 K (LT).

Table 4.15 ^{57}Fe Mössbauer parameters recorded from $Nd_2SrFe_2O_7$ at 300 K and 75 K.

Temperature / K	**Component**	**$\delta \pm 0.02$ / mms^{-1}**	**$e^2Qq/2 \pm 0.05$ / mms^{-1}**	**H ± 5 / T**	**Area / %**
300	Singlet	0.03	-	-	4
	Sextet 1	0.36	-0.20	45.7	53
	Sextet 2	0.36	-0.21	44.1	43
77	Sextet 1	0.47	-0.18	56.1	49
	Sextet 2	0.46	-0.23	55.2	51

4.3.4 Structural Characterisation of $Eu_2SrFe_2O_7$

4.3.4.1 X-ray Powder Diffraction

The structure of the oxide was characterised using XRPD data. Initially, Rietveld refinement was carried out in space group *I*4/*mmm* (χ^2 = 2.199, R_{wp} = 3.61%) but an improved fit was obtained in space group $P4_2/mnm$ (χ^2 = 1.814, R_{wp} = 3.28%) as previously reported.[2] The lattice parameters obtained in this space group are *a* = 5.48973(8) Å and *c* = 19.8332(4) Å.

The refinement profile is shown in *Figure 4.24* and refinement data are given in *Table 4.16*. The Eu / Sr distribution deduced from refinement of the X-ray powder diffraction data showed that the two crystallographically distinct sites in $Eu_2SrFe_2O_7$ are occupied in a fully ordered manner by Eu^{3+} and Sr^{2+} cation; all Sr^{2+} cations occupying the perovskite

sites and all Eu^{3+} ions are accommodated in the rock-salt units of the structure. The sample contained a perovskite impurity $EuFeO_3$ which was added in the refinement as a second phase. Neutron powder diffraction data were not obtained for $Eu_2SrFe_2O_7$ as Eu highly absorbs neutrons.

Table 4.16 Details from the refinement of $Eu_2SrFe_2O_7$ in space group $P4_2/mnm$ using XRPD data.

Atom	**Site symmetry**	***x***	***y***	***z***	$\mathbf{U_{iso} \times 100 / Å^2}$
Eu	8j	0.2305(5)	0.2305(5)	0.1824(1)	0.4(1)
Sr	4f	0.243(1)	0.243(1)	0	0.4(1)
Fe	8j	0.243(1)	0.243(1)	0.4025(3)	0.3(2)
O(1)	8h	0	0.5	0.397(3)	1.6(5)
O(2)	8j	0.290(4)	0.290(4)	0.296(1)	1.6(5)
O(3)	4e	0	0	0.087(4)	1.6(5)
O(4)	4e	0	0	0.383(4)	1.6(5)
O(5)	4g	0.292(6)	0.708(6)	0	1.6(5)

a = 5.48973(8) Å and c = 19.8332(4) Å

χ^2 = 1.814, R_{wp} = 3.28%

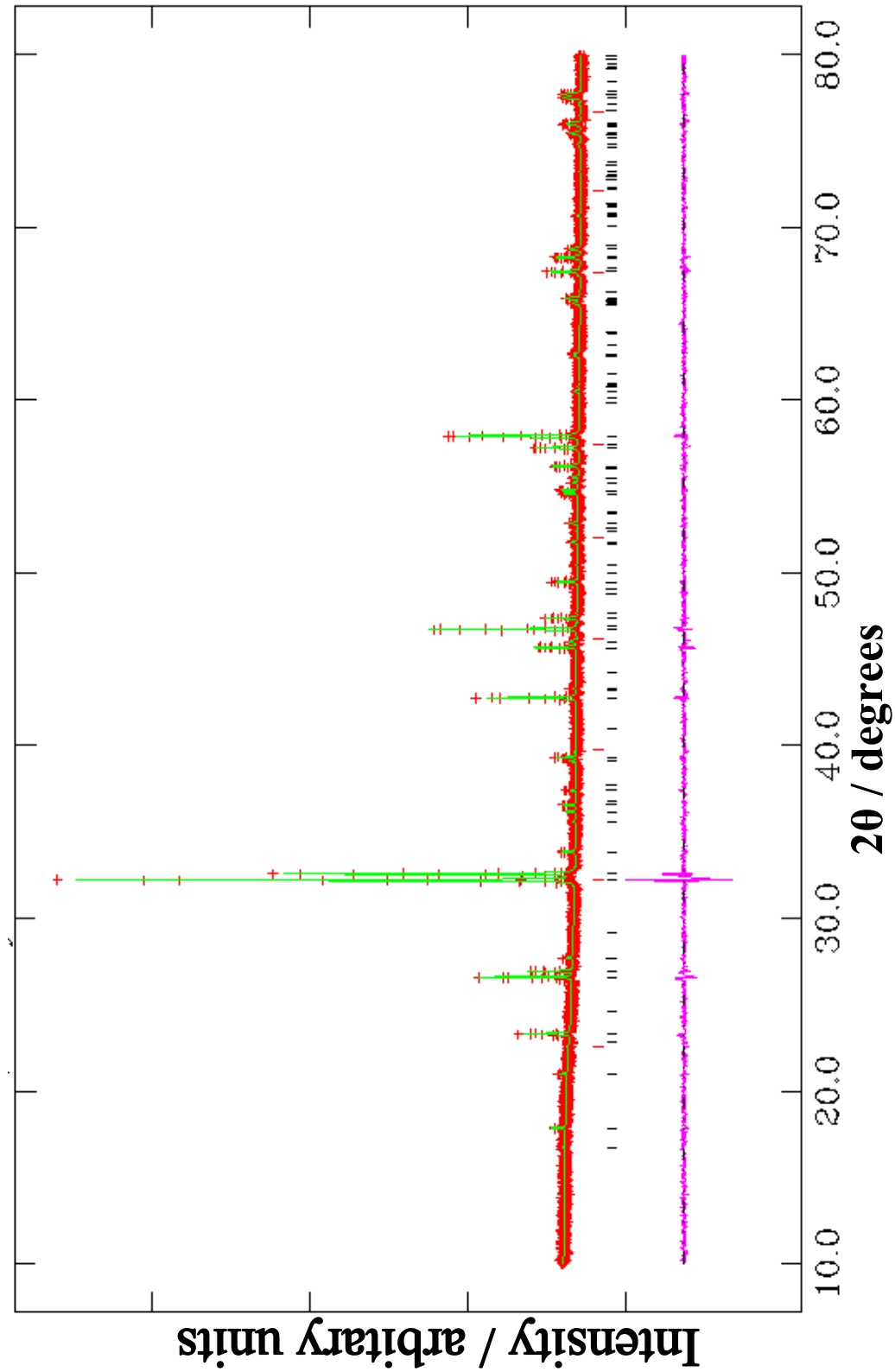

Figure 4.19 Observed (red +), calculated (green) and difference (pink) profiles of $Eu_2SrFe_2O_7$, as generated by the Rietveld refinement of XRPD data, where

Intensity / arbitrary units

Figure 4.24 Observed (red +), calculated (green) and difference (pink) profiles of $Eu_2SrFe_2O_7$, as generated by the Rietveld refinement of XRPD, where phase 1 = $Eu_2SrFe_2O_7$ (black vertical lines), phase 2 = $EuFeO_3$ (2.2(2)% by weight, red vertical lines).

4.3.4.2 Mössbauer Spectroscopy

The ^{57}Fe Mössbauer spectra recorded from $Eu_2SrFe_2O_7$ at 300 K and 77 K are shown in *Figure 4.25* and the ^{57}Fe Mössbauer parameters are contained in *Table 4.17*. The spectra, fitted to two Fe^{3+} sextets and a paramagnetic Fe^{4+} component are similar to those recorded from $La_2SrFe_2O_7$. The results show a decrease in the intensity of the singlet associated with paramagnetic Fe^{4+} as the temperature of measurement is decreased. The result is consistent with a model associating the singlet with small particle strontium-doped europium ferrite impurities in that the small particles would be expected to magnetically order at lower temperature.

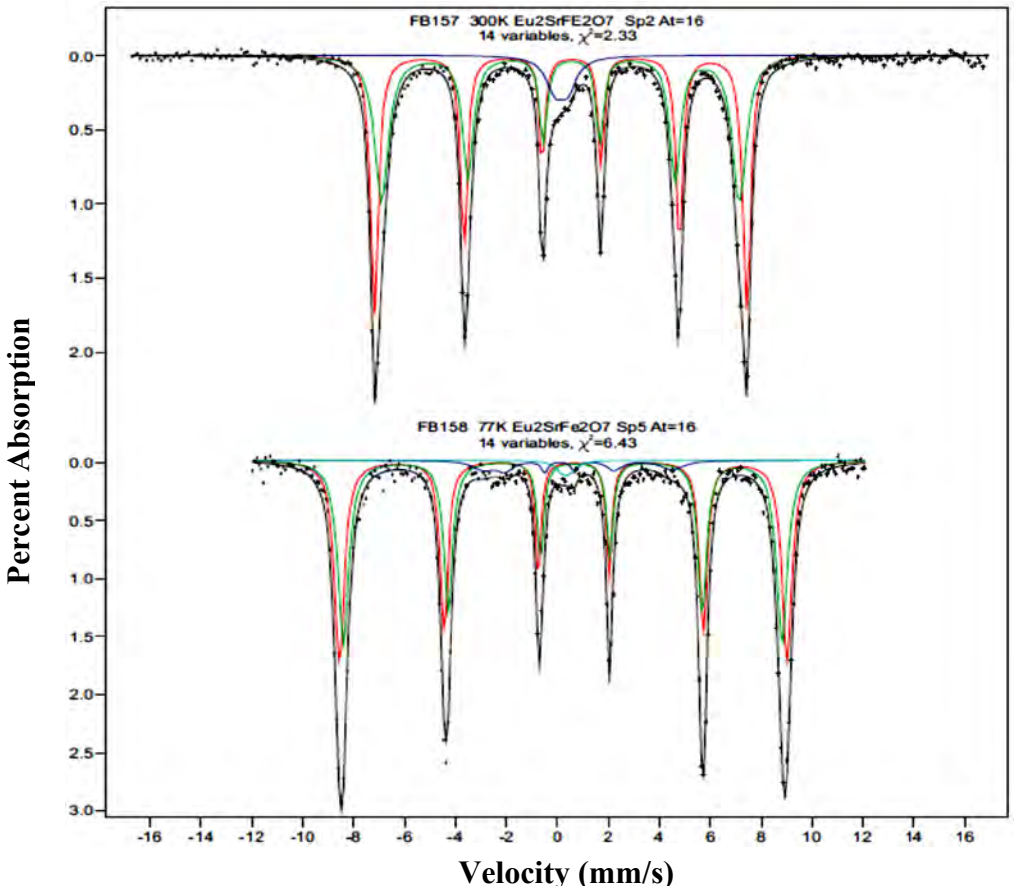

Figure 4.25 Mössbauer spectrum of $Eu_2SrFe_2O_7$ recorded at 300 K (top) and 77 K (bottom).

Table 4.17 ^{57}Fe Mössbauer parameters recorded from $Eu_2SrFe_2O_7$ at 300 K and 75 K.

Temperature of measurement / K	Assignment	$\delta \pm 0.02$ / mms^{-1}	$e^2Qq/2 \pm 0.05$ / mms^{-1}	H ± 5 / T	Area / %
300	Fe^{3+}	0.34	-0.44	45.3	49
	Fe^{3+}	0.35	-0.44	43.4	46
	Fe^{4+}	0.15			5
77	Fe^{3+}	0.44	-0.41	54.6	31
	Fe^{3+}	0.45	-0.48	53.5	61
	Fe^{3+}	0.45		19.1	3
	Fe^{4+}	0.43			5

4.3.5 Discussion

It is clear that the cation order increases with the decrease of the cation radii ratio of ln^{3+} : $Sr(Ba)^{2+}$; the cation distribution of the compounds investigated are listed in *Table 4.18*. As found previously the smaller lanthanides have a higher preference to occupy the smaller nine-coordinate site in rock-salt layers whereas the larger alkaline metals preferentially occupy the larger twelve-coordinate site in perovskite blocks.

All these materials as shown by NPD data and Mössbauer spectroscopy exhibit long-range antiferromagnetic ordering in the temperature range 2 K to 300 K. Magnetic moments obtained from NPD data for all compounds decreased with the increase of temperature, but the values obtained for the magnetic moment at 2 K are much lower than that expected for Fe^{3+} (5 μ_B) due to the participation of *d* electrons in covalent bonding.

The observed reorientation of the magnetic moments in $La_2BaFe_2O_7$ and $Nd_2SrFe_2O_7$ upon cooling is consistent with that previously reported by Samaras *et al*.[3, 5, 13] and as mentioned

at the beginning of this chapter, the temperature at which the reorientation occurs was not studied and from this work it is now clear that it is a continuous change that occurs between 210 K to 190 K in $La_2BaFe_2O_7$ and from 17 K to 9 K in $Nd_2SrFe_2O_7$. The magnetic moment in $Nd_2SrFe_2O_7$ rotates from the [100] to [001] direction in the temperature range 17 K to 9 K and on lowering the temperature to 9 K the magnetic component along *x* axis decreases gradually while the magnetic component along *z* axis increases. The reason behind this phenomenon is still unknown and further studies require developed computational analysis methods.

Table 4.18 The cation distributions in $Ln_2Sr(Ba)Fe_2O_7$ phases.

Compound	**Cation Distribution(Ln / Sr(Ba)) %**		**Ratio of Ln^{3+} / $Sr(Ba)^{2+}$**
	Rock-salt layers	**Perovskite blocks**	**radii**
$La_2SrFe_2O_7$	76 / 24	48 / 52	0.93
$La_2BaFe_2O_7$	86 / 14	28 / 72	0.83
$Nd_2SrFe_2O_7$	89 / 11	22 / 78	0.89
$Eu_2SrFe_2O_7$	100 / 0	0 / 100	0.86

The Mössbauer spectra of all these compounds consist of two sextets and a small singlet with an isomer shift typical of Fe^{4+} due to the inclusion of some Sr / Ba within a small amount of a $LnFeO_3$ (Ln = La, Nd, Eu) impurity phase. The explanation for the appearance of two sextets in all recorded spectra requires further investigation. Initially, it was thought

that the sintering effects induced by heating to 600 K give larger particles of $La_2SrFe_2O_7$ such that the smaller magnetic hyperfine field associated with the smaller particles in the pre-heated material became incorporated into the main sextet pattern. Hence, on subsequent cooling to 290 K the material, of more homogeneous and large particle size, would be represented by a sextet of narrower linewidth in the Mössbauer spectrum which is more amenable to fitting to one sextet. However, scanning electron microscopic images showed that the sintering had made no change to the particle size, see *Figures 4.26* and *4.27*. Mössbauer spectra recorded from $La_2BaFe_2O_7$, $Nd_2SrFe_2O_7$ and $Eu_2SrFe_2O_7$[5, 7, 13] in previous work were fitted to only one sextet but in these the spectral lines are very broad and would probably have been best fitted to two sextets. This is especially true of the spectra recorded from $Nd_2SrFe_2O_7$ at 4.2 K and 300 K.[5]

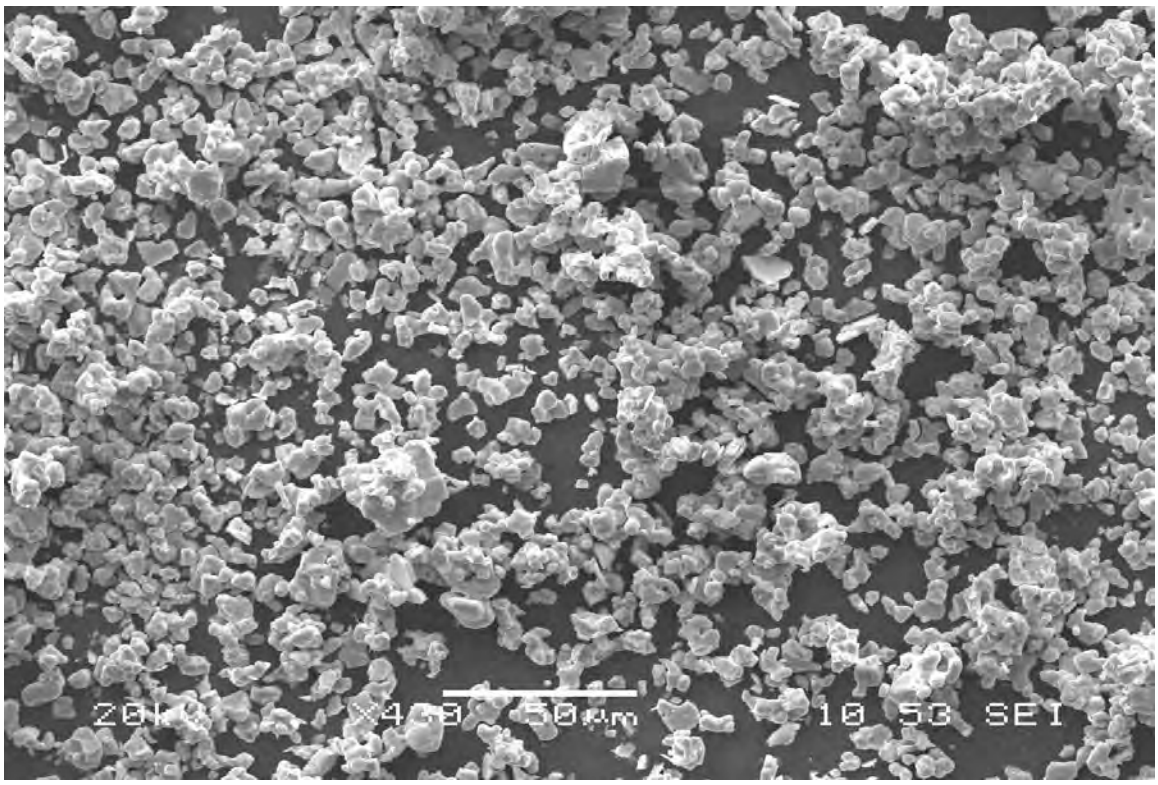

Figure 4.26 Scanning electron microscopic image of $La_2SrFe_2O_7$ before sintering at 600 K.

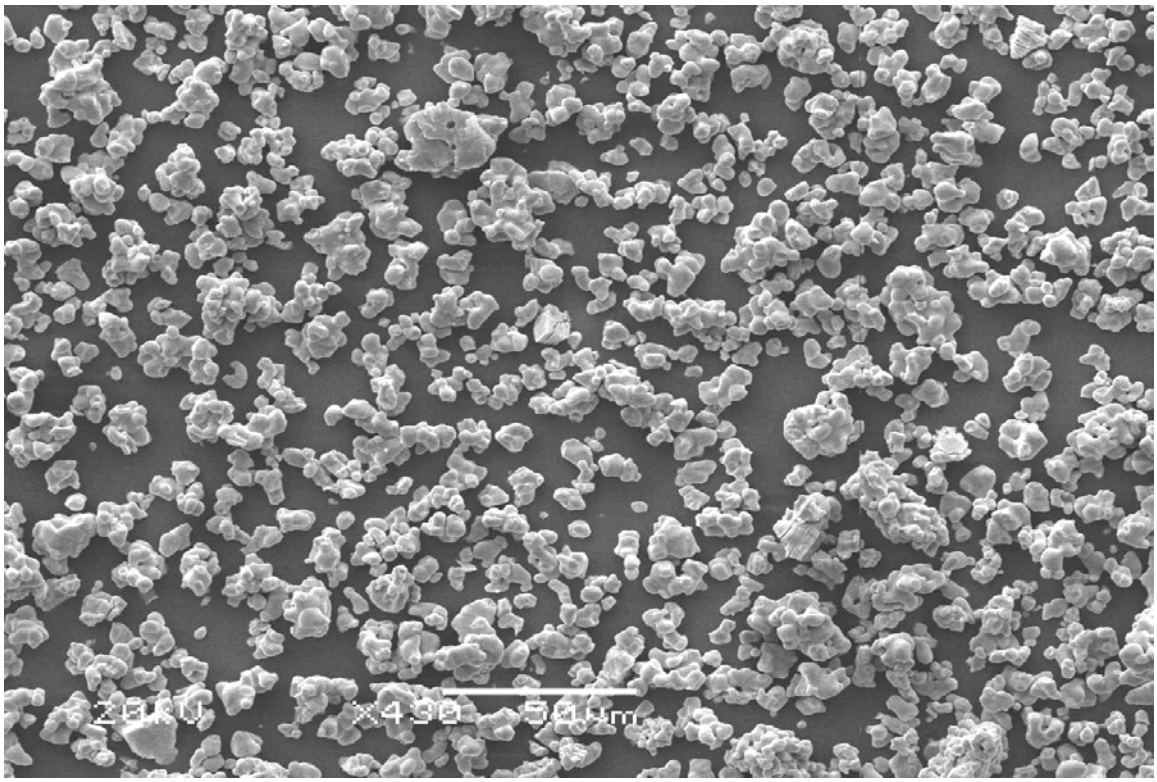

Figure 4.27 Scanning electron microscopic image of $La_2SrFe_2O_7$ after sintering at 600 K.

4.4 Conclusion

Substitution on the *A* site with smaller lanthanide and larger alkaline metal cations leads to more cation order in $Ln_2Sr(Ba)Fe_2O_7$ phases due to the greater difference in the two cation radii. $La_2SrFe_2O_7$ and $La_2BaFe_2O_7$ crystallise in tetragonal space group $I4/mmm$ and $Eu_2SrFe_2O_7$ in space group $P4_2/mnm$ in accordance with the literature.[1-4] The crystal structure of $Nd_2SrFe_2O_7$ can be best described in space group $P4_2/mnm$. All these compounds are antiferromagnetically ordered both at 300 K and 2 K. For $Nd_2SrFe_2O_7$ and $La_2BaFe_2O_7$ different magnetic orientations have been observed upon cooling. In $Nd_2SrFe_2O_7$, the magnetic moment gradually rotates from the crystallographic [100] to

[001] direction in the temperature range 17 K to 9 K whereas in $La_2BaFe_2O_7$ the moment redirects from [100] to [110] direction in the temperature range 210 K to 190 K.

4.5 References

1. Samaras, D.; Collomb, A.; Joubert, J. C. *J. Solid State Chem*. **1973**, 7, 337.
2. Joubert, J. C.; Samaras, D.; Collomb, A. *Mat*. *Res*. *Bull*. **1971**, 6, 341.
3. Samaras, D.; Collomb, A.; Joubert, J. C.; Bertaut, E. F. *J. Solid State Chem*. **1975**, 12, 127.
4. Samaras, D.; Collomb, A.; Joubert, J. C. *Mat*. *Res*. *Bull*. **1974**, 9, 693.
5. Samaras, D.; Chevalier, R. *J. Magn. Magn*. *Matter*. **1977**, 5, 35.
6. Samaras, D.; Collomb, A.; Joubert, J. C.; Chevalier, R. *Physic*. **1977**, 86-88B, 937.
7. Drofenik, M.; Hanzel, D.; Zupan, J. *Mat*. *Res*. *Bull*. **1973**, 8, 1337.
8. Fugihara, S.; Nakata, T.; Kozuka, H.; Yoka, T. *J. Solid State Chem*. **1995**, 115, 456.
9. Flem, G.; Demazeau, G.; Hagenmuller, P. *J. Solid State Chem*. **1982**, 44, 82.
10. Seshadri, R.; Martin, C.; Maignan, A.; Hervieu, M.; Raveau, B.; Rao, C. N. R. *J. Mater*. *Chem*. **1996**, 6, 1585.
11. Goodenough, J. B.; Longo, J. M., *Progress in Solid State Chemistry.* Pergamon: Oxford, 1971, 5, 145.
12. Sharma, B. I.; Singh, D.; Magotra, S. K. *J. Allo*ys *and Compounds* **1998**, 269, 13.
13. Samaras, D.; Collomb, A. *Solid State Comm*. **1975**, 16, 1279.
14. Dianoux, A. J.; Lander, G., *Neutron Data Booklet*. Institute of Laue-Langevin: France, 2003.
15. Eibschutz, M.; Shtrikman, S.; Treves, D. *Phys*. *Rev*. **1967**,156, 562.
16. Shannon, R. D., *Revised Effective Atomic Radii and Systematic Studies of Interatomic Distances in Halides and Chalcogenides*. Central Research and Development Department, Experimental Station, E. I. Du Pont de Nemours and Company: U. S. A.

CHAPTER FIVE

Fluorination Studies of n = 2 Ruddlesden-Popper Phases

$Ln_2SrFe_2O_7$ (Ln = La, Nd, Eu) and $La_2BaFe_2O_7$

5.1 Background

Fluorine insertion has proved a potentially important technique for modifying the physical properties of metal oxides and for synthesising new materials. Early work into fluorination of mixed copper oxides reports the successful formation of new superconductors.[1, 2, 3] This involves oxidative fluorine insertion into semiconducting La_2CuO_4 to form the p-type superconductor $La_2CuO_4F_\delta$.[4] Also superconducting $Sr_2CuO_2F_{2+\delta}$ has been synthesised by fluorinating Sr_2CuO_3, using F_2 gas. The fluorination process may involve both insertion of fluorine and the substitution of fluorine for oxygen. This process also accompanies a structural rearrangement that results in producing superconducting CuO_2 layers which are absent in Sr_2CuO_3.[5]

Fluorination of Ruddlesden-Popper phases is performed by the reaction of pre-formed metal oxide with a fluorinating agent to obtain the kinetically stable oxide-fluoride product. There are many fluorinating agents such as CuF_2(s), NH_4F(s), poly(vinylidene fluoride) (PVF) and F_2(g). These fluorinating agents differ in oxidising power and ability to produce pure products. In this work, 10% F_2(g) / 90% N_2(g) was used as the fluorinating agent as it is a powerful oxidising agent and has been previously used for oxidative insertion reactions involving Ruddlesden-Popper (RP) phases.[9]

Fluorination can be associated with four different routes[6, 7]: (i) one F^- anion substitutes an O^{2-} ion, this reduces the metal oxide lattice; (ii) two F^- anions replace one O^{2-} ion, neither oxidation nor reduction is caused; (iii) insertion of F^- anions into interstitial sites, causing oxidation of metal oxide lattice; (iv) structural rearrangement dictated by the site preferences of oxygen and fluorine.

Previous work carried out on fluorine insertion into layered Ruddlesden-Popper oxides suggests these materials can readily be fluorinated. Initially fluorination occurs by fluorine anions occupying interstitial sites in the rock-salt layers and the apical sites by anion exchange.[4] Fluorine insertion into the $n = 2$ Ruddlesden-Popper phase $Sr_3Ru_2O_7$ which is paramagnetic results in forming antiferromagnetic $Sr_3Ru_2O_7F_2$ which also exhibits a weak ferromagnetic moment below 185 K. The reaction happens through oxidative insertion of fluorine anions into the interstitial sites in between the rock-salt layers oxidising Ru^{4+} to Ru^{5+}.[8]

Aiken *et al*.[9] first reported the formation of a staged fluorinated product $LaSrMnO_4F$ by reacting the high fluorine content phase $LaSrMnO_4F_{1.7}$ with more of the oxide precursor. In the high fluorine content phase $LaSrMnO_4F_{1.7}$, fluoride anions almost fully occupy the interstitial sites, but in the staged product $LaSrMnO_4F$, fluoride anions occupy the interstitial sites in alternate rock-salt layers, see *Figure 5.1*. Another staged fluorinated material $La_{1.2}Sr_{1.8}Mn_2O_7F$ has been obtained by reacting the fully fluorinated $La_{1.2}Sr_{1.8}Mn_2O_7F_2$ precursor with the starting oxide $La_{1.2}Sr_{1.8}Mn_2O_7$.[9, 10]

Fluorination of $La_{1.2}Sr_{1.8}Mn_2O_7$ using CuF_2 to form the oxide-fluoride $La_{1.2}Sr_{1.8}Mn_2O_7F_2$ happens *via* oxidative insertion of fluorine anion into interstitial sites which results an expansion in *c* parameter due to the increased separation between the perovskite blocks.

The overall structure of the perovskite blocks remains the same after fluorination, but a significantly distorted structure is observed with markedly shorter bond lengths for the equatorial Mn-O bonds compared to the oxide precursor because fluorination increases the oxidation state of the Mn ion.[5] Similar structural features are present in both $LaSrMnO_4F$ and $La_{1.2}Sr_{1.8}Mn_2O_7F$ phases. Also in these two phases extremely short Mn-O apical bonds pointing towards the interstitial fluorine layers have been observed due to the electrostatic attractions between Mn and F ions and repulsions between O and F anions.[10] Even though the starting oxides $LaSrMnO_4$ and $La_{1.2}Sr_{1.8}Mn_2O_7$ exhibit long-range magnetic order at low temperature,[11, 12] both staged fluorinated materials showed no evidence of long-range magnetic ordering as strong superexchange e_g^1–O2p-e_g^1 and double exchange e_g^1–O2p-e_g^0 cannot exist for the d^3 electronic configuration of these Mn^{4+} compounds.[10] The fluorinating process of $LaSrFeO_4$ involves not only anion exchange but also oxidative insertion. According to the bond valence sum (BVS) calculations, in the fluorinated structure oxygen has a great preference to occupy the equatorial anion site and fluorine to be in the interstitial site; both oxygen and fluorine anions to present in the apical site.[13]

Both fully fluorinated and the partially fluorinated materials of $La_2SrFe_2O_7$ have been investigated. Both materials, $La_2SrFe_2O_7F_2$ and $La_2SrFe_2O_7F$ acquire distorted structures with octahedral tilting in the perovskite layers. Interestingly, the partially fluorinated phase has a staged structure with additional anions occupying the interstitial sites in alternate rock-salt layers.[13] This study revealed the necessity of further investigation on the structural and magnetic properties of fluorinated $La_2SrFe_2O_7$ phases.

As previously discussed in chapter 5, the *A* site cation order of $n = 2$ Ruddlesden-Popper phases $Ln_2SrFe_2O_7$ (Ln = La, Nd and Eu) and $La_2BaFe_2O_7$ changes with the size of the cations present in the *A* site and these materials also exhibit long-range antiferromagnetic

ordering, especially the magnetic moments in $La_2BaFe_2O_7$ and $Nd_2SrFe_2O_7$ change the direction upon cooling. So it is interesting to investigate how fluorination affects the cation order and magnetic properties of these materials. The main focus of the present study was on structural characterisation of the fluorinated $La_2BaFe_2O_7$ phases, but this chapter also describes the fluorination of other phases and the difficulties met in structural characterisation.

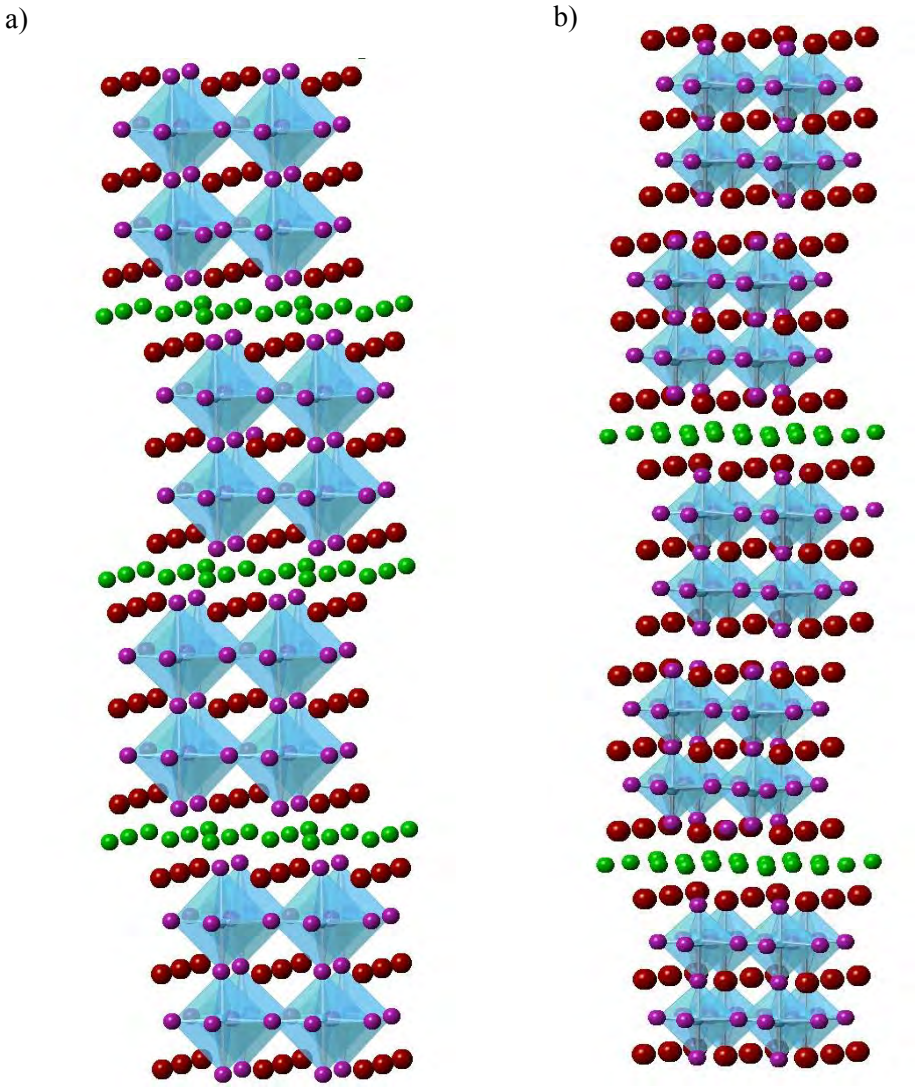

Figure 5.1 Illustration of a) fully fluorinated n = 2 RP material $A_3B_2X_9$ and b) staged fluorinated n = 2 RP material $A_3B_2X_8$, with A cations shown in red, O^{2-} anions shown in purple, interstitial anions in green and BX_6 octahedra shown in blue.

5.2 Fluorination of $La_2BaFe_2O_7$

About 100 mg sample of the precursor oxide $La_2BaFe_2O_7$ (prepared as described in Chapter 4) placed in a nickel boat was fluorinated at 290 ℃ for 15 minutes using 10% F_2(g) / 90% N_2(g) as the fluorinated agent. The reaction was carried out using the apparatus described in Section 2.2.1. The fluorinated product was characterised by XRPD and the XRPD pattern is shown in *Figure 5.2*.

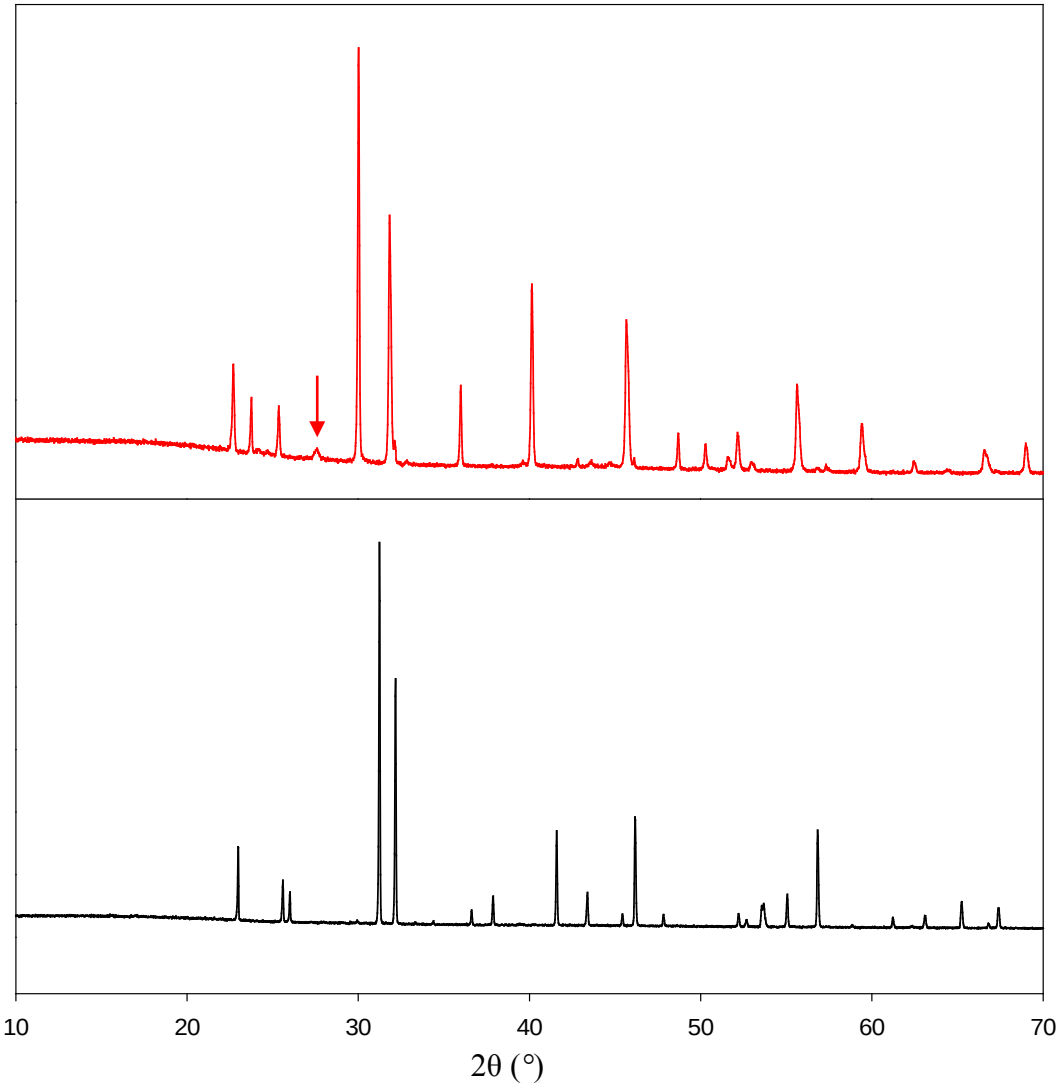

Figure 5.2 XRPD patterns showing the fluorination of $La_2BaFe_2O_7$: $La_2BaFe_2O_7$ (black), the final fluorinated phase (red) and the LaF_3 impurity is shown with an arrow.

5.2.1 Thermogravimetric Analysis of Fluorinated $La_2BaFe_2O_7$

The fluorine content of the oxide-fluoride sample was determined by heating the material to 1100 ℃ in a reducing atmosphere of flowing 10% H_2 (g) / 90% N_2 (g). The first weight loss was observed at ~350 ℃. XRPD analysis of the sample at this stage showed only a small change in the lattice parameters from the starting material. This suggests that the compound had started to decompose. The TGA trace showing the decomposition of fluorinated $La_2BaFe_2O_7$ is illustrated in *Figure 5.3*. The resultant material was a mixture of LaOF, BaF_2, Fe metal and $LaFeO_3$ as indicated by the XRPD analysis.

The original fluorinated sample contained a $LaFeO_3$ impurity (1.91(8)% by weight) and the weight loss observed from the TGA (7.01%) was corrected in order to account for the $LaFeO_3$ impurity in the oxide-fluoride sample. The corrected weight loss for the fluorinated sample is 7.15%. Calculations were carried out in two different ways: i) considering $LaFeO_3$ to be a reduced product, ii) considering only LaOF, BaF_2 and Fe metal to be decomposed products, see *Appendix 5.1* for calculations. The weight loss calculated from the first route (4.7%) was much lower than the weight loss observed from the TGA. Thus, it was considered that the fluorinated material had been decomposed to LaOF, BaF_2 and Fe metal. The weight loss obtained from the second route (7.03%) agrees well with the corrected weight loss and it suggests a composition of $La_2BaFe_2O_5F_4$ for the fluorinated material.

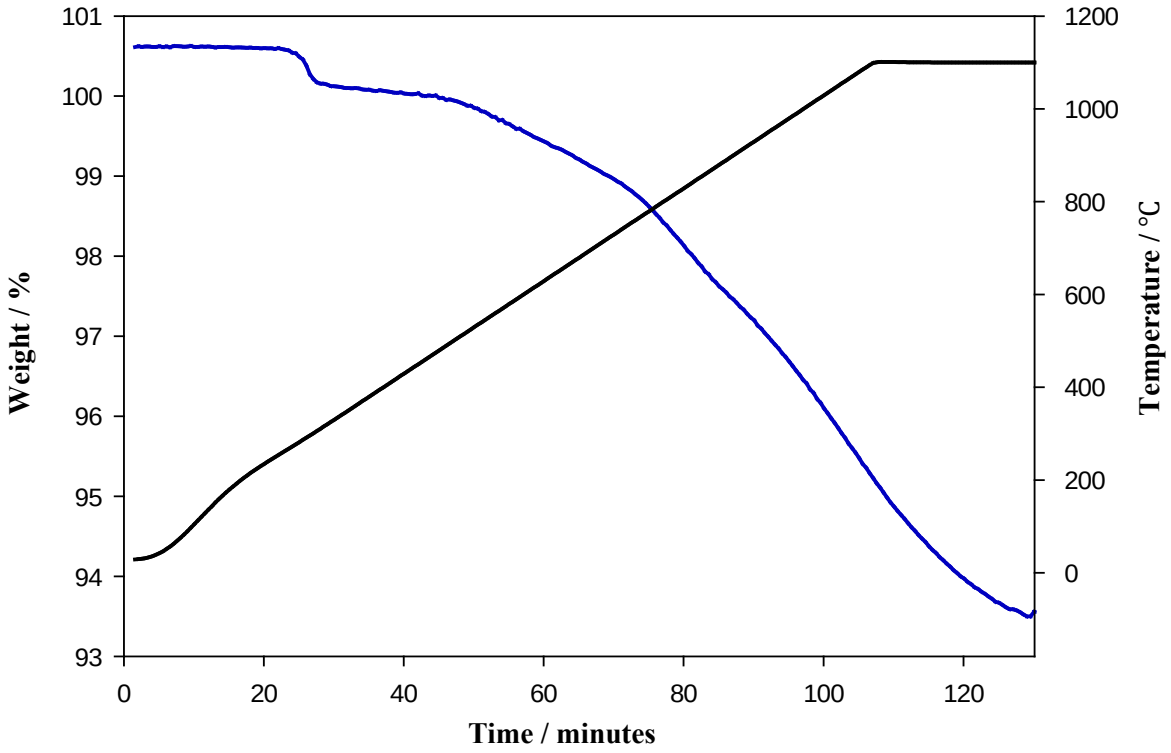

Figure 5.3 TGA trace illustrating the decomposition of fluorinated $La_2BaFe_2O_7$, weight loss shown in blue and temperature in black.

5.2.2 Structural Characterisation of Fluorinated $La_2BaFe_2O_7$

Structural characterisation of the fluorinated phase was carried out using XRPD data in the tetragonal space group *I*4/*mmm*. Additional anions were modelled as occupying interstitial sites in between the rock-salt layers. Thermal parameters for the anion sites were constrained to be equivalent to improve the stability of the refinement. The La / Ba distribution between the two sites was considered as fully ordered since X-ray scattering factors of La^{3+} and Ba^{2+} are identical. The fractional occupancies of anion sites were remained close to fully occupancy and were fixed in the final refinement. The refinement profiles are shown in *Figure 5.4* and the refined parameters are listed in *Table 5.1*.

According to refined data the change in *a* parameter compared to the parent oxide $La_2BaFe_2O_7$ is very small, but a large increase in *c* parameter (~7.6%) is observed due to the increased separation of the rock-salt layers.

Table 5.1 Refined parameters of fluorinated $La_2BaFe_2O_7$ in space group *I*4/*mmm* using XRPD data.

Atom	Site symmetry	*x*	*y*	*z*	Occupancy	$U_{iso} \times 100$ / Å^2
La	4e	0	0	0.3239(1)	1	1.26(6)
Ba	2b	0	0	0.5	1	1.26(6)
Fe	4e	0	0	0.0864(2)	1	1.39(1)
***X*(1)**	2a	0	0	0	1*	1.1(2)
***X*(2)**	8g	0	0.5	0.0981(6)	1*	1.1(2)
***X*(3)**	4e	0	0	0.8265(8)	1*	1.1(2)
***X*(4)**	4d	0.5	0	0.25	1*	1.1(2)

a = 3.96237(7) Å, *c* = 22.3972(5) Å

χ^2 = 2.491, R_{wp} = 3.65% * denotes fractional occupancy fixed

The fluorinated sample contained two more compounds other than the major fluorinated product. In order to obtain the best fit these phases were also included to the refinement. The impurity phases were $LaFeO_3$ (1.91(8)% by weight) and LaF_3 (3.4(2)% by weight).

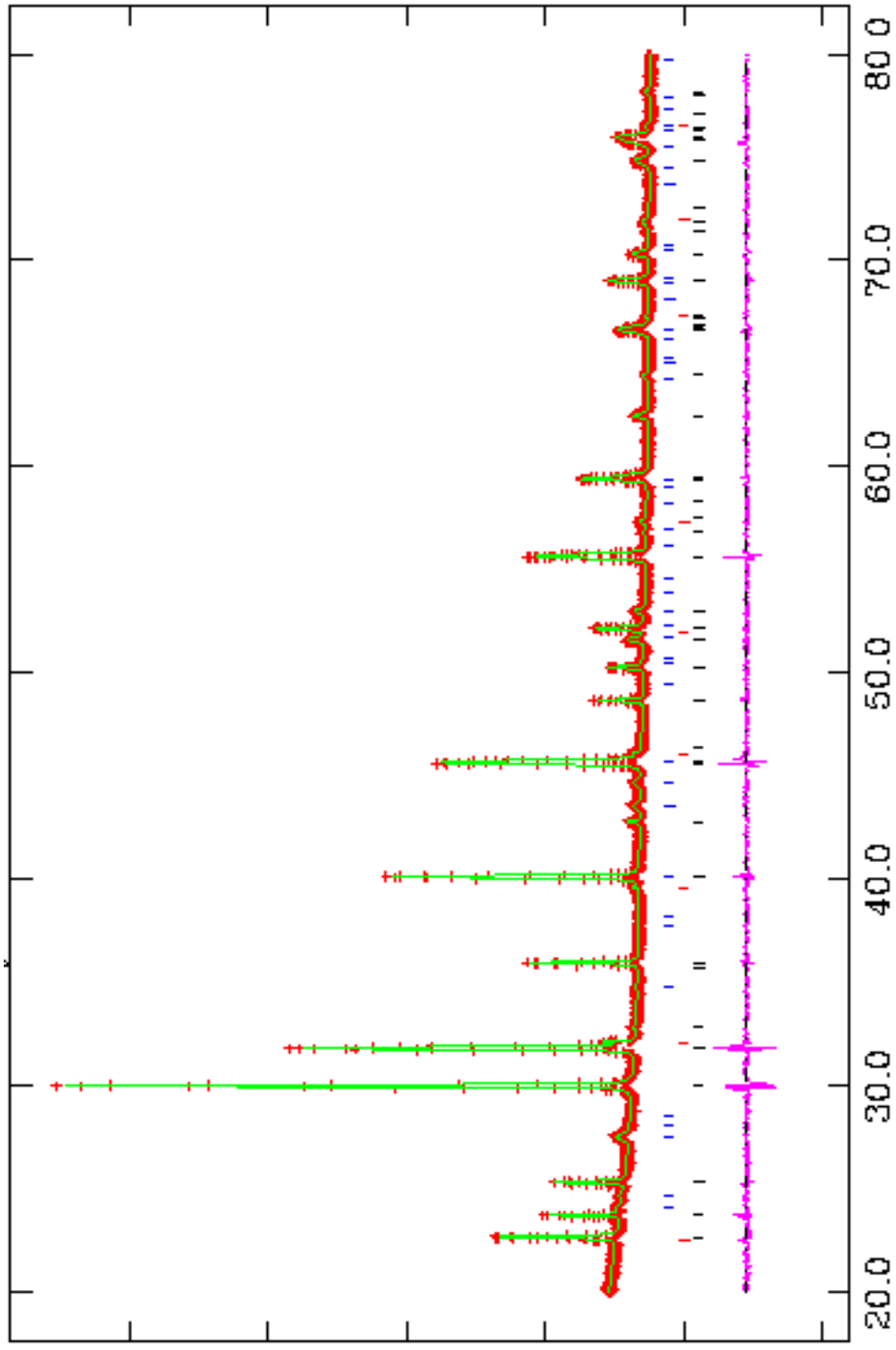

5.2.3 Magnetic Characterisation of Fluorinated $La_2BaFe_2O_7$

Both field-cooled

Figure 5.4 Observed fluorinated data, where $LaFeO_3$ (1. by weight, data, where (red vertica

its

field-cooled (zfc) susceptibilities were measured in applied magnetic field of 1000 Oe. The plots of susceptibility versus temperature and inverse susceptibility versus temperature are given in *Figure 5.5*. Both susceptibilities increase on cooling and the two datasets begin to diverge below 103 K. The zero-field-cooled plot indicates a transition around 41.7 K. Neutron powder diffraction data are required in order to determine the nature of this transition.

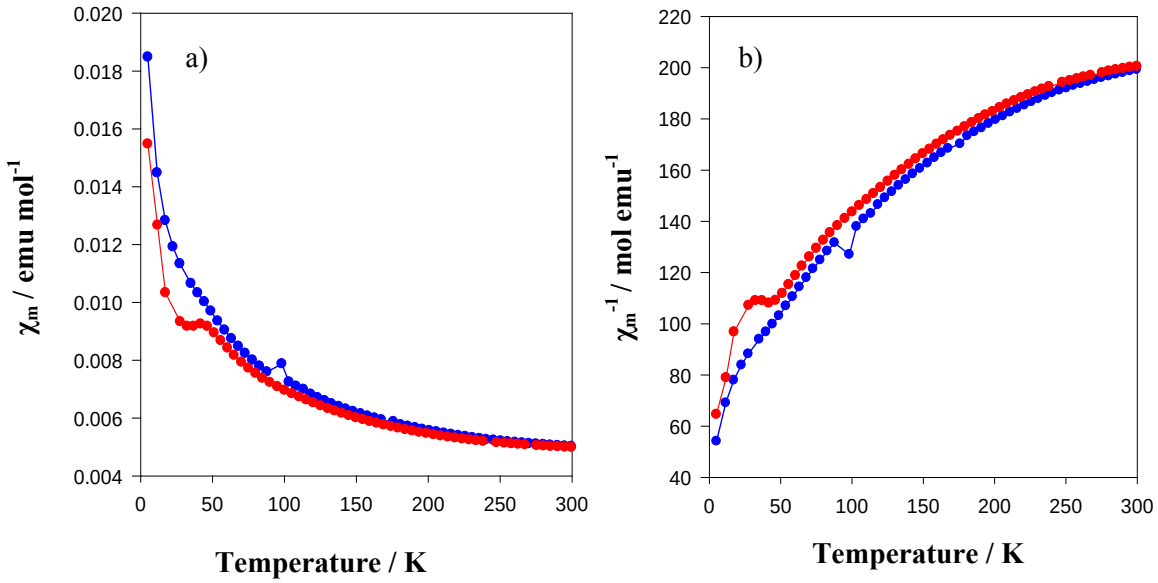

Figure 5.5 a) Variation of magnetic susceptibility with temperature and b) Variation of inverse susceptibility with temperature for fluorinated $La_2BaFe_2O_7$, field-cooled and zero-field-cooled data shown in blue and red, respectively.

5.2.4 Mössbauer Spectroscopy of Fluorinated $La_2BaFe_2O_7$

The ^{57}Fe Mössbauer spectra recorded from fluorinated $La_2BaFe_2O_7$ at 298 K and 16 K are shown in *Figure 5.6* and the fit parameters are contained in *Table 5.2*.

The spectrum recorded at 298 K showed the persistence of the minor (*ca*. 3%) singlet component characteristic of Fe^{4+} but this component was absent in the spectrum recorded at 16 K. This singlet represents the strontium-doped $LaFeO_3$ impurity phase observed in the spectrum recorded from $La_2BaFe_2O_7$ and which magnetically orders at lower temperature and becomes incorporated within the dominant sextet patterns characteristic of Fe^{3+} observed at 16 K. The major part (*ca*. 97%) of the spectrum recorded from fluorinated $La_2BaFe_2O_7$ at 298 K differs from its parent $La_2BaFe_2O_7$ phase in the appearance of a significant (*ca*. 25%) paramagnetic Fe^{3+} component. The lower intensity of the paramagnetic doublet at 16 K (*ca*. 6%) suggests that the fluorination process induces a decrease in particle size which is represented by the paramagnetic doublet observed at 298 K.

At lower temperature the small particles of the fluorinated $La_2BaFe_2O_7$ would be expected to magnetically order and to give rise to the spectrum recorded at 16 K (*Figure 5.6*) where the paramagnetic doublet decreases in magnitude to *ca*. 6% and the two sextet patterns account for *ca*. 94% of the spectral area. Importantly, the ^{57}Fe Mössbauer spectra recorded from fluorinated $La_2BaFe_2O_7$ show that all the iron is present as Fe^{3+}, which is also consistent with the composition suggested by TGA. So it is confirmed that fluorination of $La_2BaFe_2O_7$ is achieved without oxidation of iron.

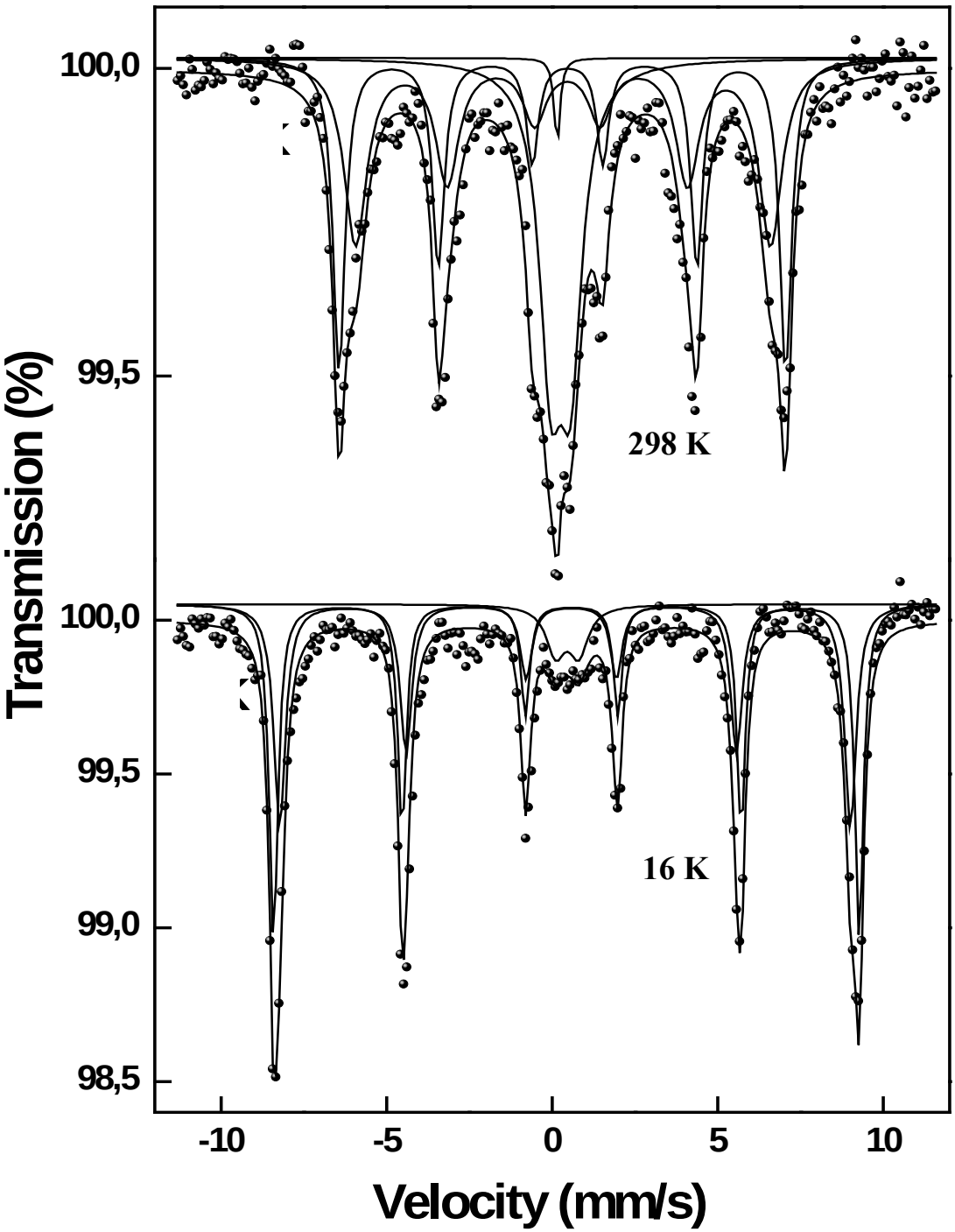

Figure 5.6 ^{57}Fe Mössbauer spectra recorded from fluorinated $La_2BaFe_2O_7$ at 298 K (top) and 16 K (bottom).

Table 5.2 ^{57}Fe Mössbauer parameters recorded from fluorinated $La_2BaFe_2O_7$.

Temperature of measurement / K	**$\delta \pm 0.02$ / mms^{-1}**	**$e^2qQ / 2 \pm 0.02$ / mms^{-1}**	**$H \pm 0.5$ / T**	**Area ± 3 %**
298	0.10			3
	0.26	0.74		25
	0.39	-0.10	42	44
	0.38	-0.09	38	28
16	0.46	0.88		6
	0.51	-0.08	55	44
	0.48	-0.09	53	49

5.2.5 Discussion of Fluorinated $La_2BaFe_2O_7$

The composition $La_2BaFe_2O_5F_4$ suggested by TGA indicates that fluorination occurs through anion exchange which involves replacement of $2O^{2-}$ by $4F^-$ ions per formula unit. This also suggests that F^- ions occupy the interstitial sites as well as the apical sites in FeX_6 octahedra. Since both X-ray and neutron scattering factors of O^{2-} and F^- are similar neither of these methods could be used directly to determine the anion distribution between the three sites; *X*(1), *X*(2) and *X*(3).

Thus, bond valence sum (BVS) calculations were carried out for the Fe-*X* bonds using r_o for Fe(III)[14], given in *Appendix 5.2*. These results indicate that the coordination of Fe is consistent with Fe^{3+} and the calculated Fe valencies for different F^- arrangements are quite

similar even though a slight preference is shown for the fluorine to occupy the equatorial *X*(2)eq sites, see *Table 5.3*. However, given the uncertainty in determining anion positions using XRPD data, it is not possible to establish the fluorine distribution with any confidence. Also the apical Fe-*X*(3) bonds in the fluorinated product are significantly shorter (*Figure 5.7*) compared to those in the precursor oxide due to electrostatic repulsions between interstitial fluoride ions and *X*(3) ions. The Fe-*X* bond lengths obtained for $La_2BaFe_2O_5F_4$ are Fe-*X*(1) = 1.934(5) Å, Fe-*X*(2) = 1.998 (2) Å [×4], Fe-*X*(3) = 1.95(2) Å and for $La_2BaFe_2O_7$ the bond distances are 1.979(4), 1.9689(9) and 2.25(1) Å, respectively.

Table 5.3 Valencies calculated for Fe for different arrangements of F^- ions in $La_2BaFe_2O_5F_4$.

Model	Fe Valency
Interstitial + F(3)	3.20
Interstitial + F(2)	3.11
Interstitial + F(1) + F(2)	3.09
Interstitial + F(1) + F(3)	3.13

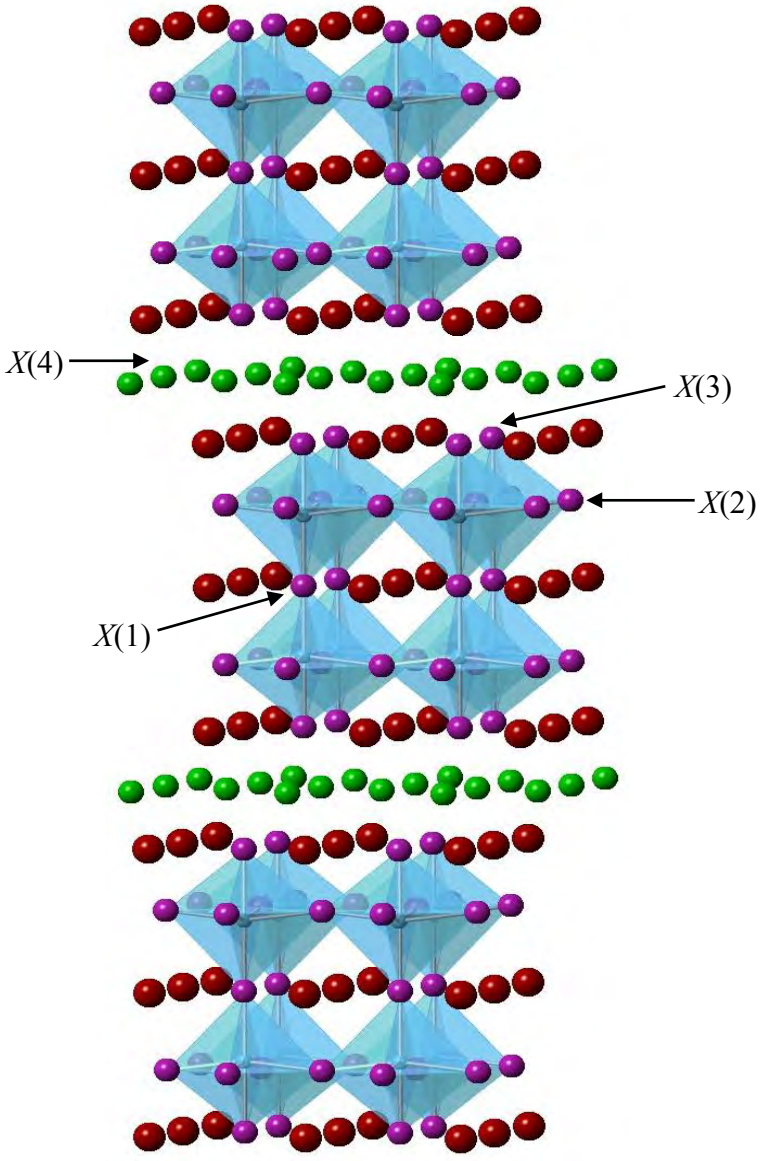

Figure 5.7 The structure of $La_2BaFe_2O_5F_4$, with *A* (La / Ba) cations shown in red, anions in FeX_6 octahedra shown in purple, interstitial anions in green and FeX_6 octahedra shown in blue.

5.3 Fluorination of $Nd_2SrFe_2O_7$

Attempts to fluorinate $Nd_2SrFe_2O_7$ (~100 mg) at 290 °C failed but the reaction began to occur at 350 °C and complete fluorination was achieved at 380 °C. The reaction was carried out in the apparatus described in Section 2.2.1 for 15 minutes using 10% F_2(g) / 90% N_2(g) as the fluorinated agent. The progress of the fluorination reaction was monitored by the XRPD and the XRPD patterns are shown in *Figure 5.8*.

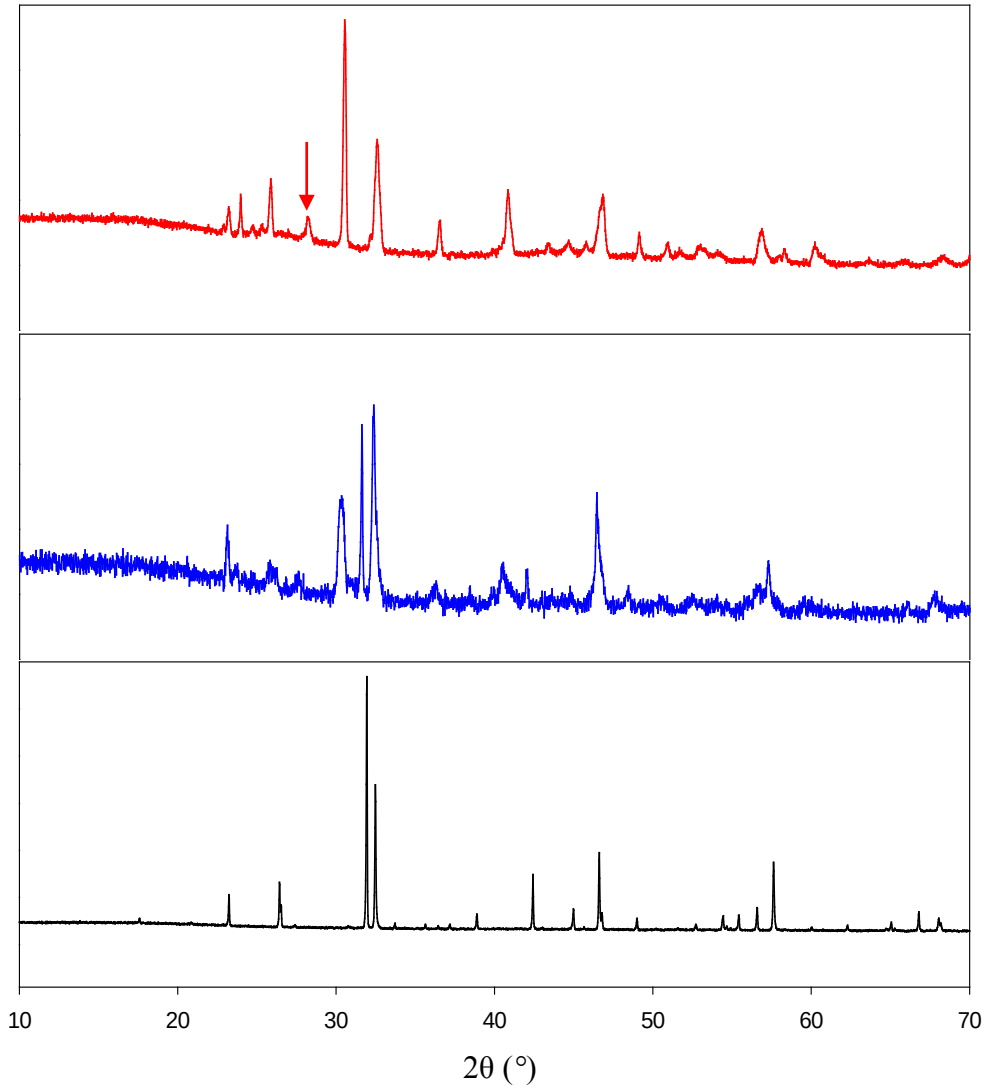

Figure 5.8 XRPD patterns showing the fluorination of $Nd_2SrFe_2O_7$, from bottom to top, pattern of $Nd_2SrFe_2O_7$, intermediate stage at 350 °C in blue, the final fluorinated phase in red, NdF_3 impurity is shown with an arrow.

5.3.1 Thermogravimetric Analysis of Fluorinated $Nd_2SrFe_2O_7$

Thermogravimetric analysis was carried out by heating the material to 1000 ℃ in 10% H_2(g) / 90% N_2(g). The TGA trace showing decomposition of fluorinated $Nd_2SrFe_2O_7$ is illustrated in *Figure 5.9*. The first weight loss occurred at ~350 ℃ similar to that observed for $La_2BaFeO_5F_4$; XRPD analysis indicated that the compound had started to decompose at this stage forming NdF_3 and Fe metal. According to the XRPD analysis, the resulting powder was a mixture of NdOF, SrF_2, Fe metal and $NdFeO_3$ which was considered to be the perovskite impurity in the initial oxide-fluoride sample (15.8(1)% by weight), see *Appendix 5.3* for calculations. Thus, it was considered that the oxide-fluoride had decomposed to NdOF, SrF_2 and Fe metal.

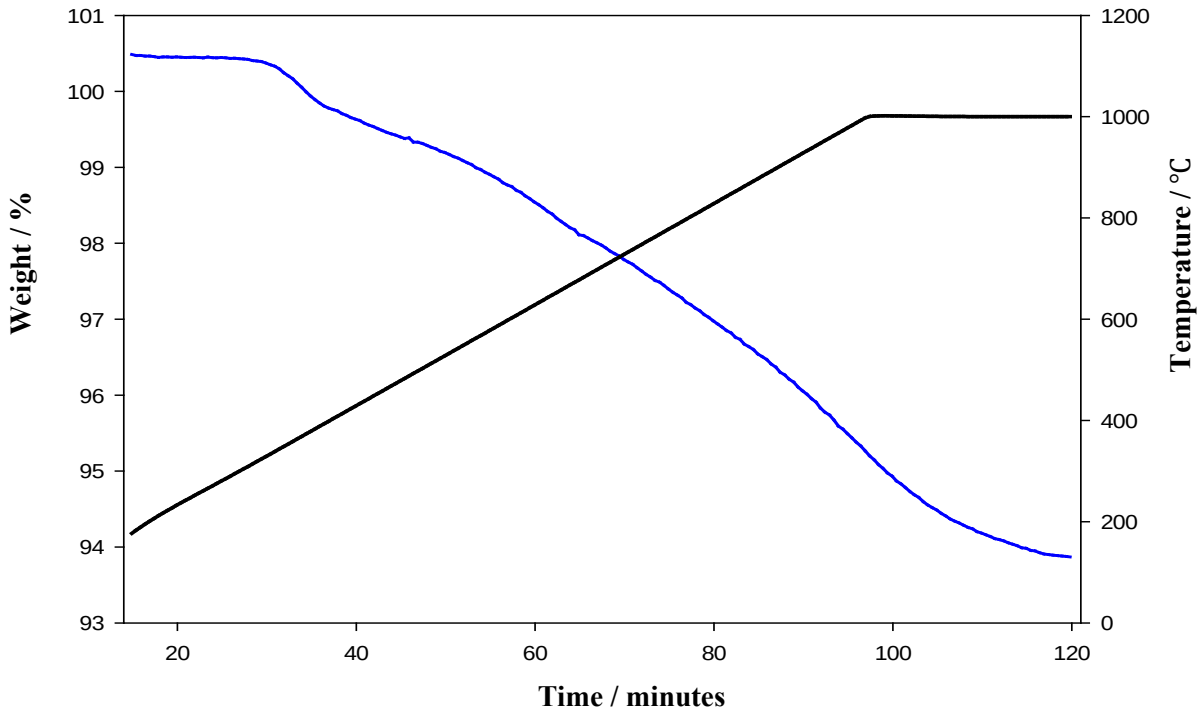

Figure 5.9 TGA trace illustrating the decomposition of fluorinated $Nd_2SrFe_2O_7$, weight loss shown in blue and temperature in black.

This indicates that the F^- ion composition in the oxide-fluoride is four and so the expected weight loss was calculated considering the oxide-fluoride composition to be $Nd_2SrFeO_5F_4$, which gave a value of 7.45% for the mass loss. The oxide-fluoride sample contained 15.8(1)% of $NdFeO_3$ impurity by weight which significantly affects the observed weight loss (6.5%). Thus, the observed weight loss was corrected in order to obtain the actual weight loss of the sample (7.7%), which is consistent with the mass loss calculated for the composition $Nd_2SrFeO_5F_4$, see *Appendix 5.3* for detailed calculations.

5.3.2 Structural Characterisation of Fluorinated $Nd_2SrFe_2O_7$

The Rietveld refinement of the fluorinated phase was carried out using XRPD data in the tetragonal space group *I*4/*mmm*. The interstitial anion sites were modelled as occupied by additional anions. Three thermal parameters: one for Nd / Sr, one for Fe and one for O / F (*X*) were refined to improve the refinement. The fractional occupancies of the anion sites remained close to full occupancy and were fixed in the final refinement. Also Nd and Sr cations were allowed to distribute between the two *A* sites with the constraint that the 2 : 1 composition ratio was maintained. The fluorinated sample contained three phases: the fluorinated product, NdF_3 (6.8(6)% by weight) and $NdFeO_3$ (15.8(1)% by weight). So in addition to the main fluorinated phase these two phases were also included in the refinement. The fitted profile is shown in *Figure 5.10* and details from the refinement are given in *Table 5.4*. Refined data indicate an expansion in the *c* parameter (~10.4%) due to the increased separation of the rock-salt layers, but the change in *a* parameter is very small. Also fluorination had made no significant change to the Nd / Sr cation distribution (for $Nd_2SrFe_2O_7$, Nd(1) / Sr(1) – 0.22(1) / 0.78(1) and Nd(2) / Sr(2) – 0.889(5) / 0.111(5)).

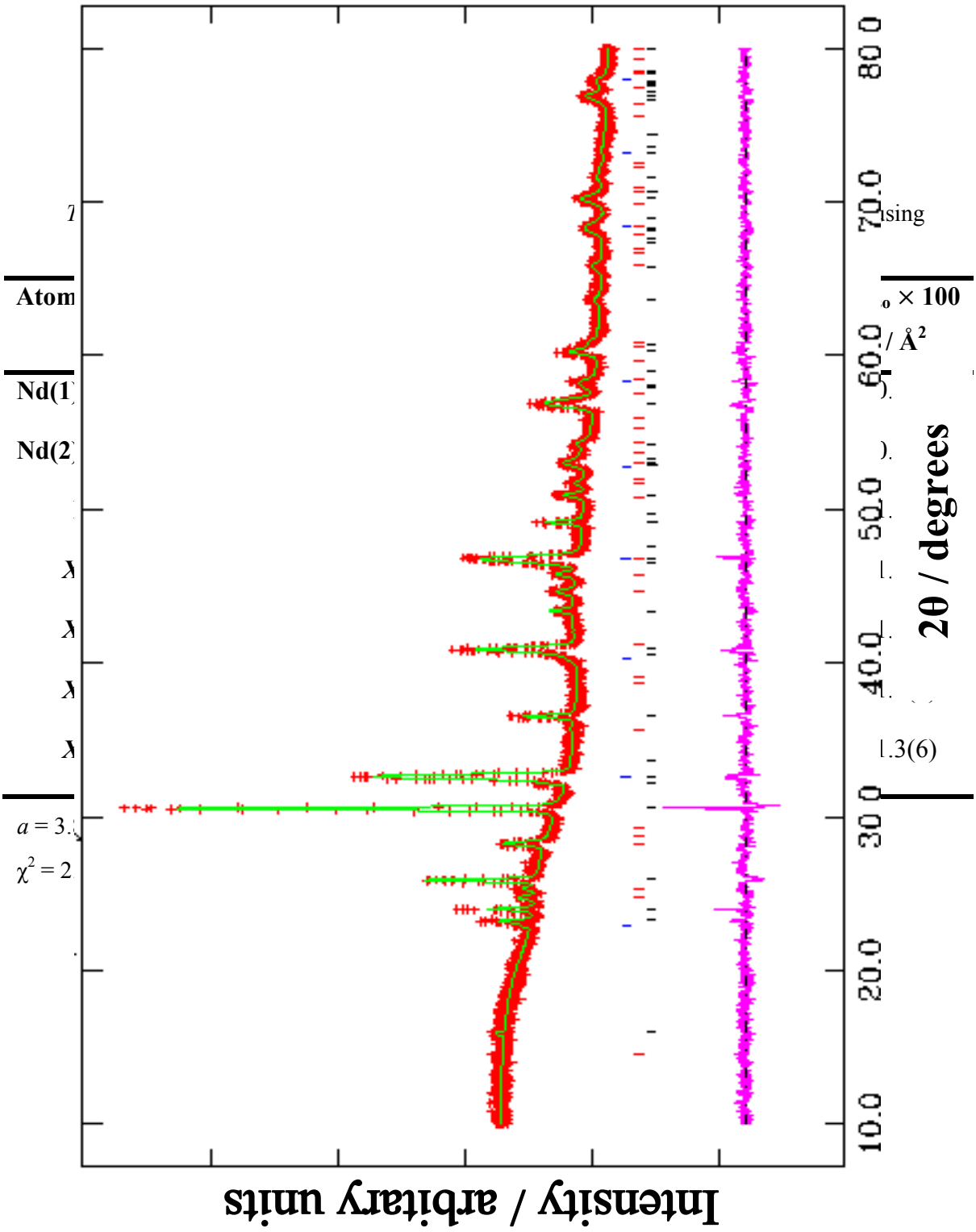

Figure 5.10 Observed (red +), calculated (green) and difference (pink) profiles of fluorinated $Nd_2SrFe_2O_7$, as generated by the Rietveld refinement of XRPD data, where phase 1 = $Nd_2SrFe_2O_5F_4$ (black vertical lines), phase 2 = NdF_3 (6.8(6)% by weight, red vertical lines) and phase 3 = $NdFeO_3$ (15.8(1)% by weight, blue vertical lines).

5.3.3 Magnetic Characterisation of Fluorinated $Nd_2SrFe_2O_7$

Both field-cooled (fc) and zero-field-cooled (zfc) susceptibilities of the fluorinated sample were recorded in applied magnetic field of 1000 Oe. Variation of susceptibility and inverse susceptibility with temperature is given in *Figure 5.11*. The data show an increase in susceptibility on cooling and the two curves diverge below 300 K which suggests probable magnetic order at temperatures higher than room temperature. Further investigation on magnetic behaviour needs NPD data.

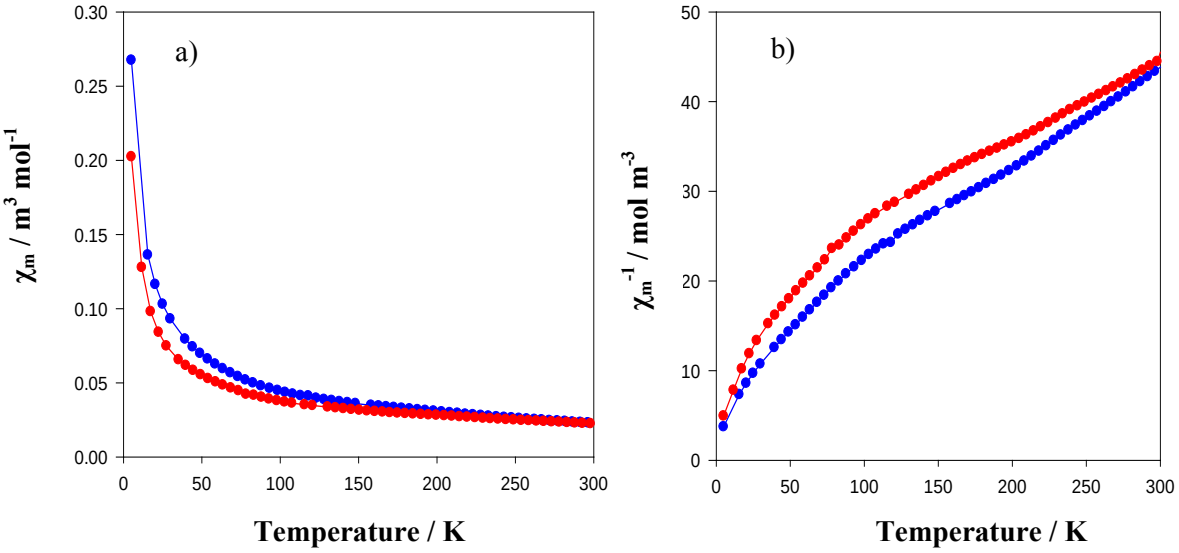

Figure 5.11 a) Variation of magnetic susceptibility with temperature and b) Variation of inverse susceptibility with temperature for fluorinated $Nd_2SrFe_2O_7$, field-cooled and zero-field-cooled data shown in blue and red, respectively.

5.3.4 Discussion of Fluorinated $Nd_2SrFe_2O_7$

Thermogravimetric analysis of the fluorinated product suggested an approximate composition $Nd_2SrFe_2O_5F_4$, which indicates that the fluorination process involves both

anion insertion and anion substitution. As the composition implies fluorine insertion has happened with no oxidation of Fe^{3+} ions, similar to that observed in the fluorinated $La_2BaFe_2O_7$ phase.

The bond lengths of $Nd_2SrFe_2O_5F_4$ obtained from structure refinements are Fe-*X*(1) = 1.84(2) Å, Fe-*X*(2) = 1.949(3) Å [×4], Fe-*X*(3) = 1.55(4) Å. The Fe-*X*(3) bond lengths are significantly short because the oxygen positions from XRPD are not reliable and the anion distribution cannot be reliably determined from bond valence calculations due to the uncertainty in the anion positions. However, further analysis, such as Mössbauer spectroscopy and NPD data are required to accurately determine the oxidation state of Fe and the crystal structure of the fluorinated phase.

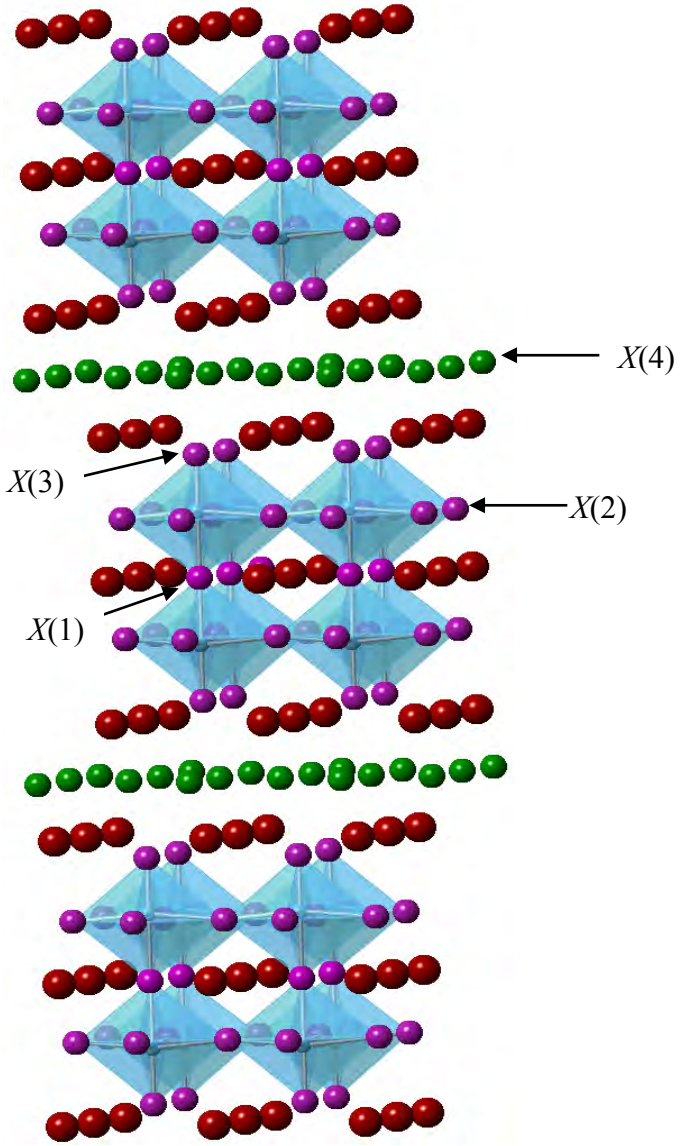

Figure 5.12 The structure of $Nd_2SrFe_2O_5F_4$, with *A* (Nd / Sr) cations shown in red, anions in FeX_6 octahedra shown in purple, interstitial anions in green and FeX_6 octahedra shown in blue.

5.4 Fluorination of $La_2SrFe_2O_7$

Fluorination of $La_2SrFe_2O_7$ at 350 ℃ was slow and complete fluorination was achieved only at 375 ℃. The oxide precursor was reacted with 10% F_2(g) / 90% N_2(g) in the apparatus described in Section 2.2.1 for 15 minutes. The XRPD patterns showing the progress of the fluorination reaction are illustrated in *Figure 5.13*.

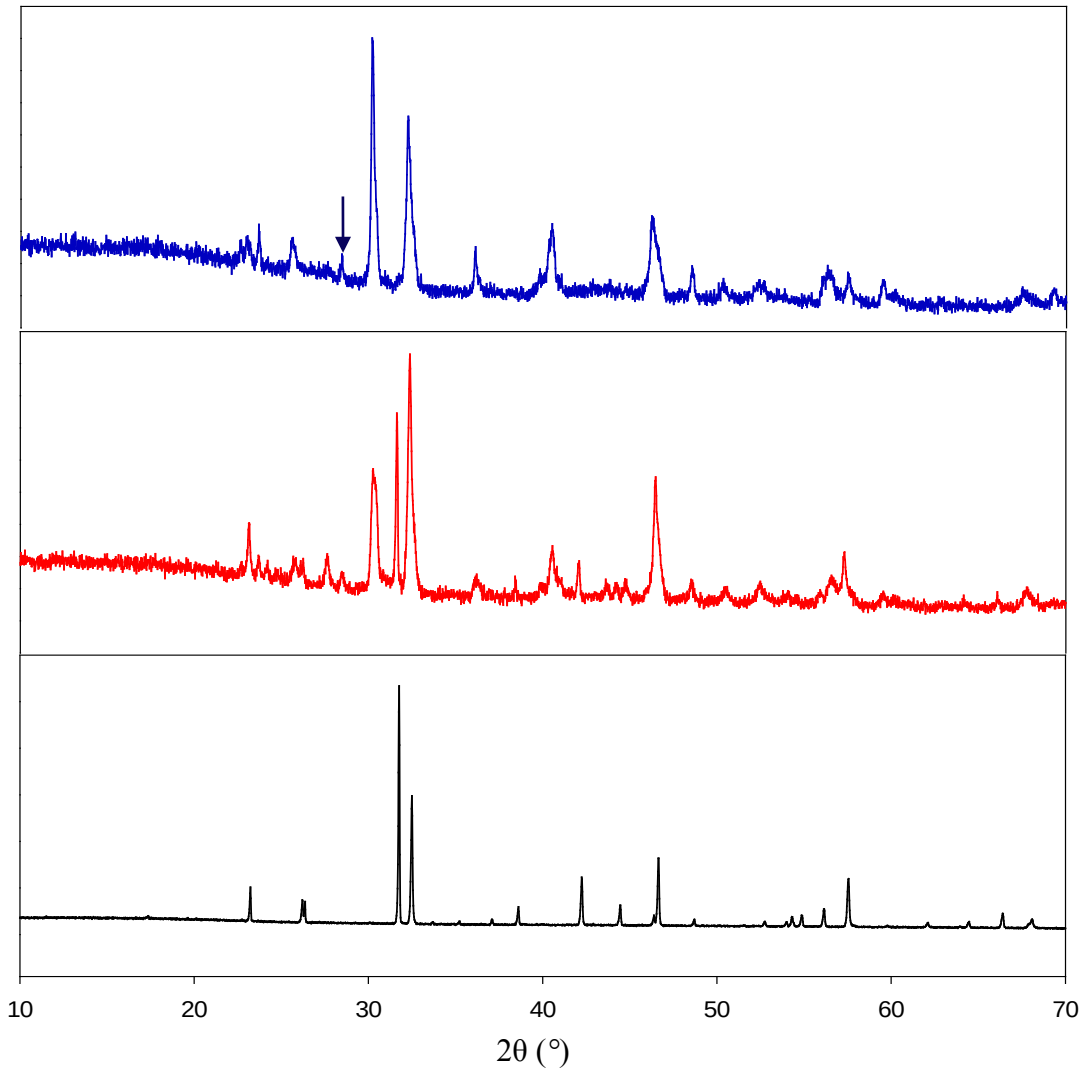

Figure 5.13 XRPD patterns showing the fluorination of $La_2SrFe_2O_7$, from bottom to top, pattern of $La_2SrFe_2O_7$, intermediate stage at 350 ℃ in red, the final fluorinated phase in blue, LaF_3 impurity is shown with an arrow.

5.4.1 Thermogravimetric Analysis of Fluorinated $La_2SrFe_2O_7$

Thermal analysis of the fluorinated material in 10% H_2(g) / 90% N_2(g) revealed a weight loss of 6.23%. The TGA trace showing the decomposition of fluorinated $La_2SrFe_2O_7$ is illustrated in *Figure 5.14*. According to the XRPD analysis, the final material was a mixture of LaOF, SrF_2, $LaFeO_3$ and Fe metal, see *Appendix 5.4*. The oxide-fluoride

material contained a significant $LaFeO_3$ impurity, and it was assumed that fluorinated phase decomposed to LaOF, SrF_2 and Fe metal. This suggests that the fluoride anion content of the original material is 4 and so the composition could be considered as $La_2SrFe_2O_5F_4$. The weight lose corresponds to this composition was determined taking the weight of the impurity $LaFeO_3$ (21.03(6)% by weight) into account.

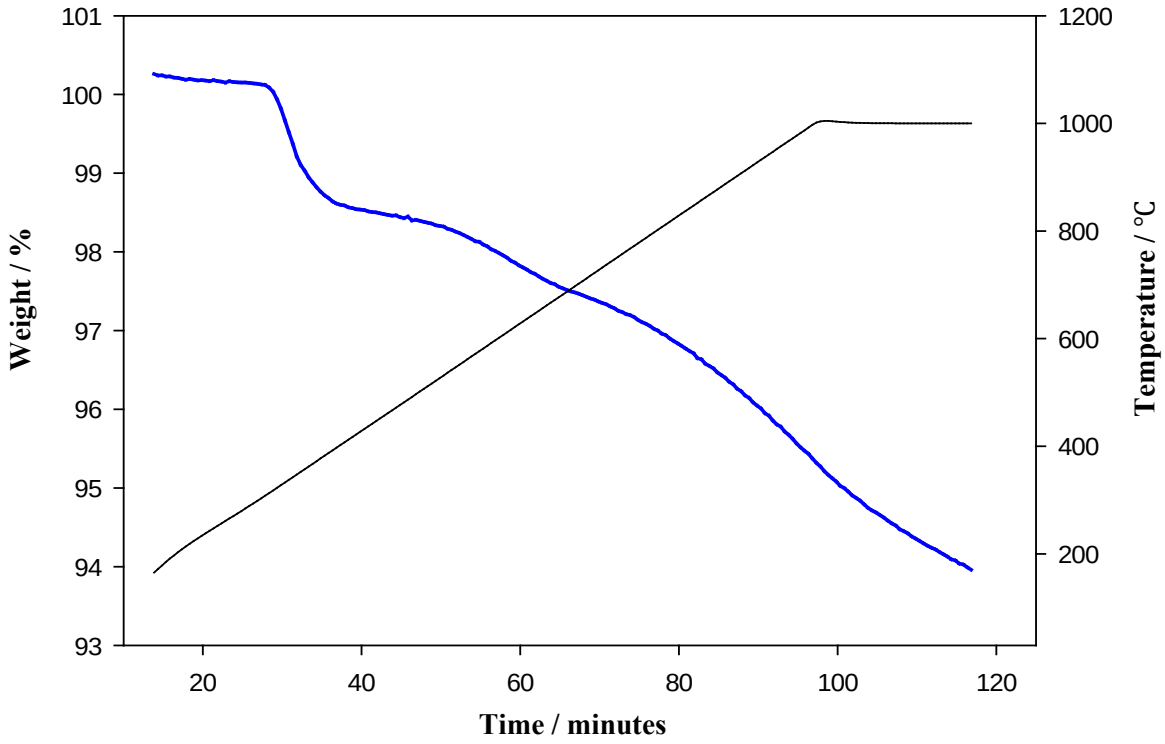

Figure 5.14 TGA trace illustrating the decomposition of fluorinated $La_2SrFe_2O_7$, weight loss shown in blue and temperature in black.

This gave a value of 5.99% for the weight loss which is consistent with the weight loss obtained from the TGA, but the suggested composition $La_2SrFe_2O_5F_4$ involves a degree of uncertainty since the decomposition has not reached a plateau. The calculations are given in *Appendix 5.4*.

5.4.1 Structural Characterisation of Fluorinated $La_2SrFe_2O_7$

According to the Rietveld refinement of XRPD data recorded for the fluorinated phase in the tetragonal space group *I*4/*mmm* fluorination has resulted in an expansion along the *c* axis (~10.1%). But as observed in previous fluorinated phases the change in *a* parameter is very small. During the refinement the interstitial anion sites were modelled as occupied by additional anions and thermal parameters for these anion sites were constrained to be equivalent. The cationic distribution of La^{3+} and Sr^{2+} over the two *A* sites was constrained in such a way that the sites remained fully occupied and the overall La^{3+} : Sr^{2+} ratio remained 2 : 1. The fluorinated sample contained two impurities: one decomposition product LaF_3 (1.1(2)% by weight) and $LaFeO_3$ (21.03(6)% by weight). The refined profiles are shown in *Figure 5.15* and the refined data are given in *Table 5.5*. The La / Sr cation distribution after fluorination is quite similar to that of the starting material $La_2SrFe_2O_7$ (La(1) / Sr(1) – 0.48(1) / 0.52 (1), La(2) / Sr(2) – 0.76 (5) / 0.24(5)) with more La^{3+} ions occupying the nine coordinate site in the rock-salt layers and Sr^{2+} the twelve coordinate perovskite site.

Figure 5.15 Observed (red +), calculated (green) and difference (pink) profiles of fluorinated $La_2SrFe_2O_7$, as generated by the Rietveld refinement of XRPD data, where phase 1 = fluorinated $La_2SrFe_2O_7$ (black vertical lines), phase 2 = $LaFeO_3$ (21.03(6)% by weight, red vertical lines) and phase 3 = LaF_3 (1.1(2)% by weight, blue vertical lines).

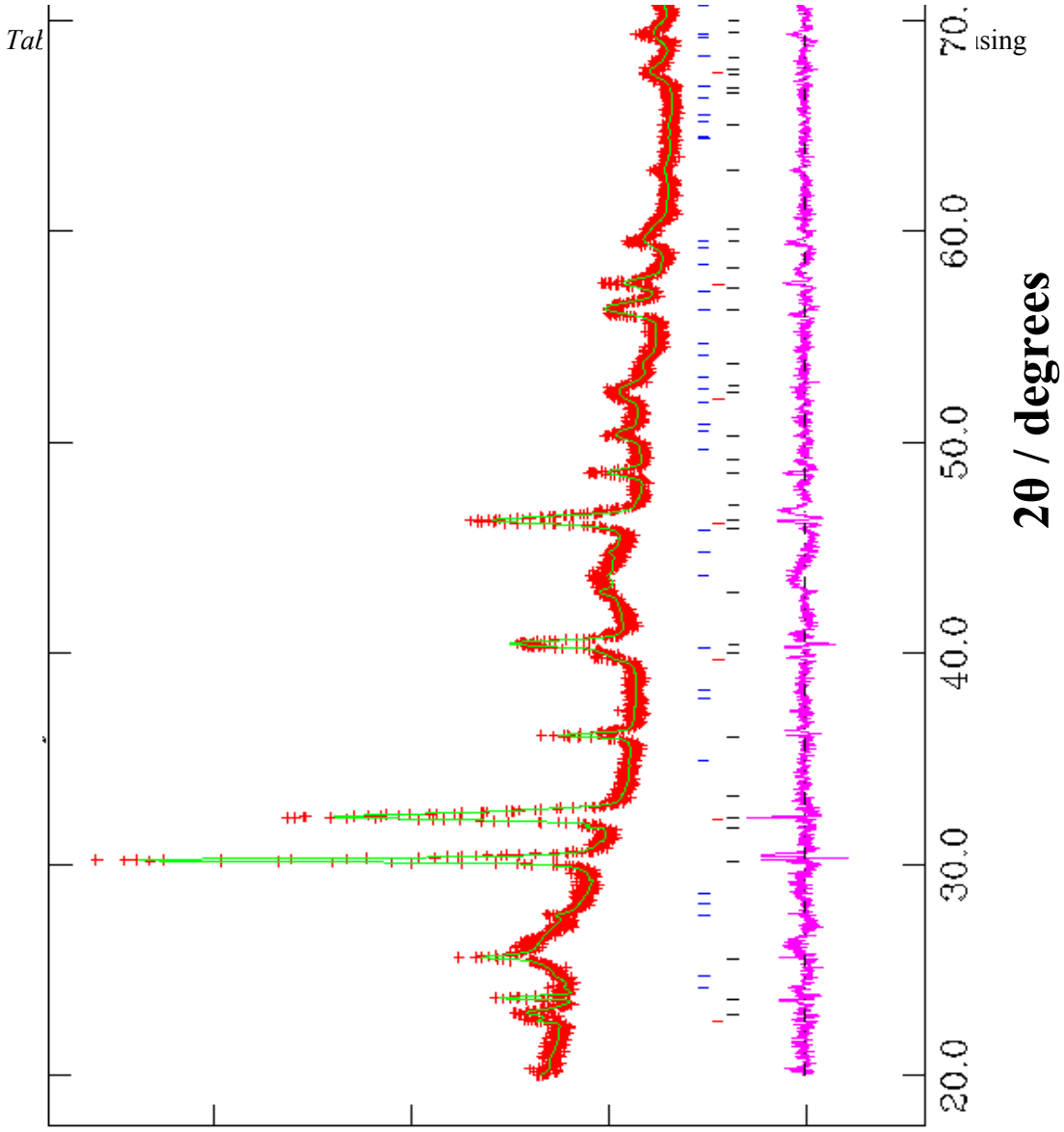

Intensity / arbitary units

Figure 5.12 Observed (red +), calculated (green) and difference (pink) profiles of fluorinated $La_2SrFe_2O_7$, as generated by the Rietveld refinement of XRPD data, where phase 1 = $La_2SrFe_2O_7$ (black vertical line), phase 2 = $LaFeO_3$ (red vertical line) and phase 3 = LaF_3 (blue vertical line).

	symmetry					/ Å^2
La(1) / Sr(1)	4e	0	0	0.5	0.41(3) / 0.59(3)	1.4(3)
La(2) / Sr(2)	2b	0	0	0.3249(3)	0.8(2) / 0.2(2)	1.4(3)
Fe	4e	0	0	0.0862(8)	1	2.0(5)
***X*(1)**	2a	0	0	0	1	3(1)
***X*(1)**	8g	0	0.5	0.088(2)	1	3(1)
***X*(1)**	4e	0	0	0.852 (3)	1	3(1)
***X*(1)**	4d	0.5	0	0.25	0.96(13)	3(1)

a = 3.9062(5) Å, c = 22.415(4) Å

χ^2 = 2.146, R_{wp} = 3.33%

5.4.3 Magnetic Characterisation of Fluorinated $La_2SrFe_2O_7$

The magnetic properties of the fluorinated material were studied by recording both field-cooled (fc) and zero-field-cooled (zfc) susceptibilities in an applied magnetic field of 1000 Oe. The curves illustrating the variation of susceptibility and inverse susceptibility with temperature are shown in *Figure 5.16*. Upon cooling both field susceptibilities increase and the two graphs diverge around 300 K which indicates the presence of some order above room temperature. Further studies based on NPD are required to confirm the magnetic behaviour of $La_2SrFe_2O_5F_4$.

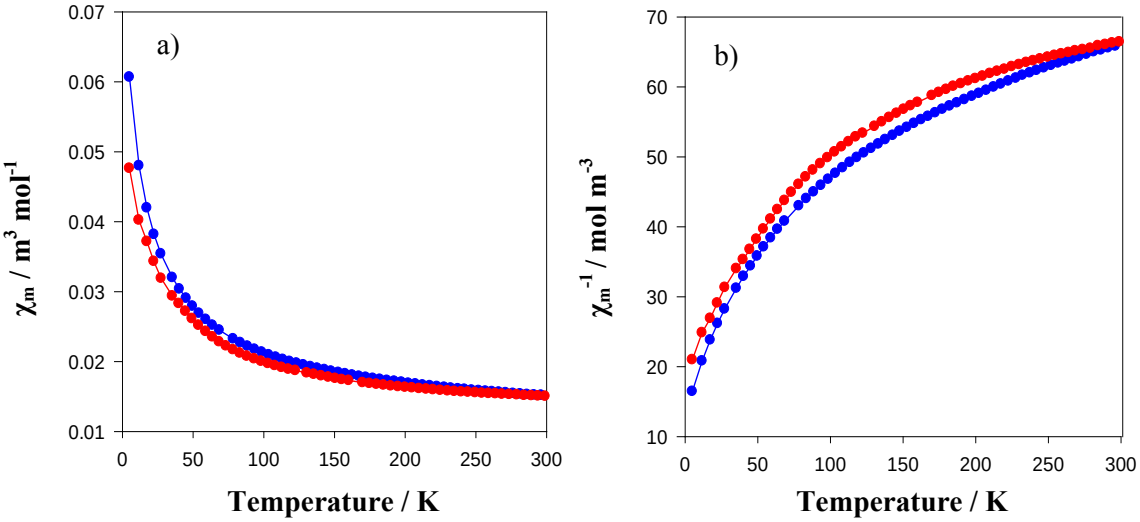

Figure 5.16 a) Variation of magnetic susceptibility with temperature and b) Variation of inverse susceptibility with temperature for fluorinated $La_2SrFe_2O_7$, field-cooled and zero-field-cooled data shown in blue and red, respectively.

5.4.4 Discussion of Fluorinated $La_2SrFe_2O_7$

The chemical composition $La_2SrFe_2O_5F_4$ obtained from thermogravimetric analysis suggests that the fluorine incorporation is *via* anion insertion and substitution of oxygen anions in the FeX_6 octahedra. As the composition implies fluorine insertion has not oxidised the Fe^{3+} ions in the FeX_6 octahedra. The Fe-*X* bond lengths obtained for the oxide-fluoride are Fe-*X*(1) = 1.932(2) Å, Fe-*X*(2) = 1.953(1) Å [× 4], Fe-*X*(3) = 1.386(6) Å. The Fe-*X*(3) bond length is surprisingly short and is unrealistic, shown in *Figure 5.17*. The oxygen positions determined from XRPD data are not reliable due to the low sensitivity of XRPD data to the light anions. Hence, the anion distribution cannot be reliably determined from bond valence sum (BVS) calculations. Further studies should be

carried out using Mössbauer spectroscopy and NPD data in order to confirm the oxidation state of Fe, structural and the magnetic properties of $La_2SrFe_2O_5F_4$ phase.

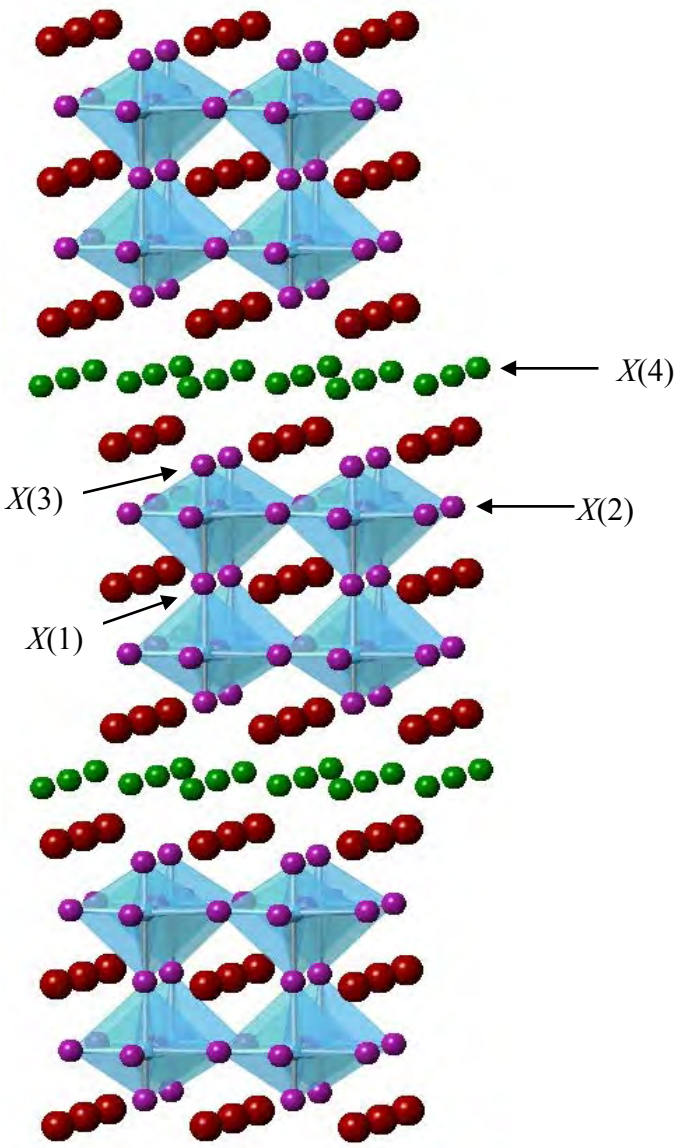

Figure 5.17 The structure of $La_2SrFe_2O_5F_4$, with *A* (La / Sr) cations shown in red, anions in the FeX_6 octahedra shown in purple, interstitial anions shown in green and FeX_6 octahedra shown in blue.

5.5 Fluorination of $Eu_2SrFe_2O_7$

Fluorination of $Eu_2SrFe_2O_7$ was investigated using 10% F_2(g) / 90% N_2(g) as the fluorinated agent. The reaction was carried out at 335 ℃ for 15 minutes using the apparatus described in Section 2.2.1. The progress of the fluorination reaction was monitored by the XRPD and the patterns are shown in *Figure 5.18*.

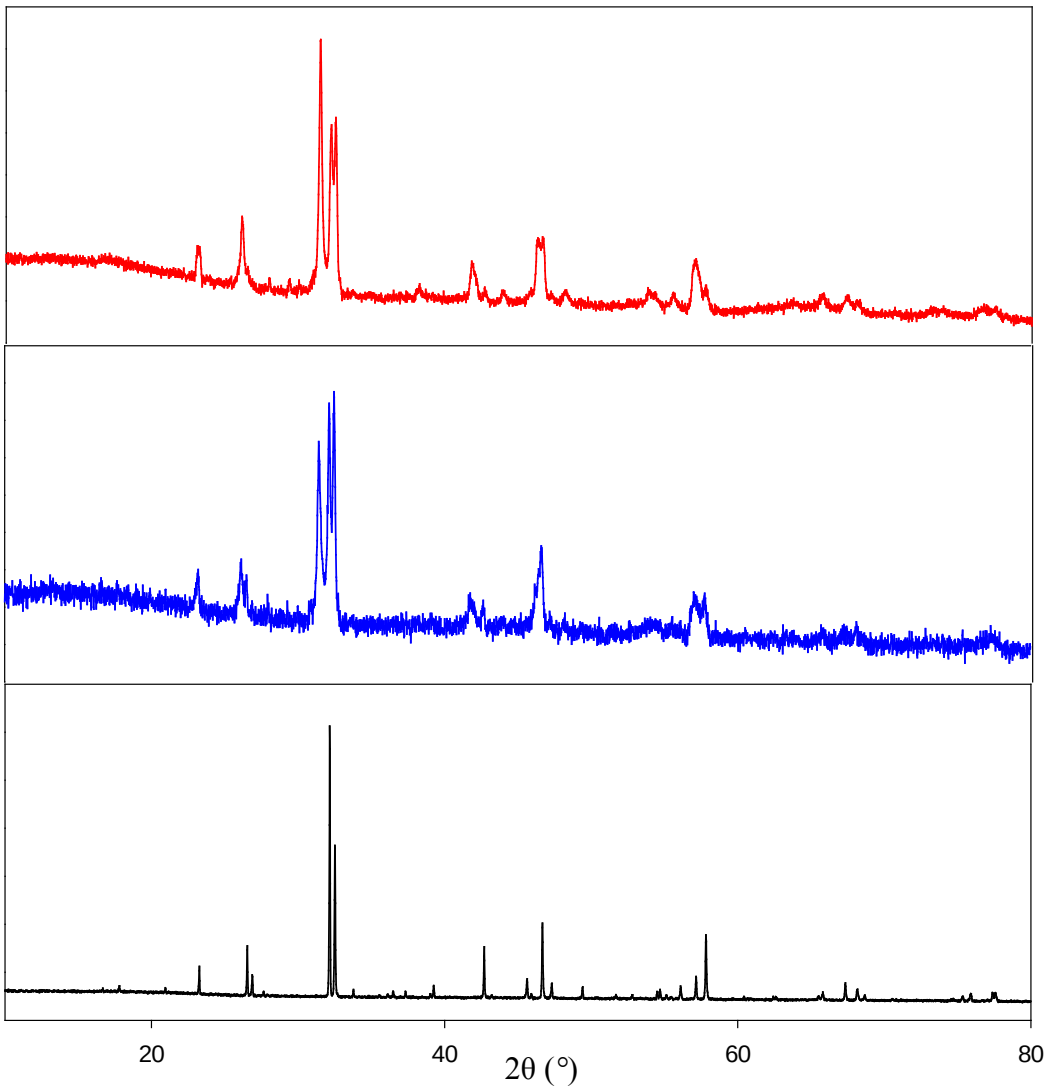

Figure 5.18 XRPD patterns showing the fluorination of $Eu_2SrFe_2O_7$, from bottom to top, pattern of $Eu_2SrFe_2O_7$, intermediate stage at 315 ℃ in blue, the final fluorinated phase in red.

5.5.1 Thermogravimetric Analysis of Fluorinated $Eu_2SrFe_2O_7$

In order to determine the fluorine content of the oxide-fluoride, TGA was carried out in 10% H_2(g) / 90% N_2(g). The TGA trace showing decomposition of fluorinated $Eu_2SrFe_2O_7$ is illustrated in *Figure 5.19*. The compound lost its weight at 450 ℃ and 800 ℃, XRPD analysis of the material at each stage revealed that the compound has started to decompose forming Eu_2O_3, SrF_2 and Fe metal. The XRPD analysis of the final material indicated the presence of $EuFeO_3$, Eu_2O_3, SrF_2 and Fe metal. However, the initial oxide-fluoride sample contained 7.1(2)% of $EuFeO_3$ impurity by weight. The observed weight loss (5.5%) was corrected in order to account for the impurity.

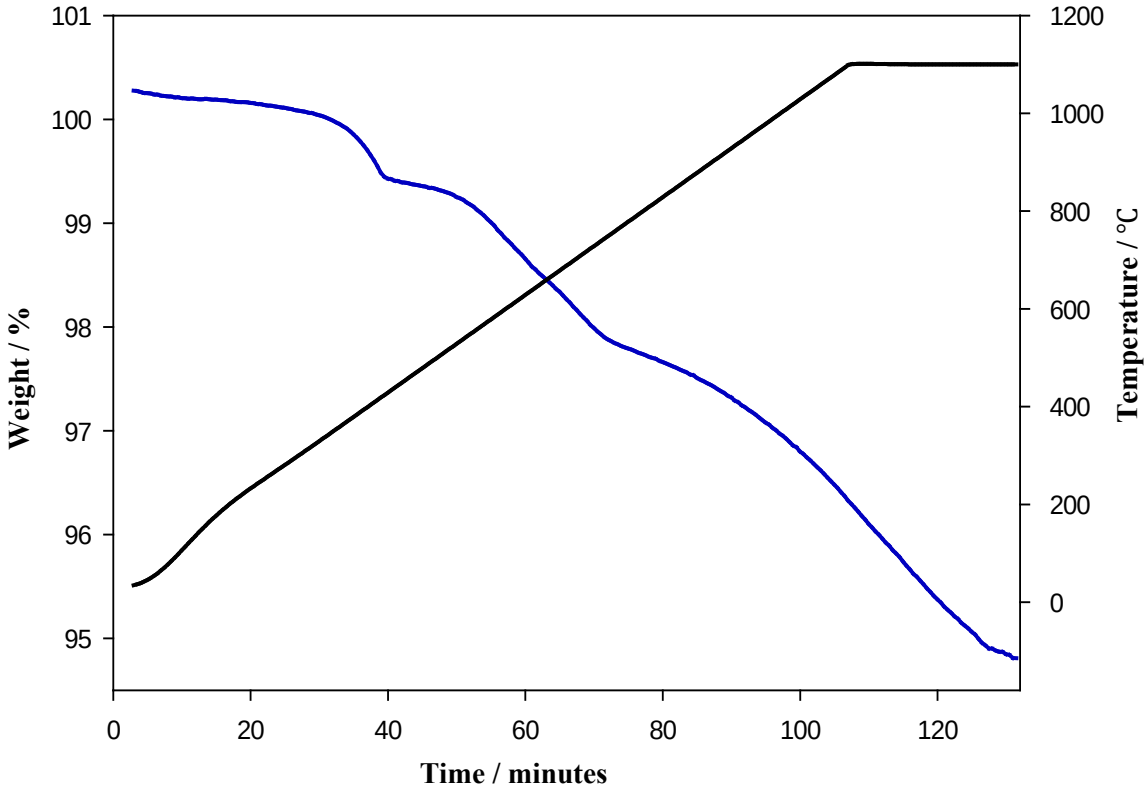

Figure 5.19 TGA trace illustrating the decomposition of fluorinated $Eu_2SrFe_2O_7$, weight loss shown in blue and temperature in black.

In order to confirm whether $EuFeO_3$ is formed during the reduction, calculations were carried out in two different ways: i) considering $EuFeO_3$ to be a reduced product, ii) considering only Eu_2O_3, SrF_2 and Fe metal to be decomposed products. Both routes suggested a composition of $Eu_2SrFe_2O_7F_2$ for the oxide-fluoride, see *Appendix 5.5*. The weight loss obtained from the first route (6.1%) agrees well with the observed weight loss. The weight loss calculated from the second route (9.8%) is large, but since the decomposition has not reached a plateau as shown in *Figure 5.19*, it is possible to assume that $EuFeO_3$ is not a reduced product. However, it is clear that the composition for the fluorinated phase is $Eu_2SrFe_2O_7F_2$.

5.5.2 Structural Characterisation of Fluorinated $Eu_2SrFe_2O_7$

The structure of the fluorinated phase was investigated using XRPD data in the tetragonal space group *I*4/*mmm*. Interstitial sites were modelled as occupied by F^- anions. The thermal parameters for the anion sites were also constrained to be equivalent. The fractional occupancy of the interstitial anion site was close to full occupancy. Hence, the occupancy of this site was fixed in the final refinement. The Eu^{3+} and Sr^{2+} cations distribute between the two *A* sites in fully ordered manner as in $Eu_2SrFe_2O_7$. In order to improve the refinement $EuFeO_3$ was included as a secondary phase (7.1(2)% by weight). The refinement profiles are shown in *Figure 5.20* and the refined parameters are listed in *Table 5.6*. The observed expansion along *c* axis (~4.02%) is very small compared to that observed in other fluorinated phases.

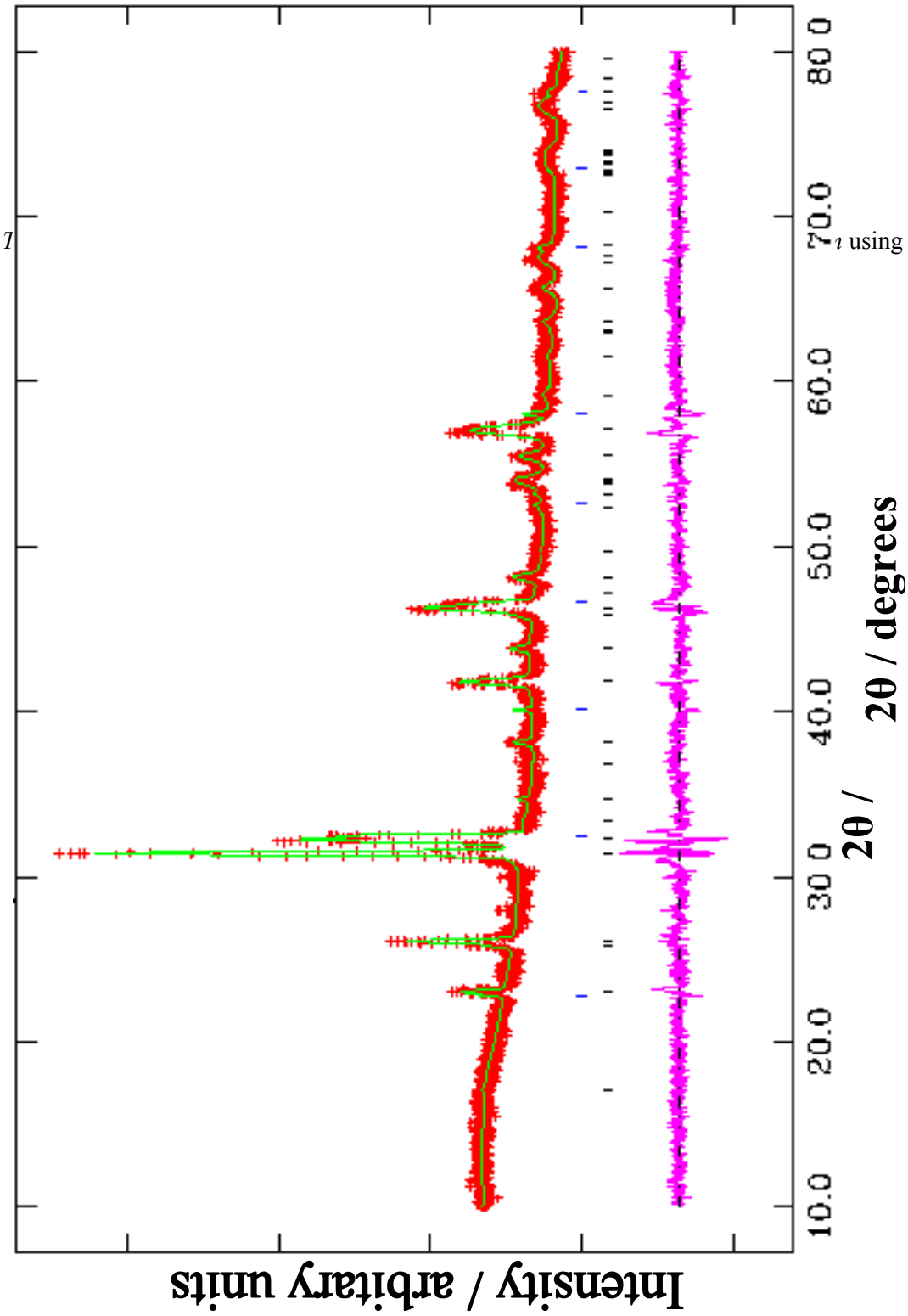

Figure 5.20 Observed (red +), calculated (green) and difference (pink) profiles of fluorinated $Eu_2SrFe_2O_7$, as generated by the Rietveld refinement of XRPD data, where phase 1 = fluorinated $Eu_2SrFe_2O_7$ (black vertical lines), phase 2 = $EuFeO_3$ (7.1(2)% by weight, blue vertical lines).

Atom	Site symmetry	*x*	*y*	*z*	Occupancy	$U_{iso} \times 100$ / Å^2
Eu(1)	4e	0	0	0.3179(3)	1	1.1(2)
Sr(1)	2b	0	0	0.5	1	1.1(2)
Fe	4e	0	0	0.0911(6)	1	0.3(4)
O(1)	2a	0	0	0	1	9.8(7)
O(2)	8g	0	0.5	0.099(3)	1	9.8(7)
O(3)	4e	0	0	0.816(3)	1	9.8(7)
F(4)	4d	0.5	0	0.25	1*	9.8(7)

a = 3.9090(7) Å, *c* = 20.630(5) Å
χ^2 = 2.842, R_{wp} = 3.26% * denotes fractional occupancy fixed

5.5.3 Magnetic Characterisation of Fluorinated $Eu_2SrFe_2O_7$

The variation of both field-cooled and zero-field-cooled magnetic susceptibilities with temperature is shown in *Figure 5.21a.* Also illustrates the variation of inverse susceptibility with temperature in *Figure 5.21b.* The measurements were carried out in an applied magnetic field of 1000 Oe. As observed in previous fluorinated phases, both field-cooled (fc) and zero-field-cooled (zfc) susceptibilities increase on cooling and the two datasets begin to diverge below 115 K which indicates the presence of some order above this temperature. The plot of inverse susceptibility versus temperature is nonlinear below 130 K and so Curie-Weiss paramagnetic moment was calculated using only the high temperature range. The estimated effective moment, μ_{eff} = 11.0 μ_B is higher than the calculated magnetic moment (8.3 μ_B, considering high spin electron configuration for Fe^{4+}). This could be due to the presence of the impurity phase $EuFeO_3$.

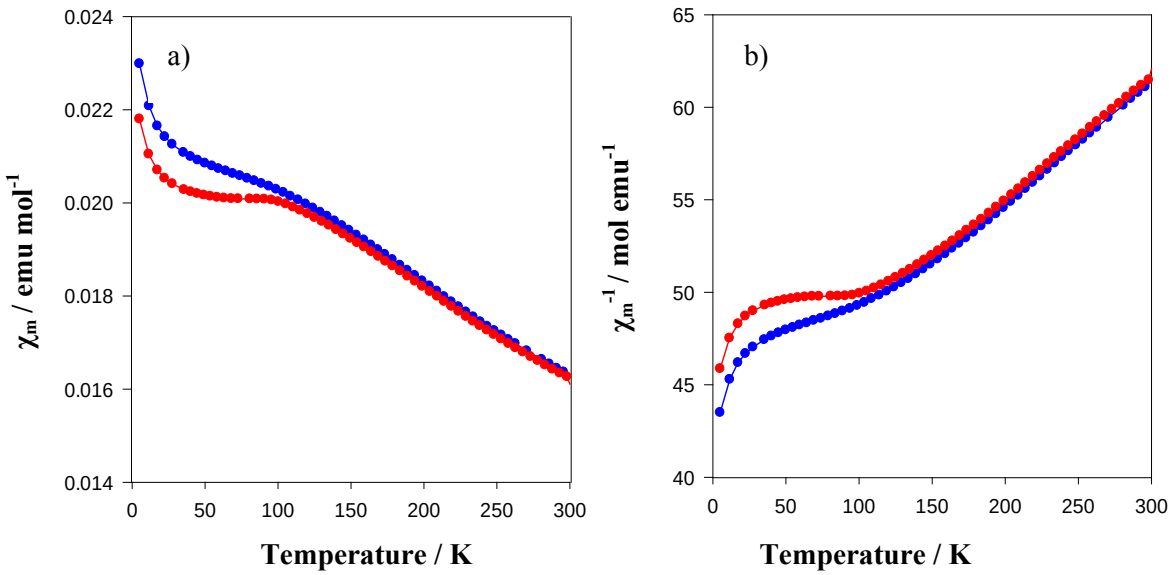

Figure 5.21 a) Variation of magnetic susceptibility with temperature and b) Variation of inverse susceptibility with temperature for fluorinated $Eu_2SrFe_2O_7$, field-cooled and zero-field-cooled data shown in blue and red, respectively.

5.5.4 Discussion of Fluorinated $Eu_2SrFe_2O_7$

The composition $Eu_2SrFe_2O_7F_2$ obtained from TGA suggests that the fluorination reaction happens through oxidative anion insertion oxidising the metal oxide lattice. The F^- anions occupy the interstitial sites as indicated by structure refinement, see *Figure 5.22*. Bond valence sum (BVS) calculations carried out for the Fe-O bonds using r_o for Fe(III)[14] gave a value of 3.6 for Fe coordination which is consistent with Fe^{4+}, calculations are given in *Appendix 5.6*. Also the Fe-O bond lengths obtained for the oxide-fluoride phase (Fe-O1 = 1.88(1) Å, Fe-O2 = 1.964(4) Å [×4], Fe-O3 = 1.93(6) Å) are quite similar to the Fe-O bond distances in the precursor oxide. The Fe-O bond distances in $Eu_2SrFe_2O_7$ are Fe-O1 = 1.950(6) Å, Fe-O2 = 1.947 (2) Å [×4], Fe-O3 = 2.10(2) Å. It should be also noted that the

thermal parameters obtained for the anions from XRPD refinement are rather large. So it is not possible to accurately determine the oxidation state of Fe due to the uncertainty in determining anion positions using XRPD data. Further studies using Mössbauer spectroscopy are now under way to confirm the oxidation state of Fe and the magnetic properties of the fluorinated phase since neutron powder diffraction cannot be used for the analysis as Eu highly absorbs neutrons.

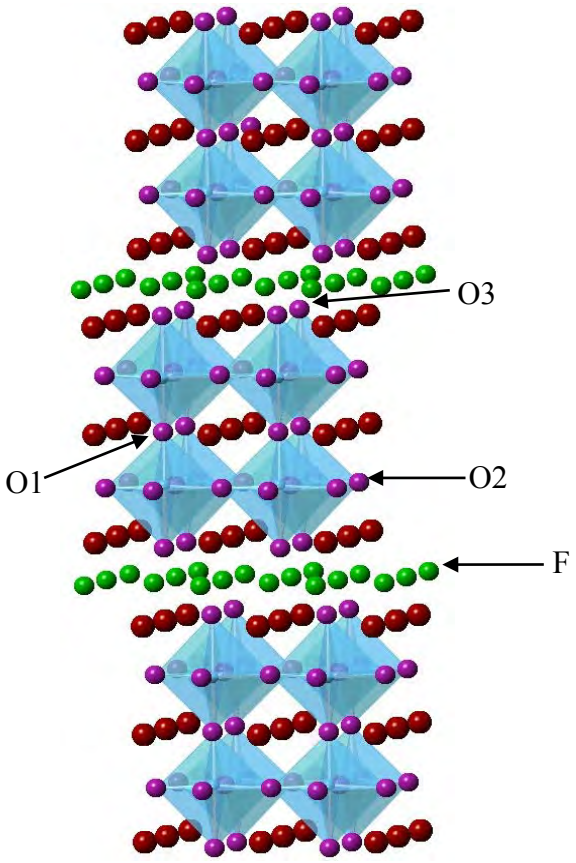

Figure 5.22 The structure of $Eu_2SrFe_2O_7F_2$, with *A* (Eu / Sr) cations shown in red, O^{2-} anions shown in purple, interstitial F^- anions in green and FeO_6 octahedra shown in blue.

5.6 Conclusion

The structures of all fluorinated phases, $La_2BaFe_2O_5F_4$, $Nd_2SrFe_2O_5F_4$, $La_2SrFe_2O_5F_4$, and $Eu_2SrFe_2O_7F_2$ have been determined using X-ray powder diffraction and thermogravimetric analysis. In the first three compounds fluorination happens through anion substitution and anion insertion, surprisingly without oxidising the metal oxide lattice which is confirmed for $La_2BaFe_2O_5F_4$ by Mössbauer spectroscopy. The fluorine content in the latter compound is lower than that in the other phases and the fluorination happens *via* oxidising the metal oxide lattice. The oxides of the first three compounds exhibit partial cation ordering at the *A* site while the oxide of the latter compound is fully ordered. Further, among these phases $Eu_2SrFe_2O_7F_2$ got the smallest overall size for the *A* site cations. Thus, the high fluorine content in fluorinated $La_2BaFe_2O_7$, $Nd_2SrFe_2O_7$ and $La_2SrFe_2O_7$ could be due to the overall size of the *A* site cations or partial cation ordering at the *A* site. However, detailed structural and magnetic properties of these fluorinated phases need to be investigated using NPD data and Mössbauer spectroscopy.

5.7 References

1. Greaves, C.; Kissick, J. L.; Francesconi, M. G.; Aikens, L. D.; Gillie, L. J. *J. Mater. Chem*. **1999**, 9, 97.
2. Hadermann, J.; Abakumov, A. M.; Lebedev, O. I.; van Tenderloo, G.; Rozova, M. G.; Shpanchenko, R. V.; Pavljuk, B. P.; Kopnin, E. M.; Antipov, E. V. *J. Solid State Chem.* **1999**, 147, 647.
3. Corbel, G.; Attfield, J. P.; Hadermann, J.; Abakumov, A. M.; Aleskseeva, A. M.; Rozova, M. G.; Antipov, E. V. *Chem. Mater*. **2003**, 15, 189.
4. Chevalier, B.; Tressaud, A.; Lepine, B.; Amine, K.; Dance, J. M.; Lozano, L.; Hickey, E.; Etourneau, J. *Phys*. C **1990**, 167, 97.
5. Al-Mamouri, M.; Edwards, P. P.; Greaves, C.; Slaski, M. *Nature* **1994**, 364, 382.
6. Francesconi, M. G.; Greaves, C. *Supercond. Sci. Technol.* **1997**, 10, A29.
7. Greaves, C.; Francesconi, M. G. *Curr. Opin. Solid State Mater. Sci.* **1998**, 3, 132.
8. Li, R. K.; Greaves, C. *Phys*. *Rev*. *B* **2000**, 62, 3811.
9. Aikens, L. D.; Greaves, C. *Chem. Commun.* **2000**, 2129.
10. Aikens, L. D.; Gillie, L. J.; Li, R. K.; Greaves, C. *J. Mater. Chem*. **2002**, 12, 264.
11. Kawano, S.; Achiwa, N.; Kamegashira, N.; Aoki, A. *J. Phys*. *IV* **1988**, C8, 829.
12. Argyriou, D. N.; Mitchell, J. F.; Radaelli, P. G.; Bordallo, H. N.; Cox, D. E.; Medarde, M.; Jorgenson, J. D. *Phys*. *Rev*. *B* **1999**, 59, 8695.
13. McCabe, E. E.; Greaves, C. *J*. *Fluor*. *Chem*. **2007**, 128, 448.
14. Brown, I. D.; Altermatt, D. *Acta Cryst*. **1985**, B41, 244.

CHAPTER SIX

Insertion of Oxy-anions into Perovskite Structures: $SrFeO_{3-\delta}$ and $CaMnO_{3-\delta}$

6.1 Background

Although few perovskite oxides have the ideal cubic perovskite structure described in Chapter 1, many of these materials have slightly distorted structures with lower symmetry (e.g. hexagonal or orthorhombic). Many perovskite oxides also display large cation and / or oxygen deficiencies.[1] These materials exhibit a large variety of properties such as high catalytic activity, good electronic and ionic conductivity as well as mixed ionic and electronic conductivity because of the diversity in structures and chemical composition. Based on these electronic properties, perovskite oxides have been widely used for the cathodes of SOFCs.[2, 3, 4]

Fuel cell technology is a promising method to convert chemical energy of hydrocarbon fuels into electricity without generating air pollutants. Among the many types of fuel cells solid oxide fuel cells are the most efficient and have several advantages such as flexibility in fuel and high reliability. The application of many perovskite oxides particularly, Co- and Mn- containing perovskites have been extensively studied from the beginning of SOFC development.[5]

The structure and the electronic properties of perovskites can be changed by atomic substitution in addition to phase transformations that result from temperature and pressure change.[1] Cation substitution is the most common type of substitution. But anion (F^-, Cl^-

etc) and oxy-anion (PO_4^{3-}, SO_4^{2-}, CO_3^{2-} etc) substitution mechanism can also be used to modify the structural and electronic properties of perovskites.[1, 6-9, 24-28] Previous work carried out on oxy-anion substitution into perovskite-type cuprate superconductors and related phases have proved the ability to synthesise new materials with modified electronic and structural features.[6–23] Recently, oxy-anion incorporation has been employed to modify the structural and electronic properties of perovskite systems with potential applications in SOFCs.[24-28]

At room temperature $Ba_2In_2O_5$ adopts an orthorhombic brownmillerite-type structure consisting of ordered ion vacancies with alternating layers of InO_6 octahedra and InO_4 tetrahedra. Incorporation of phosphate and sulphate has led to a transition in the crystal structure from an orthorhombic brownmillerite to a cubic perovskite. The higher symmetry with increased oxygen vacancy disorder has resulted in an increase in the ionic conductivity below 800 °C.[24, 25]

This behaviour was also observed in oxy-anion doped $SrCoO_3$ phases. Insertion of phosphate and sulphate anions into $SrCoO_3$ has also led to a change in the crystal structure from a 2*H*-perovskite to a 3*C*-perovskite. The oxy-anion doped phases exhibited higher conductivity compared to that of parent material. But further investigation on these doped samples has revealed that the phases are metastable, transforming back to the hexagonal structure on annealing at intermediate temperatures.[26]

Further, Porras-Vazquez *et al.*[27] recently reported the successful incorporation of borate and phosphate anions into $CaMnO_{3-\delta}$ and borate anions into $La_{1-y}Sr_yMnO_{3-\delta}$ (y = 0.3, 0.4 and 0.5). Incorporation of oxy-anions has been achieved up to 5% for all compounds with no change in cell symmetry on doping, but at higher doping levels secondary phases have

been observed. The cell volumes of all borate doped $La_{1-y}Sr_yMnO_{3-\delta}$ phases were slightly larger than those of the parent compounds due to the small level of Mn^{4+} present in borate doped phases as indicated by the TGA data. The expanded cell volumes observed in phosphate doped $CaMnO_{3-\delta}$ phases is consistent with the greater reduction of Mn^{4+} indicated by the TGA. But the cell volumes obtained for borate doped $CaMnO_{3-\delta}$ phases were smaller than that of $CaMnO_{3-\delta}$ due to the lower reduction of Mn^{4+} and the small size of boron ion. The electronic conductivity of $La_{1-y}Sr_yCaMnO_{3-\delta}$ decreased upon inserting borate anions, but phosphate and borate doped $CaMnO_{3-\delta}$ phases have exhibited enhanced conductivity. The conductivity of borate doped $CaMnO_{3-\delta}$ phases changed slightly with the dopant level whereas in phosphate doped phases the conductivity changed significantly with the dopant level.[27]

This work shows the ability of modifying the structural features of $CaMnO_{3-\delta}$ through oxy-anion insertion. So it is important to find out the maximum level of phosphate anions that can be incorporated into the structure and the possibility of inserting other oxy-anions such as sulphate into the structure. This chapter describes the synthesis and the characterisation of $CaMnO_{3-\delta}$ phases with higher levels of phosphate and sulphate doped $CaMnO_{3-\delta}$ phases. As described at the beginning of this chapter, oxy-anions have only been inserted into Co- and Mn- containing perovskite oxides and in this work the potential of inserting phosphate and sulphate anions into $SrFeO_{3-\delta}$ has also been investigated.

6.2 Insertion of Phosphate into $SrFeO_{3-\delta}$

Polycrystalline samples of $SrFeO_{3-\delta}$ and $SrFe_{1-x}P_xO_{3-\delta}$ ($0.02 \leq x \leq 0.15$) were synthesised by reacting the stoichiometric quantities of high purity Fe_2O_3, $SrCO_3$ and $(NH_4)H_2PO_4$ (Aldrich, >99%). Reactants were initially ground together and heated at 1200 ℃ for 36 hrs in air with intermittent grinding. All these phases were initially characterised using X-ray powder diffraction.

6.2.1 Structural Characterisation

X-ray powder diffraction data confirmed the successful synthesis of single phase samples of $SrFeO_{3-\delta}$ and $SrFe_{1-x}P_xO_{3-\delta}$ in the range $0.02 \leq x < 0.15$. All phosphate doped phases were cubic. The XRPD patterns of $SrFeO_{3-\delta}$ and phosphate doped phases are shown in *Figures 6.1* and *6.2*.

At higher phosphate levels (x = 0.15, 0.18) a secondary phase $Sr_9Fe(PO_4)_7$ was formed (*Figure 6.1*). Insertion of phosphate at each level was confirmed by the corresponding Fe deficient samples $SrFe_{1-x}O_{3-\delta}$ ($0.02 \leq x \leq 0.15$). X-ray powder diffraction patterns of these samples indicated the presence of two phases; $SrFeO_{3-\delta}$ and $Sr_3Fe_2O_{6.9}$ due to the Fe deficiency in the structure (*Figure 6.1*). This in return showed that the phosphate anion insertion stabilises the $SrFe_{1-x}O_{3-\delta}$ structure. Rietveld refinement was performed on XRPD data to obtain the cell parameters. The unit cell *a* parameter increased with the increase of phosphate level as illustrated in *Figure 6.3*. The cell parameters are listed in *Table 6.3*.

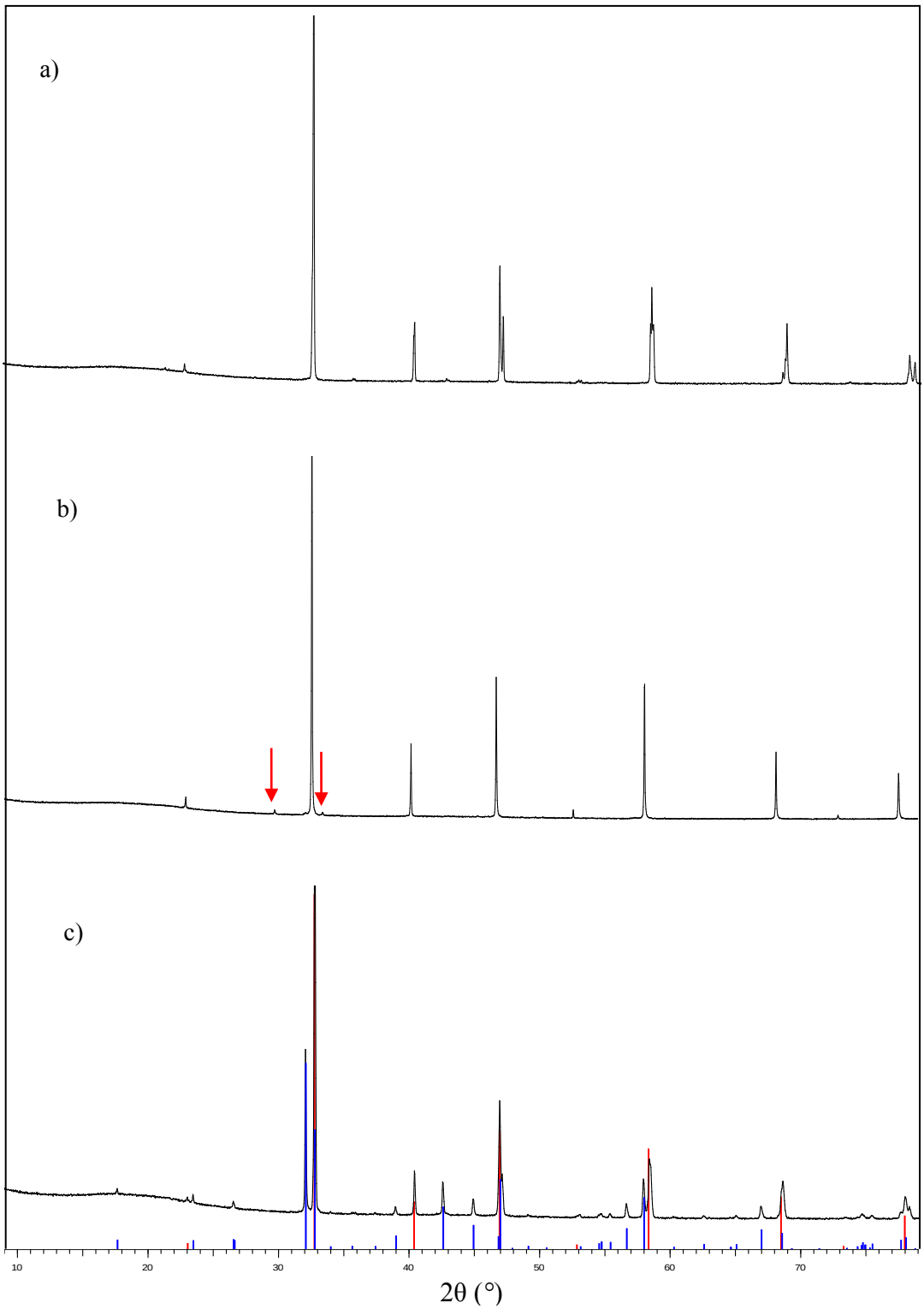

Figure 6.1 X-ray diffraction patterns of a) $SrFeO_{3-\delta}$ b) $SrFe_{0.82}P_{0.18}O_{3-\delta}$, impurity ($Sr_9Fe(PO_4)_7$) peaks highlighted with red arrows c) $SrFe_{0.85}O_{3-\delta}$ showing $SrFeO_{3-\delta}$ (red lines) and $Sr_3Fe_2O_{6.9}$ (blue lines).

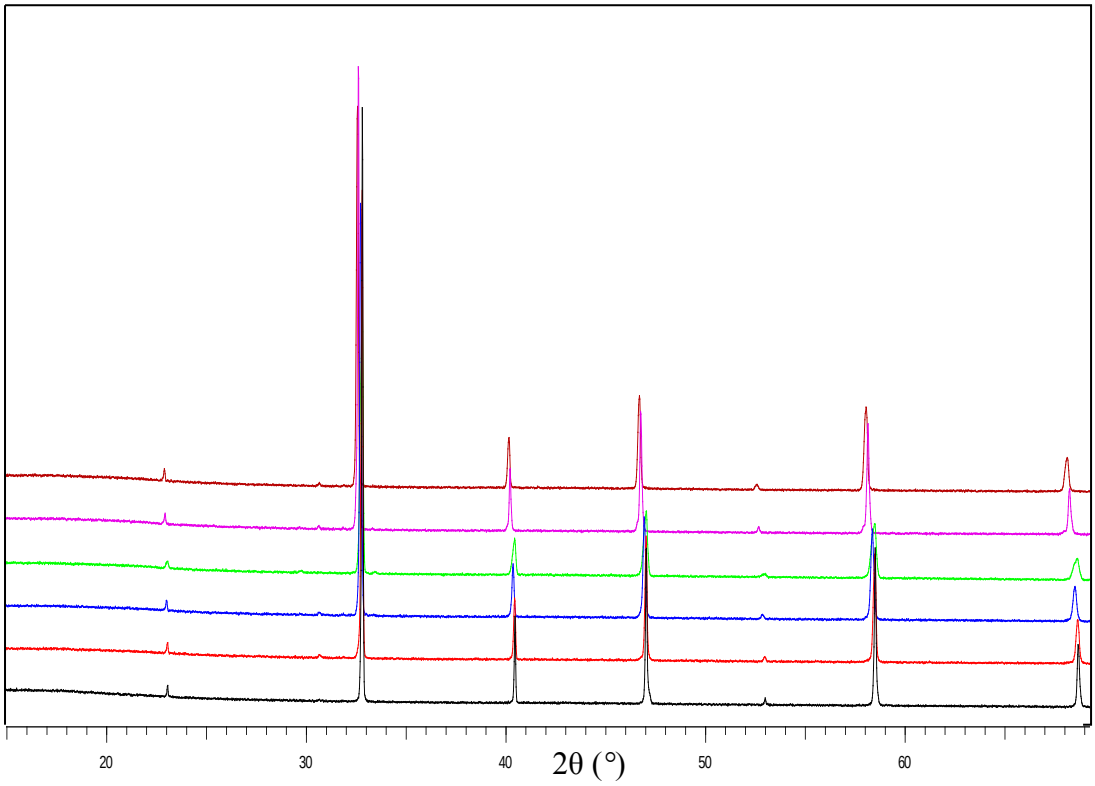

Figure 6.2 XRPD patterns of $SrFe_{1-x}P_xO_{3-\delta}$ phases, $x = 0.02$ (black), $x = 0.04$ (red), $x = 0.06$ (blue), $x = 0.08$ (green), $x = 0.10$ (purple), $x = 0.12$ (brown).

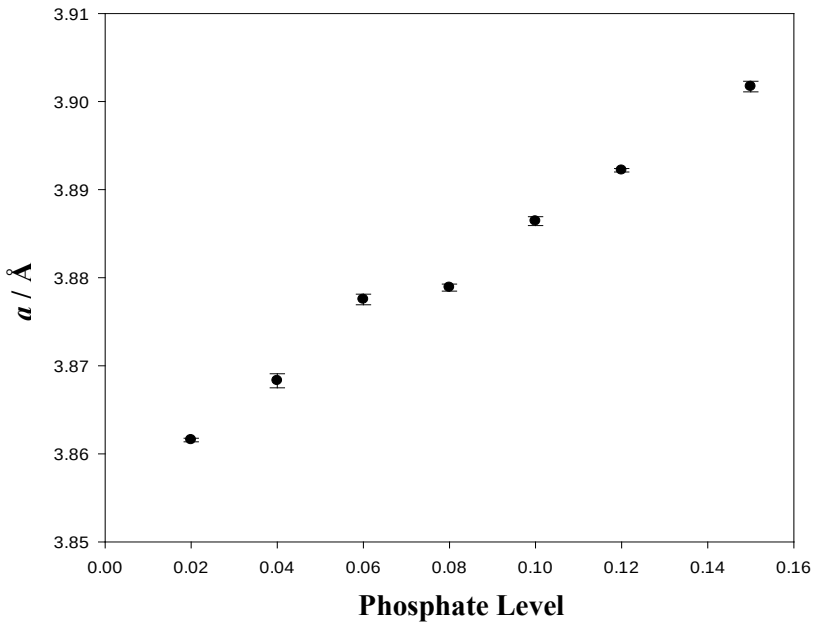

Figure 6.3 Variation of *a* parameter with phosphate level in $SrFe_{1-x}P_xO_{3-\delta}$ phases.

6.2.1.1 Oxygen content and Oxidation state of Fe in $SrFe_{1-x}P_xO_{3-\delta}$ Phases

Mössbauer spectroscopy recorded on some of these samples suggested that similar amount of Fe^{3+} and Fe^{4+} is present in phosphate doped phases, listed in *Table 6.1*. These data were confirmed by thermogravimetric analysis. Both $SrFeO_{3-\delta}$ and $SrFe_{1-x}P_xO_{3-\delta}$ phases were heated in flowing 10% H_2(g) / 90% N_2(g) to 650 ℃ and maintained at this temperature.

Table 6.1 ^{57}Fe Mössbauer parameters recorded from phosphate doped phases.

Compound		**$\delta \pm 0.05$ / mms^{-1}**	**$e^2Qq/2 \pm 0.1$ / mms^{-1}**	**Area $\pm$ 5 %**
$SrFeO_{3-\delta}$	Fe^{4+}	0.04	0.12	28
	Fe^{3+}	0.35	1.26	29
	$Fe^{4+} \leftrightarrow Fe^{3+}$	0.14	0.69	43
$SrFe_{0.98}P_{0.02}O_{3-\delta}$	Fe^{4+}	0.09	0.64	53
	Fe^{3+}	0.41	0.73	47
$SrFe_{0.96}P_{0.04}O_{3-\delta}$	Fe^{4+}	0.04	0.61	50
	Fe^{3+}	0.29	0.62	50
$SrFe_{0.9}P_{0.1}O_{3-\delta}$	Fe^{4+}	0.14	0.62	67
	Fe^{3+}	0.43	0.69	33
$SrFe_{0.85}P_{0.15}O_{3-\delta}$	Fe^{4+}	0.12	0.86	50
	Fe^{3+}	0.47	0.91	50

XRPD analysis of the resulting materials revealed that $SrFeO_{3-\delta}$ and $SrFe_{1-x}P_xO_{3-\delta}$ (x = 0.02, 0.04) decomposed to $Sr_2Fe_2O_5$ and phosphate substituted analogues (*Figure 6.4*). The

Rietveld refinement of XRPD data and the Mössbauer spectrum recorded on the reduced sample of $SrFeO_{3-\delta}$ are consistent with the structural data reported for $Sr_2Fe_2O_5$ in the literature.[29, 30] The Mössbauer spectrum recorded on the reduced sample of $SrFeO_{3-\delta}$ is shown in *Figure 6.5* and the Mössbauer parameters are listed in *Table 6.2*. The spectrum was fitted to two sextets with isomer shifts characteristic of Fe^{3+}.

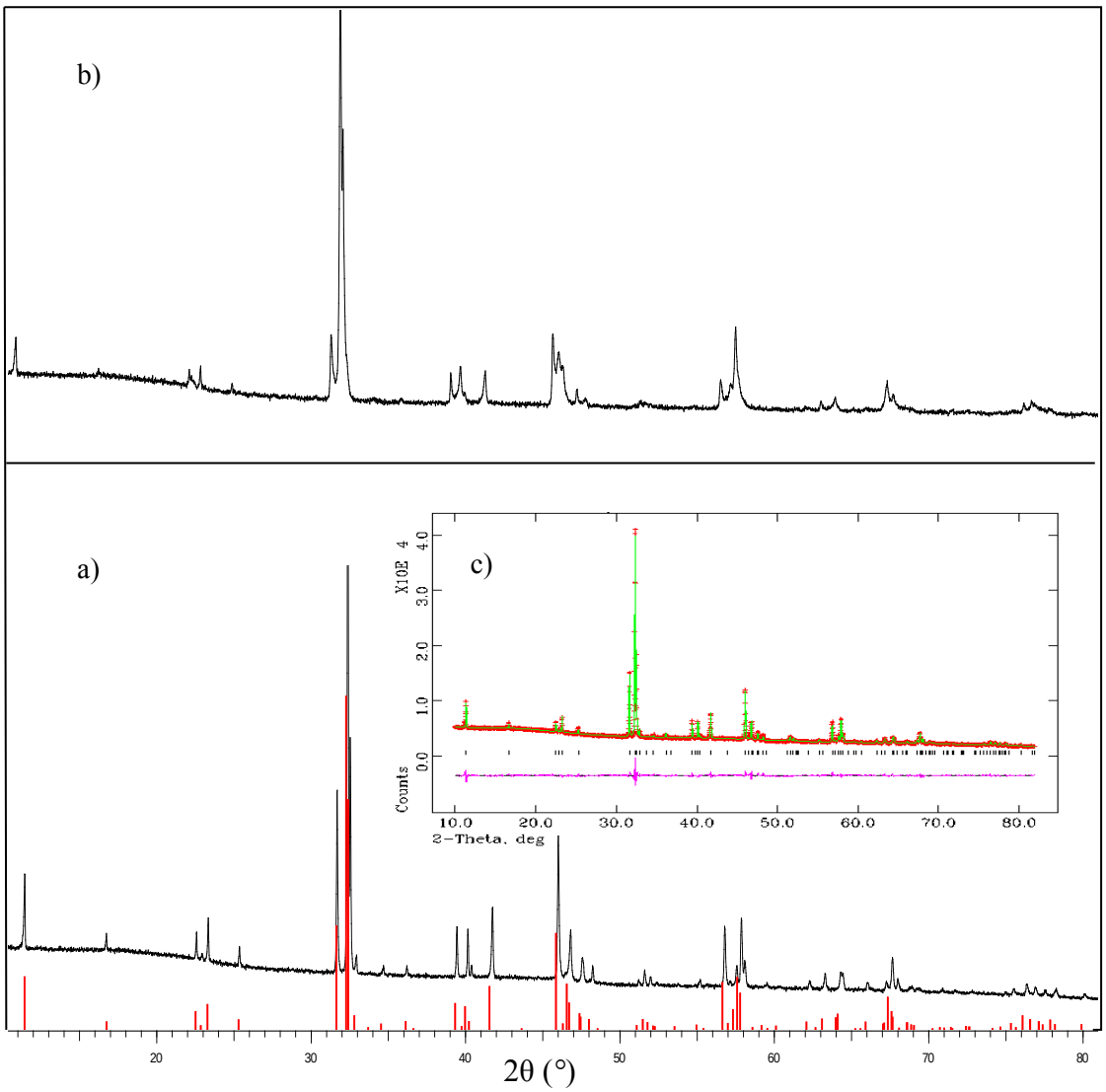

Figure 6.4 XRPD patterns of reduced a) $SrFeO_{3-\delta}$ ($Sr_2Fe_2O_5$ in red lines) b) $SrFe_{0.98}P_{0.02}O_{3-\delta}$ c) observed (+), calculated (-) and difference (-) profiles of reduced $SrFeO_{3-\delta}$ from the refinement of XRPD data, $\chi^2 = 3.369$, $R_{wp} = 0.03$, the reflection positions of main phase $Sr_2Fe_2O_5$ are marked with black vertical lines.

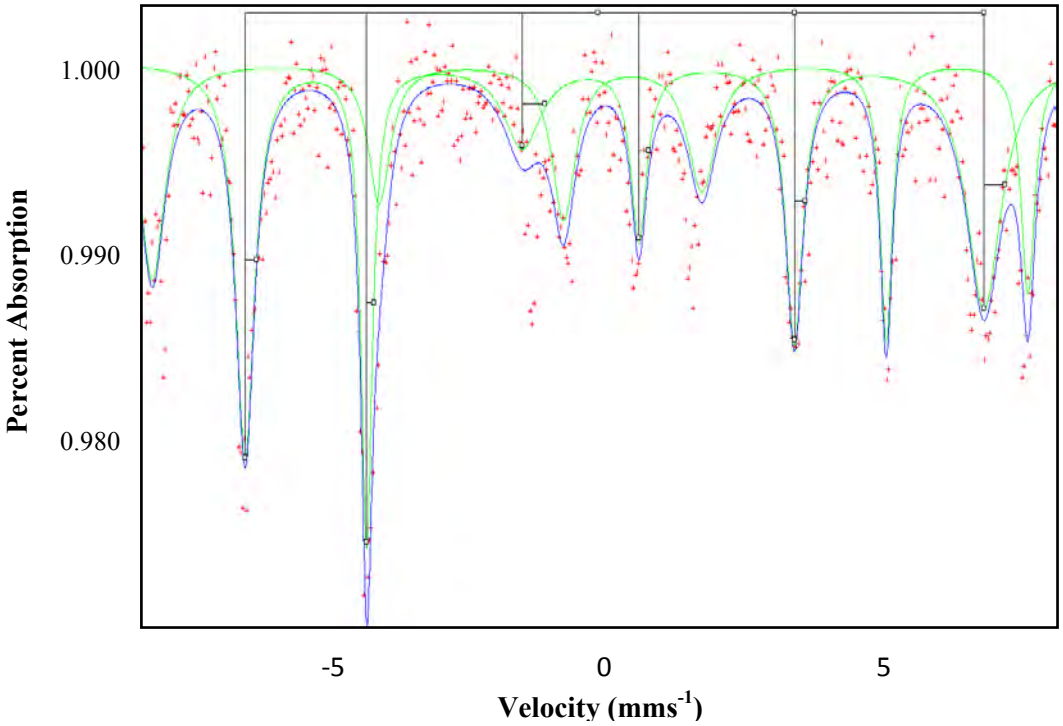

Figure 6.5 Mössbauer spectrum of reduced $SrFeO_{3-\delta}$ sample, identified as $Sr_2Fe_2O_5$.

Table 6.2 ^{57}Fe Mössbauer parameters recorded from the reduced $SrFeO_{3-\delta}$.

Component	$\delta \pm 0.02$ mms^{-1}	$e^2Qq/2 \pm 0.05$ mms^{-1}	H ± 5 T	Area ± 5 %
Sextet 1	0.14	0.31	42.5	58.72
Sextet 2	0.39	-0.39	49.2	41.28

The reduced samples of the higher phosphate doped phases ($0.06 \leq x \leq 0.15$) were all cubic (*Figure 6.6*) and the cell parameters were determined from the XRPD data. The variation of *a* parameter of the reduced phases with the phosphate level is shown in *Figure 6.7*. An expansion in the cell volume is observed in reduced phases due to the reduction of

Fe^{4+} to Fe^{3+} (*Table 6.3*). The oxygen contents in the phosphate doped phases were calculated using the weight loss obtained from TGA considering only Fe^{3+} to be present in the reduced samples. The data are given in *Table 6.4*.

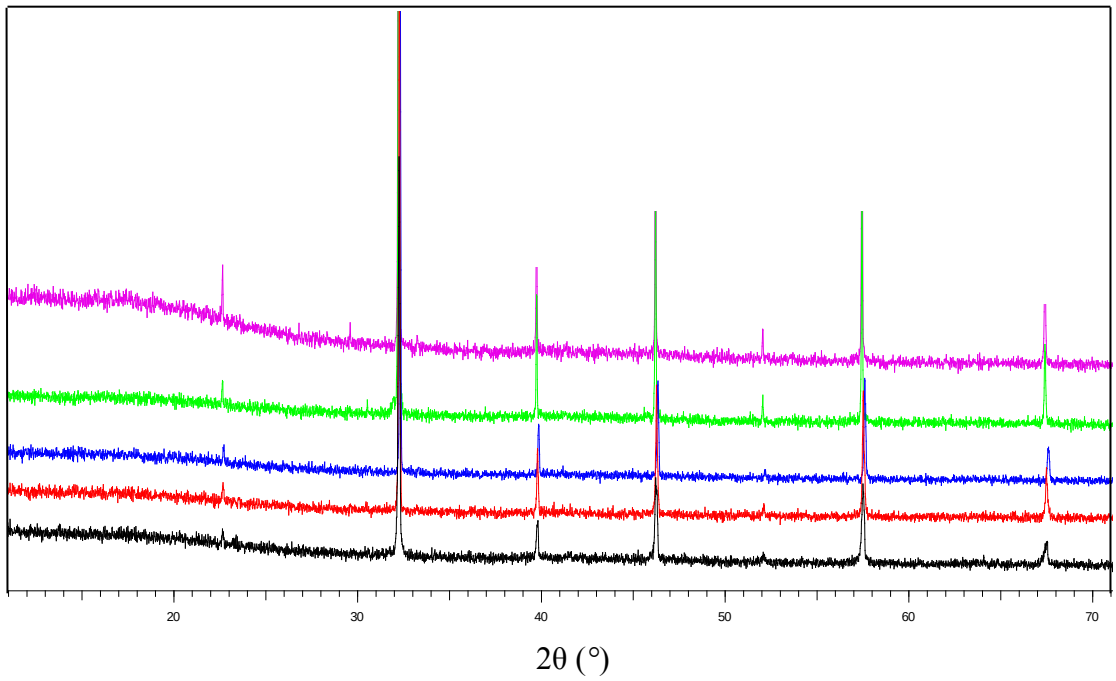

Figure 6.6 XRPD patterns of reduced $SrFe_{1-x}P_xO_{3-\delta}$ phases, $x = 0.06$ (black), $x = 0.08$ (red), $x = 0.10$ (blue), $x = 0.12$ (green) and $x = 0.15$ (purple).

Table 6.3 Cell parameters of $SrFe_{1-x}P_xO_{3-\delta}$ phases before and after the TGA.

Phosphate Level	**0.06**	**0.08**	**0.10**	**0.12**	**0.15**
***a* / Å Original**	3.87753(6)	3.87888(4)	3.88642(5)	3.89220(2)	3.90171(6)
***a* / Å Reduced**	3.91647(8)	3.91761(1)	3.91874(7)	3.92003(3)	3.92128(6)

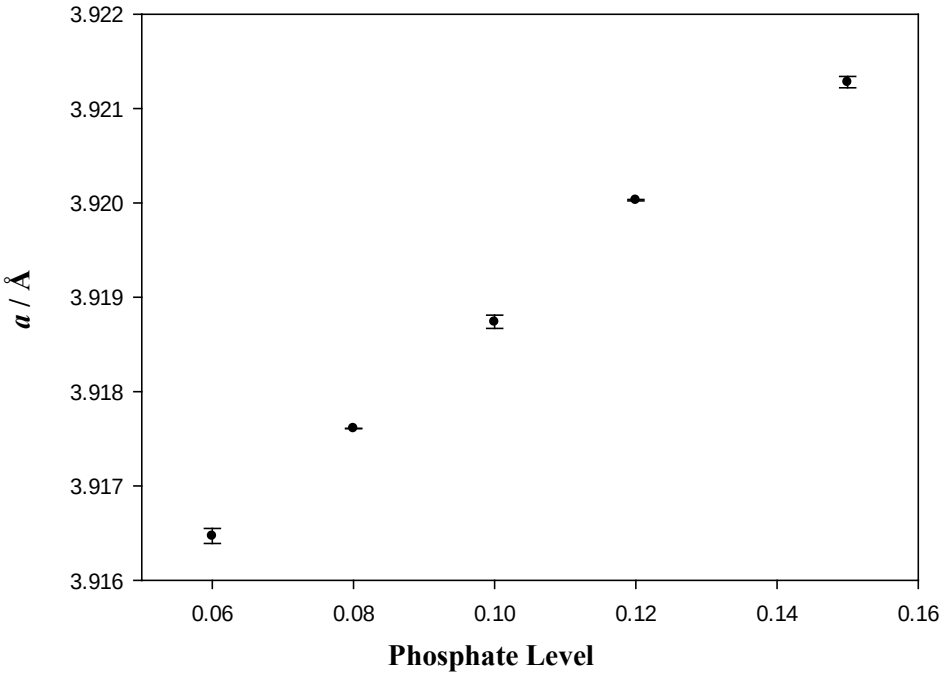

Figure 6.7 Variation of *a* parameter of reduced $SrFe_{1-x}P_xO_{3-\delta}$ phases with the phosphate level.

The percentages of Fe^{3+} and Fe^{4+} calculated from TGA are in good agreement with the Mössbauer data. Mössbauer spectroscopy suggested that nearly equal amounts of Fe^{3+} and Fe^{4+} are present in all phosphate doped phases. According to the TGA results, about 40% of Fe^{3+} and 60% of Fe^{4+} are present in lower phosphate doped phases while at higher levels around 60% of Fe^{3+} and 40% of Fe^{4+} are present. The greater reduction of Fe^{4+} in higher phosphate doped phases as indicated by TGA is responsible for the increase observed in unit cell volumes of these phases.

Table 6.4 Oxygen content and oxidation state of Fe in $SrFe_{1-x}P_xO_{3-\delta}$ phases from TGA.

Phosphate level	Oxygen content	Fe Oxidation state		
		Fe^{n+}	Fe^{3+}	Fe^{4+}
0.00	2.79	3.58	42	58
0.02	2.85	3.67	33	67
0.04	2.88	3.71	29	71
0.06	2.84	3.60	40	60
0.08	2.86	3.60	40	60
0.10	2.81	3.47	53	47
0.12	2.80	3.40	60	40
0.15	2.83	3.42	58	42

6.3 Insertion of Sulphate into $SrFeO_{3-\delta}$

Insertion of sulphate anions ($0.02 \leq x \leq 0.08$) into $SrFeO_{3-\delta}$ was carried out by reacting the stoichiometric quantities of high purity Fe_2O_3, $SrCO_3$ and $(NH_4)_2SO_4$ (Aldrich, >99%) at 1200 ℃ for 36 hrs in air. The products $SrFe_{1-x}S_xO_{3-\delta}$ ($0.02 \leq x \leq 0.08$) were characterised using XRPD.

6.3.1 Structural Characterisation

According to XRPD data, all sulphate doped phases in the range $0.02 \leq x \leq 0.08$ were cubic as shown in *Figure 6.8*. At higher dopant levels an impurity phase $Sr_3Fe_2O_7$ was formed (*Figure 6.8*). As mentioned in the previous section, insertion of sulphate at each level was confirmed by corresponding Fe deficient samples $SrFe_{1-x}O_{3-\delta}$ ($0.02 \leq x \leq 0.08$). The unit cell parameters obtained from Rietveld refinement of XRPD data are given in *Table 6.5* and the variation of *a* parameter with the sulphate level is shown in *Figure 6.9*.

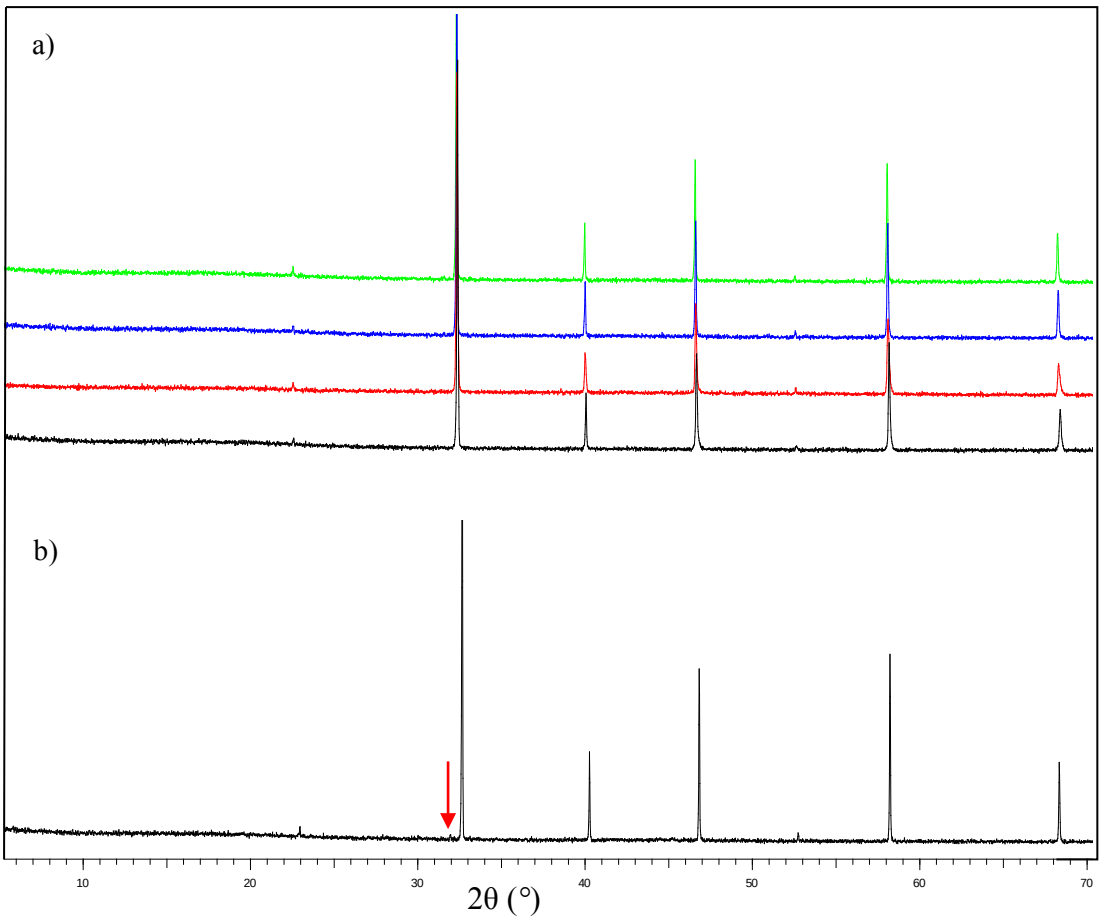

Figure 6.8 X-ray diffraction patterns of a) $SrFe_{1-x}S_xO_{3-\delta}$ phases, x = 0.02 (black), x = 0.04 (red), x = 0.06 (blue), x = 0.08 (green) b) $SrFe_{0.9}S_{0.1}O_{3-\delta}$ phase, impurity peak ($Sr_3Fe_2O_7$) shown with an arrow.

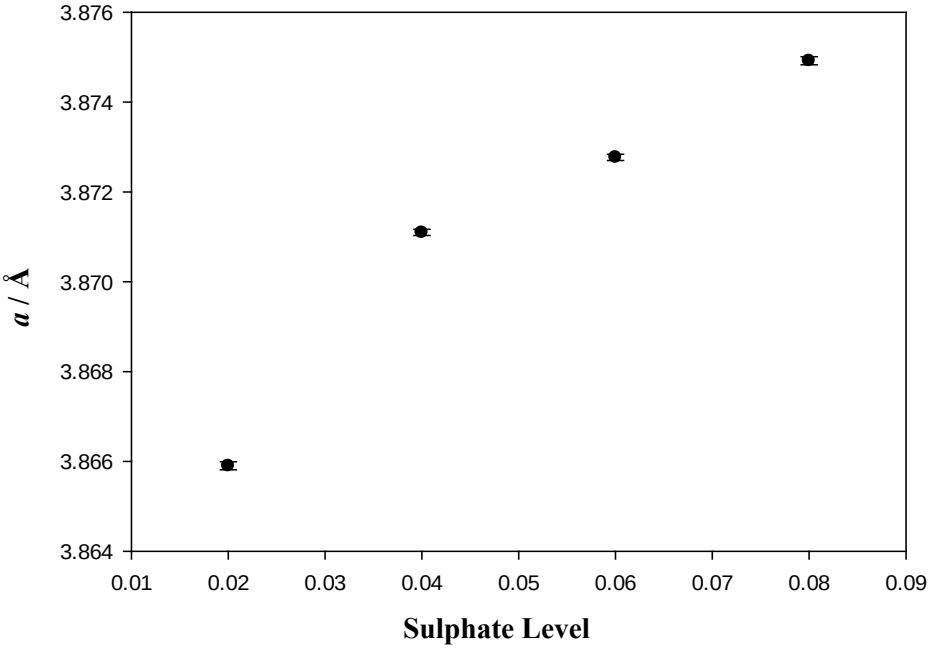

Figure 6.9 Variation of *a* parameter with the sulphate level in $SrFe_{1-x}S_xO_{3-\delta}$ phases.

Table 6.5 Cell parameters for $SrFe_{1-x}S_xO_{3-\delta}$ phases.

Sulphate Level	*a* / Å
0.02	3.86590(9)
0.04	3.87109(7)
0.06	3.87277(7)
0.08	3.87492(9)

Thermogravimetric analysis of $SrFeO_{3-\delta}$ and sulphate doped phases was carried out in 10% H_2(g) / 90% N_2(g) at 650 ℃. XRPD analysis of the final materials showed that all these compounds had been decomposed to sulphate containing analogues of $Sr_2Fe_2O_5$ (*Figure 6.10*). The oxygen content and the average oxidation state of Fe in these phases were

determined using the weight loss observed for each compound assuming only Fe^{3+} to be present in the reduced samples. The data are listed in *Table 6.6*.

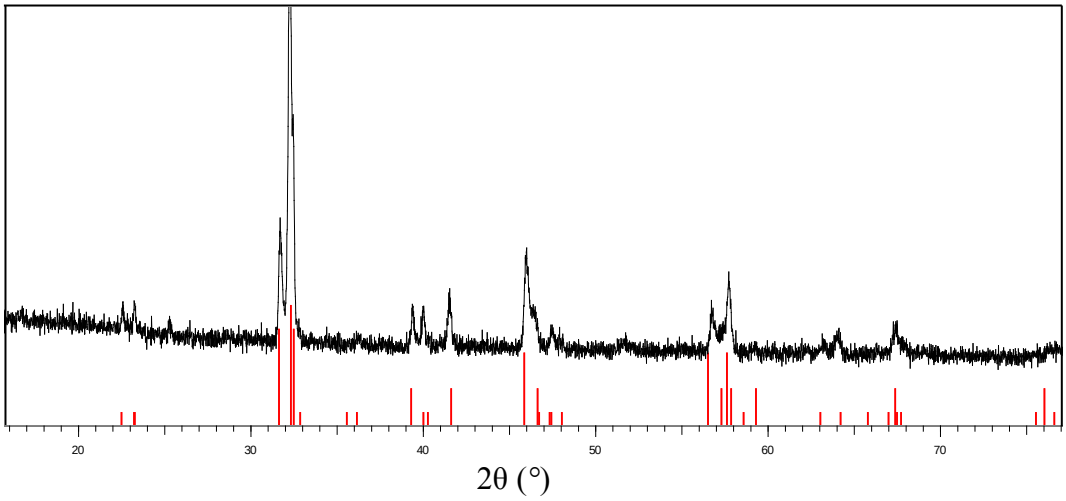

Figure 6.10 X-ray diffraction pattern of reduced $SrFe_{0.94}S_{0.06}O_{3-\delta}$ phase, identified as $Sr_2Fe_2O_5$ (red lines).

Table 6.6 Oxygen content and oxidation states of Fe in $SrFe_{1-x}S_xO_{3-\delta}$ phases.

Sulphate level	Oxygen content	Fe Oxidation state
0.02	2.93	3.82
0.04	2.94	3.79
0.06	2.97	3.80
0.08	3.00	3.83

According to the TGA results, the oxygen content increases slightly with the sulphate level and are much higher compare to those of phosphate doped phases. It can also be noted that the level of Fe^{3+} present in these phases is very low due to the smaller degree of reduction.

6.4 Insertion of Phosphate into $CaMnO_{3-\delta}$

Both $CaMnO_{3-\delta}$ and $CaMn_{1-x}P_xO_{3-\delta}$ ($0.02 \leq P \leq 0.15$) were synthesised by reacting the stoichiometric quantities of high purity Mn_2O_3, $CaCO_3$ and $(NH_4)H_2PO_4$ (Aldrich, >99%) at 1325 ℃ for 48 hrs in air with intermittent grinding. X-ray powder diffraction was used to confirm the successful synthesis of these phases.

6.4.1 Structural Characterisation

According to X-ray powder diffraction data, phosphate insertion was successful in the range $0.02 \leq x \leq 0.12$. No change in cell symmetry was observed at lower phosphate levels ($x < 0.08$) and those were all orthorhombic while all higher phosphate doped phases were cubic. The X-ray powder diffraction patterns of these phases are shown in *Figures 6.11* and *6.12*.

Higher dopant levels ($x = 0.15$) led to the formation of a secondary phase $Ca_3(PO_4)_2$. The corresponding Mn deficient samples $CaMn_{1-x}O_{3-\delta}$ ($0.02 \leq x \leq 0.15$) formed two phases; $CaMnO_{3-\delta}$ and $Ca_4Mn_3O_{10}$ (*Figure 6.11*) due to the Mn deficiency, which in return confirmed the incorporation of phosphate ions into $CaMnO_{3-\delta}$. Rietveld refinement was carried out on XRPD data to obtain the unit cell parameters listed in *Table 6.7*. The pseudo cubic lattice parameter was calculated for $CaMnO_{3-\delta}$ and lower phosphate doped phases as those phases were orthorhombic. The variation of *a* parameter with the phosphate level is plotted in *Figure 6.13*.

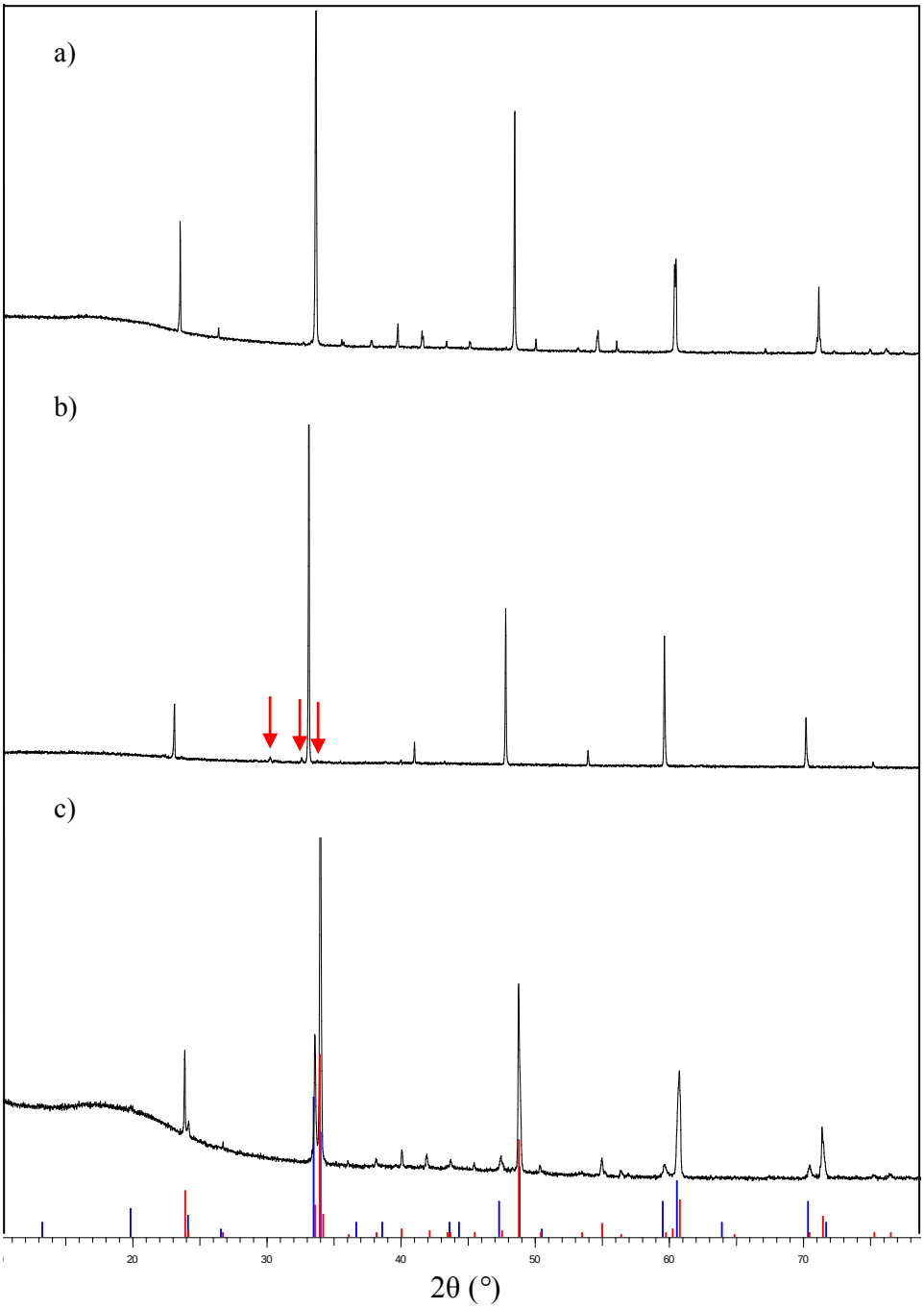

Figure 6.11 X-ray diffraction patterns of a) $CaMnO_{3-\delta}$ b) $CaMn_{0.85}P_{0.15}O_{3-\delta}$ showing impurity peaks ($Ca_3(PO_4)_2$) with red arrows c) $CaMn_{0.85}O_{3-\delta}$ showing $CaMnO_{3-\delta}$ (red lines) and $Ca_4Mn_3O_{10}$ (blue lines).

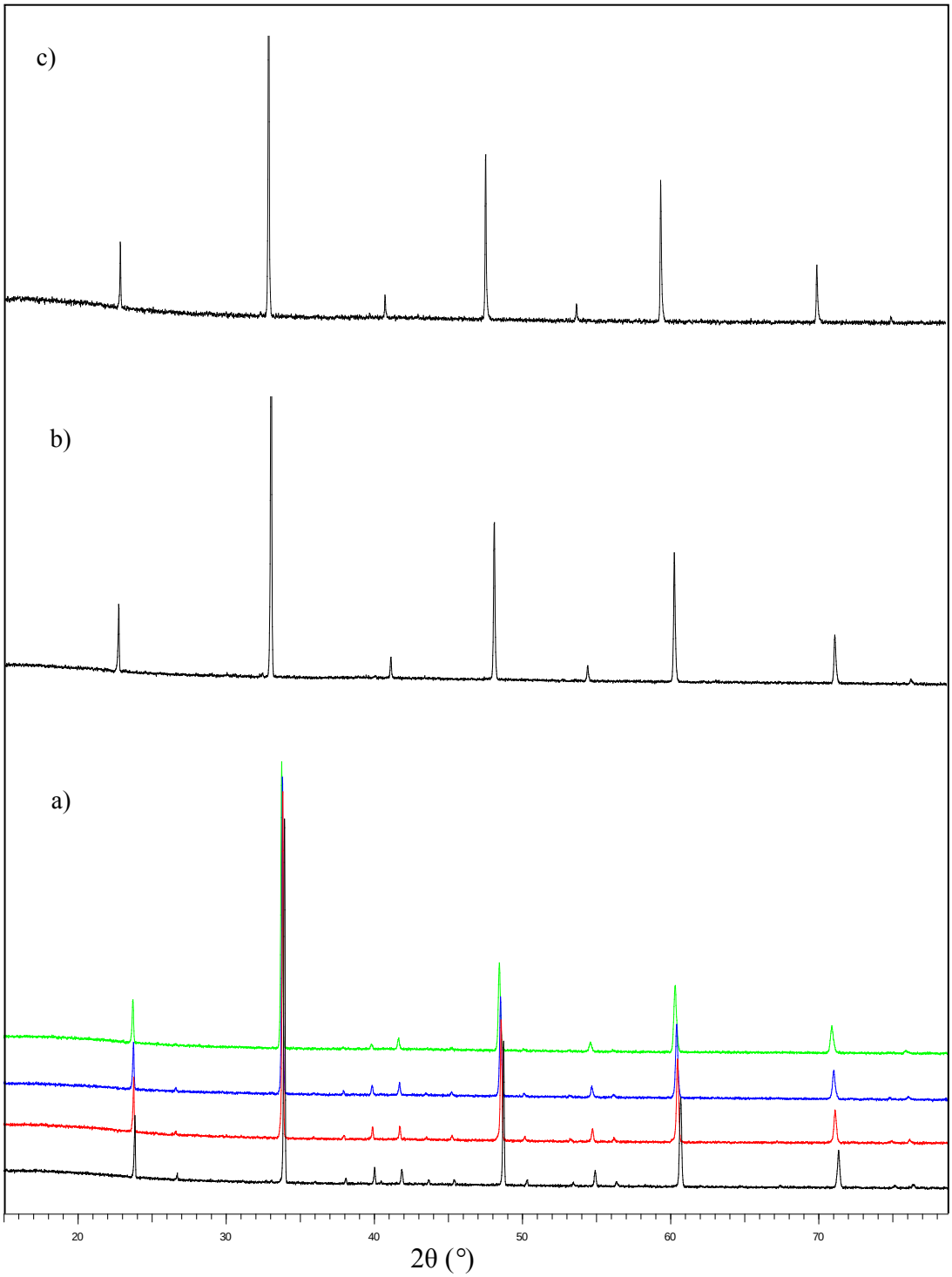

Figure 6.12 XRPD patterns of a) lower phosphate doped $CaMnO_{3-\delta}$ phases, x = 0.02 (black), x = 0.04 (red), x = 0.06 (blue) and x = 0.08 (green) b) $CaMn_{0.90}P_{0.1}O_{3-\delta}$ phase c) $CaMn_{0.88}P_{0.12}O_{3-\delta}$ phase.

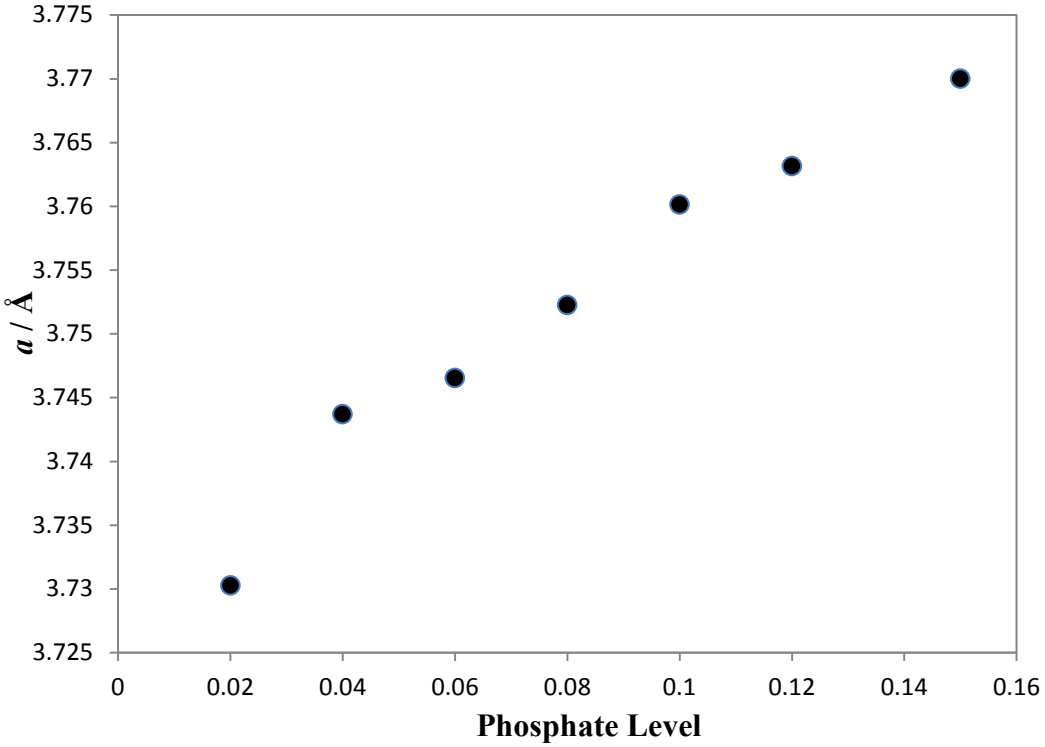

Figure 6.13 Variation of *a* parameter (pseudo cubic parameter for $x < 0.08$) with the phosphate level in $CaMn_{1-x}P_xO_{3-\delta}$ phases (the error bars are not used since pseudo cubic parameters were used for $x < 0.08$ phases).

Table 6.7 Cell parameters for $CaMn_{1-x}P_xO_{3-\delta}$ phases.

Phosphate Level	*a* / Å	*b* / Å	*c* / Å	Pseudo cubic lattice parameter
0.00	5.28310(6)	7.45727(8)	5.26759(6)	3.7297
0.02	5.2832(1)	7.4567 (1)	5.2703(2)	3.7303
0.04	5.2878(1)	7.4791(1)	5.3068(3)	3.7437
0.06	5.2944(2)	7.48717(7)	5.3066(4)	3.7465
0.08	3.75224(7)			
0.10	3.76014(6)			
0.12	3.76315(4)			
0.15	3.76999(3)			

Thermogravimetric analysis was carried out by heating $CaMnO_{3-\delta}$ and $CaMn_{1-x}P_xO_{3-\delta}$ phases to 900 ℃ in 10% H_2(g) / 90% N_2(g). XRPD analysis of the resulting material revealed that $CaMnO_{3-\delta}$ had been decomposed to $CaMnO_2$ (*Figure 6.14*) and this was in accordance with the mass loss observed in thermogravimetric analysis. All phosphate doped phases had been decomposed to a mixture of $CaMnO_2$ and $Ca_2P_2O_7$. The weight loss observed for each compound was used to determine the oxygen content and the data are given in *Table 6.8*.

Table 6.8 Oxygen content and oxidation state of Mn in $CaMn_{1-x}P_xO_{3-\delta}$ phases (from TGA).

Phosphate level	Oxygen Content	Mn Oxidation State
0.00	2.98	3.96
0.02	2.95	3.88
0.04	2.92	3.79
0.06	2.91	3.74
0.08	2.90	3.70
0.10	2.93	3.73
0.12	2.82	3.45
0.15	2.82	3.40

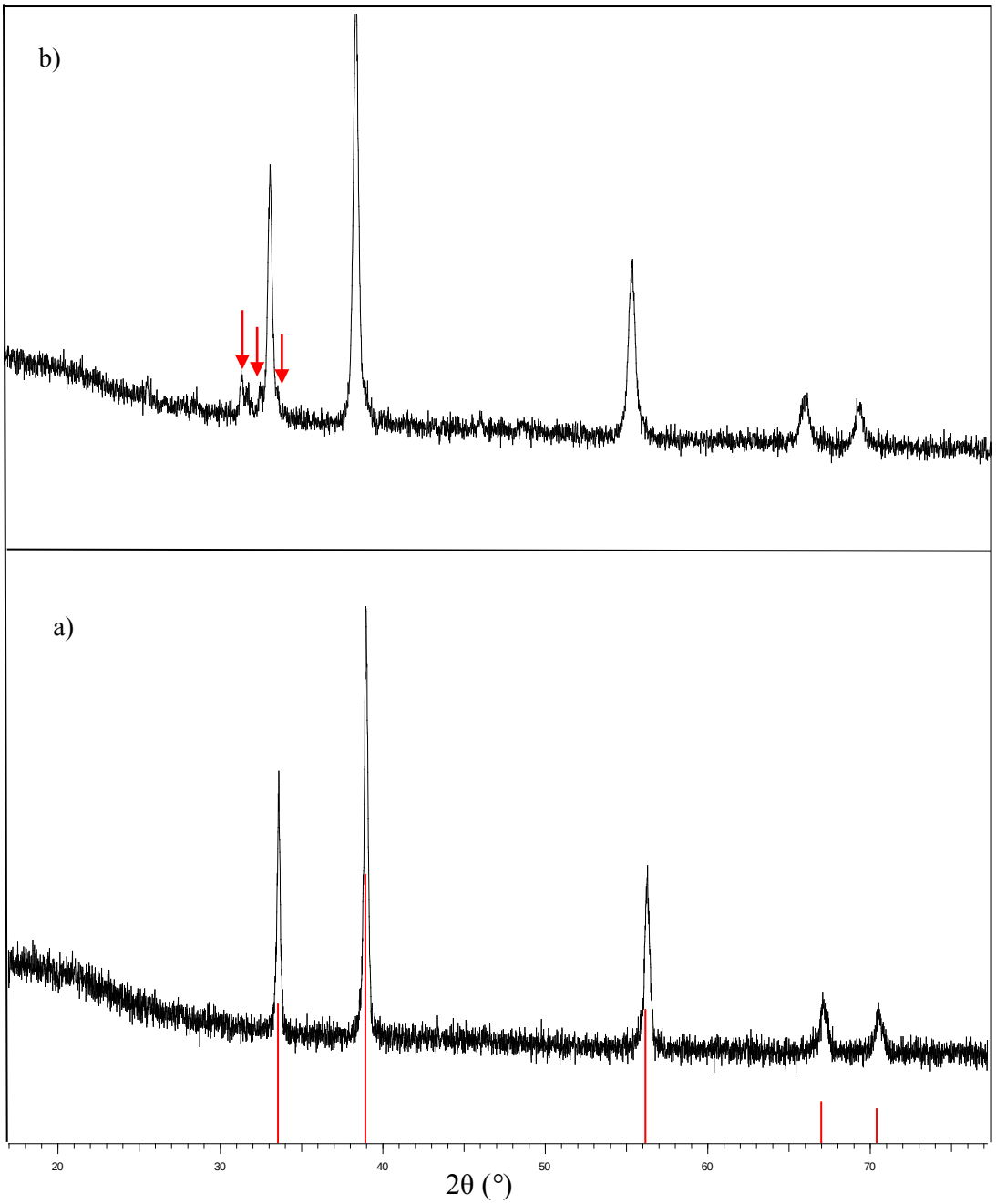

Figure 6.14 XRPD patterns of reduced product of a) $CaMnO_{3-\delta}$ ($CaMnO_2$ in red lines) b) $CaMn_{0.92}P_{0.08}O_{3-\delta}$ ($CaMnO_2$ and $Ca_2P_2O_7$ (shown by arrows)).

In phosphate doped $CaMnO_{3-\delta}$ phases the oxygen content and the oxidation state of Mn decrease with the increase of phosphate level as indicated by TGA data. The greater reduction of Mn^{4+} at higher phosphate levels results in an expansion of the unit cell volume. Similar observations have been reported for the phosphate doped $CaMnO_{3-\delta}$ phases (x = 0.025, 0.05) by Porras-Vazquez *et al.*[27] except for the higher oxygen deficiency observed in $CaMn_{0.95}P_{0.05}O_{3-\delta}$ (x = 0.05). The reported oxygen content for $CaMn_{1-x}P_xO_{3-\delta}$ (x = 0.025, 0.05) phases are 0.08 and 0.15, respectively. Thermogravimetric analysis to estimate the oxygen content had been carried out at 1200 ℃ in N_2(g), whereas in current work TGA was carried out at 900 ℃ in 10% H_2(g) / 90% N_2(g). But the cell parameters and the cell volumes reported for these two phases (*Table 6.9*) are consistent with the data obtained in present work for the $CaMn_{1-x}P_xO_{3-\delta}$ phases (x = 0.02, 0.04 and 0.06).

Table 6.9 Cell parameters reported for $CaMn_{1-x}P_xO_{3-\delta}$ phases by Porras-Vazquez *et al.*[27]

Phosphate Level	***a* / Å**	***b* / Å**	***c* / Å**	***V* / Å**
0.00	5.2828(1)	7.4574(1)	5.2672(1)	207.57(1)
0.025	5.2825(4)	7.4684(2)	5.2783(4)	208.24(2)
0.05	5.3000(3)	7.4923(2)	5.2911(3)	210.11(2)

6.5 Insertion of Sulphate into $CaMnO_{3-\delta}$

High purity Mn_2O_3, $CaCO_3$ and $(NH_4)_2SO_4$ (Aldrich, >99%) were used to synthesise the $CaMn_{1-x}S_xO_{3-\delta}$ ($0.02 \leq x \leq 0.06$) phases. The stoichiometric amounts of the reactants were ground together and heated at 1325 ℃ for 48 hrs in air with intermittent grinding. XRPD was used to check the formation and purity of these phases.

6.5.1 Structural Characterisation

Single phase samples of $CaMn_{1-x}S_xO_{3-\delta}$ were obtained only at x = 0.02 and 0.04 as indicated by X-ray powder diffraction data. No change in cell symmetry from the original material $CaMnO_{3-\delta}$ was observed and both phases were orthorhombic. The X-ray powder diffraction patterns of these phases are shown in *Figure 6.15*. As previously observed in other doped phases, at higher dopant levels (x = 0.06) a secondary phase $CaMn_2O_4$ was formed (*Figure 6.15*). Sulphate anion insertion at each level was confirmed by corresponding Mn deficient samples $CaMn_{1-x}O_{3-\delta}$ ($0.02 \leq x \leq 0.06$). The unit cell parameters determined from XRPD data using Rietveld refinement are given in *Table 6.10*.

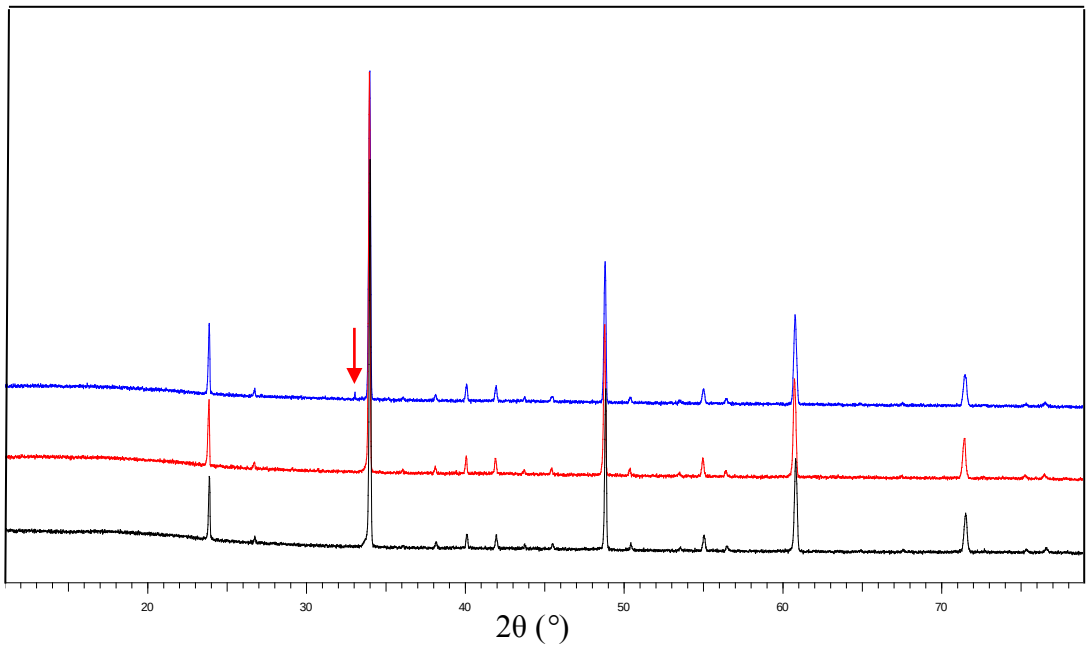

Figure 6.15 XRPD patterns of sulphate doped $CaMnO_{3-\delta}$ phases, x = 0.02 (black), x = 0.04 (red) and x = 0.06 (blue), impurity phase ($CaMn_2O_4$) is shown with a red arrow.

Table 6.10 Cell Parameters for $CaMn_{1-x}S_xO_{3-\delta}$ phases.

Sulphate Level	***a* / Å**	***b* / Å**	***c* / Å**
0.00	5.28310(6)	7.45727(8)	5.26759(6)
0.02	5.2772 (1)	7.4491(2)	5.2638(2)
0.04	5.2782(1)	7.4483(2)	5.2653(1)

Thermogravimetric analysis was used to estimate the oxygen content of these phases. The sulphate doped $CaMnO_{3-\delta}$ samples were heated in flowing 10% H_2(g) / 90% N_2(g) to 900 ℃ and maintained at this temperature. XRPD analysis of the resulting materials

revealed that all sulphate doped phases decomposed to a mixture of $CaMnO_2$ and CaS_2O_7 (*Figure 6.16*). The weight loss observed for each compound was used to determine the oxygen content and for both, a total oxygen content of 3 was indicated. The oxidation state of Mn in $CaMn_{0.98}S_{0.02}O_{3-\delta}$ and $CaMn_{0.96}S_{0.04}O_{3-\delta}$ phases are 3.96 and 3.91, respectively. Even though the unit cell sizes of these phases slightly increase with the increase of sulphate level due to the reduction of Mn^{4+} both unit cells are smaller in size than that of $CaMnO_{3-\delta}$. This could be due to the small size of sulphur.

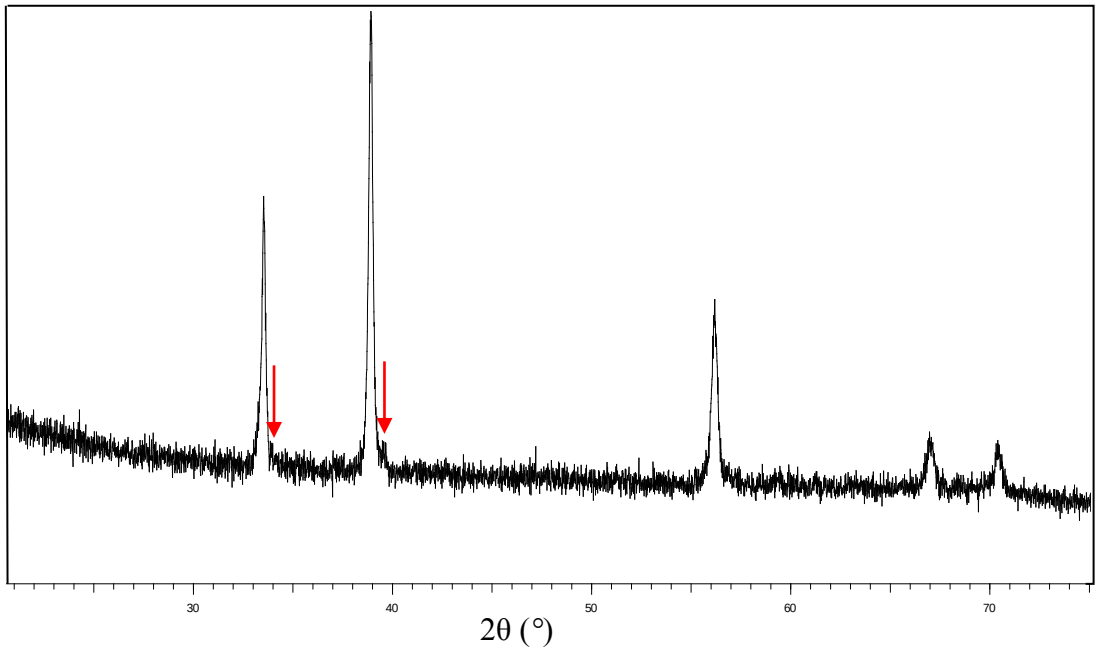

Figure 6.16 X-ray powder diffraction pattern of reduced $CaMn_{0.98}S_{0.02}O_{3-\delta}$ phase ($CaMnO_2$ and CaS_2O_7 (shown with red arrows)).

6.6 Conclusion

In this work, phosphate and sulphate anions have been successfully inserted into the perovskite structures; $SrFeO_{3-\delta}$ and $CaMnO_{3-\delta}$. The level of phosphate that could be inserted into both of these phases is higher than that of sulphate anions. In all sulphate doped phases the oxygen content found to be close to 3. Incorporation of phosphate and sulphate anions into $SrFeO_{3-\delta}$ stabilised the cubic structure at all levels. In oxy-anion doped $CaMnO_{3-\delta}$ phases, the cubic structure was stabilised only at higher dopant levels and at lower levels the phases were orthorhombic. The unit cell sizes of all oxy-anion incorporated phases increased with the dopant level. The reduction of B^{4+} (B = Fe, Mn) to B^{3+} could result in an increase in the unit cell. However, according to the TGA data the degree of reduction is relatively low. The smaller unit cell volumes in $CaMn_{1-x}S_xO_{3-\delta}$ phases compare to that of the parent oxide could be due to the smaller size of S^{6+} ions. Furthermore, incorporation of oxy-anions into $SrFeO_{3-\delta}$ and $CaMnO_{3-\delta}$ failed to introduce more oxygen deficiencies as it would if BO_6 octahedra being replaced by phosphate (PO_4^{3-}) or sulphate (SO_4^{2-}) anions.

6.7 References

1. Mitchell, R. H., *Perovskites: Modern and Ancient*. Almaz Press: Canada, 2002.
2. Orera, A.; Slater, P. R. *Chem. Mater.* **2010**, 22, 675.
3. Jacobson, A. J. *Chem. Mater.* **2010**, 22, 660.
4. Lastaberg, A.; Skinner, S. J. *J. Mater. Chem.* **2006**, 16, 3161.
5. Ishihara, T., *Perovskite Oxide for Solid Oxide Fuel Cells*. Springer: 2009.
6. von Schnering, H. G.; Hartweg, M.; Walz, L.; Popp, T.; Becker, T.; Schwarz, M. *Jahresber MPI Festkörperf (Stuttgart)* **1988**, p 94.
7. Müller-Buschbaum, H. K. *Angew. Chem. Int. Edn. Engl.* **1989**, 28, 1472.
8. Fomichev, D. V.; Kharlanov, A. L.; Antipov, E. V.; Kovba, L. M. *Sverhprovodimost* **1990**, 3, 1280.
9. Greaves, C.; Slater, P. R. *J. Mater. Chem.* **1991**, 1, 17.
10. Greaves, C.; Slater, P. R. *Physica* C **1991**, 175, 172.
11. Miyazaki, Y.; Yamane, H.; Ohnishi, N.; Kajitani, T.; Hiraga, K.; Morii, Y.; Funahashi, S.; Hirai, T. *Physica* C **1992**, 198, 7.
12. Miyazaki, Y.; Yamane, H.; Kajitani, T.; Kobayashi, N.; Hiraga, K.; Morii, Y.; Funahashi, S.; Hirai, T. *Physica* C **1994**, 230, 89.
13. Akimitsu, J.; Uehara, M.; Ogawa, M.; Nakata, H.; Tomimoto, K.; Miyazaki, Y.; Yamane, H.; Hirai, T.; Kinoshita, K.; Matsui, Y. *Physica* C **1992**, 201, 320.
14. Maignan, A.; Hervieu, M.; Michel, C.; Raveau, B. *Physica* C **1993**, 208, 116.
15. Li, J. Q.; Zhu, W. J.; Zhao, Z. X.; Yin, D. L. *Solid State Commun*. **1993**, 85, 739.
16. Zhu, W. J.; Yue, J. J.; Huang, Y. Z.; Zhao, Z. X. *Physica* C **1993**, 205, 118.
17. Slater, P. R.; Greaves, C.; Slaski, M.; Murihead, C. M. *Physica* C **1993**, 208, 193.
18. Krekels, T.; Milat, O.; van Tendeloo, G.; van Landuyt, J.; Amelinckx, S.; Slater, P. R.; Greaves, C. *Physica* C **1993**, 210, 439.
19. Slater, P. R.; Greaves, C.; Slaski, M.; Murihead, C. M. *Physica* C **1993**, 213, 14.
20. Nagarajan, R.; Aygappan, S.; Rao, C. N. R. *Physica* C **1994**, 220, 373.
21. Slater, P. R.; Greaves, C.; Slaski, M. *Physica* C **1994**, 235, 741.
22. Greaves, C.; Al Mamouri, M.; Slater, P. R.; Edwards, P. P. *Physica* C **1994**, 235, 158.
23. Slater, P. R.; Greaves, C. *Physica* C **1994**, 223, 37.
24. Shin, J. F.; Hussey, L.; Orera, A.; Slater, P. R. *Chem. Commun*. **2010**, 46, 4613.

25. Shin, J. F.; Orera, A.; Appereley, D. C.; Slater, P. R. *J. Mater. Chem*. **2011**, 21, 874.
26. Hancock, C. A.; Slade, R. C. T.; Varcoe, J. R.; Slater, P. R. *J. Solid State Chem*. **2011**, 184, 2972.
27. Porras-Vazquez, J. M.; Kemp, T. F.; Hanna, J. V.; Slater, P. R. *J. Mater. Chem*. **2012**, 22, 8287.
28. Porras-Vazquez, J. M.; Slater, P. R. *J. Power Sources* **2012**, 209, 180.
29. Greaves, C.; Jacobson, A. J.; Tofield, B. C.; Fender, B. E. F. *Acta Cryst*. **1975**, B31, 641.
30. Gallagher, P. K.; MacChesney, J. B.; Buchanan, D. N. E. *J. Chem. Phys.* **1964**, 41, 2429.

CHAPTER SEVEN

Conclusions and Further Work

7.1 Synthesis and Characterisation of Double Perovskites $LaSr_2Fe_2SbO_9$ and $La_2Sr_2Fe_3SbO_{12}$

The double perovskites $LaSr_2Fe_2SbO_9$ and $La_2Sr_2Fe_3SbO_{12}$ which are analogues of Sr_2FeSbO_6 have been successfully synthesised. A G-type long-range antiferromagnetism is present in these materials at 300 K and 2 K, and the Néel temperatures for both compounds are higher than 300 K. The distribution of Fe^{3+} between the two *B* sites as confirmed by Mössbauer spectroscopy is of 1 : 2 ratio for both compounds. It would be interesting to investigate the crystal and magnetic structures of similar phases with different lanthanide (Nd, Eu) and alkaline metal (Ca, Sr, Ba) cations in the *A* site, to study how *A* site cation size affects to the cation distribution at the *B* site and on magnetic properties. Another aspect of future work would be to investigate the possibility of obtaining mixed ion valencies (Fe^{3+} / Fe^{4+}) in these types of materials for ionic conductivity.

7.2 Synthesis and Characterisation of *n* = 2 Ruddlesden-Popper Phases $Ln_2SrFe_2O_7$ (Ln = La, Nd, Eu) and $La_2BaFe_2O_7$

It is confirmed that the cation order depends on the size of the two cations present in the *A* site. The smaller lanthanide cations in the rock-salt layers and larger alkaline metal cations in the perovskite blocks result in fully ordered cation distribution at the *A* site. As proved

by neutron powder diffraction data and Mössbauer spectroscopy, these phases are antiferromagnetically ordered at 300 K and 2 K. The reason behind the magnetic moment reorientation observed in $Nd_2SrFe_2O_7$ and $La_2BaFe_2O_7$ is still not clear and needs further investigation. Also the two sextets appeared in Mössbauer spectra recorded for these phases and fluorinated $La_2BaFe_2O_7$ phase require an explanation and so further analysis is required to resolve these problems.

7.3 Fluorination of *n* = 2 Ruddlesden-Popper Phases $Ln_2SrFe_2O_7$ (Ln = La, Nd, Eu) and $La_2BaFe_2O_7$

Fluorination of $Ln_2SrFe_2O_7$ (Ln = La, Nd, Eu) and $La_2BaFe_2O_7$ have been investigated using X-ray powder diffraction. In $La_2SrFe_2O_5F_4$, $La_2BaFe_2O_5F_4$ and $Nd_2SrFe_2O_5F_4$, the reaction happened *via* anion insertion and anion substitution without oxidising the metal cation in the FeO_6 octahedra which has never been reported in previous work. This was confirmed for $La_2BaFe_2O_5F_4$ using Mössbauer spectroscopy, which also indicated the presence of long-range magnetic ordering in $La_2BaFe_2O_5F_4$ at 298 K and 16 K. In contrast to these three fluorinated phases, the fluorination of $Eu_2SrFe_2O_7$ happened *via* oxidative insertion, oxidising Fe^{3+} to Fe^{4+}. This work shows the possibility of controlling the oxidative effect of fluorination in layered structures. Structural and magnetic properties of these phases will be thoroughly investigated using neutron powder diffraction data and Mössbauer spectroscopy.

7.4 Insertion of Oxy-anions into Perovskite Structures $SrFeO_{3-\delta}$ and $CaMnO_{3-\delta}$

The phosphate and sulphate anion doped phases of $SrFeO_{3-\delta}$ and $CaMnO_{3-\delta}$ have been investigated using XRPD data and thermogravimetric analysis. The results suggest mixed ionic and electronic conducting characteristic in these phases due to the oxygen vacancies and *B* site mixed valency (B^{4+} / B^{3+}) created by oxy-anion incorporation. Insertion of phosphate anions compared to that of sulphate anions has been proved to be more promising in terms of introducing oxygen vacancies. It would also be interesting to investigate the possibility of inserting other oxy-anions such as carbonate and borate anions into these two phases.

Appendix 5.1 The XRPD pattern of the decomposed sample and the calculations for the composition of fluorinated $La_2BaFe_2O_7$ phase.

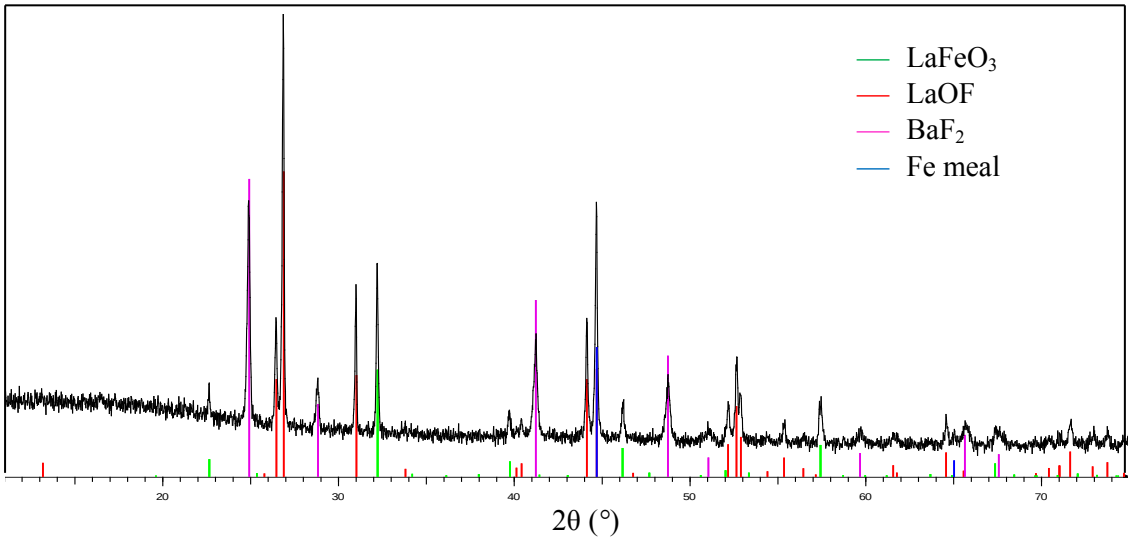

Calculations:

1) The fluorinated sample contained an impurity $LaFeO_3$ (1.91(8)% by weight). So the observed weight loss was corrected in order to obtain the actual weight loss of the pure fluorinated sample.

Weight loss obtained from TGA = 7.01%

Corrected weight loss:

$$\frac{7.01}{(100 - 1.91)} \times 100 = 7.15\%$$

2) Considering $LaFeO_3$ to be a decomposed product:

$La_2BaFe_2O_yF_x \longrightarrow LaFeO_3 + LaOF + BaF_2 + Fe$ } 647.82 g mol^{-1}

This indicates that the F^- content $x = 3$

Thus, the weight loss expected for the composition $La_2BaFe_2O_6F_3$ (679.85 g mol^{-1}) is:

$$\frac{679.85 - 647.82}{679.85} \times 100 = 4.71\%$$

This value indicates that $LaFeO_3$ is not a decomposed product.

3) Calculations for the composition of fluorinated $La_2BaFe_2O_7$ phase:

$La_2BaFe_2O_yF_x \longrightarrow 2\ LaOF + BaF_2 + 2\ Fe \}$ 634.85 g mol^{-1}

This suggests that the fluorine ion content $x = 4$

The expected weight loss is then calculated as shown below considering the composition of the fluorinated product to be $La_2BaFe_2O_5F_4$ (682.85 g mol^{-1}):

$$\frac{682.85 - 634.85}{682.85} \times 100 = 7.03\%$$

The calculated weight loss is consistent with the corrected weight loss obtained from TGA. Hence, the composition is $La_2BaFe_2O_5F_4$.

Appendix 5.2 Bond valence sum calculations using bond lengths obtained from Rietveld profile refinement using the space group *I*4/*mmm* based on XRPD data of fluorinated $La_2BaFe_2O_7$ phase.

Refined bond lengths:

Fe-O1 ap: *r* = 1.934(5)

Fe-O2 eq: *r* = 1.9984(17)

Fe-O3 ap: *r* = 1.951(19)

r_0 values:

Fe(III)-O: r_0 = 1.759(3)

Fe(III)-F: r_0 = 1.679(5)

S = exp $\left[\frac{r_0 - r}{B}\right]$ where B = 0.37

Fe-O1ap S = exp [(1.759 – 1.934) / 0.37] = 0.62315

Fe-O2eq S = exp [(1.759 – 1.9984) / 0.37] = 0.52360

Fe-O3ap S = exp [(1.759 – 1.951) / 0.37] = 0.59516

Fe-F3ap S = exp [(1.679 – 1.951) / 0.37] = 0.47944

Fe-F2eq S = exp [(1.679 – 1.9984) / 0.37] = 0.42179

Fe-F1ap S = exp [(1.679 – 1.934) / 0.37] = 0.50198

Oap: V_i = (1 × Fe-O1ap) + (4 × Fe-O2eq) + (1 × Fe-O3ap) = 3.31271

F3ap: V_i = (1 × Fe-O1ap) + (4 × Fe-O2eq) + (1 × Fe-F3ap) = 3.19699

F2eq: V_i = (1 × Fe-O1ap) + (2 × Fe-F2eq) + (2 × Fe-O2eq) + (1 × Fe-O3ap) = 3.10909

F1ap + F3ap : V_i = (1 × Fe-F1ap) + (4 × Fe-O2eq) + (0.5 × Fe-F3ap) + (0.5 × Fe-O3ap)
= 3.13368

F1ap + F2eq : V_i = (1 × Fe-F1ap) + (1 × Fe-F2eq) + (3 × Fe-O2eq) + (1 × Fe-O3ap)
= 3.0897

Appendix 5.3 The XRPD pattern of the decomposed sample and the calculations for the composition of fluorinated $Nd_2SrFe_2O_7$ phase.

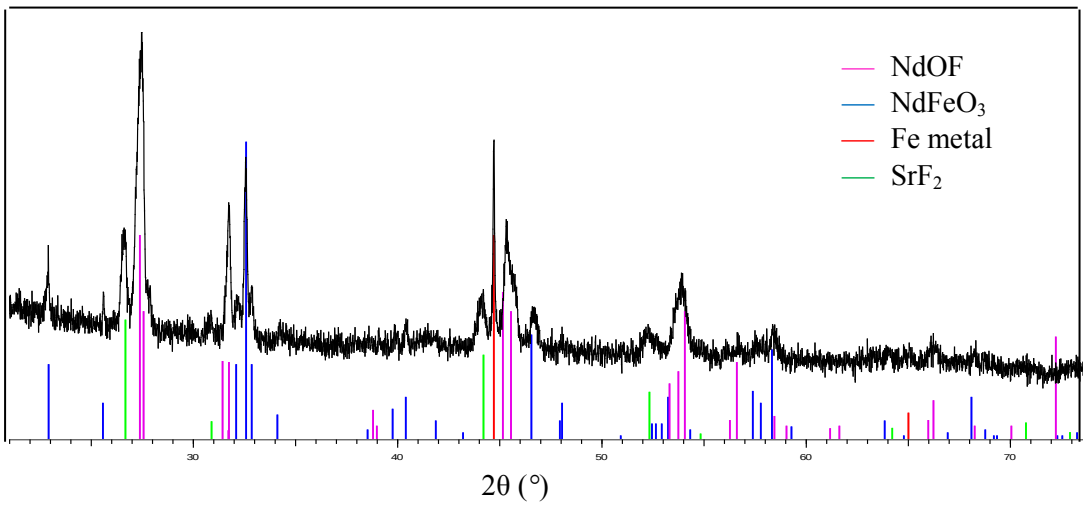

Calculations:

1) The sample consisted of a perovskite impurity $NdFeO_3$ (15.8(1)% by weight)

Weight loss obtained from TGA = 6.5%

Corrected weight loss:

$$\frac{6.5}{(100 - 15.8)} \times 100 = 7.7\%$$

2) Considering $NdFeO_3$ as a decomposed product:

$$Nd_2SrFe_2O_yF_x \longrightarrow NdFeO_3 + NdOF + SrF_2 + Fe \} \ 608.8 \text{ g mol}^{-1}$$

This suggests that fluorine ion content $x = 3$

Thus, the weight loss expected for the composition $Nd_2SrFe_2O_6F_3$ (640.8 g mol^{-1}) is:

$$\frac{640.8 - 608.8}{640.8} \times 100 = 4.99\%$$

This value indicates that $NdFeO_3$ is not a decomposed product.

3) Calculations for the composition of fluorinated $Nd_2SrFe_2O_7$ phase:

$$Nd_2SrFe_2O_yF_x \longrightarrow 2\ NdOF + SrF_2 + 2\ Fe\ \} \ 595.8\ g\ mol^{-1}$$

This suggests that the fluorine content $x = 4$

The expected weight loss is then calculated as shown below considering the composition of the fluorinated product to be $Nd_2SrFe_2O_5F_4$ (643.8 g mol^{-1}):

$$\frac{643.8 - 595.8}{643.8} \times 100 = 7.45\%$$

The calculated weight loss is consistent with the corrected mass loss obtained from TGA. Hence, the composition is $Nd_2SrFe_2O_5F_4$.

Appendix 5.4 The XRPD pattern of the decomposed sample and the calculations for the composition of fluorinated $La_2SrFe_2O_7$ phase.

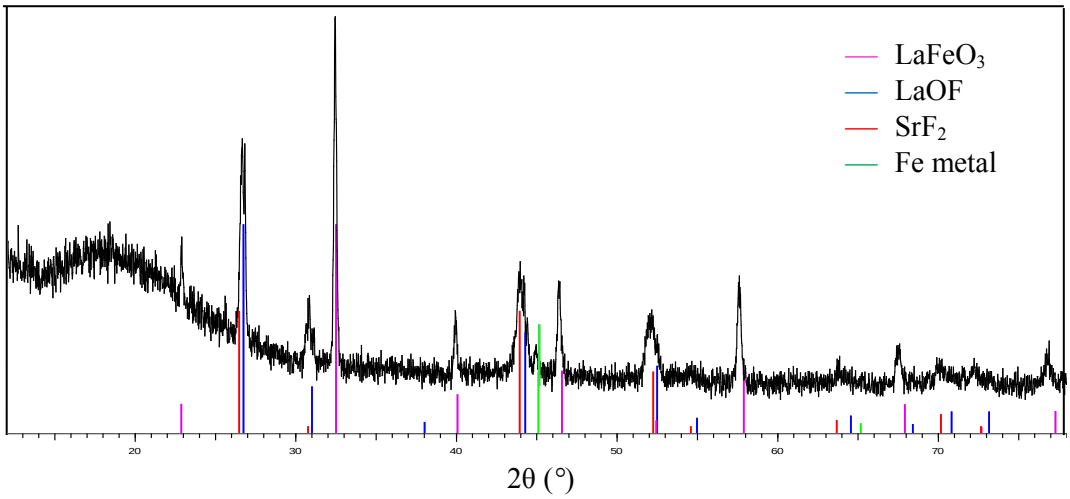

Calculations:

1) Considering $LaFeO_3$ as a decomposed product:

The sample consisted of an impurity $LaFeO_3$ (21.03(6)% by weight)

Weight loss obtained from TGA = 6.23%

For 1 mol of oxide-fluoride material:

$La_2SrFe_2O_6F_3 \longrightarrow LaOF + SrF_2 + Fe + LaFeO_3$

630.14 g 598.14 g

Weight of the impurity in 1 mol of $La_2SrFe_2O_6F_3$ = 167.808 g

Weight of the initial material = 797.948 g Weight of the final material = 765.948 g

Expected weight loss:

$$\frac{797.948 - 765.948}{797.948} = 4.01\%$$

This confirms that $LaFeO_3$ is not a decomposed product.

2) Calculation for the composition:

$La_2SrFe_2O_yF_x \longrightarrow 2\ LaOF + SrF_2 + 2\ Fe\ \}\ 585.14\ g\ mol^{-1}$

This suggests that the fluorine content $x = 4$

The expected weight loss for the composition $La_2SrFe_2O_5F_4$ (633.14 g mol^{-1}):

Weight of the impurity in 1mol of $La_2SrFe_2O_5F_4$ = 168.607 g

$$\frac{801.747 - 753.747}{801.747} \times 100 = 5.99\%$$

This confirms that the composition of the fluorinated product is $La_2SrFe_2O_5F_4$.

Appendix 5.5 The XRPD pattern of the decomposed sample and the calculations for the composition of fluorinated $Eu_2SrFe_2O_7$ phase.

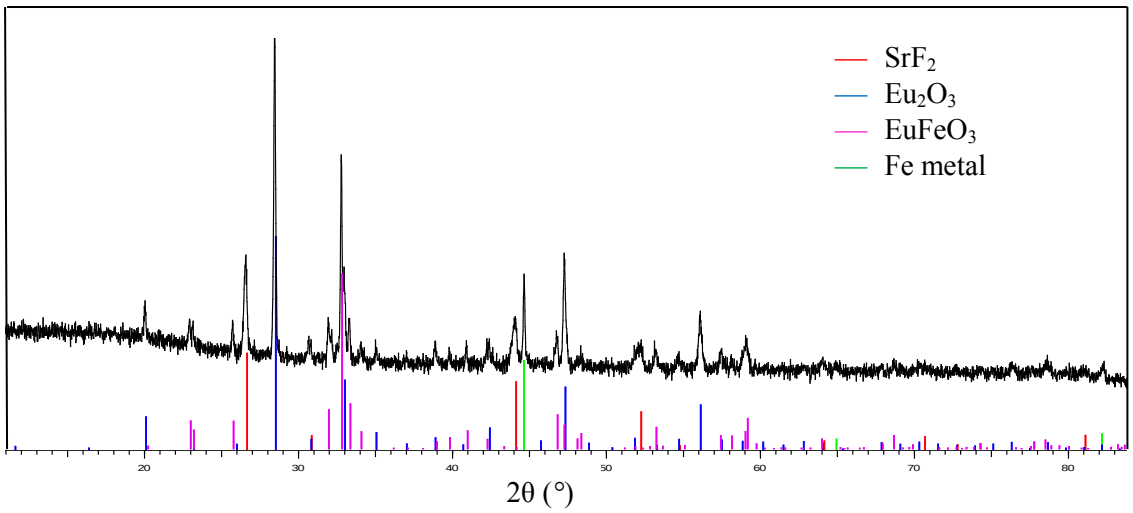

Calculations:

1) The sample consisted of an impurity $EuFeO_3$ (7.1(2)% by weight)

Weight loss obtained from TGA = 5.5%

Corrected weight loss:

$$\frac{5.5}{(100-7.1)} \times 100 = 5.9\%$$

2) Considering $EuFeO_3$ as a decomposed product:

$$Eu_2SrFe_2O_yF_x \longrightarrow EuFeO_3 + \frac{1}{2}Eu_2O_3 + SrF_2 + Fe \} \ 613.25 \text{ g mol}^{-1}$$

This suggests that fluorine content $x = 2$

Thus, the weight loss expected for the composition $Eu_2SrFe_2O_7F_2$ (653.25 g mol^{-1}):

$$\frac{653.25-613.25}{653.25} \times 100 = 6.1\%$$

The calculated weight loss is consistent with the corrected mass loss obtained from TGA and indicates the possibility of considering $EuFeO_3$ as a decomposed product.

3) Calculations for the composition of fluorinated $Eu_2SrFe_2O_7$ phase considering only Eu_2O_3, SrF_2 and Fe to decomposed products:

$$Eu_2SrFe_2O_yF_x \longrightarrow Eu_2O_3 + SrF_2 + 2\ Fe\ \} \ 589.25\ g\ mol^{-1}$$

This also indicates that the fluorine content $x = 2$

The expected weight loss for the composition $Eu_2SrFe_2O_7F_2$ (653.25 g mol^{-1}):

$$\frac{653.25 - 589.25}{653.25} \times 100 = 9.8\%$$

Above calculation also suggests a composition $Eu_2SrFe_2O_7F_2$ for the fluorinated $Eu_2SrFe_2O_7$ phase but the weight loss calculated for this composition is too large.

Appendix 5.6 Bond valence sum calculations using bond lengths obtained from Rietveld profile refinement using the space group *I*4/*mmm* based on XRPD data of fluorinated $Eu_2SrFe_2O_7$ phase.

Refined bond lengths:

Fe-O1 ap: *r* = 1.88(1)

Fe-O2 eq: *r* = 1.964(4)

Fe-O3 ap: *r* = 1.93(6)

r_0 values:

Fe(III)-O: r_0 = 1.759(3)

Fe(III)-F: r_0 = 1.679(5)

$S = \exp\left[\frac{r_0 - r}{B}\right]$ where B = 0.37

Fe-O1ap S = exp [(1.759 – 1.88) / 0.37] = 0.721064

Fe-O2eq S = exp [(1.759 – 1.964) / 0.37] = 0.574616

Fe-O3ap S = exp [(1.759 – 1.93) / 0.37] = 0.629920

Oap: V_i = (1 × Fe-O1ap) + (4 × Fe-O2eq) + (1 × Fe-O3ap) = 3.649448